POLYTECHNIQUE MONTRÉAL

affiliée à l'Université de Montréal

Characterization of brittle deformation in geological composite materials (felsic mylonites and layered sedimentary rocks) and estimation of paleostresses

LE LI

Département des génies civil, géologique et des mines

Thèse présentée en vue de l'obtention du diplôme de *Philosophiae Doctor*

Génie minéral

Janvier 2022

© Le Li, 2022.

POLYTECHNIQUE MONTRÉAL

affiliée à l'Université de Montréal

Cette thèse intitulée :

Characterization of brittle deformation in geological composite materials (felsic mylonites and layered sedimentary rocks) and estimation of paleostresses

présentée par **Le LI**

en vue de l'obtention du diplôme de *Philosophiae Doctor*

a été dûment acceptée par le jury d'examen constitué de :

Li LI, président

Shaocheng JI, membre et directeur de recherche

Félix GERVAIS, membre

James KIRKPATRICK, membre externe

DEDICATION

To everyone who loves me.

ACKNOWLEDGEMENTS

First of all, I would like to thank my supervisor, Prof. Shaocheng Ji, not only for providing me the opportunity and financial support to study in École Polytechnique de Montréal, but also for his guidance, help and patience for me during my whole doctoral study. His enthusiasm in classes, intelligence and diligence on research inspire me, his rigorous and efficient work habits benefit me and his insights and thoughts on various scientific problems encourage me to explore more research fields in geology in my future career.

I am also grateful to Prof. Denis Marcotte for his patient instruction and explanation on topics in courses and the project in seminar. I should also thank Profs. Li Li as the President of the jury, James Kirkpatrick as the external examinator, and Félix Gervais as the member of jury for their critical but constructive comments and suggestions which are helpful for the clarification and presentation of the dissertation.

I appreciate École Polytechnique de Montréal for exempting most of my tuition fee. I also want to thank Mrs. Monique Malouin, Mrs. Myriam Fortin, Mrs. Sooraya Balgobin and Mrs. Margareth Mompoint for their help and support during the last 5 years.

I would also like to thank Prof. Wei Lin and Prof. Jun Gao, both from the Institute of Geology and Geophysics, Chinese Academy of Sciences, for their guidance and support at the beginning of my research career, and their encouragement for me to study here in Canada.

Thanks to all my friends in Montreal for their companion and help during the last 5 years, and may our friendship last forever.

Finally, I need to thank my family for their unreserved love and support for me.

RÉSUMÉ

La rhéologie des roches polyphasées (par exemple, les roches polyminérales et les roches sédimentaires stratifiées) est devenue l'un des domaines de recherche les plus dynamiques des sciences de la Terre au cours des 25 dernières années. Cependant, les processus de déformation des matériaux composites géologiques sont compliqués car les composants compétents et incompétents ont tendance à se déformer de différentes manières sous les mêmes conditions de température et de pression. La déformation fragile des composants compétents est généralement contrôlée par la déformation ductile des composants incompétents dans lesquels ils sont encastrés. Par conséquent, la déformation fragile et les microstructures résultantes des composants compétents contiennent des informations importantes pour interpréter les propriétés mécaniques et le comportement rhéologique de leurs matériaux incompétents environnants, ainsi que des informations sur l'amplitude de la contrainte géologique. Sur la base de mesures et d'analyses sur la caractérisation de la déformation fragile dans les gneiss et mylonites felsiques, et les roches sédimentaires intercalées, la présente étude vise à trouver des piézomètres appropriés pour estimer les contraintes différentielles dans les matériaux composites géologiques de la croûte terrestre.

Cette thèse se compose de cinq chapitres. Le chapitre 1 introduit les concepts de base de la mécanique des milieux continus et les modèles mécaniques pour décrire les processus de déformation des matériaux composites géologiques. Dans ce cadre, chaque aspect lié à la déformation des matériaux composites géologiques, les méthodes de mesure de la contrainte, de la déformation et de la vitesse de déformation, les divers mécanismes de déformation et les structures correspondantes, la mécanique de la rupture, la loi d'écoulement et les modèles mécaniques existants sont brièvement présentés avec une revue critique.

Le chapitre 2 traite des données de micro-boudinage de tourmaline mesurées à partir d'échantillons de gneiss granitique et de mylonite felsique des zones de cisaillement Gaoligong et Chongshan dans le Province de Yunnan, dans le sud-ouest de la Chine. Après avoir examiné de manière critique le piézomètre construit sur le modèle de fracturation à mi-parcours, un nouveau piézomètre de micro-boudinage est développé sur la base du modèle de transfert de contrainte induite par cisaillement interfacial. Le nouveau piézomètre de micro-boudinage a une forme simple: $\tau = 0.25C/(L/W)$, où τ est la contrainte d'écoulement de cisaillement de la matrice ductile

(par exemple, le quartz polycristallin), C représente la résistance à la rupture par traction d'un minéral colonnaire (par exemple, tourmaline), et L et W sont la longueur et largeur du micro-boudin, respectivement. En prenant la résistance à la traction de la tourmaline C=145 MPa comme la valeur estimée, l'application du piézomètre sur les échantillons des zones de cisaillement de Gaoligong donne des contraintes d'écoulement de cisaillement de 21-61 MPa pour les gneiss granitiques et les mylonites felsiques. Les micro-boudins formés plus tôt ont des rapports longueur/largeur moyens toujours plus élevés que ceux formés plus tard, ce qui suggère que les roches ont enregistré une histoire tectonique de durcissement continu avant la cessation de la plasticité du quartz. L'application du piézomètre sur des échantillons de la zone de cisaillement de Chongshan, combinée à des observations microstructurales, des estimations indépendantes de la température de déformation, des âges géochronologiques précis de divers systèmes isotopiques et des données géophysiques régionales, fournissent des informations sur les taux de déformation ($\dot{\varepsilon}$), les contraintes différentielles (σ) et leurs corrélations avec la température et la profondeur correspondante pour la matrice de quartz polycristallin. Le profil de résistance à l'écoulement naturel sous la transition fragile-ductile donne une loi d'écoulement : $\dot{\varepsilon} = A\sigma^n exp(-Q/RT)$ avec n=4, Q=184 kJ/mol et A=7.180×10^{-7} MPa^{-n}s^{-1}. Les contraintes différentielles calibrées par cette loi d'écoulement sont encadrées par les bornes inférieure et supérieure obtenues respectivement par Luan et Paterson (1992) et Gleason et Tullis (1995), et sont très proches de la moyenne géométrique de ces deux bornes.

Le chapitre 3 vise à étendre l'applicabilité du piézomètre de micro-boudinage établi à base de tourmaline à d'autres minéraux. Le feldspath, en tant que l'un des minéraux les plus abondants dans la croûte, présente généralement un comportement fragile dans une matrice déformée plastiquement dans les conditions du faciès des schistes verts, ce qui en fait un excellent choix pour l'expansion du piézomètre. Différent des micro-boudins de tourmaline de forme régulière, les micro-boudins de feldspath sont traités comme des fibres circulaires-tronquées-coniques dans l'analyse mécanique. Un piézomètre de micro-boudinage de feldspath est établi avec la résistance à la traction estimée du feldspath. Nous appliquons le piézomètre sur des échantillons de mylonite granitique, dans lesquels des micro-boudins de feldspath incrustés dans la matrice ductile de quartz, provenant des zones de cisaillement de la rivière Rouge, de Chongshan et de Gaoligong dans le Yunnan, dans le sud-ouest de la Chine. Les contraintes différentielles estimées à partir des micro-boudins de feldspath formés plus tard sont plus importantes que celles formées

plus tôt, représentant une évolution au cours de l'exhumation de la mylonite vers le haut de la transition cassante-ductile. Les résultats du piézomètre à micro-boudinage à feldspath et du piézomètre à quartz recristallisé sont largement cohérents dans la plage d'incertitudes. Le piézomètre de micro-boudinage, combiné aux résultats des mesures de déformation finie, aux estimations de température de déformation et aux données thermochronologiques, offre des informations assez précieuses sur les propriétés rhéologiques des roches felsiques déformées.

Le chapitre 4 rapporte la caractérisation de deux types de joints orthogonaux (réseau en échelle et système de grille de fractures) dans des roches sédimentaires stratifiées à Sainte-Anne-des-Monts, (Québec, Canada), Ausable Chasm (NY, USA) et Beauharnois (Québec, Canada), et propose une nouvelle interprétation pour la formation des joints orthogonaux de type grille de verrouillage. Les relations entre l'espacement des joints (s) et l'épaisseur du lit (t) des joints systématiques et des joints croisés dans les lits de grès de la Formation de la Tourelle dans la région de Sainte-Anne-des-Monts sont étudiées. Sur la base d'une analyse avec le modèle de transfert de contrainte de fracturation proche de l'extrémité, une loi de puissance: $s=mt^{1-1/k}$ est proposée pour la relation entre s et t, où m est égal à la moitié du rapport de la résistance à la traction de la couche à la contrainte de cisaillement d'interface, et k est le module de Weibull. Avec la valeur m, la contrainte de cisaillement prévalant dans le schiste peut être calculée si la résistance à la traction du grès a été déterminée expérimentalement. La valeur m est significativement plus grande pour les joints croisés que pour les joints systématiques, ce qui indique que la contrainte de cisaillement interfaciale normale aux joints systématiques était supérieure à la contrainte de cisaillement interfaciale normale aux joints croisés, d'un facteur moyen de 3.1, au cours de leurs formations. Sur la base de l'investigation anatomique des joints orthogonaux de type grille de verrouillage dans le grès de Potsdam d'âge cambrien à Ausable Chasm (NY, USA) et Beauharnois (Québec, Canada), une nouvelle interprétation est proposée selon laquelle les joints orthogonaux verticaux peuvent résulter de la effets auxétiques du grès riche en quartz en l'absence de rotation des contraintes locales ou régionales. Dans les terrains de grès à plat avec des joints orthogonaux verticaux largement espacés et étroitement espacés, σ_2* et σ_3* sont respectivement en traction et perpendiculaires à des ensembles largement espacés et étroitement espacés, alors que la contrainte verticale (pression de surcharge) est toujours compressive (σ_1), au moment de la fracturation. Le rapport d'aspect des blocs de grès délimités par des joints orthogonaux est corrélé à la valeur du coefficient de Poisson négatif du grès.

Le chapitre 5 est une discussion générale reliant les résultats et les interprétations des chapitres précédents et enfin le chapitre 6 expose brièvement les principales conclusions de la présente étude et énumère les travaux qui devraient être menés à l'avenir.

ABSTRACT

Rheology of polyphase rocks (e.g., polymineralic rocks and layered rock terrains) has become one of the most active frontiers of Earth sciences during the last 25 years. However, the deformation processes of geological composite materials are complicated because competent and incompetent components tend to deform in different manners under the same temperature and pressure conditions. Brittle deformation in competent components is generally controlled by ductile deformation of the incompetent components in which they embedded. Therefore, brittle deformation and resultant microstructures in competent components bear significant information for interpreting the mechanical properties and deformation behavior of their surrounding incompetent materials, as well as information for the stress magnitude. Based on measurements and analysis on characterization of the brittle deformation in felsic gneisses, mylonites and interlayered sedimentary rocks, the present study aims to find out proper piezometers to estimate the differential stresses prevailing in geological composite materials and to explore their applications on calibrating the paleostresses for the rocks deformed in the Earth's crust.

This dissertation consists of five chapters. Chapter 1 introduces basic concepts in continuum mechanics and the mechanical models for describing the deformation processes of geological composite materials. Under this framework, each aspect related to deformation of geological composite materials, measurement methods of stress, strain and strain rate, various deformation mechanisms and corresponding structures, fracture mechanics, flow law, and the existing mechanical models, are introduced in detail with critical review.

Chapter 2 deals with tourmaline microboudin data measured from felsic gneiss and mylonite samples from the Gaoligong and Chongshan shear zones in Yunnan, Southwest China. After critically reviewing the piezometer built on the mid-point fracturing model, a new microboudinage piezometer is developed based on interfacial shear-induced near-end fracturing stress transfer model. The new microboudinage piezometer has a simple form: $\tau = 0.25C/(L/W)$, where τ is the shear flow stress of the ductile matrix (e.g., polycrystalline quartz), C is the tensile fracture strength of a columnar mineral (e.g., tourmaline), and L/W is the length/width ratio of the microboudin. Taking tourmaline tensile strength C=145 MPa as estimated, the application of the piezometer on the samples from the Gaoligong shear zones yields the shear flow stresses of 21-61 MPa for felsic gneisses and mylonites. The earlier formed microboudins have consistently

larger mean length/width ratios than the later formed ones, suggesting that the rocks recorded a tectonic history of continuous hardening prior to the cessation of quartz plasticity. Meanwhile, application of the piezometer on samples from the Chongshan shear zone, combined with microstructural observations, independent estimates of deformation temperature, accurate geochronological ages of various isotopic systems and regional geophysical data, provides constraints on strain rates ($\dot{\varepsilon}$), differential stresses (σ) and their correlations with temperature and corresponding depth for the polycrystalline quartz matrix. The naturally constrained flow strength profile below the brittle-ductile transition yields a flow law of $\dot{\varepsilon}=A\sigma^n\exp(-Q/RT)$ with n=4, Q=184 kJ/mol and A=7.180×10^{-7} MPa^{-n}s^{-1}. The differential stresses calibrated by this flow law are bracketed by the lower and upper bounds obtained by Luan and Paterson (1992) and Gleason and Tullis (1995), respectively, and are very close to the geometrical mean of these bounds.

Chapter 3 aims to expand the applicability of the microboudinage piezometer established based on tourmaline to other minerals. Feldspar, as one of the most abundant minerals in the crust, commonly exhibits brittle behavior in plastically deformed matrix under the greenschist-facies conditions, which makes it an excellent selection for the expansion of the piezometer. Different from the tourmaline microboudins with regular shape, the feldspar microboudins are treated as a circular-truncated-conical fibers in the mechanical analysis. A feldspar microboudinage piezometer is established with the estimated tensile strength of feldspar. We apply the piezometer on granitic mylonite samples, in which feldspar microboudins embedded in the ductile matrix of quartz, from the Red River, Chongshan and Gaoligong shear zones in Yunnan, Southwest China. The differential stresses estimated from the later formed feldspar microboudins are larger than the earlier formed ones, depicting an evolution during exhumation of the mylonite upwards the brittle-ductile transition. The results from the feldspar microboudinage piezometer and the quartz recrystallized grain-size piezometer are largely consistent within the range of uncertainties. The microboudinage piezometer, combined with results of finite strain measurements, deformation temperature estimates, and thermochronological data, offers valuable information about rheological properties of deformed felsic rocks.

Chapter 4 reports the characterization of two types of orthogonal joints (ladder-pattern network and fracture grid-lock system) in layered sedimentary rocks in Sainte-Anne-des-Monts, (Quebec, Canada), Ausable Chasm (NY, USA) and Beauharnois (Quebec, Canada), and proposes a new

interpretation for the formation of the grid-lock type orthogonal joints. Joint spacing (s)-bed thickness (t) relationships of the ladder-pattern systematic and cross joints in the sandstone beds of the Tourelle Formation in the region of Sainte-Anne-des-Monts are investigated. Based on analysis with the near-end fracturing stress transfer model, a power law: $s=mt^{1-1/k}$ is proposed for the s-t relationship, where m equals half the ratio of layer tensile strength to interface shear stress, and k is the Weibull modulus. With the m value, the shear stress prevailing in shale can be calculated if the tensile strength of sandstone has been experimentally determined. The m value is significantly larger for cross joints than systematic joints, indicating that the interfacial shear stress normal to systematic joints was higher than the interfacial shear stress normal to cross joints, by a mean factor of 3.1, during their formations. Based on the anatomic investigation on the grid-lock type orthogonal joints in the Potsdam sandstone of Cambrian age at Ausable Chasm (NY, USA) and Beauharnois (Quebec, Canada), a new interpretation is proposed that the vertical orthogonal joints may result from the auxetic effects of quartz-rich sandstone in the absence of local or regional stress rotation. In the terrains of flat-lying sandstone with widely spaced and narrowly spaced vertical, orthogonal joints, both σ_2^* and σ_3^* are tensile and perpendicular to widely spaced and narrowly spaced sets, respectively, whereas the vertical stress (overburden pressure) is always compressive (σ_1), at the time of fracturing. The aspect-ratio of sandstone blocks bounded by orthogonal joints is correlated with the value of negative Poisson's ratio of the sandstone.

Chapter 5 is a general discussion linking results and interpretations of former chapters and finally Chapter 6 briefly outlines the main conclusions of the present study and lists the work that should be conducted in the future.

TABLE OF CONTENTS

DEDICATION III

ACKNOWLEDGEMENTS IV

RÉSUMÉ V

ABSTRACT IX

TABLE OF CONTENTS XII

LIST OF TABLES XVI

LIST OF FIGURES XVII

LIST OF SYMBOLS AND ABBREVIATIONS XXXII

LIST OF APPENDICES XXXIII

CHAPTER 1 INTRODUCTION 1

1.1 Objectives and organization of the dissertation 1

1.2 Continuum mechanics basics in geology 3

1.3 Deformation mechanisms and structures 11

1.3.1 Brittle mechanisms and structures 12

1.3.2 Ductile mechanisms and structures 13

1.4 Fracture theory and flow laws 16

1.4.1 Fracture theory 17

1.4.2 Flow laws 19

1.5 Mechanic models 23

1.5.1 Shear-lag model 23

1.5.2 Stress transfer model (refined shear-lag model) 24

CHAPTER 2 MICROBOUDINAGE PALEOPIEZOMETER OF TOURMALINE AND ITS APPLICATIONS 28

2.1 Introduction 28

2.2 Critical reviews of previous work 30

2.3 Microboudin piezometer based on stress transfer model 38

2.4 Study samples and geological setting 44

2.5 Microstructural observations 47

2.6 Methodology 51

2.6.1 Measurements of tourmaline microboudins and strain 52

2.6.2 Estimates of tensile strength of tourmaline 53

2.6.3 Estimates of the temperature 54

2.7 Analysis of measured data 57

2.7.1 Measurements of the geometric features of tourmaline microboudins 57

2.7.2 Measurements of strains and estimates of strain rates 66

2.8 Estimates of paleostresses 70

2.8.1 Paleostresses in the Gaoligong shear zone 70

2.8.2 Paleostresses in the Chongshan shear zone 71

2.9 Discussion 73

2.9.1 Exhumation-induced hardening in the Gaoligong shear zone 73

2.9.2 Rheological properties of the Chongshan shear zone 75

2.9.2.1 Flow law of quartz derived from the Chongshan shear zone 75

2.9.2.2 Application of the quartz flow law to the Chongshan shear zone 77

2.10 Conclusions 91

CHAPTER 3 MICROBOUDINAGE PALEOPIEZOMETER OF FELDSPAR AND ITS APPLICATIONS 94

3.1 Introduction 94

3.2 Microboudin piezometer for feldspar 95

3.3 Geological setting 100

3.4 Optical microstructures 104

3.5 Methodology 110

3.5.1 Measurements of feldspar microboudins and strain 110

3.5.2 Estimates of tensile strength of feldspar 111

3.5.3 Estimates of the temperature 112

3.6 Analysis of measured data 112

3.6.1 Measurements of feldspar microboudins 112

3.6.2 Measurements of strains and assessment of strain rates 116

3.6.3 Estimates of temperature 118

3.7 Assessment of differential stresses 118

3.8 Discussion 122

3.9 Conclusions 125

CHAPTER 4 CHARACTERIZATION AND INTERPRETATION FOR FORMATION OF ORTHOGONAL JOINTS IN SEDIMENTARY ROCKS 127

4.1 Introduction 127

4.2 Geological setting 131

4.2.1 Geological setting of the Tourelle Formation 131

4.2.2 Geological setting of the Potsdam Group 133

4.3 Field observations 135

4.3.1 Observation on the systematic and cross joints (Sainte-Anne-des-Monts) 136

4.3.2 Observation on the grid-lock type orthogonal joints (Ausable Chasm and Beauharnois) 141

4.4 Methodology 147

4.5 Results of measurements 148

4.5.1 Joint spacing of the systematic and cross joints (Sainte-Anne-des-Monts) 148

4.5.2 Joint spacing of the grid-lock type orthogonal joints (Ausable Chasm) 154

4.6 Discussion 155

4.6.1 Relationship between joint spacing and layer thickness 155

4.6.2 Estimation of the interfacial shear stress 156

4.6.3 Formation of orthogonal joints 156

4.6.3.1 Existent models 157

4.6.3.2 A new interpretation 161

4.6.4 Implications 166

4.7 Conclusions 166

CHAPTER 5 GENERAL DISSCUSION 168

5.1 Significance of the research 168

5.2 Comparison between microboudinage and quartz recrystallized grain size piezometers 170

5.3 Stereological correction for the estimation of the microboudin aspect-ratios (*L/W*) ... 173

CHAPTER 6 CONCLUSIONS AND FUTURE WORK 175

6.1 Main conclusions 175

6.2 Future work 178

6.3 Contribution of the author 181

BIBLIOGRAPHY 183

APPENDICES 229

LIST OF TABLES

Table 1.1 Dislocation density piezometers of quartz 6

Table 1.2 Piezometers of recrystallized grain size and subgrain size for minerals.....7

Table 1.3 Geological strain rates estimated from the Earth's crust 9

Table 1.4 Power flow law parameters for polycrystalline monophase aggregates of quartz deformed in the regime of dislocation creep 22

Table 2.1 Young's moduli and tensile strength of 33 engineering materials* 43

Table 2.2 Localities of tourmaline-bearing rock samples from the Gaoligong and Chongshan shear zone, west Yunnan, China 46

Table 2.3 Summary of the parameters measured for tourmaline microboudins from GLG shear zone in Yunnan.....58

Table 2.4 **S**hear flow stress estimated using the tourmaline microboudinage piezometer for each sample from the Gaoligong shear zone 70

Table 2.5 Dislocation creep law parameters of quarztites 76

Table 2.6 Heat flow data measured from the study region 80

Table 3.1 Young's moduli and estimated tensile strength of 15 common minerals.....99

Table 3.2 Localities of granitic mylonite samples from the Gaoligong, Chongshann and Red River shear zones, Yunnan, China 102

Table 3.3 Representative data of feldspar microboudins measured and estimated from optical observations of petrographic thin sections for samples CS10 and CS45 (Chongshan Shear Zone) from which recrystallized grain sizes of quartz have been measured for comparison 114

Table 4.1 Statistical analyses of joint spacing data measured from sandstone layers of the Tourelle Formation in the region of Ste-Anne-des-Monts (Quebec, Canada).....148

Table 5.1 Data of the aspect-ratio (*L/W*) and grain size (*d*) of recrystallized quartz and flow stress (σ) estimation for granitic mylonites from the Chongshan shear zone 170

LIST OF FIGURES

Figure 1.1 Sketches of geological composite material. Polymineralic rock, represented by deformed rocks with foliations (planes defined by grey lines) and lineations (defined by the long axis orientation of the competent mineral fibers) (a); Layered rock terrains, which can be typically represented by interlayered sedimentary rocks (b). 4

Figure 1.2 A rod with squared ends (area: A_0) (a) stretched under a tension force F (b). In an equilibrium state, the tension force equals to $A\sigma$ (c). 5

Figure 1.3 Typical stress-strain curve of rocks under uniaxial tensile testing. 11

Figure 1.4 The deformation mechanisms map for a grain size of 10 μm of single dry quartz crystals under confining pressure of 100 MPa, and strain rate contours are shown on this map (10^{-6} to 10^{-15} s^{-1}). N-H: Nabarro-Herring. Modified from Passchier and Trouw (2005). 12

Figure 1.5 Typical microstructures formed by three mechanisms of dynamic recrystallization in quartz (Qtz). (a) Bulging (BLG) (Yunkai Mountain, Guangdong, China), (b) subgrain rotation (SGR) (Red River shear zone, Yunnan, China), and (c) grain boundary migration (GBM) (Morin shear zone, Rawdon, Québec, Canada). The neograin sizes from BLG, SGR and GBM are inferior, equal and superior to the subgrain size, respectively. SG: subgrain. Modified from Ji et al. (2021b). 15

Figure 1.6 Diagram illustrating composite failure envelope and stress circles under various circumstances. C: tensile strength; a: tensile fracture; b: tensile fracture caused by the critical differential stress; c: extensional shear fracture; d: compressional shear fracture. The regimes of compression and tension occur when the normal stress is above and below zero, respectively. Modified from Etheridge (1983). 18

Figure 1.7 Flow strength of quartz as a function of temperature for each flow law listed in Table 1.4. The strain rate is taken as 10^{-14} s^{-1}. Modified from Ji et al. (2021b). 21

Figure 1.8 Schematic illustration for different stress transfer models. Thin lines as passive markers showing displacements during deformation. (a) The initial state of unstressed layered composite (grey: competent; white: incompetent). (b) and (c) The states of stressed layered composite. As a uniform extensional strain is applied at the ends of the incompetent

components, no slip occurs on interfaces of the competent and incompetent components in (b), and partially slip takes place on interfaces of the competent and incompetent components in (c). The width of the fractures are exaggerated in the schematic illustration. Modified after Ji et al. (1998).....25

Figure 2.1 Pressure-temperature stability of tourmaline. Experimental data represented by circles, solid lines and squares. Mineral abbreviations: Dia–Diamond; Gr–Graphite; Coe–Coesite; Qtz–Quartz; Ms–Muscovite; Ab–Albite; Kfs–K-feldspar; Fl–Fluid; Sil–Sillimanite; And–Andalusite. Modified from Dutrow and Henry (2011). 29

Figure 2.2 Photomicrographs of fractured garnet crystals (a-c) and tourmaline (d) in plastically deformed matrix of quartz. (a-c) from the Morin shear zone, Quebec, Canada (Ji & Martignole, 1994; Ji et al., 1997), and (d) from Fortaleza, NE Brazil (Passchier & Trouw, 2005). Tensile fractures are perpendicular to the foliation and stretching lineation. Mean fracture spacing to grain width ratios in (a), (b), (c) and (d) are 0.94±0.37, 0.99±0.44, 0.51±0.21 and 0.46±0.21, respectively. The ratios are much smaller than unity, which cannot be explained by the conventional shear-lag model. Some fractures taper from the grain boundary toward the core, indicating that the fractures were initiated at the grain boundaries and then propagated inwards. Gt: garnet; Qtz: quartz; Kf: K-feldspar; Tur: tourmaline. XZ section.....30

Figure 2.3 Schematic illustration of theoretical basis of the shear-lag model. (a) The unstressed composite unit. (b) Homogeneous deformation of the pure matrix material when the fiber is absent. (c) Differential displacement, introduced by the presence of the fiber, in the matrix. (d) Predicted tensile stress variations along the fiber before fracturing (solid line) and fragments after fracturing (dashed line) according to the shear-lag model. Variables are defined in text.....32

Figure 2.4 Photomicrographs of fractured tourmaline (Tur) and piedmontite (Pi) in plastically deformed matrix of quartz. (a), (b), (c) and (d) are from Matsumura et al. (2017), Masuda and Kimura (2004), Masuda et al. (2003) and Omori et al. (2016), respectively. No evidence is observed for the common presence of mid-point fracturing. 33

Figure 2.5 Elastic moduli (bulk modulus *K*, shear modulus *G* and Young's modulus *E*) and Poisson's ratio of quartz (a-b) and quartzite (c-d) as a function of temperature at room pressure (Lakshtanov et al., 2007) and 600 MPa (Barruol & Mainprice, 1993).....36

Figure 2.6 Schematic illustration of the near-end fracturing process and the mechanical equilibrium analysis for derivation of Eq. (2.14). (a) The unit cell; (b) Prism with an n-sided regular polygon base (*n*=6); (c) Cylindrical fiber; (c) Square prism. Variables are defined in text.....39

Figure 2.7 Tensile strength (*C*) versus Young's modulus (*E*) for 33 engineering materials at ambient conditions (Ashby, 2016; Howatson, 2012, Table 2.1). Be: Beryllium; Dia: diamond; Spr: Sapphire; W: Tungsten. The tensile strength is expected to be higher at a higher confining pressure.....42

Figure 2.8 (a) Simplified geological map of the Tibetan plateau and surrounding regions. Red lines show main shear zones or fault zones: (1) Gaoligong shear zone; (2) Chongshan shear zone; (3) Ailao Shan-Red River shear zone; (4) Indus-Tsangpo suture zone; (5) Main boundary thrust; (6) Sagaing Fault; and (7) Longmen Shan fault; Box refers to Figure 2.8b. (b) Sampling locations (black stars) within the Gaoligong and Chongshan shear zones, west Yunnan, China. Modified from Zhang et al. (2012a and b).....45

Figure 2.9 Tensile fracture microboudins of tourmaline in mica-bearing quartzofeldspathic mylonites from the GLG shear zone, Yunnan Province, China. Note that tourmaline grains were broken into fragments of different lengths. 48

Figure 2.10 Reflected light micrographs of typical fractured tourmaline crystals (black) in felsic gneisses and mylonites from the CS shear zone, west Yunnan, China. Tensile fractures are approximately perpendicular to the foliation and stretching lineation.....49

Figure 2.11 Photomicrographs of fractured tourmaline (Tur) in plastically deformed quartz (Qtz) matrix of felsic gneisses and mylonites from the CS shear zone, west Yunnan, China. The interboudin gaps are filled with quartz and muscovite (Ms).....50

Figure 2.12 Photomicrographs showing brittle deformation of feldspar and tourmaline in which tensile fractures are mutually parallel. Samples from the CS shear zone, west Yunnan, China. 51

Figure 2.13 Schematic illustration of the strain reversal method (Ferguson, 1981; Lloyd & Ferguson, 1981, 1989; Lloyd & Condliffe, 2003) which has been used to recover the fracturing history of each tourmaline crystal. The gaps are ordered according to their lengths from large to small, indicating the sequence of fracturing. In each reversal stage, the remaining smallest gap is closed, while the length of the rest gaps is reduced by the length of the smallest gap. The natural strains (ε_n) of different reversal stages are calculated from the equations listed alongside, where L_0 is the sum length of all the microboudin segments, which is equal to the initial length of the original crystal before fracturing, G_t is the total length of the gaps before reverse, and G_n is the sum length of all the remaining gaps after the reversal of the nth gap (n = number of gaps). 52

Figure 2.14 Schematic illustration of estimating the tensile strength (*C* value) of tourmaline crystals. The *C* value is affected by the degree of crystal quality and internal flaws, such as microcracks, inclusions, heterogeneities, and surface rugosity. 53

Figure 2.15 The solubility of tourmaline in granitic melt (black solid line) and in aqueous solutions (grey dashed line) as functions of temperature and of the B_2O_3 content of the melt or fluid. Modified from London (2016). See the text for discussion. 56

Figure 2.16 Schematic illustration of estimating the temperatures when each fracture formed with the strain reversal method assuming that the temperature (*T*) decreases along with the increasing strain in a linear relation. The meanings of the symbols are the same as those in Fig. 2.13. The starting temperature (T_s) is commonly taken as 450 °C according to the microstructural observation and corresponds to the opening of the first fracture. This starting temperature can also be adjusted, if minerals form at lower temperature are observed to occur in the first gap (g_1). The cease of the plasticity or the finite strain (ε) of the matrix mainly consisting of quartz corresponds to the temperature of 300 °C. 57

Figure 2.17 Histograms for initial aspect ratios (L_0/W_0) and plots of length L_0 versus width W_0 of the original tourmaline grains prior to fracturing. (a-b) and (c-d) for samples YN1397 and GLG325, respectively. N: number of grains; M: Mean; S. Dev.: Standard deviation. 60

Figure 2.18 Histograms for the length/width ratios of tourmaline microboudins formed by each generation of fracture in sample YN1397. (a) 191 grains prior to fracturing; (b) and (c) shorter and longer segments divided by the first generation of fracture, respectively; (d) 49

among the 191 longer segments were broken by the second generation of fracture; (e) and (f) shorter and longer segments divided by the second generation of fracture, respectively; (g) only 4 among the 49 longer segments were broken by the third generation of fracture; (h) and (i) longer and shorter segments divided by the third generation of fracture, respectively. 61

Figure 2.19 Histograms for length/width (L_0/W_0) ratios and plots of length L_0 versus width W_0 of the unbroken tourmaline grains in samples YN1397 (a-b) and GLG325 (c-d). N: number of grains; M: Mean; S. Dev.: Standard deviation. 62

Figure 2.20 Plots of length versus width of the tourmaline microboudins formed by the first (a-c), second (d-f) and third (g-i) generations of tensile fracturing in samples YN1397. Each tensile fracture formed two fragments of unequal lengths. A linear correlation between fracture spacing and tourmaline width is observed (b and e).....63

Figure 2.21 Histograms for the aspect ratios of tourmaline microboudins formed by each generation of fracture in sample GLG325. (a) 173 grains prior to fracturing; (b) and (c) shorter and longer segments divided by the first generation of fracture, respectively; (d) 46 among the 173 longer segments were broken by the second generation of fracture; (e) and (f) shorter and longer segments divided by the second generation of fracture, respectively. (g) 5 among the 46 longer segments were broken by the third generation of fracture; (h) and (i) shorter and longer segments divided by the third generation of fracture, respectively. 64

Figure 2.22 Data measured from sample CS45. (a) Plots of length versus width of 47 original grains before fracturing (solid circle) and their 250 microboudins after fracturing (open circle). (b) and (c) Histograms of length/width (aspect) ratios for the intact grains before fracturing and their microboudins after fracturing, respectively. Fracturing results in decreasing length/width ratios of tourmaline fragments. N: number of measurements; M: mean; Me: median. 65

Figure 2.23 Extension strains measured from microboudins of 85 tourmaline grains using the strain reversal method. N: number of intact grains; M: mean; Me: median; Mo: mode.....67

Figure 2.24 A compilation of available accurate data of zircon U-Pb, monazite U-Th/Pb , muscovite and biotite $^{40}Ar/^{39}Ar$, and zircon and apatite (U-Th)/He ages for the CS shear

zone (Akciz et al., 2008; Zhang et al., 2010, 2012a; Wang Y. et al., 2018). Conditions where tourmaline crystallized and broke are indicated. 68

Figure 2.25 Extension strain rates estimated for 85 tourmaline grains, assuming the fracturing took place at 450-300 ºC (a) and 400-300 ºC (b). N: number of intact grains; M: mean; Me: median; Mo: mode. 69

Figure 2.26 "Best" tensile strength estimates for the tourmaline grains from the CS shear zone according to their crystal quality and internal flaws such as microcracks, inclusions, heterogeneities, and surface rugosity. N: number of fractures; M: mean. 71

Figure 2.27 Plots of shear flow stress versus temperature for the quartz matrix surrounding the tourmaline microboudins. Largest uncertainties in deformation temperature and shear flow stress are ±20 °C and ±15 MPa, respectively. The data in the ductile regime yields a flow law defined by Eq. (2.19) with n=4, Q=184 kJ/mol and A=7.180×10^{-7} MPa^{-n}s^{-1}. Results calculated from extrapolation of quartzite flow laws assuming a strain rate of 10^{-14} s^{-1} (LP: Luan & Paterson, 1992; GT: Gleason & Tullis, 1995), and their arithmetic and geometric means (AM and GM) are also shown. 72

Figure 2.28 Schematic strength profile for the quartz-rich part of the continental crust. The strength is controlled by the Byerlee friction law down to the brittle-ductile transition, and then decreases non-linearly with depth following a power flow law of wet quartz below the transition. Smaller length/width ratios of microboudins form successively when the ductile rock becomes stronger due to cooling caused by tectonic exhumation until the brittle-ductile transition is reached (path 1). In contrast, greater length/width ratios of microboudins are sequentially produced when the ductile rock becomes warmer and weaker due to burial and temperature increase (path 2). A switch from dislocation creep to Coble creep due to grain size reduction (dynamical recrystallization or retrogressive metamorphic reactions) induces a weakening and thus forms greater length/width ratios of microboudins (path 3). 74

Figure 2.29 Three-layer model lithosphere of the Chongshan region, western Yunnan China: 20 km-thick granitic upper crust (k=3.1 Wm^{-1}°C^{-1}, A=1.0×10^{-6} Wm^{-3}, ρ=2600 kg/m^3), 18 km-thick dioritic lower crust (k=4.0 Wm^{-1}°C^{-1}, A=7.0×10^{-7} Wm^{-3}, ρ=2650 kg/m^3), and peridotitic upper mantle (k=2.5 Wm^{-1}°C^{-1}, A=0 Wm^{-3}, ρ=3300 kg/m^3), where k is the thermal conductivity, A is the radioactive heat productivity, and ρ is the density. The lithological

structure derived from regional seismic data (e.g., He et al., 2009; Sun et al., 2012; Hu et al., 2013; Zha & Lei, 2013; Deng et al., 2014; Sun et al., 2014; Wang F. et al., 2018). 78

Figure 2.30 Temperature-depth (a) and geothermal gradient-depth (b) variations, computed from the surface heat flow, thermal conductivity and radioactive heat generation, for the Chongshan shear zone (Yunnan, Southwest China). 81

Figure 2.31 Histograms for the crustal thickness (a) and V_p/V_s ratio (b), measured for the Chongshan shear zone (Yunnan, Southwest China) using the method of function analysis (He et al., 2009; Sun et al., 2012; Hu et al., 2013; Zha & Lei, 2013; Deng et al., 2014; Sun et al., 2014; Wang F. et al., 2018). N: number of measurements; M: mean; Me: median; Mo: mode. 81

Figure 2.32 Variations of the crustal thickness (a) and V_p/V_s ratio (b) with latitude, and plots of V_p/V_s ratio versus the crustal thickness (c) for the Chongshan shear zone (west Yunnan, China). N: number of measurements.....82

Figure 2.33 P-wave velocities as a function of depth (circles), measured by seismic tomography across the Chongshan shear zone (Data from Xu et al., 2013), and comparison with the V_p-depth curve calculated from extrapolation of experimentally measured data for felsic gneiss (solid line AB). 84

Figure 2.34 Rheological strength (differential stress) of quartzite as a function of depth, estimated for the Chongshan shear zone (west Yunnan, China) at a typical strain rate of 10^{-14} s^{-1}. The frictional strengths (differential stresses) are obtained from multiplying the frictional shear stresses of the Byerlee's law (μ=0.75, λ=0; μ=0.75, λ=0.43) by a factor of 3 (Paterson & Olgaard, 2000; Behr & Platt, 2014). Results estimated using the tourmaline microboudinage piezometer for quartzite in ductile and elastic-brittle regimes are represented by open circles and crosses, respectively. Previous flow laws (LP: Luan & Paterson, 1992; GT: Gleason & Tullis, 1995; HTD: Hirth et al., 2001; LJ: Lu & Jiang, 2019) are also shown for comparison. AM and GM represent for the arithmetic and geometric means of the LP and GT flow strengths, respectively. 86

Figure 2.35 Effects of strain rates on the rheological strength-depth profile in the crust dominated by quartz (example of the CS shear zone). Strain rates for (a), (b), (c) and (d) are 10^{-16} s^{-1},

10^{-15} s^{-1}, 10^{-13} s^{-1}, 10^{-12} s^{-1}, respectively. Results estimated using the tourmaline microboudinage piezometer for quartzite in ductile and elastic-brittle regimes are represented by open circles and crosses, respectively. LP: Luan and Paterson (1992); GT: Gleason and Tullis (1995); HTD: Hirth et al. (2001); LJ: Lu and Jiang (2019). AM and GM represent for the arithmetic and geometric means of the LP and GT flow strengths, respectively.....87

Figure 2.36 Depth distribution of seismicity (Mw≥2.7) in the Chongshan shear zone (west Yunnan, China) during a period of 40 years (1978-2018). Mw: Moment magnitude of earthquake; N: number of earthquakes.....90

Figure 3.1 Schematic diagram to illustrate an ellipsoidal segment (a) and its volume (b), base surface area (c) and lateral surface area (d) as a function of h_2. The numerical calculations were based on the data (a=2 mm, c=10 mm, b=25 mm, h_1=0 mm). The mathematic equations were given in Tee (2005). 96

Figure 3.2 Schematic representation for the longitudinal section of a fractured porphyroclast, cut parallel to the XZ plane. Larger and smaller gaps occur at the sites of earlier (F_1) and later (F_2) fractures, respectively. The length (L), diameters of the smaller and larger ends (D_1 and D_2), and the angle between the generator and the symmetry axis (θ) are indicated for the microboudin resulted from fracture F_1. 97

Figure 3.3 Tensile strength (C) versus Young's modulus (E) for engineering and geological materials. C = 2.32 × 10^{-3}*E for the engineering materials (a, squares, measured, Ashby, 2016; Howatson, 2012, Table 2.1 and Table 3.1), and C = 7.20×10^{-4}*E for natural minerals (b, circles, predicted). Abbreviations: An, anorthite; Ap, apatite; Di, diopside; Ep, epidote; Grt, garnet; Hbl, hornblende; Kfs, K-feldspar; Omp, omphacite; Opx, orthopyroxene; Rt, rutile; Sil, sillimanite; Spl, spinel; T, tourmaline. 99

Figure 3.4 (a) Simplified geological map of the southeastern Tibetan plateau and the surrounding regions. Red lines represent the main shear or fault zones: (1) Gaoligong shear zone; (2) Chongshan shear zone; (3) Ailao Shan-Red River shear zone; (4) Indus-Tsangpo suture zone; (5) Main boundary thrust; (6) Sagaing Fault; and (7) Longmen Shan fault; Box refers to Figure 3.2b. (b) Sample locations (black dots) within the Gaoligong, Chongshan and Red

River shear zones, Yunnan, China. Abbreviations: ALS: Ailao Shan; DCS: Diancang Shan; XLS: Xuelong Shan. Modified from Zhang et al. (2012a and b).....101

Figure 3.5 Extensional fractures and resultant microboudinage of feldspar porphyroclasts in fine-grained muscovite-quartz aggregates from granitic mylonites of the Gaoligong shear zone (Yunnan, China). (a), (b), (c) and (d) from samples GLG11A, GLG 317, GLG14B and GLG14A, respectively. Abbreviation: f, foliation; S, S plane; C, C plane.....105

Figure 3.6 Tensile fractures and resultant pull-apart structures of feldspar porphyroclasts in granitic mylonites from the Chongshan shear zone (Yunnan, China). (a) and (d) from samples LS4 and CS10E, respectively, and (b)-(c) from samples CS45E. Abbreviations: B, biotite; F, feldspar; f, foliation; Q, quartz; T, tourmaline.....106

Figure 3.7 Microstructures of fragmented feldspar porphyroclasts in granitic mylonites from Ailaoshan (e, sample R82), Diancangshan (c, sample D10; f, sample D9) and Xuelongshan (a, sample YN1361D; b, sample YN1329C; d, sample YN1328) in the Red River shear zone (Yunnan, China). Abbreviations: B, biotite; F, feldspar; f, foliation; My, myrmekite; Q, quartz.....107

Figure 3.8 Preferred orientation of tensile fractures with respect to the long axes of feldspar porphyroclasts. (a), (b), and (c) measured from the Gaoligong, Chongshan and Red River shear zones, respectively. N: number of measurements; M: mean; Me: median; Sk: skewness. 108

Figure 3.9 Typical mica fishes in granitic mylonites from the Gaoligong shear zone (right-lateral strike slip). (a), (b), (c), and (d) from granitic mylonite samples GLG11A, GLG45B, GLG86B and GLG86C, respectively. Abbreviation: f, foliation.....109

Figure 3.10 Schematic illustration of the strain reversal method used to recover the fracturing history of each feldspar porphyroclast. The gaps are ordered according to their lengths from large to small, indicating the sequence of fracturing. In each reversal stage, the remaining smallest gap is closed, whereas the length of the rest gaps is reduced by the same amount of the smallest gap. The natural strain (ε_n) after each reversal stage is calculated from the equation listed on the right side, where L_0 is the sum length of all the microboudin segments or the initial length of the original crystal before fracturing, G_t is the total length of the gaps

before reverse, and G_n is the sum length of all the remaining gaps after the reversal of the nth gap (n = gap number). 111

Figure 3.11 Distributions of intact grain size (a-c), aspect ratio (length/width, d-f), and length-width plots (g-i) for feldspar porphyroclasts measured from the Gaoligong (left column), Chongshan (middle column) and Red River (right column) shear zones. N: number of intact grains; M: mean; SD: standard deviation. 113

Figure 3.12 Histograms for the extensional finite strains recorded by feldspar boudinage in the granitic mylonites from the Gaoligong, Chongshan and Red River shear zones. N: number of intact grains; M: mean; SD: standard deviation. 117

Figure 3.13 Histograms for the extensional strain-rates estimated by combining feldspar boudinage piezometer results and thermochronological data from the granitic mylonites in the Gaoligong (a), Chongshan (b), and Red River (c) shear zones. N: number of measurements; M: mean; SD: standard deviation; Me: median; Sk: skewness. 118

Figure 3.14 “Best” or “guideline” values of the tensile strength estimated for the feldspar porphyroclasts of granitic mylonites according to their crystal quality and internal flaws (e.g., microcracks, inclusions, cleavage orientation, and surface roughness) observed under the microscope. N: number of fractures; M: mean; SD: standard deviation. The estimated tensile strengths follow a Weibull distribution with a scale parameter of 55.1 MPa and a shape parameter of 8.2.....119

Figure 3.15 Distributions of the differential stresses estimated from the feldspar microboudinage piezometer in the ductile (a-c) and brittle (d-f) matrixes of granitic mylonites from the Gaoligong (left column), Chongshan (middle column) and Red River (right column) shear zones. 120

Figure 3.16 Plot of lnσ versus 10^4/T for the Gaoligong (a), Chongshan (b) and Red River (c-d) shear zones. Data in (a-c) from the estimates of feldspar microboudinage piezometer while those in (d) from quartz recrystallized grain size piezometer of Stipp and Tullis (2003), with data compiled from An and He, (1987), Zhang et al. (2008) and Boutonnet et al. (2013). .121

Figure 3.17 Flow strength-depth profiles calculated using various polycrystalline quartz flow laws for a continental crust (20 °C/km) deformed at strain rates of 10^{-14} s^{-1}. GT (Gleason &

Tullis, 1995), HTD (Hirth et al., 2001), LJ (Lu & Jiang, 2019), LP (Luan & Paterson, 1992), RB (Rutter & Brodie, 2004), THB1 (laboratory fit) and THB2 (extrapolation fit) of Tokle et al. (2019), and YN (Yunnan, this study). 124

Figure 4.1 Traces of orthogonal systematic joints defining a grid-lock pattern. (a-c) Views on a bedding surface of quartz sandstone from Eaglehawk Neck, Tasmania, Australia (a-b) and St. Mary's Chapel, Caithness, Scotland (c). (d) Orthogonal fractures produced in brittle varnish by orthogonal loadings (Rives et al., 1994). Courtesy Carolyn Bell, Stephanie Sykora, and Mike Norton for pictures (a), (b) and (c), respectively. 130

Figure 4.2 Simplified geological map displaying the study area. (a) and (b) are modified from Cousineau (1998), Malo et al. (2001) and Ji et al. (2021).....132

Figure 4.3 (a-b) Satellite images showing the sites of measurements on the rocky beaches of Saint-Joachin-de-Tourelle, Quebec, Canada. Modified from Ji et al. (2021a). 133

Figure 4.4 Simplified geological map showing the distribution of the Potsdam sandstone and the sites of study. Modified from Lowe et al. (2015). Stratigraphic column of the study region can be found from Globensky (1987) and Salad Hersi et al. (2003).....134

Figure 4.5 Tide-formed ripple marks observed on the upper bedding surface of quartz sandstone at the Ausable Chasm (New York State, USA). The mechanical pencil is 14.5 cm.....135

Figure 4.6 Photographs of the typical outcrops (a and b, NE to SW) of interlayered sandstone (siltstone) and shale in the study area. Saw-teeth-shaped small-scale landforms (c and d) created by gently-dipping (J1) systematic joints and steeply dipping (J2) cross joints in thin beds of sandstone. 136

Figure 4.7 Preferential orientations of J1 and J2 joints in sandstone layers in the study area. 156 measurements (N(J1)=77 and N(J2)=79). The average attitudes of J1 and J2 joints are (148º, 22º) and (018º, 78º), respectively. 137

Figure 4.8 Ladder-pattern of orthogonal joints (sets J1 and J2) observed on sandstone bedding surfaces. J2 joints, which are less persistent than J1, extend across intervals between J1 joints and abut J1 joints at ~90º angles. Scale in (a) is 1 m. 137

Figure 4.9 Steeply-dipping J2 joints observed on the J1 joint surfaces in thick sandstone layers. The joint spacing of J2 and particularly that of J1 are significantly smaller than the bed thickness. 138

Figure 4.10 Plumose structures observed on the J1 joint surface in a fine-grained sandstone. The propagation direction of the fracture is indicated by arrow. 139

Figure 4.11 Plumose structures observed on the J2 joint surface in sandstone layers. The plumose diverges from a point on (a) and near (b) the lithological interface and within the layer (c). The propagation direction of the fracture is indicated by arrow. 140

Figure 4.12 Characteristics of orthogonal joints (set J1 and J2) observed in quartz sandstone at Ausable Chasm (New York State, USA). Set 1 is generally more persistent than set 2. Note that the observation surface in (d) is parallel to joint plane of set 1. In central part of (d), a throughgoing open fracture developed late by coalescence and linkage of joint J2 across bed boundaries. The pen is 13.5 cm. 142

Figure 4.13 Geometrical relationships between two sets of orthogonal systematic joints (set J1 and J2), observed on bedding-parallel surface of quartz sandstone at Ausable Chasm (New York State, USA). Mutual intersecting and abutting suggest that the orthogonal joints are geologically coeval. NSJ: Non-systematic joint. 143

Figure 4.14 Preferential orientations of orthogonal joints in quartz sandstone at Ausable Chasm (New York State, USA). N: number of measurements. 144

Figure 4.15 Rectangular cuboidal sandstone blocks bounded by vertical orthogonal joints and horizontal bedding surface at Ausable Chasm (New York State, USA). 145

Figure 4.16 Orthogonal joints control on gorge orientation at Ausable Chasm (New York State, USA). The Ausable River makes a right-angle turn from the northwest direction (joint set J1) to a northeast direction (joint set J2) near the highway bridge (a) and the Whirlpool basin (b). 146

Figure 4.17 Orthogonal joints (a) and their preferential orientations (b) in sandstone at Beauharnois. Quebec, Canada. N: number of measurements. 147

Figure 4.18 Plots of joint spacing (s) versus bed thickness (t) for 109 layers of sandstone measured along a bedding-perpendicular scanline on the beach of Saint-Joachin-de-Tourelle, Quebec, Canada. (a) joint set J1, and (b) joint set J2. 150

Figure 4.19 Plots of median joint spacing versus bed thickness for joints of sets 1 and 2 in sandstone layers. Data measured collected from 14 sandstone layers of the Tourelle Formation. 151

Figure 4.20 Plots of joint spacing versus thickness of shale layer below (*d1*) and above (*d2*) the jointed sandstone bed. (a)-(c) joints of set 1, and (b)-(d) joints of set 2. 152

Figure 4.21 Data of joint set J2 (attitude: 002º, 89º), measured from a continuous sandstone layer with a quasi-constant thickness (18.2 ± 0.5 cm), at site 16 (49.15645°N, 66.42905°). 324 measurements. (a) Distribution of joints, and (b) Variation of *s/t* ratio along the layer. Joint spacing and *s/t* ratio systematically decrease near each fault. Arrow: the location of minor fault.....153

Figure 4.22 Plot of joint spacing for set 1 (s_{J1}) versus joint spacing for set 2 (s_{J2}) for quartz sandstone at Ausable Chasm (New York State, USA). Spacing s_{J1} and s_{J2} are the length and width of each rectangle bounded by joint set J1 and J2, measured on the bedding-parallel surface. 154

Figure 4.23 Schematic illustration of different models to interpret the development of ladder-pattern (cross joints, a and b) and grid-lock pattern (c) orthogonal joints in a flat-lying sandstone bed. (a) Cross joints develop perpendicular to the systematic joints due to regional stress rotation. (b) Cross joints form laterally between adjacent systematic joints due to stress rotation caused by local stress release or reduced joint spacing to bed thickness ratio (*s*/*t*). (c) Grid-lock joints formed by repeated extension along two orthogonal directions in sandstone due to the auxetic effects (negative Poisson's ratio). The effective maximum principal stress σ_1^* (overburden) is compressive and normal to the sandstone layer, whereas both effective immediate and minimum principal stresses (σ_2^* and σ_3^*) are tensile and perpendicular to widely spaced and narrowly spaced joint sets, respectively, at the time of fracturing. Joint set J1 and J2, which are normal to σ_3^* and σ_2^*, respectively, display spacings of s_{J1} and s_{J2}. Different joints nucleated at flaws with varying shape and size, where the

materials had different tensile strengths and stress concentration factors. A new joint could crosscut healed or partially sealed fractures. 158

Figure 4.24 Examples of jointed calcareous greywacke beds with joint spacing to bed thickness ratio $s/t \leq 0.2$ but without cross joints developed as predicted by numerical models of Bai et al. (2002). Calcareous greywacke consisting of quartz, feldspar, calcite and clay has a positive Poisson's ratio (Ji et al., 2002). Samples collected from the External Humber Zone of the Appalachian orogen at Petite Vallée, Quebec, Canada (GPS coordinates 49.22133° N, 65.03569° W). (a-b) View from a plane perpendicular to the bedding surface and to the systematic joints. (c and f) Jointed sandstone resembling a sliced-up loaf of bread. (d-e) View from the bedding surface. 160

Figure 4.25 Horizontal effective stress (σ_3^*) within a flat-lying layer due to the vertical overburden (σ_1^*) at a depth of 4 km. Conditions with different pore fluid factors (λ) have been considered. λ=0 and λ=0.4 represent lithostatic and hydrostatic conditions, respectively. Tensile σ_3^* occurs only when the material is auxetic with negative Poisson's ratios or $P_f > \sigma_3$ (not shown). The density is taken to be 2.5 g/cm^3. 163

Figure 4.26 Sandstones with zero or negative values of Poisson's ratio. Poisson's ratio as a function of density (a), porosity (b), and confining pressure (c-d). Experimental data in (a-c) from Freund (1992) and (d) from Ji et al. (2018). Samples numbers are also indicated in (c-d). Data of Ken-Betwa sandstone from Bandyopadhyay and Abdullah (2013) are indicated in (b). 165

Figure 5.1 Comparison between the paleodifferential stresses estimated from feldspar microboudinage and quartz recrystallized grain size piezometers in granitic mylonite samples CS10 (a) and CS45 (b) from the Chongshan shear zone. Quartz recrystallized grain size piezometer of Stipp and Tullis (2003) was used. 171

Figure 5.2 (a, b) Widths of possible longitudinal sections through a six-sided prism (a) and a cylindrical prism (b). Variations of $W/(2r)$ ratios for a series of consecutive sections cut longitudinally through the six-sided prism (c) and the cylindrical prism (d). r is the radius of the circumscribed circle. The average sectional widths for the six-sided and cylindrical prisms are, respectively, 74.4% and 76.3% of the maximum values ($2r$), respectively. Each thin-section has a thickness of 30 μm. For (c) and (d), r=0.7275 mm and r= 0.6 mm. 173

Figure 6.1 Volume fraction (*V*) of dynamic recrystallization (a) and quartz grain size (b-d) as a function of distance (*D*) from the center of each ductile shear zone. Modified from Ji et al. (2021b). 180

LIST OF SYMBOLS AND ABBREVIATIONS

Symbols and abbreviations	Notation
C	Tensile strength
CS	Chongshan
E	Young's modulus
f_w	Water fugacity
G	Shear modulus
g	Gravitational acceleration
GLG	Gaoligong
K	Bulk modulus
P	Pressure
Q	Activation energy
R	Gas constant
RR	Red River
T	Temperature
V_p	Compressional wave velocity
V_s	Shear wave velocity
ΔV	Activation volume
z	Depth
σ	Stress
ε	Strain
$\dot{\varepsilon}$	Strain rate
τ	Shear stress
ρ	Density
μ	Coefficient of friction
ν	Poisson's ratio

LIST OF APPENDICES

APPENDIX A DATA MEASURED OF SAMPLE FROM THE CHONGSHAN SHEAR ZONE 229

APPENDIX B STRAIN, SHEAR STRESS AND DEFORMATION DEFORMATION ESTIMATED FOR EACH MICROBOUDIN FROM THE STUDIED SAMPLES.....237

CHAPTER 1 INTRODUCTION

1.1 Objectives and organization of the dissertation

Geological materials from the Earth's crust and mantle (e.g., polymineralic rocks and layered rock terrains) are essentially composite materials, and deform when they are subjected to tectonic stress. Competent components in the geological composite materials may deform in a brittle manner, while incompetent components tend to deform in a ductile manner due to the considerable strength contrast. Researches on the deformation mechanisms and mechanical models of geological composite materials are significant for us to understand the mechanical properties and deformation behavior of polyphase rocks in the Earth's crust and mantle. Meanwhile, the corresponding complicated deformation processes of geological composite materials in turn record the information of the stress field, which is critical to comprehend the geodynamic processes in the Earth.

The main objectives of this Ph. D. dissertation are:

(1) Find out a proper mechanical model to explain the characterization of brittle deformation in geological composite materials such as mineral microboudins embedded in matrix of felsic gneisses and mylonites and joints in sandstones interlayered with continuous mudstones or shales;

(2) Establish a new microboudinage piezometer and apply the piezometer to estimate the paleostress for deformed rocks from shear zones;

(3) Elucidate the characterization and interpret the formation of orthogonal joints in layered sedimentary rocks.

Based on the near-end fracturing stress transfer model (refined shear-lag model) and combined with measured microboudin (tourmaline and feldspar) data, a new microboudinage piezometer has been built to estimate the differential stress for deformed rocks in shear zones. Meanwhile, a generalized power law relationship is proposed for joint spacing and bed thickness data over the full range of measured bed thickness.

Tourmaline, as a rigid columnar mineral, is commonly observed to be broken into microboudins separated by brittle fractures in host felsic gneisses and mylonites. A microboudinage piezometer using tourmaline microboudins scattered in ductile matrix has been built by Masuda and his

coworkers to estimate the magnitude of differential stress. However, their piezometer was derived from the assumption of mid-point fracturing and perfectly welded fiber/matrix interfaces, which is not the common case in plastically deformed rocks. In Chapter 2, we establish a new microboudinage piezometer based on near-end fracturing and fiber/matrix interfacial shear, which is consistent with the observation. With the estimated tensile strength of tourmaline, we apply the piezometer on the measured tourmaline microboudin data to estimate the shear flow stress of some representative felsic gneiss and mylonite samples from the Gaoligong and Chongshan shear zones in Yunnan, Southwest China. We also measured the strain recorded by the tourmaline fractured segments and gaps for the samples from the Chongshan shear zone. Combination of microstructural observations and independent estimates of deformation temperature, accurate geochronological ages and regional geophysical data, makes it possible to constrain the strain rates ($\dot{\varepsilon}$), differential stresses (σ) and their correlations with temperature and corresponding depth for the polycrystalline quartz matrix in which elongate tourmaline grains have been fragmented into microboudins. The results yield a flow law for naturally deformed quartzite which can provides a reliable interpretation for the distribution of focal depths and electrical resistivity structure of the Chongshan shear zone.

While tourmaline is usually an accessory mineral, feldspar is one of the most abundant minerals in deformed rocks in the crust. Feldspar microboudins scattered in plastic quartz matrix commonly occur in felsic gneisses and mylonites. It will largely extend the application range of the microboudinage piezometer, if a feldspar microboudinage piezometer can be established. However, the microboudinage piezometers of tourmaline, which were derived on an assumption that this type of columnar minerals has a cylindrical shape, cannot be directly applied to the feldspar porphyroclasts that apparently display ellipsoidal shapes. In Chapter 3, we treat each of the feldspar microboudin as a circular-truncated-conical fiber, which is close to the ellipsoidal shape and makes the calculation much simplified, and then establish the feldspar microboudin piezometer with the estimated tensile strength of feldspar. The feldspar microboudin piezometer is applied in estimating the magnitude of differential stress recorded by felsic rocks from the Red River, Chongshan, and Gaoligong shear zones in Yunnan, China.

The mechanical process of joints infilling in sandstone beds embedded in mudstone or shale beds is similar to the fracturing process of mineral crystals embedded in plastically deformed matrix. The mechanical model for mineral microboudin can also be applied for analysis on joints in

layered sedimentary rocks. Longstanding problems in the study of joints in layered sedimentary rocks include the ideal relationship between joint spacing (s) and bed thickness (t) and the interpretation for the formation of orthogonal joints. In Chapter 4, based on analysis with the near-end fracturing stress transfer model, we propose a power law: $s=mt^{1-1/k}$, where m equals half the ratio of layer tensile strength to interface shear stress, and k is the Weibull modulus, for the relationship between the joint spacing of both the systematic and cross joints and bed thickness. This power-law equation provides an excellent description for the data measured from the interlayered sandstone and shale beds in the Sainte-Anne-des-Monts, Quebec, Canada. The m value of the cross joints is 3.1 times larger than that of the systematic joints, which indicates that the interfacial shear stress normal to the systematic joints was higher than the interfacial shear stress normal to the cross joints. Meanwhile, a new interpretation for the formation of vertical orthogonal joints in flat-lying sandstones is proposed based on the anatomic investigation on the grid-lock type orthogonal joints in the Potsdam sandstone of Cambrian age at Ausable Chasm (NY, USA) and Beauharnois (Quebec, Canada) that the joints may result from the auxetic effects of quartz-rich sandstone in the absence of local or regional stress rotation. The aspect-ratio of sandstone blocks bounded by orthogonal joints is related to the value of Poisson's ratio of the sandstone.

Chapter 5 discusses the significance of the study on geological composite materials based on the refined shear-lag model, the comparison between the tourmaline and feldspar piezometer and the quartz recrystallized grain size piezometer and the stereological correction for the estimation of the microboudin aspect-ratios. Finally, in Chapter 6 I draw a concise summary of the main conclusions and present the work that needs to be conducted in the future.

To facilitate reading of the thesis, the basic concepts and theory of continuum mechanics applied in geology (Section 1.2), the deformation mechanisms for materials and corresponding structures (Section 1.3), fracture theory and flow laws (Section 1.4) and the mechanical models for composite materials under deformation (Section 1.5) are introduced in the following.

1.2 Continuum mechanics basics in geology

Geological materials with components of difference in competence can be simplified as competent fibers embedded in incompetent matrix such as competent columnar mineral occurring

in ductile polycrystalline matrix (Fig. 1.1a) or competent layers bounded by incompetent layers such as sandstones or limestones interlayered with mudstones and shales (Fig. 1.1b). The deformation of geological materials also follows the rules of continuum mechanics. In the following, basic concepts of continuum mechanics and corresponding measuring methods for geological materials will be introduced.

In continuum mechanics, stress (σ) is defined as the internal forces that adjacent particles exert on each other in a continuous material. In a simple situation that a straight rod with uniform material and a cross section (A_0) (Fig. 1.2a), is subjected to a tension force F, assuming that the rod is stretched in an equilibrium state (Fig. 1.2b), the stress throughout the rod normal to the cross section (A) can be expressed as (Fig. 1.2c):

$$\sigma = F/A \qquad (1.1)$$

Stress in the crust is distributed in a large range. Taking the vertical stress, also known as the lithostatic pressure, as an example, it is calculated by the equation:

$$\sigma = \rho g z \qquad (1.2)$$

where ρ is the density of overburden rock, g is the gravitational acceleration and z is the depth.

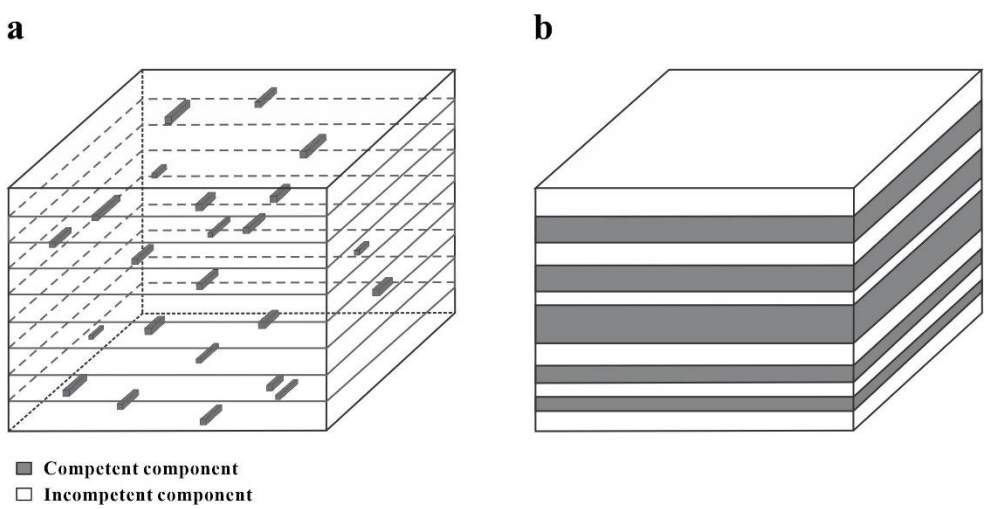

Figure 1.1 Sketches of geological composite material. Polymineralic rock, represented by deformed rocks with foliations (planes defined by grey lines) and lineations (defined by the long axis orientation of the competent mineral fibers) (a); Layered rock terrains, which can be typically represented by interlayered sedimentary rocks (b).

Assuming the average density of the crust is 2.7 g/cm^3, and an average crustal thickness of 40 km, the vertical stress is increasing from 0 MPa at the surface of the crust to about 1000 MPa at the bottom of the crust. Knowledge of the stress state in the crust is critical not only to solve problems with rocks in civil, energy and mining engineering, but also to deal with problems in geology, geophysics and geodynamics (McGarr & Gay, 1978; Zoback, 2007; Zang & Stephansson, 2010; Lei & Gao; 2018; Delorey et al., 2021). For example, in civil and mining engineering, it is essential to know the rock stresses and stress changes as precisely as possible while designing and excavating underground openings in stressed rock mass to avoid rock bursting and collapse (Zang & Stephansson, 2010). It is also significant to extract information of the stress field, which is preserved in deformed rock, in order to understand the tectonic evolution and geodynamical process of a study region (Lithgow-Bertelloni & Guynn, 2004). Therefore, measurements of the state of stress of different depth levels in the crust are required for both engineering and fundamental research.

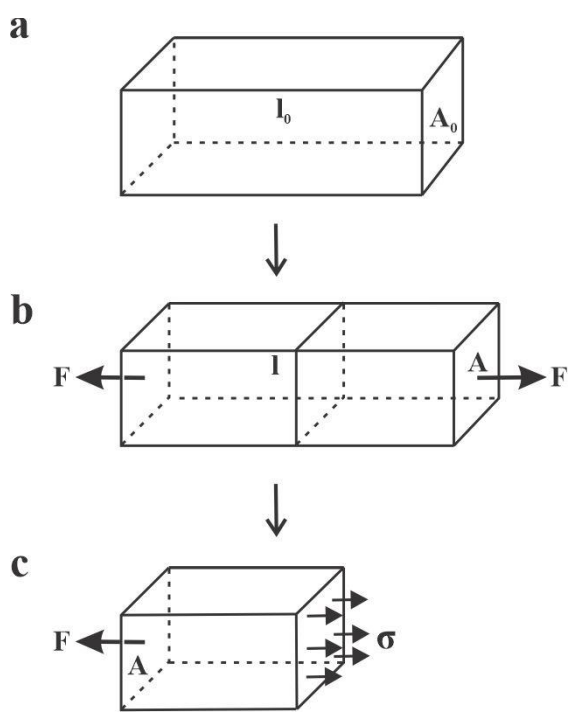

Figure 1.2 A rod with squared ends (area: A_0) (a) stretched under a tension force F (b). In an equilibrium state, the tension force equals to $A\sigma$ (c).

Methods measuring the stress field of present day include stress relief method and hydraulic fracturing method (McGarr & Gay, 1978; Amadei & Stephansson, 1997; Ljunggren et al., 2003;

Jaeger et al., 2009). Stress relief method is commonly performed by a trepanning or overcoring process. After removing the ambient stress exerting on rock, the following strain relief can be measured. The stress correlated to the measured strain relief then can be calculated and related to the state of the ambient stress field (Amadei & Stephansson, 1997; de Mello Franco et al., 2002). measuring after Hydraulic fracturing method pumps fluid into an isolated section of a borehole and records the history of pressure-time for the hydraulic fluid. The maximum principal stress then can be calculated by the theory for fracture close to a pressurized borehole developed by Hubbert and Willis (1957) and Kehle (1964) (Rummel et al., 2002; Ljunggren et al., 2003). These methods can only measure the stress field near the surface, commonly less than a depth of 1500 m (McGarr & Gay, 1978; Ljunggren et al., 2003).

Compared to the stress field near the surface, the information of the stress state in deep Earth's crust is harder to be acquired directly. However, deformed rock exposed to the surface carries information of the state of stress in deep crust in the past, and the interpreted stress is referred to as paleostress. Structural geologists have been calibrating the magnitude of paleostress by microstructures in deformed rocks since the 1970s (see Table 1.1 and 1.2). The characteristic microstructures that can be applied include dislocation density and grain size of subgrain and dynamically recrystallized grain (the details in Section 1.3.2). The piezometer of dislocation density (ρ, cm^{-2}) is expressed as:

$$\sigma = h\rho^{i} \qquad (1.3)$$

where h and i are the experimental parameters. Table 1.1 lists the parameters for dislocation density piezometers of quartz.

Table 1.1 Dislocation density piezometers of quartz

Reference	***h***	***i***
Twiss, 1977	2.47E-03	0.5
McCormick, 1977	1.64E-04	0.66
Kohlstedt and Weathers, 1980	2.89E-04	0.67
Goetze, 1975	6.30E-03	0.5
Weathers et al., 1979	6.60E-03	0.5

σ in MPa and ρ in cm^{-2}. Modified from Ji et al. (2021b).

Table 1.2 Piezometers of recrystallized grain size and subgrain size for minerals

Mineral	Mechanism	*p*	*q*	Reference
Recrystallized grain				
Qtz	undistinguished	381	0.71	Mercier et al., 1977
Qtz	undistinguished	603	0.68	Twiss, 1977
Qtz	undistinguished	36279	1.695	Koch, 1983
Qtz	SGR + GBM	669	0.794	Stipp et al., 2003
Qtz	BLG	1264.1	1.639	Stipp et al., 2003
Qtz	undistinguished	451	0.629	Cross et al., 2017
Qtz（wet）	undistinguished	4090	1.11	Christie et al., 1980
Qtz（dry）	undistinguished	3902	1.43	Christie et al., 1980
Qtz	SGR + GBM	489.73	0.794	Holyoke and Kronenberg, 2010
Qtz	BLG	883.93	1.639	Holyoke and Kronenberg, 2010
Ab	GBM	433.4	1.52	Post and Tullis, 1999
An	undistinguished	855	0.68	Twiss, 1977
Hl	SGR	116.4	0.85	Guillope et al., 1979
Hl	GBM	1274.9	0.78	Guillope et al., 1979
Cal	SGR	813	0.88	Rutter, 1995
Cal	GBM	2188	0.89	Rutter, 1995
Cal	undistinguished	1972	0.71	Friedman and Higgs, 1981
Cal	undistinguished	822	0.68	Twiss, 1977
Cpx	undistinguished	9451	1.11	Mercier, 1985
Opx	undistinguished	9274	1.18	Mercier, 1985
Ol（wet）	undistinguished	1900	0.67	Post, 1977
Ol (dry）	undistinguished	4815	0.79	Ross et al., 1980
Ol	undistinguished	2095	0.85	Karato et al., 1980
Ol	undistinguished	1601	0.68	Twiss, 1977
Ol	undistinguished	1380	0.75	Van der Wal et al., 1993
Py	undistinguished	1453	0.9	Cox et al., 1981
Subgrain				
Qtz	dislocation climb	200	1	Twiss, 1977
Hl	dislocation climb	80	1	Guillope et al., 1979
Hl	dislocation climb	190	1	Carter et al., 1982
Hl	dislocation climb	209	1.03	Hansen, 1987
Hl	dislocation climb	136	0.92	Carter et al., 1993
Hl	dislocation climb	116	0.88	Carter et al., 1982
Hl	dislocation climb	106	0.87	Handin et al., 1986
Opx	dislocation climb	2939	1.308	Linckens et al., 2014
Ol（wet）	dislocation climb	5057.6	1.449	Ross et al., 1980
Ol (dry）	dislocation climb	21600.64	1.613	Ross et al., 1980
Ol	dislocation climb	4492	1.49	Karato et al., 1980

Abbreviations: Ab, albite; An, anorthite; Cal, calcite; Cpx, clinopyroxene; Hl, halite; Ol, olivine; Opx, orthopyroxene; Py, pyrite; Qtz, quartz; BLG, bulging; SGR, subgrain rotation; GBM, grain boundary migration. Modified from Ji et al. (2021b).

The piezometer of subgrain and dynamically recrystallized grain (d, μm) has the following form:

$$\sigma = pd^{-q} \qquad (1.4)$$

where p and q are the experimental parameters. Table 1.2 lists the parameters for piezometers of recrystallized grain size and subgrain size for different minerals.

Piezometers of dislocation density and subgrain size are rarely used nowadays because these two methods require the use of a transmission electron microscope, which is time-consuming and expensive, and it is hard to determine whether the subgrain and dislocation density in the measured rocks were formed during steady-state creep. The recrystallized grain size piezometers have been widely applied to estimate the stresses for plastically deformed rocks from deep crust (e.g., Twiss, 1977; Karato et al., 1980; Stipp et al., 2003; Holyoke & Kronenberg, 2010). There are other piezometers that can be used to estimate the magnitude of stress from deformed rocks, such as the microboudinage piezometer (Masuda & Kuriyama, 1988; Masuda et al., 1989; 2008; Omori et al., 2016; Matsumura et al., 2017), and the comparison between the recrystallized grain size piezometer and microboudinage piezometer will be focused in Chapter 2.

Strain (ε) is a measure of deformation, which represents the total displacement between particles in a material relative to a length of reference. Assuming that the straight rod with an original length of l_0 is stretched to a finite length of l under the tension force F (Fig. 1.2b), the strain along the direction of F can be expressed as:

$$\varepsilon = (l - l_0)/l_0 \qquad (1.5)$$

Strain rate ($\dot{\varepsilon}$) is defined as the change in strain of a material within a unit time. In the nature, geological composite materials like rocks unusually deform at much slower strain rates, which are hard to be observed by eyes. Table 1.3 lists the strain rates estimated from different tectonic environments in all over the world, most of which are between 10^{-13} and 10^{-15} s^{-1}, and the average strain rate is 10^{-14} s^{-1}. Strain and strain rate quantify the deformation processes and results caused by applied stress.

Table 1.3 Geological strain rates estimated from the Earth's crust

Region	Tectonic domain	Methods	Strain rate (s^{-1})	Deformation	Reference
Ruby Cap duplex, Australia	Contractional	Finite strain + isotopic age	5×10^{-14}-10^{-15}	Ductile	Hirth et al., 2001
Athens Dome, Vermont	Contractional	Finite strain + isotopic age	2.4×10^{-14}	Ductile	Christensen et al., 1989
Pyrenees, France	Contractional	Finite strain + isotopic age	1.1×10^{-15}- 7.7×10^{-15}	Semi-brittle	Müller et al., 2000
Ailaoshan-red river fault, Yunnan	Strike-slip	Finite strain + isotopic age	1.3×10^{-13}-2.5×10^{-15}	Ductile	Boutonnet et al., 2013
Karakoram fault	Strike-slip	Finite strain + isotopic age	1.6×10^{-13}-10^{-14}	Ductile	Boutonnet et al., 2013
Basin and range province	Extensional	Paleostress + flow law	10^{-12}-10^{-15}	Ductile	Campbell-Stone and John, 2002; Gans and Bohrson,1998
Whipple Mountains	Extensional	Paleostress + flow law	10^{-12}-10^{-15}	Ductile	Behr and Platt, 2011
Tinos island, Greece	Extensional	Paleostress + flow law	2.6×10^{-14}	Ductile	Gueydan et al., 2005
Tinos island, Greece	Extensional	Paleostress + flow law	1.5×10^{-15}	Ductile	Gueydan et al., 2005
Alpine fault, New Zealand	Strike-slip	Paleostress + flow law	10^{-13}	Ductile	Cross et al., 2015
Alpine fault, New Zealand	Strike-slip	Paleostress + flow law	2×10^{-12}	Ductile	Norris and Cooper, 2003; Suther et al., 1995
Alto Adige, northern Italy	Strike-slip	Paleostress + flow law	10^{-13}-10^{-14}	Ductile	Stöckhert et al., 1999
Raft river extensional shear zone, Utah	Extensional	Paleostress + flow law	10^{-12}-10^{-15}	Ductile	Gottardi and Teyssier, 2013
Ruby Cap duplex, Australia	Contractional	Paleostress + flow law	10^{-13}-10^{-15}	Ductile	Dunlap et al., 1997
Carpathian Mountains	Extensional	Paleostress + flow law	9×10^{-12}- 6×10^{-14}	Ductile	Jeřábek et al., 2007
Basin and range province	Extensional	Paleostress + flow law	10^{-15}	Ductile	Lynch and Morgan, 1987
		Theoretical analysis	10^{-15}	Ductile	Fagereng and Biggs, 2019
		Theoretical analysis	10^{-14}	Ductile	Fagereng and Biggs, 2019
Channel flow		Theoretical analysis	10^{-14}- 10^{-13}	Surface displacement	Fagereng and Biggs, 2019
Subducting plate		Seismic data	10^{-15}	Brittle	Bevis,1988; Holt et al., 1995
		Geodetic	10^{-13}-10^{-15}	Surface displacement	Pfiffner and Ramsay, 1982
		Geodetic	10^{-14}	Surface displacement	Twiss and Moores, 2001
	Contractional	Geodetic	1.33×10^{-15}	Surface displacement	Foster and Gray, 2007
Mid-ocean ridge	Extensional	Geodetic	1.4×10^{-14}	Surface displacement	Fagereng and Biggs, 2019
Tibet Plateau		Geodetic	$<5\times10^{-15}$	Surface displacement	Flesch et al., 2001
Tibet Plateau		Geodetic	10^{-16}- 10^{-15}	Surface displacement	England and Molar, 1997
Tibet Plateau		Geodetic	10^{-15}	Surface displacement	Wang and Wright, 2012; Garthwaite et al., 2013
Tianshan	Contractional	Geodetic	10^{-15}	Surface displacement	England and Molar, 2015
Arab-European terrain		Geodetic	3×10^{-16}- 3×10^{-15}	Surface displacement	Walters et al., 2017
Anatolia fault, Turkey	Strike-slip	Geodetic	6×10^{-17}- 6×10^{-15}	Surface displacement	England et al., 2016
Apennines, Italy		Geodetic	2×10^{-15}	Surface displacement	D'Agostino et al., 2014
San Andres fault, USA	Strike-slip	Geodetic	10^{-14}	Surface displacement	Fagereng and Biggs, 2019

Modified from Ji et al. (2021b).

Strain and strain rate on the surface of the crust can be obtained by geodetic surveys such as measurement of the relative displacement between GPS stations during a certain period. However, it is difficult to infer the strain rate of ductile deformation in the deep crust from the strain rate of the crust surface, since the dominant deformation mechanism of crustal rocks transits from brittle to brittle-ductile, and then to complete ductile as the depth increases. However, the strain rate in the deep crust could be measured from deformed rocks exposed in shear zones on the crust surface. There are three approaches: (1) Determining finite strain and deformation period simultaneously. For example, Christensen et al. (1989) used the garnet snowball structure in the shear zone of the Athens dome in the Southeast Vermont, USA to estimate the strain rate, which is about 2.4×10^{-14} s^{-1}. Müller et al. (2000) estimated the strain rate to be 1.1×10^{-15}-7.7×10^{-15} s^{-1} with pressure shadow structure of pyrite in slate in the northern Pyrenees, France. Sassier et al. (2009) measured the finite strain and obtained the Th-Pb age of the monazite of the felsic dikes in the Ailaoshan shear zone in Yunnan, China. The results indicate that the sinistral strike-slip of the shear zone lasted from 30 to 17 Ma, and the strain rate is about 3.5×10^{-14} s^{-1}. (2) Estimating deformation temperatures and paleostress of deformed rocks with geothermometers and paleo-piezometers, and then calculating strain rates with experimentally determined rock flow laws (Gueydan et al., 2005; Jeřábek et al., 2007). (3) Theoretical estimation. With known width, displacement (offset), and deformation period of shear zones, the overall average strain rates can be estimated (Pfiffner & Ramsay, 1982; Twiss & Moores, 2001; Boutonnet et al., 2013). A ductile shear zone with a width of 1 km and a displacement of 1 km during 2 Ma, leads to an average strain rate of 1.585×10^{-14} s^{-1}.

Other concepts that are essential to understand material deformation processes are introduced in the following. In the uniaxial tensile testing similar to that in Fig. 1.2, the material deformation could be similar to the process depicted by Fig. 1.3. The material will first go through the elastic deformation regime in which the strain can be completely recovered after the force is removed. Deformation in this regime can be described by the Hooke's law, and the ratio of the Rise and Run is the Young's modulus. As the strain increases, the stress in the material exceeds the yield strength, at which point the material deformation enters into plastic regime. In this regime, the stress is also called as flow stress, which means the stress keeps the material flowing, and the strain cannot be completely recovered after removing the force. In most cases the stress will increase with the strain in a process of strain hardening, and it will finally reach to the maximum

value, which is also known as the ultimate strength or tensile strength, leading to the final break of the material.

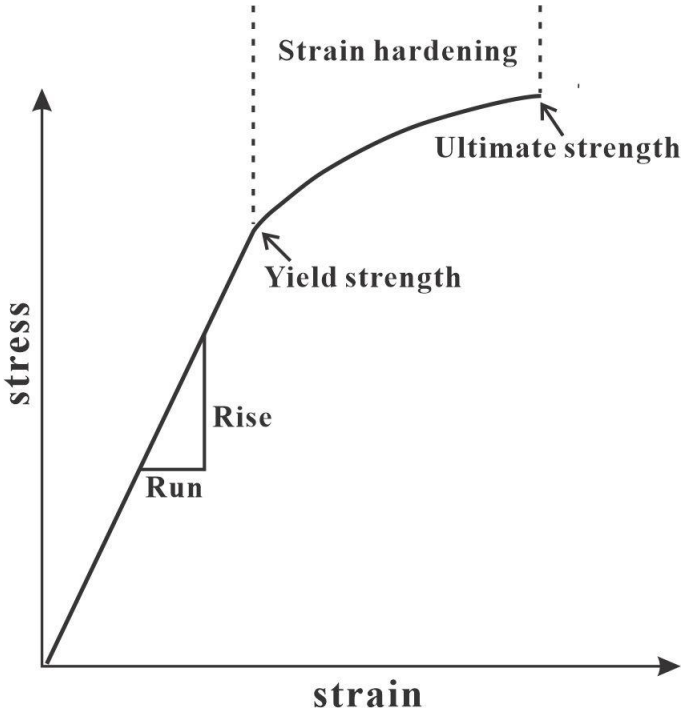

Figure 1.3 Typical stress-strain curve of rocks under uniaxial tensile testing.

1.3 Deformation mechanisms and structures

Geological materials are essentially composite materials, and will deform when they are subjected to tectonic stress (e.g., Tullis et al., 1991; Ji & Zhao, 1993; Handy, 1994; Ji & Xia, 2002; Ji, 2004). Deformation mechanisms that control deformation processes are determined by not only the internal factors of materials (e.g., composition, grain size and porosity), but also the external environment conditions (e.g., T, P, σ and fluid). Generally, deformation mechanisms can be divided into two categories: brittle and ductile. Brittle deformation mechanisms commonly control the deformation that occurs at relative high strain rate and low temperature in the upper crust, whereas ductile deformation mechanisms dominate at deeper crustal levels (Passchier & Trouw, 2005). Brittle mechanisms include fracturing and cataclastic flow. Ductile mechanisms include dissolution-precipitation, grain boundary sliding, dislocation creep, diffusion creep and dynamic recrystallization, etc. Deformation of the same material can be controlled by different

mechanisms, which is commonly a comprehensive result of factors such as stress, strain rate, and temperature (Fig. 1.4). Meanwhile, strong and weak components of composite material under a uniform stress field could be deformed by different mechanisms. Deformation mechanisms and corresponding structures that involve in this dissertation will be introduced in detail in the following section.

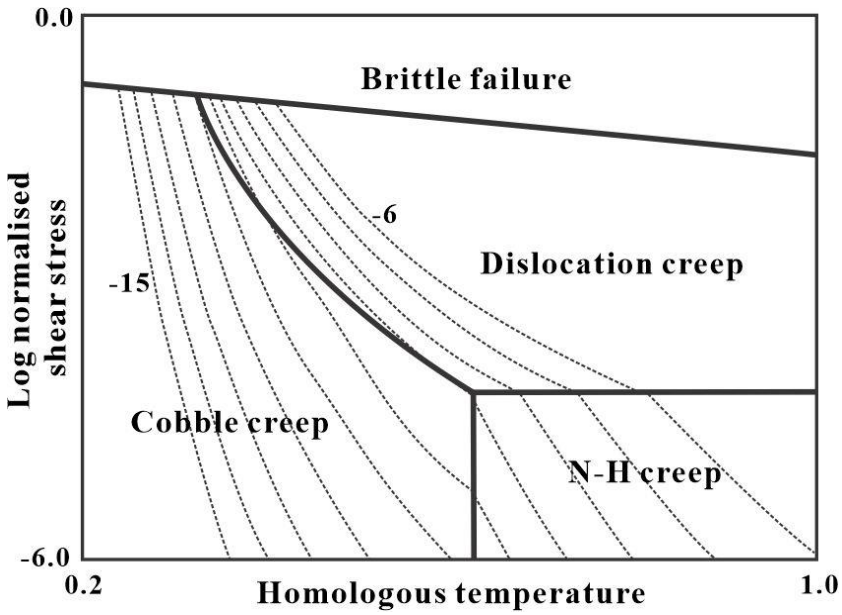

Figure 1.4 The deformation mechanisms map for a grain size of 10 μm of single dry quartz crystals under confining pressure of 100 MPa, and strain rate contours are shown on this map (10^{-6} to 10^{-15} s^{-1}). N-H: Nabarro-Herring. Modified from Passchier and Trouw (2005).

1.3.1 Brittle mechanisms and structures

In geological material like rocks, strong fibers or competent layers in weak matrix commonly deform in brittle manner when they are subjected to differential stress. Fracturing is the common mechanism controlling this process by creating permanent linear breaks in both strong single mineral grains in weak polymineralic matrix and competent rock layers in layered rock terrains (e.g., crack and joint). Starting from microcracks, which nucleate on grain boundaries, intracrystalline solid or fluid inclusions, or flaws in crystal lattice, fractures propagate rapidly when the stress at the fracture tips reach a critical value. If the stress at the fracture tips is lower than the critical value, fractures can grow slowly by the process of subcritical microcrack growth (Atkinson, 1982; Darot et al., 1985; Olson, 2004; Olson et al., 2009). If the stress reach the

critical value, the velocity of fracture propagation will be comparable to the velocity of elastic waves in the material (Lawn, 1995; Passchier & Trouw, 2005). If the stress is lower than the critical value, the velocity of subcritical microcrack growth will be affected by temperature and chemical environment, especially the fluid around the fracture tips, and will be much slower (Olson et al., 2002; Passchier & Trouw, 2005). Results of rapid fracturing can be recognized by structures on fracture planes, such as plume structure, and the infillings intruded into fractures. In this dissertation, it is focused on fractures caused by rapid fracturing and the process of subcritical microcrack growth will not be discussed further.

Fractures can be divided into brittle and ductile types based on the amount of plastic deformation before fracturing. If a material breaks without apparent plastic deformation, the fracture is brittle. Otherwise, like the situation in Fig. 1.3, the fracture is ductile. This dissertation focuses on brittle fractures in the strong phase components of composite geological materials. Fractures can be classified as cracks, joints and faults. There is no lateral displacement on planes of cracks or joints, whereas discernible displacement occurs on planes of faults. This dissertation focuses on fractures with no shear displacement, such as fractures in mineral fibers and joints in sandstones. Fractures can also be divided into three modes according to the relation between directions of stress and crack front. Mode I is also called as opening mode, for which the tensile stress is normal to the crack plane. Mode II is also called as sliding mode, for which the shear stress is parallel to the crack plane and perpendicular to crack front. Mode III is also known as tearing mode, for which the shear stress is acting parallel to the crack plane and to the crack front. Mode I is also referred as to extension or tensile fracture, whereas Mode II and III belong to shear fracture (Twiss and Moores, 2001). This dissertation concentrates the study on tensile fractures.

1.3.2 Ductile mechanisms and structures

Incompetent components in geological composite materials generally tend to deform in ductile manners by mechanisms such as dissolution-precipitation, dislocation creep, diffusion creep, dynamic recrystallization and grain boundary sliding. Brief introduction on each mechanism and corresponding structures are given below.

At relative low pressure and temperature conditions, such as diagenetic to low-grade metamorphic conditions, dissolution-precipitation is the main deformation mechanism. For example, it can be a significant deformation mechanism for incompetent layers of terrains

consisting of embedded sandstones and mudstones when they are subjected to tectonic stress at shallow crustal level. Dissolution occurs at grain boundary contact where the differential stress is high, and the dissolved material will be transferred to localities with lower differential stress by aqueous fluid and redeposit. This is because the solubility of a mineral commonly increases with stress. After dissolution-precipitation process, mineral grains change in shape without intracrystalline deformation (Passchier & Trouw, 2005). The typical structure caused by dissolution-precipitation mechanism in granular polymineralic rocks is mineral pressure shadow.

Different from dissolution-precipitation mechanism, when rocks are under higher metamorphic conditions, intracrystalline deformation begins. In this regime, under relatively lower temperature, differential stress causes dislocation growth from lattice defects in mineral crystals. Ductile deformation of mineral crystals takes place with the movement of dislocations. This process is dislocation creep (Fig. 1.4), which includes dislocation glide and dislocation climb process. Dislocations commonly glide along certain slip systems, and in most situation more than one slip system in rock-forming minerals, such as in quartz and feldspar, can be simultaneously active. When dislocation density increases and dislocations of different slip system get entangled during the formation and movement process, mineral crystals become more difficult to deform. The process is strain hardening (Fig. 1.3). Common microstructures that are related to dislocation creep, are undulose extinction, deformation lamellae, subgrains, dynamic recrystallization-induced neograins and lattice-preferred orientation (LPO).

When temperature gets higher, mineral crystals will deform by migration of vacancies through the lattice. This process is known as diffusion creep, which can be classified into two types: Coble creep and Nabarro-Herring creep (Fig. 1.4) (Wheeler, 1992). Coble creep operates by diffusion of vacancies along grain boundaries, and is also named as grain boundary diffusion. Nabarro-Herring creep functions by diffusion of vacancies throughout the crystal lattice, and therefore it also known as volume diffusion (Knipe, 1989). Different from dislocation creep, few microstructures are regarded as the results of pure diffusion creep.

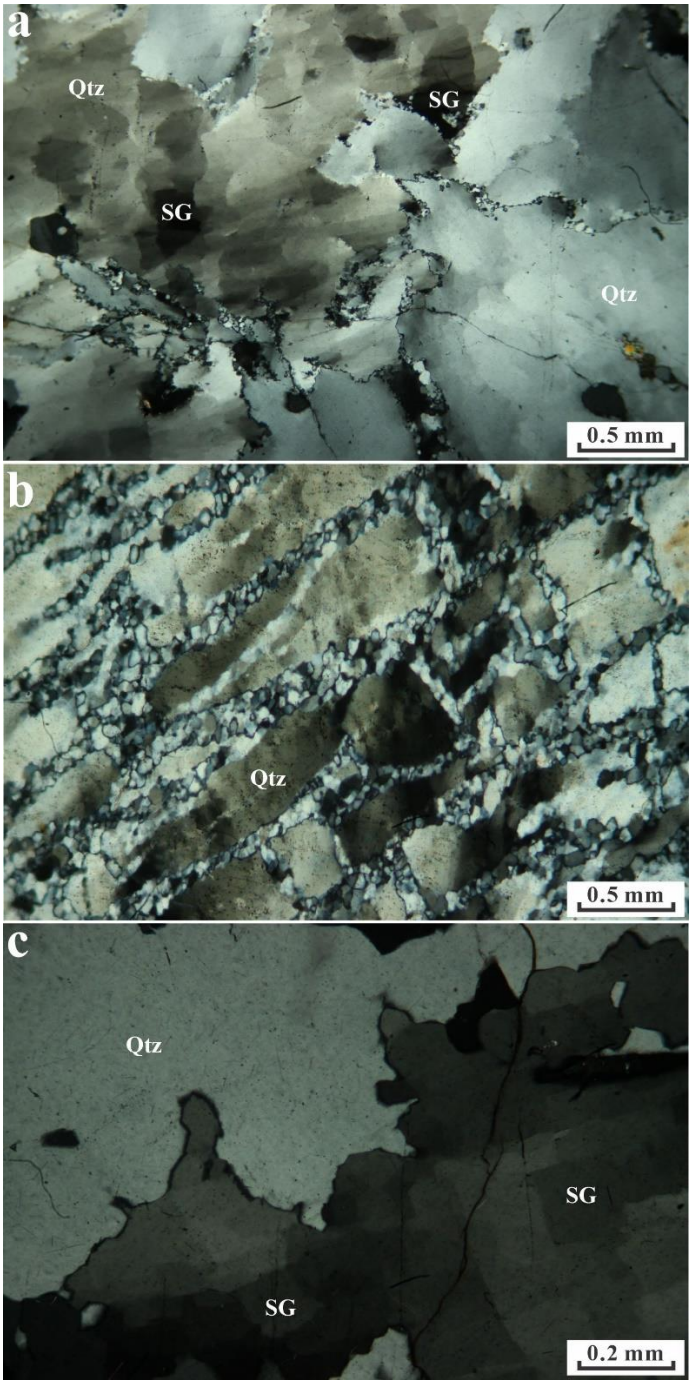

Figure 1.5 Typical microstructures formed by three mechanisms of dynamic recrystallization in quartz (Qtz). (a) Bulging (BLG) (Yunkai Mountain, Guangdong, China), (b) subgrain rotation (SGR) (Red River shear zone, Yunnan, China), and (c) grain boundary migration (GBM) (Morin shear zone, Rawdon, Québec, Canada). The neograin sizes from BLG, SGR and GBM are inferior, equal and superior to the subgrain size, respectively. SG: subgrain. Modified from Ji et al. (2021b).

Combined with dislocation and diffusion creep, dynamic recrystallization is a significant recovery mechanism to reduce dislocation density. As temperature increases and flow stress decreases, dynamic recrystallization can be subdivided into three types, thus bulging (BLG), subgrain rotation (SGR) and grain boundary migration (GBM) recrystallization (Fig. 1.5; e.g., Stipp et al., 2002, 2006; Passchier & Trouw, 2005; Jeřábek et al., 2007). BLG mechanism occurs at grain boundaries under relatively lower temperature, when dislocation climb is hampered and the grain boundary mobility is low. Small new grains form along boundaries of host grains, especially at the triple junctions (Fig. 1.5a), and when host grains are surrounded by new grains, core-and-mantle structures are present (Passchier & Trouw, 2005). For SGR and GBM mechanisms, dislocation climb assisted by diffusion plays an important role (Hirth & Tullis, 1992; Hirth et al., 2001). SGR mechanism is activated at temperatures higher than that activates BLG mechanism. When strain is low, core-and-mantle structures can also form, but will be replaced by sheets consisting of new grains and subgrains of the same shape and size (Fig. 1.5b) when strain increases and the host grains will be totally replaced.

At even higher temperatures, increasing grain boundary mobility favors GBM mechanism, which commonly results in lobate grain boundaries and grains of variable size (Fig. 1.5c; Passchier & Trouw, 2005). Size of recrystallized grains are believed to be related to the applied differential stress, which is the theoretical base for recrystallized grain size piezometer (e.g., Twiss, 1977; Karato et al., 1980; Mercier, 1985; Stipp et al., 2003; Holyoke & Kronenberg, 2010). Each recrystallization mechanism during steady-state creep results in a specific mean size of neograins. So far the piezometers of quartz recrystallized grain sizes have been calibrated in laboratory only for the mechanisms of bulging recrystallization and subgrain rotation recrystallization. No piezomenter is available yet for quartz deformed by grain boundary migration recrystallization. Grain size can be measured by various methods including the mean linear intercept method and image analysis techniques (Twiss & Moores, 2001; Passchier & Trouw, 2005) The limitations of the recrystallized grain size piezometers have been discussed in Passchier and Trouw (2005), Li et al. (2020) and Li and Ji (2021).

1.4 Fracture theory and flow laws

As different components in geological composite materials may deform in brittle or ductile manners, it is important that there are theories and rules to explain and forecast the deformation

behaviors. Fracture theory and flow laws are rules that describe the relationship between external factors and brittle and ductile deformation behaviors of materials, respectively.

1.4.1 Fracture theory

The Griffith fracture theory provides an excellent explanation for fracture experiments on brittle materials. Assuming that the materials are distributed with microcracks, which is the case in geological materials like minerals and rocks, this theory predicts that high tensile stress will take place around ends of microcracks when materials are applied to certain level of differential stress. Fractures will grow from ends of microcracks due to the tensile stress (Paterson & Wong, 2005). Based on this theory, failure envelope illustrating the stress conditions needed to create fractures in rocks can be expressed by the equation (Secor, 1965; Etheridge, 1983):

$$\tau^2 - 4C\sigma - 4C^2 = 0 \qquad (1.6)$$

Where τ is shear stress, σ is the normal stress components on planes of the most critically orientated microcracks, and C is the tensile strength. As the failure stress predicted by this equation is significantly lower than experimental results in the compression region, the segment of parabolic line in the compression region given by the Griffith fracture theory was modified to be a straight line (McLintock & Walsh, 1962). The parabolic segment in the tension region connects the straight segment where the slopes of the segments are the same, forming the composite failure envelope (Fig. 1.6).

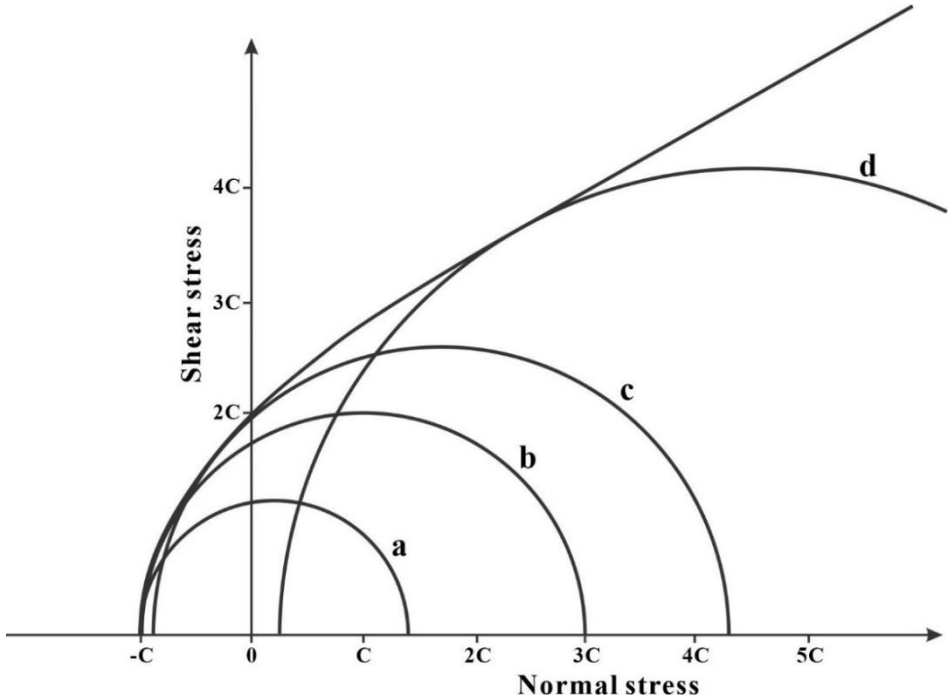

Figure 1.6 Diagram illustrating composite failure envelope and stress circles under various circumstances. *C*: tensile strength; a: tensile fracture; b: tensile fracture caused by the critical differential stress; c: extensional shear fracture; d: compressional shear fracture. The regimes of compression and tension occur when the normal stress is above and below zero, respectively. Modified from Etheridge (1983).

Fracture will occur when the stress circles are tangent with the composite failure envelope. Figure 1.6 also illustrates the relationship between fracture types with the applied stress. Tensile fractures can merely take place under the condition that:

$$\sigma_3^* = -C;\ \sigma_1^* \leq 3C \text{ or } \sigma_1^*\text{-}\sigma_3^* \leq 4C \qquad (1.7)$$

where σ_1^* and σ_3^* are the maximum and minimum principal effective stress, and (σ_1^*-σ_3^*) is the differential stress (Secor, 1965; Etheridge, 1983; Passchier & Trouw, 2005; Sibson, 2017).

In Fig. 1.6, the cohesion or the shear strength (τ_0) is taken to be equal to 2*C*, where *C* is the tensile strength. The relationship between shear strength and tensile strength may vary from material to material, depending on the composition and crystal structure of the constitutive minerals. For pure Al, stainless steel, brass, and pure Zn, τ_0=1.8*C* (Guduru et al., 2005). The systematic investigations on the correlation between τ_0 and *C* are still lacking for complex natural rocks.

It is worth noting that the C value in Eqs. (1.6 and 1.7) is not a constant value due to the size effects (e.g., Bažant, 2000; Paterson & Wong, 2005; Askeland et al., 2010). Previous theoretical analyses reveal that the tensile strength of a material are strongly affected by the size, shape, orientation and distribution of internal flaws (e.g., Weibull, 1951; Paterson & Wong, 2005; Dodson, 2006). Detailed analysis and discussion will be presented in following chapters.

1.4.2 Flow laws

When geological materials, especially single-phase mineral aggregates, are deformed in ductile manners (e.g., dislocation creep), it is the flow laws that can be used to describe the relation between external factors, such as temperature, pressure, stress, and deformation behaviors. Flow laws commonly have a form of equation as:

$$\dot{\varepsilon} = Ad^{-m} f_w{}^{r} \sigma^{n} \exp\left[-\frac{Q+P\Delta V}{RT}\right] \qquad (1.8)$$

where $\dot{\varepsilon}$ is the strain rate, A is the experimental constant, n is the stress exponent, d is the grain size in diameter, m is the grain size exponent, f_w is the water fugacity, r is the water fugacity exponent, Q is the activation energy, R is the gas constant (8.314 J/mol/K), and T is in absolute temperature (K), P is the pressure, and ΔV is the activation volume.

The effects of pressure and temperature on the deformation process are incorporated into the flow law. Water can cause minerals and rocks to become weak (Shao et al., 2013), however, the change of water content with space and time in minerals and rocks is extremely complicated. Even within the scale of hand specimens, the water content of different minerals and different parts is varying. The water fugacity exponent r for the main rock-forming minerals (quartz, feldspar and pyroxene) in the crust has been measured by only a few experiments so far (Hirth et al., 2001; Rybacki et al., 2006; Tokle et al., 2019), and the error of measurements is large. There is no experimental data for the r value of polymineralic rocks. The calculation of water fugacity fw is generally based on the water state equation in Tödheide (1972) or Pitzer and Sterner (1994), and it is assumed that the partial pressure of water is equal to the lithostatic pressure. In fact, water fugacity at a certain depth in the middle and lower crust is still unknown now. In addition, the dislocation creep is dominant (Ji & Xia, 2002; Karato, 2010) while grain size sensitive superplastic deformation mechanism occurs only in very local, discontinuous narrow bands (Rutter & Brodie, 1992; Fusseis et al., 2009), and is limited to high temperature and small grain

size polymineralic rocks in the ductile deformation domains of the middle and lower crust and upper mantle. Superplastic deformation can cause weakening of rock (e.g., Wang & Ji, 2000; Karato et al., 2008). The ΔV values of the main minerals and rocks in the crust and the crust-mantle transition zone have not been accurately determined by experiments so far, and are initially estimated to be between 0 and 20 cm^3/mol (Béjina et al., 1999; Zhang & Green, 2007; Lu & Jiang, 2019). Term $P\Delta V$ is much smaller than the Q value, so the influence of the confining pressure on the flow strength of crustal rocks can be negligible (Karato, 2010). Therefore, the terms of water fugacity, grain size and $P\Delta V$ in the flow law are commonly neglected, and the flow law can be presented in a more brief form:

$$\dot{\varepsilon} = A\sigma^n \, exp(-\frac{Q}{RT}) \qquad (1.9)$$

In most of the experimental studies on ductile deformation, it is the differential stress, temperature and strain rate data that can be controlled and collected to fit into the flow law (Paterson & Luan, 1990; Luan & Paterson, 1992; Rybacki & Dresen, 2000).

Among the main rock-forming minerals in the crust, quartz is the most common, and it plays a significant role in ductile deformation process of rocks especially in the middle crust. Therefore, deformation behaviors of quartz have been extensively studied under experimental conditions (e.g., Kronenberg & Tullis, 1984; Paterson & Luan, 1990; Luan & Paterson, 1992; Gleason & Tullis, 1995; Rutter & Brodie, 2004). The abundant previous studies make quartz a good example to illustrate the state of art of flow law.

Figure 1.7 illustrates that the flow strength of quartz changes with temperature at $\dot{\varepsilon}=10^{-14}$ s^{-1}. For example, at temperature of 400 °C, the flow strength of quartz given by different flow laws differs greatly, and the maximum value (271.7 MPa, Rutter & Brodie, 2004) is 2434 times higher than the minimum value (0.11 MPa, Wang et al., 1994). Assuming that the far-field differential stress is 50 MPa, at each given temperature, the strain rate calculated by the flow laws of different authors differs by 5 to 6 orders of magnitude (Fig. 1.7) (Ji et al., 2021b).

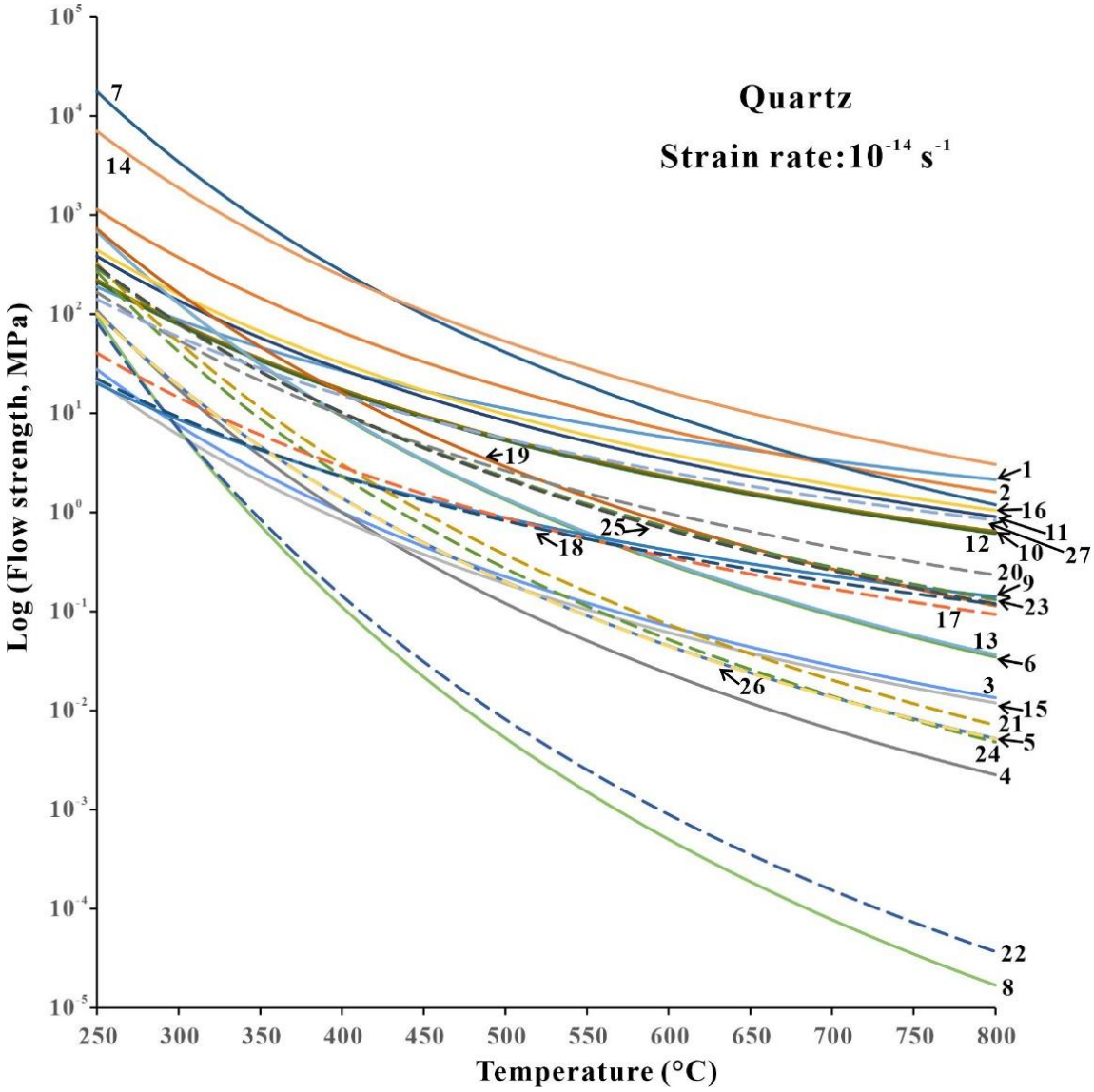

Figure 1.7 Flow strength of quartz as a function of temperature for each flow law listed in Table 1.4. The strain rate is taken as 10^{-14} s^{-1}. Modified from Ji et al. (2021b).

Table 1.4 Power flow law parameters for polycrystalline monophase aggregates of quartz deformed in the regime of dislocation creep

No.	Mineral	*n*	*Q* (kJ/mol)	*A* (MPa^{-n}/s)	References
1	Qtz	4	152	1.198E-08	Luan and Paterson, 1992
2	Qtz	4	223	1.095E-04	Gleason and Tullis, 1995
3	Qtz	1.9	123	3.470E-05	Hansen and Carter, 1982
4	Qtz	1.9	174	3.160E-01	Hansen, 1982
5	Qtz	1.8	151	2.884E-03	Jaoul et al., 1984
6	Qtz	2	168	1.260E-03	Shelton and Tullis, 1981
7	Qtz	2.97	242	3.553E-03	Rutter and Brodie, 2004
8	Qtz (dry)	1	132	1.570E-03	Wang et al., 1994
9	Qtz (dry)	2.4	101	9.140E-08	Wang et al., 1994
10	Qtz (dry)	2.7	134	1.100E-07	Koch, 1983
11	Qtz (dry)	2.9	149	2.400E-07	Koch et al., 1980
12	Qtz (dry)	2.7	134	1.260E-07	Koch, 1983, Carter and Tsenn, 1987
13	Qtz (dry)	2	167	1.000E-03	Shelton and Tullis, 1981
14	Qtz (dry)	2.8	184	3.980E-07	Jaoul et al., 1984
15	Qtz (dry)	1.9	121	3.500E-05	Hansen and Carter, 1982
16	Qtz (dry)	2.9	149	1.580E-07	Koch, 1983
17	Qtz (wet)	3.1	135	6.500E-08	Paterson and Luan, 1990
18	Qtz (wet)	2.7	120	2.200E-06	Kronenberg and Tullis, 1984
19	Qtz (dry)	2.3	171	3.100E-04	Jaoul et al., 1984
20	Qtz (wet)	2.6	145	5.050E-06	Koch et al., 1989
21	Qtz (wet)	1.9	173	3.160E-02	Hansen and Carter, 1982
22	Qtz (wet)	1.2	149	3.740E-02	Koch et al., 1980
23	Qtz (wet)	2.4	157	5.750E-05	Koch et al., 1980
24	Qtz (wet)	1.8	167	2.000E-02	Hansen and Carter, 1982
25	Qtz (wet)	2.6	134	1.580E-05	Kronenberg and Tullis, 1984
26	Qtz (wet)	2.4	160	1.000E-04	Koch et al., 1980
27	Qtz (wet)	1.8	151	2.910E-03	Jaoul et al., 1984
28	Qtz (wet)	3.1	135	6.500E-08	Paterson and Luan, 1990
29	Qtz (wet)	2.7	120	2.200E-06	Kronenberg and Tullis, 1984

Modified from Ji et al. (2021b).

The reasons for the above phenomenon are complicated. Although the different water content of specimens can explain the differences in some experimental results, the most significant reason is that researchers adapt different experimental deformation apparatuses with different measurement accuracy on the applied stress and determination standards for steady-state creep. For example, the Griggs apparatus using traditional solid confining pressure media (e.g., Shelton & Tullis, 1981; Koch, 1983; Kronenberg & Tullis, 1984), has considerable errors in the measurement of differential stress due to internal friction and other factors. Furthermore, temperature in samples

may also be unevenly distributed. The flow laws of Rutter and Brodie (2004, No. 7) and Jaoul et al. (1984) seriously overestimate the flow strength of dry quartz. The flow laws of Jaoul et al. (1984), Kronenberg and Tullis (1984) and Paterson and Luan (1990) underestimated the flow strength of wet quartz, which may be caused by partial melting of the samples during high temperature deformation (Paterson & Luan, 1990). According to the current data, the flow laws of Gleason and Tullis (1995) and Luan and Paterson (1992) are proper to be used to calculate the flow strength of dry and wet quartz, respectively (Ji et al., 2021b). Discussion about flow laws of quartz will be one of the focuses in Chapter 2 and 3.

1.5 Mechanic models

Mechanic models describing the deformation of geological materials, such as polymineralic rocks and layered rock terrains, are significant in understanding the process of deformation and predicting the deformation result. Different mechanic models for composite materials deformation have been introduced into geological materials research since the 1950s (Ramberg, 1955; Hobbs, 1967; Lachenbruch, 1961; Sowers, 1973; Pollard & Segall, 1987; Souffaché & Angelier, 1989). Among them, the shear-lag model of Cox (1952), introduced by Hobbs (1967), is the most widely applied model, and has been modified and improved to explain the deformation process and result of geological composite materials (McQuillan, 1973; Lloyd et al., 1982; Ferguson & Lloyd, 1982; Masuda et al., 1989; Gross, 1993; Zhao & Ji, 1997; Bai & Pollard, 2000; Li & Yang, 2007; Schöpfer et al., 2011; Matsumura et al., 2017).

1.5.1 Shear-lag model

Hobbs (1967) first applied the shear-lag model on explanation of tensile joints in layered sedimentary rock. He treated layered strata as a lamellar composite material consisting of aligned and continuous competent and incompetent layered components of equal length (e.g., Figs. 1.1b and 1.8a). Then, he assumed that all the components deform in a totally linear-elastic manner, in which no plastic yielding occurred. He also assumed that both bounding layers of incompetent components have the same elastic moduli lower than that of the competent components, and that the thickness of the incompetent layers is greater than that of the layer of competent components. Furthermore, residual stress effects were also ignored in the treatment. When applying stress on the composite material along the direction parallel to the layers, shear stresses are built on the

boundaries as a result of differences in elastic displacement between the bounding incompetent layers and embedded competent layer. Tensile stress in the competent layered components will increase due to existence of the shear stresses. At the initial stage of extension, all the layered components remain unfractured. However, as the extensional strain increases progressively, the tensile stress in the competent layer will eventually exceed the critical tensile strength of the competent components, and therefore a fracture propagates. The newly formed fracture is assumed to be a tensile stress free surface. As the extensional strain further increases, more fractures will then form in the competent layered components at positions where their critical tensile strengths have been reached by the tensile stress. All the fractures terminate at boundaries with the bounding incompetent layered components, for the incompetent layered components yields at notably higher magnitudes of extensional strain than the competent layered components (Garrett & Bailey, 1977; Ji & Saruwatari, 1998).

1.5.2 Stress transfer model (refined shear-lag model)

Several assumptions, such as those on the deformation manner, the elastic modulus and the thickness of each component in the original shear-lag model may not be consistent with the reality. For example, in polymineralic rocks, while the competent components tend to deform in a linear-elastic manner, the incompetent components tend to deform in a ductile manner under the same pressure and temperature conditions. The competent and incompetent components in composite materials are commonly different in their mechanic properties (e.g., elastic moduli, Poisson’s ratio, yield strength). The assumption that the thickness of the incompetent layers is much greater than the thickness of the layer of competent component is also in contrast to the fact that the thickness of incompetent layers is thinner than the competent layer in many sedimentary rocks (Narr & Suppe, 1991; Gross, 1993; Ji et al., 1998).

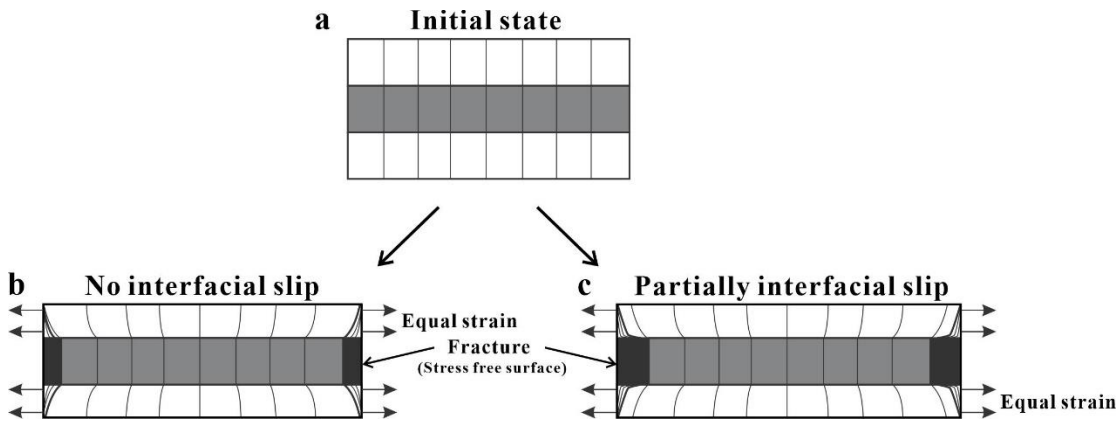

Figure 1.8 Schematic illustration for different stress transfer models. Thin lines as passive markers showing displacements during deformation. (a) The initial state of unstressed layered composite (grey: competent; white: incompetent). (b) and (c) The states of stressed layered composite. As a uniform extensional strain is applied at the ends of the incompetent components, no slip occurs on interfaces of the competent and incompetent components in (b), and partially slip takes place on interfaces of the competent and incompetent components in (c). The width of the fractures are exaggerated in the schematic illustration. Modified after Ji et al. (1998).

In order to analyze deformation of various geological composite systems more accurately, the original shear-lag model was then improved by modifications on the impractical assumptions mentioned above. Based on the previous attempt of taking plastic properties of incompetent component into account (Kelly & Tyson, 1965; Nardone & Prewo, 1986; Ji & Zhao, 1994), Zhao and Ji (1997) reconsidered the basic mechanical equilibrium and physical boundary conditions in the original shear-lag model. After critical analysis on the approximations in the derivation of the original model, a refined shear-lag model was built and will be referred to as stress transfer model in this dissertation. In the stress transfer model, the competent component deforms in a linear-elastic manner, while the incompetent component deforms in a plastic manner. Meanwhile, the thickness of incompetent components is not required to be greater than that of the competent components. Masuda and his coworkers (Masuda et al., 2008; Omori et al., 2016; Matsumura et al., 2017) applied the stress transfer model to refine their microboudinage piezometer, which will be presented and reviewed in detail in Chapter 2.

Another significant issue related to the applicability of the stress transfer model is the boundary condition between the incompetent and competent components (Fig. 1.8). Both situations of well-

bonded boundary and slip-occurring boundary are considered in the stress transfer model (Ji & Saruwatari, 1998; Ji et al., 1998). As illustrated in Fig. 1.8, when the layered composite are applied with stress resulting in a uniform extensional strain, the difference on the interfaces between the incompetent and competent components will lead to different results. If the boundary between the incompetent and competent components is well fixed (Fig. 1.8b), the tensile stress in the layer of competent component increases gradually from a minimum at the ends of the segment to a maximum at its mid-point position. When tensile stress at the mid-point of the fiber exceeds the tensile strength of the competent layer, a tensile fracture will form. As extensional strain increases progressively, the layers of competent component will fracture to a critical length, at which the shear stress on the interfaces will no longer built up tensile stress that can exceed the tensile strength of the competent component. The critical length (L_c) and the thickness of the competent layer (t) follows the equation:

$$L_c = 2\left[t(1+\nu_m)M\frac{E_f}{E_m}\right]^{\frac{1}{2}} cosh^{-1}\left(\frac{E_f\varepsilon}{E_f\varepsilon - C}\right) \qquad (1.10)$$

Where ν_m is the Poisson's ratio of the incompetent component, E_f and E_m are the Young's modulus of the competent and incompetent components, respectively, C is the tensile strength of the competent component, ε is the strain, and M, which is defined by Eq. (17) in Ji and Saruwatari (1998), is a value related to the decay of shear stress in the incompetent components. M increases with the thickness of the incompetent layer in an approximately linear manner and is independent of t. Therefore, the length of segments of the final stage of fracturing will be in the range from $L_c/2$ to L_c. If length of the segments follows a normal distribution, the mean fracture spacing (s), which is defined as the perpendicular distance between two adjacent fractures, will be:

$$s = \frac{3}{4}L_c \qquad (1.11)$$

However, when slip occurs on the interfaces between the competent and incompetent components, the situation become much simpler. The competent component will fracture when:

$$2\tau s = Ct \qquad (1.12)$$

where τ is shear stress on the interfaces when interfacial slip occurs (Ji et al., 1998), and thus the predicted fracture spacing is：

$$s = \frac{C}{2\tau}t \qquad (1.13)$$

The mechanic principle described by Eqs. (1.12-1.13) has been given and applied widely in previous studies (Kelly & Tyson, 1965; Lloyd et al., 1982; Price & Cosgrove, 1990; Tripathi & Jones,1998; Mandl, 2005; Abe & Urai, 2012).

In geological composite materials such as particulate polymineralic rocks and layered rocks, shear may occur along the interfaces between the components with contrasting mechanical competences. This dissertation will take into consideration the effects of interfacial shear on the transfer of stresses from the surrounding incompetent material to the competent component.

CHAPTER 2 MICROBOUDINAGE PALEOPIEZOMETER OF TOURMALINE AND ITS APPLICATIONS

2.1 Introduction

This chapter presents a new perspective on paleopiezometry of tourmaline microboudins and its significance for better understanding the rheological properties, deformation conditions and tectonic processes of its host rocks. The main results of the study have been published in two research papers (Li & Ji, 2020; Li et al., 2020).

Tourmaline is an accessory mineral commonly with an elongate, prismatic shape in deformed felsic rocks (e.g., granitic, granodioritic and pegmatitic gneisses and mylonites), wherein its abundance (volume fraction) rarely exceeds 1%. Previous experiments and field observations reveal that tourmaline has a wide stability field in terms of pressure, temperature and fluid composition, which ranges from zeolite to granulite and even ultrahigh pressure eclogite facies (Fig. 2.1; Dutrow, 1992, 2018; Kawakami, 2004; Ertl et al. 2010; London, 2011; Van Hinsberg et al., 2011). Because its negligible diffusivity for major and trace elements up to high temperatures, strong refractory properties, and high mechanical resistance to subsequent alteration and weathering, tourmaline has been regarded as a good indicator of the physical, chemical and petrogenetic conditions (e.g., Dutrow & Henry, 2011) and a suitable isotopic systematics for determining the absolute age of thermal events it has undergone (Martínez-Martínez et al., 2010).

Like other columnar minerals, such as piedmontite and amphibole, or even elongate mineral, such as garnet (Ji & Martignole, 1994; Ji et al., 1997; Figs. 2.2a-c), tourmaline is also commonly observed to be subjected to tensile fracturing in plastically deformed felsic or quartz matrix (e.g., Ji & Zhao, 1993; Masuda et al., 2003; Matsumura et al., 2017). The segments of fractured tourmaline crystals are referred to as microboudins (Fig. 2.2d). Masuda and his coworkers have established a microboudinage piezometer using tourmaline microboudins scattered in ductile matrix to estimate the magnitude of differential stress (Masuda et al., 1990, 2008; Matsumura et al., 2017). However, their piezometer was derived from the assumption of mid-point fracturing and perfectly welded fiber/matrix interfaces, which is not the common case in plastically deformed rocks.

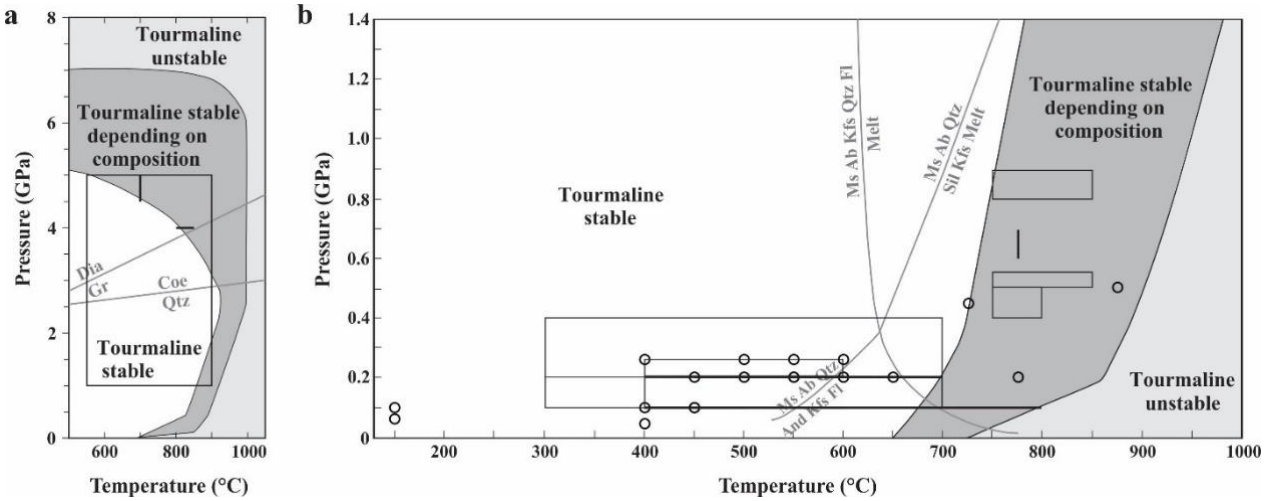

Figure 2.1 Pressure-temperature stability of tourmaline. Experimental data represented by circles, solid lines and squares. Mineral abbreviations: Dia–Diamond; Gr–Graphite; Coe–Coesite; Qtz–Quartz; Ms–Muscovite; Ab–Albite; Kfs–K-feldspar; Fl–Fluid; Sil–Sillimanite; And–Andalusite. Modified from Dutrow and Henry (2011).

In this chapter, we first review the theoretical basis of the microboudinage piezometer established by Masuda and his coworkers, and document evidence that the assumptions of mid-point fracturing and perfectly welded fiber/matrix interfaces are not valid. Then a new microboudin paleopiezometer based on near-end fracturing stress transfer model with fiber/matrix interfacial shear (Kelly & Tyson, 1965; Morrison et al., 1988; Ji et al., 1998; Tripathi & Jones, 1998) is proposed and applied to the estimation of shear flow strength for some representative felsic gneisses and mylonites from the Gaoligong and Chongshan shear zones, Yunnan, China. This piezometer has no limitations faced by the recrystallized grain size piezometer. Strain rates were determined using a combination of microboudin-based strain analysis and geochronological data (e.g., $^{40}Ar/^{39}Ar$ ages of muscovite and biotite over a narrow interval of ≤3 Ma). Application of this piezometer, combined with microstructural observations and independent calibrations of deformation temperature, available $^{40}Ar/^{39}Ar$ ages of muscovite and biotite, and regional geophysical data (e.g., heat flow, focal depths, seismic velocity structure, V_p/V_s ratios, and electrical conductivity structure), provides constraints on strain rates, flow stress and their correlations with temperature and depth for the polycrystalline quartz matrix in which elongate tourmaline grains have been fractures into microboudins.

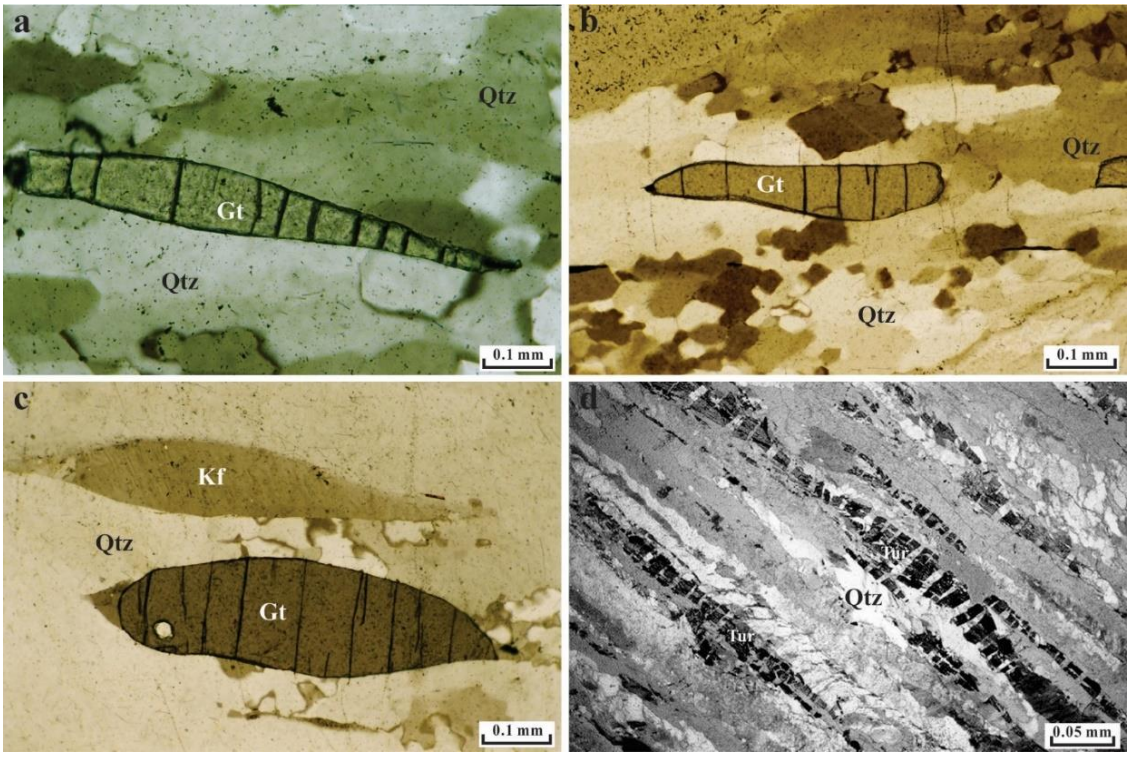

Figure 2.2 Photomicrographs of fractured garnet crystals (a-c) and tourmaline (d) in plastically deformed matrix of quartz. (a-c) from the Morin shear zone, Quebec, Canada (Ji & Martignole, 1994; Ji et al., 1997), and (d) from Fortaleza, NE Brazil (Passchier & Trouw, 2005). Tensile fractures are perpendicular to the foliation and stretching lineation. Mean fracture spacing to grain width ratios in (a), (b), (c) and (d) are 0.94±0.37, 0.99±0.44, 0.51±0.21 and 0.46±0.21, respectively. The ratios are much smaller than unity, which cannot be explained by the conventional shear-lag model. Some fractures taper from the grain boundary toward the core, indicating that the fractures were initiated at the grain boundaries and then propagated inwards. Gt: garnet; Qtz: quartz; Kf: K-feldspar; Tur: tourmaline. XZ section.

2.2 Critical reviews of previous work

Masuda and his coworkers have used microboudins of brittle columnar minerals scattered in a ductile matrix as a piezometer to estimate the magnitude of differential stress (Masuda & Kuriyama, 1988; Masuda et al., 1989; 2008; Omori et al., 2016; Matsumura et al., 2017). Their piezometer was based on fiber-loading theory (Lloyd et al., 1982; Ferguson & Lloyd, 1982, 1984; Masuda & Kuriyama, 1988) or shear-lag model that was originally proposed by Cox (1952) and subsequently improved by others (Zhao & Ji, 1992, 1997; Ji & Zhao, 1993) for describing the

strengthening effect of an aligned short, circular, cylindrical fiber embedded in a ductile soft matrix (Fig. 2.3). The model assumes that the fiber/matrix boundaries are so perfectly welded that no slip between them is possible and the stress is transferred from the soft matrix to the strong fiber by means of interfacial shear stresses. In so doing, the model predicts that the tensile stress in the fiber increases progressively from a minimum at the ends of the homogenous fiber to a maximum at its center (Fig. 2.3d). A tensile fracture will instantaneously form at the mid-point of the fiber where the maximum internal tensile stress first exceeds the tensile fracture strength of the fiber (e.g., Lloyd et al., 1982; Ferguson & Lloyd, 1982; Masuda et al., 1989; Ji & Zhao, 1993; Matsumura et al., 2017). During progressive deformation, two segments separated by a fracture are pulled apart and the inter-segment gap can be filled by the surrounding flow matrix material or minerals precipitated from solution (e.g., diffusive mass transfer). The above process will continue until a fiber is reduced to segments, all of which are shorter than a critical length, for which the maximum tensile stress at the mid-point becomes smaller than the tensile fracture strength of the fiber. The mid-point fracturing is a successive process (e.g., Ferguson & Lloyd, 1982; Lloyd et al., 1982; Masuda & Kuriyama, 1988; Ji & Zhao, 1993). Consequently, inter-segment gaps filled with the soft ductile materials display unequal lengths; the separation is larger across earlier fractures (e.g., Ferguson, 1981, 1987; Ferguson & Lloyd, 1982; Lloyd & Condliffe, 2003). In addition, the maximum tensile stress in a fiber decreases when the fiber aspect ratio (length/width) decreases. According to the shear-lag model, fibers with high aspect ratios break first while those with aspect ratios smaller than the critical value (the maximum tensile stress becomes smaller than the tensile fracture strength of the fiber) remain unbroken.

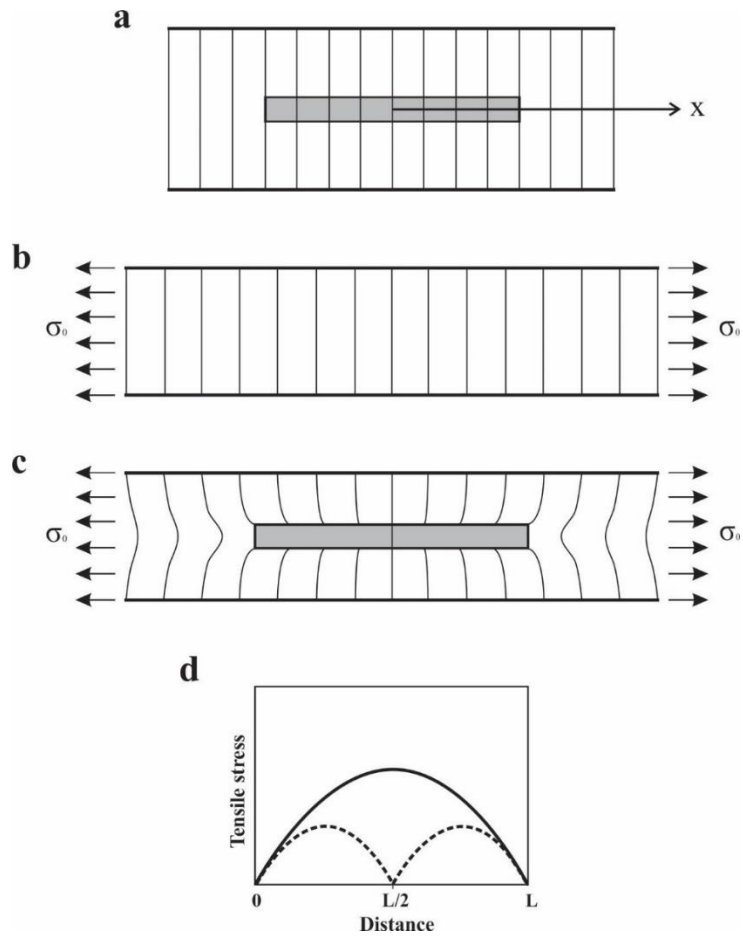

Figure 2.3 Schematic illustration of theoretical basis of the shear-lag model. (a) The unstressed composite unit. (b) Homogeneous deformation of the pure matrix material when the fiber is absent. (c) Differential displacement, introduced by the presence of the fiber, in the matrix. (d) Predicted tensile stress variations along the fiber before fracturing (solid line) and fragments after fracturing (dashed line) according to the shear-lag model. Variables are defined in text.

However, a careful inspection of fracture distribution in tourmaline in the polycrystalline quartz matrix (for example, Fig. 1a in Matsumura et al., 2017; Fig. 2a in Masuda et al., 2003; Fig. 1 in Masuda & Kimura, 2004; and Fig. 6.32 in Passchier & Trouw, 2005) indicates that the tensile fracture generally does not occur at the center of the columnar grain (Fig. 2.4). This immediately leads to suspicion on the general validity of the mid-point fracturing predicted by the shear-lag model, in which no interfacial slip occurring on the interfaces between the fiber and matrix and a uniform value of tensile strength for the fiber are assumed.

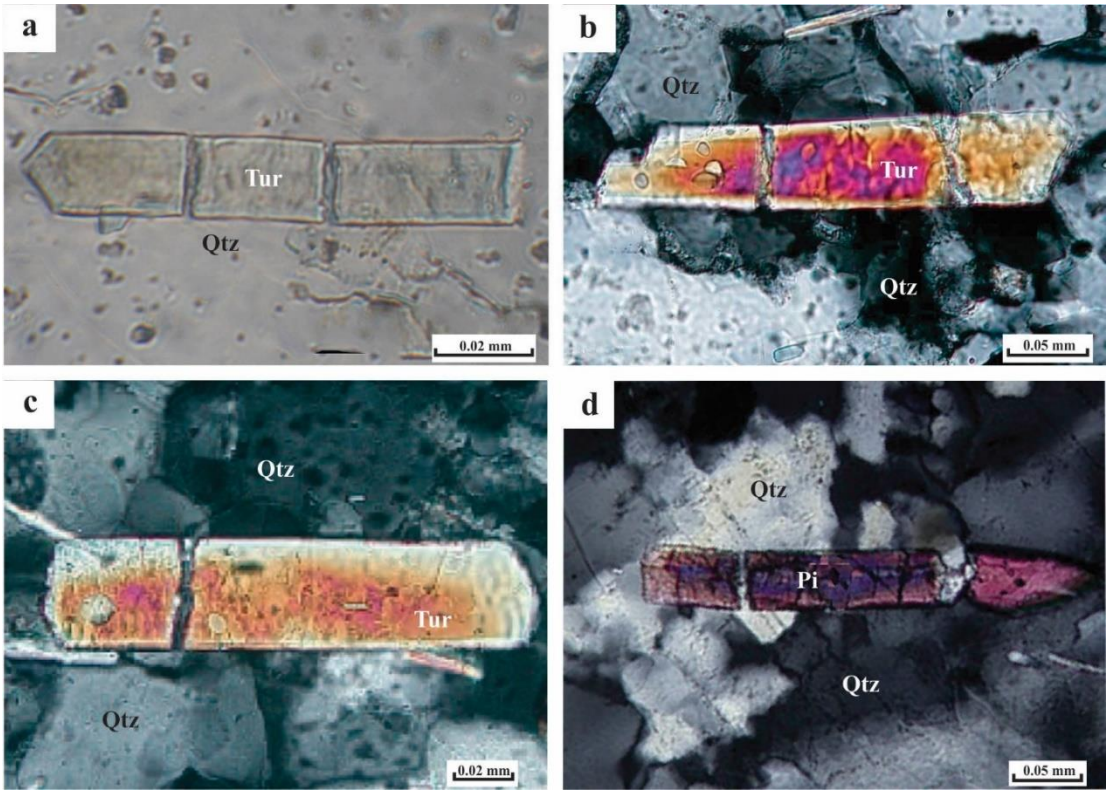

Figure 2.4 Photomicrographs of fractured tourmaline (Tur) and piedmontite (Pi) in plastically deformed matrix of quartz. (a), (b), (c) and (d) are from Matsumura et al. (2017), Masuda and Kimura (2004), Masuda et al. (2003) and Omori et al. (2016), respectively. No evidence is observed for the common presence of mid-point fracturing.

The microboudinage piezometers proposed in Masuda and Kuriyama (1988) and Masuda et al. (1989, 1990, 1995) were based on the following equation:

$$\sigma_f = \frac{E_f}{E_m}\sigma_0\left[1-\frac{1}{\cosh(\beta s)}\right] \qquad (2.1)$$

where σ_f is the maximum tensile stress at the midpoint of a cylindrical fiber during extension, E_f and E_m are Young's moduli for the fiber and matrix, respectively, σ_0 is interpreted by these authors as the far-field stress in the matrix ($\sigma_0=E_m\varepsilon_m$, where ε_m is the far-field strain in the matrix), s is the fiber aspect-ratio (length-to-width ratio), and β is a parameter defined by Eq. (2.2):

$$\beta = \left[\frac{2\pi G_m}{E_f A_f \ln\left(\frac{R_0}{r_0}\right)} \right]^{1/2} \qquad (2.2)$$

In Eq. (2.2), G_m is the shear modulus of the matrix, R_0 is the radius of the unit cell, which is equal to half of the mean distance between adjacent fibers, and r_0 is the radius of the cylindrical fiber. The β value obviously depends on the volume fraction of fibers in the composite concerned. Although A_f in Eq. (2.2) for a cylindrical fiber should be equal to πr_0^2, Masuda et al. (1989) took $A_f = W^2 = 4r_0^2$ (W is the width of the prism) and transformed Eq. (2.2) to:

$$\beta = \frac{1}{2r_0}\left[\frac{2\pi E_m}{E_f\left(1+\upsilon_m\right)\ln\left(\frac{R_0}{r_0}\right)} \right]^{1/2} = \frac{1}{W}\left[\frac{2\pi E_m}{E_f\left(1+\upsilon_m\right)\ln\left(\frac{R_0}{r_0}\right)} \right]^{1/2} \qquad (2.3)$$

If there is no mechanical contrast between fiber and matrix, $E_f = E_m$, no stress transfer should occur from the matrix to the fiber, and thus $\sigma_f = \sigma_0$. Clearly, Eq. (2.1) cannot satisfy this boundary condition, and hence the microboudinage piezometers presented in Masuda and Kuriyama (1988) and Masuda et al. (1989, 1990) are flawed.

Then, Masuda et al. (2003, 2004, 2011), Masuda and Kimura (2004); Kimura et al. (2006; 2010), Matsumura et al. (2017) and Omori et al. (2016) changed to use, in their new microboudinage piezometers, an equation developed in Ji and Zhao (1994) and Zhao and Ji (1997):

$$\sigma_f(x) = \frac{E_f}{E_m}\left[1 + \left(\frac{E_m}{E_f} - 1\right)\frac{\cosh(\alpha x)}{\cosh(\alpha L)} \right]\sigma_0 \qquad (2.4)$$

where

$$\alpha = \frac{s}{L}\left[\frac{E_m}{E_f\left(1+\upsilon_m\right)\ln\frac{R_0}{r_0}} \right]^{1/2} = B\frac{s}{L} \qquad (2.5)$$

The deformation in either fiber or matrix is assumed to be purely elastic. In Eq. (2.5),

$$B = \left[\frac{E_m}{E_f \left(1+\upsilon_m\right) \ln \frac{R_0}{r_0}} \right]^{1/2} \qquad (2.6)$$

Equation (2.4) describes the distribution of tensile stress in a cylindrical fiber with a length 2*L* and a radius of r_0, embedded in a continuous soft matrix. The maximum σ_f occurs at x=0 (i.e., the mid-point):

$$\sigma_f = \frac{E_f}{E_m} \left[1 + \left(\frac{E_m}{E_f} - 1 \right) \frac{1}{\cosh\left(\alpha L\right)} \right] \sigma_0 \qquad (2.7)$$

In the case of tourmaline grains embedded in a matrix of alpha-quartz, E_f=201.5 GPa (Özkan, 1979), E_m=95.6 GPa, and v_m=0.08 (McSkimin et al., 1965) at room temperature and pressure. Masuda et al. (2003) and Matsumura et al. (2017) postulated that E_f/E_m=2 and v_m=0.08 under the temperature and pressure conditions of greenschist to amphibolite-facies metamorphism.

Figure 2.5 illustrated variations of elastic moduli (bulk modulus *K*, shear modulus *G* and Young's modulus *E*) and Poisson's ratio *v* of quartz (a-b, Lakshtanov et al., 2007) and quartzite (c-d, Barruol & Mainprice, 1993) as a function of temperature at 0.1 MPa (a-b) and 600 MPa (c-d), respectively. Both E and *v* display pronounced changes with temperature, particularly across the α-β quartz transition temperature (573 °C at 0.1 MPa, and 650 °C at 600 MPa). Negative *v* values occur from 450 °C to 577 °C at 0.1 MPa and 470-665 °C at 600 MPa (Ji et al., 2018). The assumption that E_f, E_m and v_m are independent on temperature or pressure (Masuda et al., 2003; Matsumura et al., 2017), may be doubtful.

In the calculation of *α*, Masuda et al. (2003), Kimura et al. (2006, 2010) and Matsumura et al. (2017) assumed that R_0/r_0=10 or *B*=0.4 (tourmaline) or 0.5 (piedmontite) for simplicity. In reality, R_0/r_0 ratio depends on the volume fraction and spatial distribution of the columnar minerals in each part of the rock (see Eq. 17 in Zhao & Ji, 1997). In other words, the stress transfer from the matrix to the fiber depends on the volume of the near-fiber matrix cylinder which corresponds to the area influenced by the fiber on the matrix. The R_0/r_0 ratio will have different values for different columnar grains in different samples.

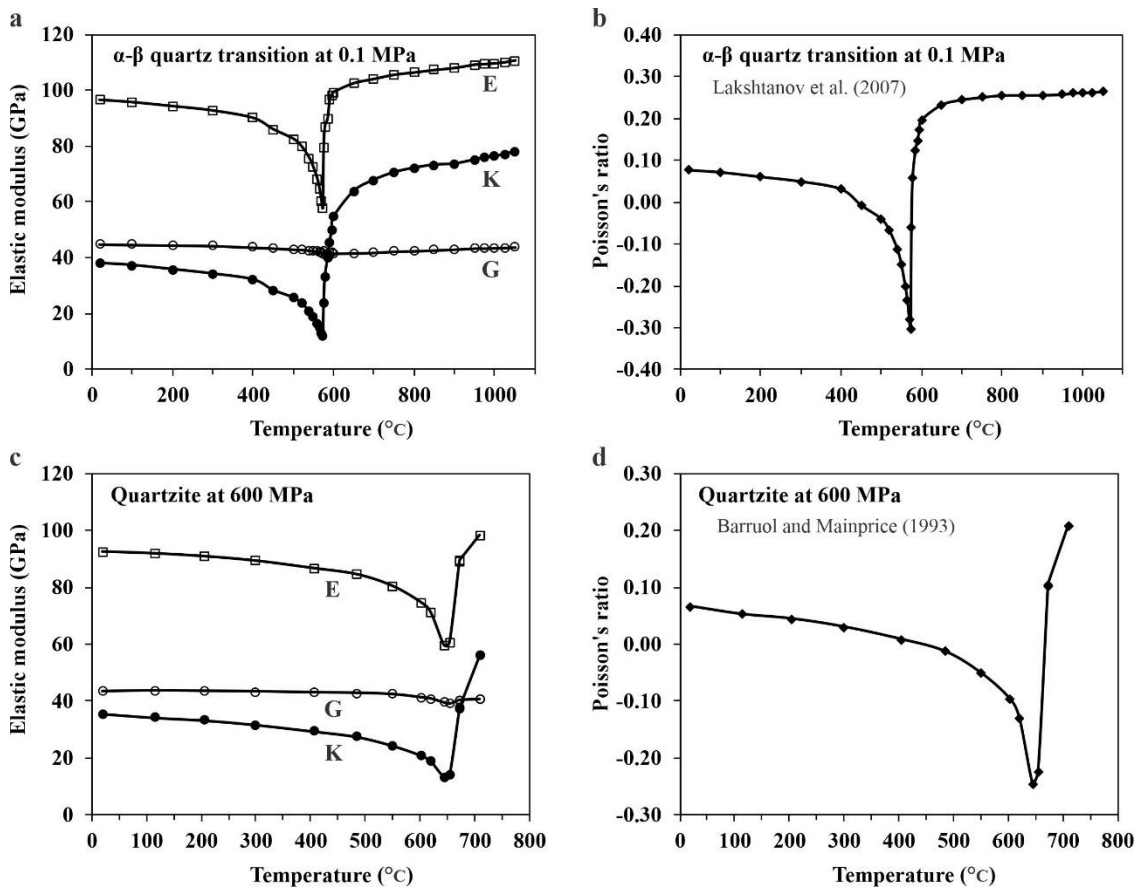

Figure 2.5 Elastic moduli (bulk modulus *K*, shear modulus *G* and Young's modulus *E*) and Poisson's ratio of quartz (a-b) and quartzite (c-d) as a function of temperature at room pressure (Lakshtanov et al., 2007) and 600 MPa (Barruol & Mainprice, 1993).

In Eq. (2.4), σ_0 is the stress transferred to the ends of a fiber from the matrix when the composite is subjected to an extensional strain along the axial direction x (Ji & Zhao, 1994; Zhao & Ji, 1997). However, Masuda and coworkers took σ_0 as the far-field differential stress applied on the bulk matrix (they assumed that $\sigma_0=E_m\varepsilon_m$), and considered that a fiber will break into two segments with uniformly equal lengths when the maximum tensile stress at x=0 reaches to the tensile strength of the fiber (*C*).

$$\sigma_0 = \frac{C\cosh(\alpha L)}{\frac{E_f}{E_m}\left[1+\left(\frac{E_m}{E_f}-1\right)\right]} = \frac{C\cosh(\alpha s r_0)}{\frac{E_f}{E_m}\left[1+\left(\frac{E_m}{E_f}-1\right)\right]} \qquad (2.8)$$

where *s* is the aspect-ratio of the fiber ($s=L/r_0$). Neither Eq. (2.4) nor Eq. (2.8) predicts a linear correlation between fracture spacing and columnar mineral width.

Considering that the fracture strength of a given columnar mineral in nature, which may not be strictly a constant, but varies following the Weibull distribution, Masuda et al. (2003) set:

$$\sigma_0 = \lambda S^* \qquad (2.9)$$

where σ_0 is the far-field differential stress applied to the matrix, S^* is the modal fracture strength of the fiber mineral with as an aspect ratio of 1, and λ is a parameter obtained from fitting theoretical curves to the measured data of the proportion of boudinaged grains as a function of aspect ratio. Based on the above equations, Masuda and coworkers estimated paleo-stresses (σ_0) based on statistical analyses of microboudin length and width data measured from thin-sections of deformed rocks containing broken tourmaline, piedmontite, or amphibole (Masuda et al., 2003, 2011; Kimura, 2006; Omori et al., 2016; Matsumura et al., 2017).

However, a major limitation associated with the microboudin piezometer of Masuda and coworkers is its inability to consider the effect of matrix plastic flow. In other words, the elastic mechanic model is inaptly applied to quantify the plastic behavior of the matrix material surrounding the columnar minerals. The fact that the matrix material (i.e., quartz) was plastically flowing before, during, and after the fragmentation of tourmaline indicates that the applied differential stress exceeded the yield strength of the matrix. The elastic deformation of the matrix material occurred only below the yield strength where plastic deformation had not started yet. This situation severely deviates from linear elastic behavior of the matrix, which is required in the shear-lag model (Cox, 1952; Zhao & Ji, 1997). The paleopiezometer proposed in the chapter, which incorporated the effect of matrix plasticity in the stress transfer model, thus circumvent the above problem encountered in the shear-lag model.

Furthermore, whether σ_0 can be regarded as the far-field differential stress applied on the bulk matrix is very controversial. As the fiber and the matrix are different materials with distinct mechanical properties (Fig. 2.3), there should be misfit stress and strain near the fiber ends in the matrix, where either stress or strain becomes heterogeneously distributed (Tripathi & Jones, 1998). Moreover, the fiber ends generally is not perfectly bonded with the matrix. The presence of abundant microstructures such as fringes and pressure shadows (e.g., Passchier & Trouw, 2005) indicates that the interface between stiff fiber end and matrix is often decoupled and even temporally opened with new crystalline materials crystallized from fluids pumped into

extensional gashes. In addition, any newly formed open (Mode I) fracture is a free surface across which no stress can be transferred, then σ_0 should be zero.

Hence, the microboudinage piezometer method proposed by Masuda and his coworkers is involved with several unconfirmed assumptions and undetermined parameters, labor intensive measurements and treatments of data, and thus time consuming (Matsumura et al., 2017). This could be the reason that few investigators other than their group has applied the technique to the estimation of paleo-stresses.

2.3 Microboudin piezometer based on stress transfer model

Based on mechanical analysis for formation of microboudins, a new microboudinage piezometer is established on the near-end fracturing stress transfer model including fiber/matrix interfacial shear.

Let us consider a stiff *n*-sided prism, having regular polygon ends and rectangular sides, which is aligned parallel to the extension direction, and completely embedded in a continuous solid matrix capable of plastic deformation (Fig. 2.6a, b). This prism is characterized by the following parameters: L is the height of the prism, and n, a, b, and r are the number of sides, the length of the apothem, the length of the side, and the circumradius (radius of the circumscribed circle) of the base of the prism, respectively. The n value should not be less than 3. The prism is cylindrical when n approaches infinity (Fig. 2.6c). The relationship among a, b and r is described by:

$$r = \frac{a}{\cos\left(\frac{\pi}{n}\right)} = \frac{b}{2\sin(\frac{\pi}{n})} \qquad (2.10)$$

The area A of the base of the prism is given:

$$A = \frac{n}{2} r^2 \sin\left(\frac{2\pi}{n}\right) = na^2 \tan\left(\frac{\pi}{n}\right) = \frac{\pi}{4} b^2 \cot\left(\frac{\pi}{n}\right) = \frac{n}{2} ab \qquad (2.11)$$

According to Kelly and Tyson (1965), Morrison et al. (1988), Tripathi and Jones (1998), the mechanic equilibrium of such a system immediately before fracturing can be simply described by the following equation:

$$nbL\tau = AC \qquad (2.12)$$

or

$$\tau = \frac{AC}{nbL} \qquad (2.13)$$

where τ is the interfacial shear stress between the fiber and matrix, C is the tensile strength of the fiber.

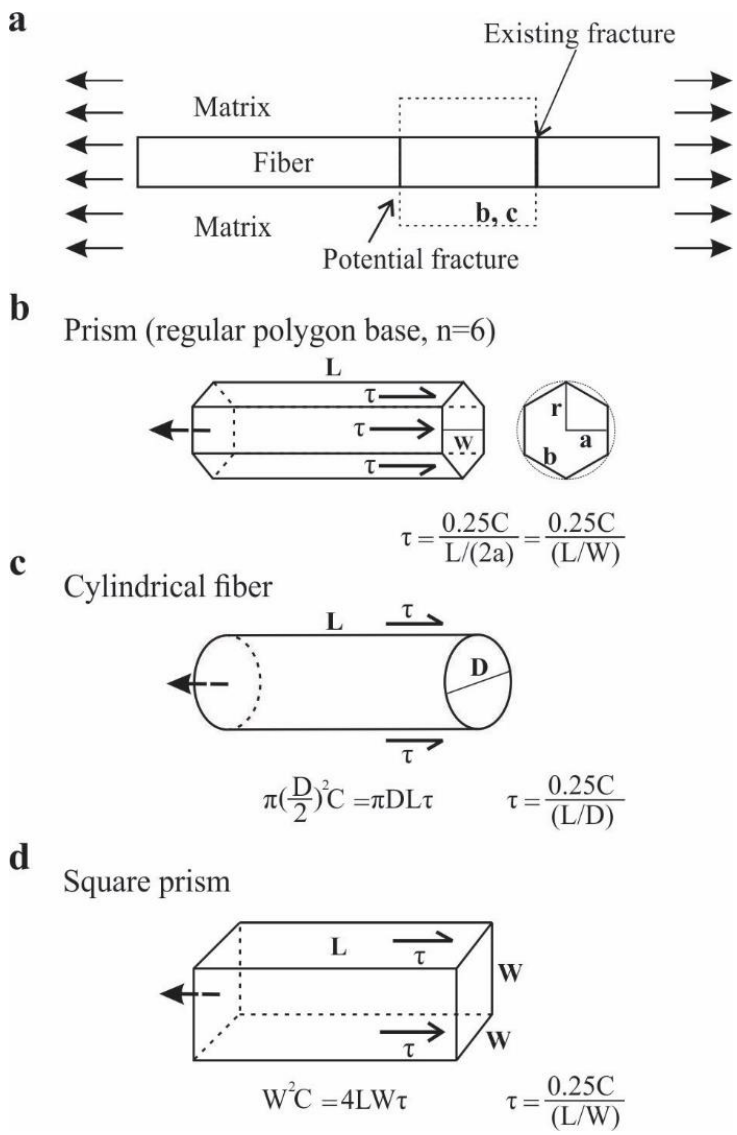

Figure 2.6 Schematic illustration of the near-end fracturing process and the mechanical equilibrium analysis for derivation of Eq. (2.14). (a) The unit cell; (b) Prism with an n-sided regular polygon base (n=6); (c) Cylindrical fiber; (c) Square prism. Variables are defined in text.

Substituting Eq. (2.11) into Eq. (2.13), we obtain:

$$\tau = \frac{aC}{2L} = \frac{C}{4(L/W)} = \frac{0.25C}{L/W} \qquad (2.14)$$

In Eq. (2.14), W=2a, where W is the width of the longitudinal section, which is generally observed in the petrographic thin sections cut parallel to the XZ plane (Fig. 2.6).

Equation (2.13) can also be rewritten as

$$\tau = \frac{rC\cos\left(\frac{\pi}{n}\right)}{2L} = \frac{\cos\left(\frac{\pi}{n}\right)}{4}\frac{C}{(L/D)} = \frac{\Phi C}{(L/D)} \qquad (2.15)$$

where D is the circumdiameter (diameter of the circumscribed circle) of the base of the prism and thus D=2R. In Eq. (2.15), Φ is a geometrical coefficient which depends on the n value:

$$\Phi = \frac{1}{4}\cos\left(\frac{\pi}{n}\right) \qquad (2.16)$$

Φ=0.125, 0.177, 0.202 and 0.217 for n=3, 4, 5, 6, respectively. For a right circular cylindrical fiber (Fig. 2.6c), n is an infinity, Φ=0.25, and then Eqs. (2.14) and (2.15) become the same.

The shear flow stress (τ) of the polycrystalline quartz matrix surrounding the tourmaline grain can be estimated according to Eq. (2.14). This equation is applicable when the quartz matrix deforms in either ductile or elastic-brittle regime (Li & Ji, 2020). Then the differential stress (σ_d=σ_1- σ_3) can be estimated by:

$$\sigma_d = \sqrt{3}\tau = \frac{\sqrt{3}C}{4(L/W)} \qquad (2.17)$$

where the coefficient of $\sqrt{3}$ is derived from Paterson and Olgaard (2000).

We will take L/W as the length/width ratio or aspect ratio of the microboudin formed by near-end fracturing. The aspect-ratio is inversely proportional to τ, as indicated by Eq. (2.14). This is because the magnitude of the tensile stress transferred to the fiber through a stronger interface is increased and then results in a smaller aspect ratio of fragments. It is important to note that Eq. (2.14) predicts a linear correlation between fracture spacing (L) and width of the columnar mineral (Fig. 2.14b, e). Equation (2.14) is also independent on the n value, and thus valid for whatever shape of the regular polygon ends.

The mechanic principle of Eq. (2.12) is similar to that used in the analysis of rigid cylindrical fiber pullout from a soft matrix (Kelly & Tyson, 1965; Morrison et al., 1988; Tripathi & Jones, 1998; Chapter 1). To gain a better understanding, consider a process of pulling a nail out from a piece of timber. The pulling force should be equal to or higher than the frictional shear stresses along the whole cylindrical surface of the nail. The greater the embedment depth is in the timber, the more pulling force is needed to get the nail out since the frictional forces between the nail and the surrounding timber is directly proportional to the embedment depth. If the embedment depth is longer than a critical length given by $C*D/(4\tau)$, the frictional shear stresses build up sufficient tensile stress ($\geq C$) to break the nail. The principle expressed by Eq. (2.12) has been used to the interpretation of the linear relationship between fracture spacing (L) and bed thickness (t) in a competent rock layer (e.g., sandstone or limestone) between two incompetent beds (e.g., shale and mudstone) (Price & Cosgrove, 1990; Ji et al., 1998; Mandl, 2005; Price, 2016). Because the layers are continuous along the bedding plane, $L/t=C/(2\tau)$, where C is the tensile strength of the competent layer and τ is the shear strength of the interbed boundary (e.g., Lloyd et al., 1982; Price & Cosgrove, 1990; Ji et al., 1998; Price, 2016).

The transfer of stresses from the matrix to the fiber segment depends essentially on the interfacial adhesion between the fiber and the surrounding matrix. The interfacial shear strength (τ) or adhesion strength in the brittle regime may be governed by the interfacial cohesion (τ_0), the friction coefficient (μ=0.60-0.85, Byerlee, 1978), the normal stress on the interface (σ_n) and the pore fluid pressure (P_f) if the Mohr-Coulomb failure criterion is applicable (Sibson, 1974).

$$\tau = \tau_0 + \mu\left(\sigma_n - P_f\right) = \tau_0 + \mu\rho g z\left(1-\beta\right) \qquad (2.18)$$

where ρ is the average density of the overlying rocks from the surface to depth z, and g is the gravitational acceleration, and β is the factor of fluid, and equal to $P_f/(\rho g z)$. The σ_n value increases with the depth of burial. According to Eq. (2.18), an increase in overburden depth or a decrease in P_f will lead to a decrease in L/D and fracture spacing (Jain et al., 2007). In dry rocks (P_f=0) at depths of 15 and 30 km, for example, the τ values given by Eq. (2.18) can be slightly higher than 303 MPa and 606 MPa, respectively, taking ρ=2.75 g/cm^3. However, such a high interfacial shear strength is almost impossible because it cannot exceed the shear flow strength of the matrix in the ductile regime within the middle and lower crust. Accordingly, the τ value

calculated from Eq. (2.14) can be taken reasonably as the shear flow strength of the ductile matrix:

Clearly, the paleostress estimation needs the tensile strengths of tourmaline at each confining pressure and temperature. However, there is a dearth of such data for natural tourmaline crystals from laboratory experiments. According to Idrissi et al. (2016), a perfect crystal has an ideal tensile strength of about $E/10$, where E is Young's modulus. E=201.5 GPa for tourmaline (Özkan, 1979), yielding an ideal tensile strength of ~20 GPa. As illustrated in Fig. 2.7, the actual tensile strengths of engineering materials display an approximately linear correlation with their Young's moduli: $C=2.324\times10^{-3}E$ (R^2=0.89). This empirical correlation yields a tensile strength of 468 MPa for gem-quality tourmaline crystals (E=201.5 GPa), which should be regarded as the upper limit for the tourmaline grains from the study rocks.

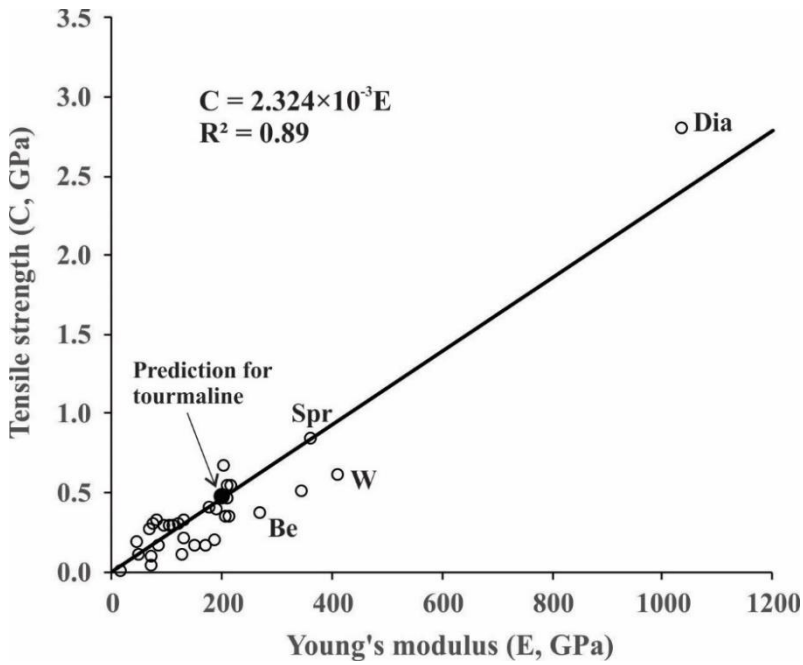

Figure 2.7 Tensile strength (C) versus Young's modulus (E) for 33 engineering materials at ambient conditions (Ashby, 2016; Howatson, 2012, Table 2.1). Be: Beryllium; Dia: diamond; Spr: Sapphire; W: Tungsten. The tensile strength is expected to be higher at a higher confining pressure.

Table 2.1 Young's moduli and tensile strength of 33 engineering materials*

Material	**Young's modulus (GPa)**	**Tensile strength (GPa)**
AlSi6150 alloy steel	201.60	0.670
Aluminium	70.00	0.045
Aluminum alloys	75.00	0.304
Alumiun 6061-T6	69.16	0.276
Beryllium	269.26	0.370
Cast iron	175.00	0.410
Cast iron, gray	110.00	0.295
Copper	130.00	0.210
Copper alloys	130.00	0.325
Diamond	1033.89	2.800
High carbon steel	210.00	0.550
Ion	211.00	0.350
Lead	16.00	0.012
Low alloy steel	215.00	0.550
Low carbon steel	210.00	0.465
Magnesium alloys	44.50	0.190
Nickel	170.00	0.168
Nickel alloys	205.00	0.350
Sapphire	362.08	0.840
Silica glass	71.00	0.103
Silicon	150.00	0.170
Silver	83.00	0.170
Stainless steel	200.00	0.480
Steel (A36)	189.01	0.400
Tantalum	186.00	0.200
Tin	47.00	0.108
Titanium	120.00	0.308
Titanium alloys	105.00	0.300
Tungsten alloys	345.00	0.510
Tunsten	411.00	0.620
Zinc alloy	95.00	0.300
Zinc alloys	81.50	0.330
Zirconia	128.55	0.115

*Data from Ashby (2016) and Howatson (2012)

Taking the theoretical limits and the lack of experimental data on tensile strength of tourmaline into consideration, the estimate of the *C* value is 145 MPa for tourmaline in mylonites, which is lower than the flexure fracture strengths of good crystal quality tourmaline (198-283 MPa,

Kimura et al., 2006; Masuda et al., 2008). With the estimated tensile strength of tourmaline, we then apply the piezometer to estimate the shear flow stress recorded by tourmaline microboudins in mylonite samples from the Gaoligong and Chongshan shear zones in Yunnan, Southwest China.

2.4 Study samples and geological setting

Samples were collected from seven sites (GLG 14, GLG93, GLG104, GLG201, GLG317, GLG325 and YN1397) in the Gaoligong (GLG) shear zone and three sites (CS10, CS45, and CS151) in the Chongshan (CS) shear zone (Fig. 2.8).

These shear zones are located in the southeast part of the Eastern Himalayan Syntaxis (Table 2.2). The GLG shear zone lies between the Tengchong and Baoshan Blocks in the Yunnan Province (China). It consists of felsic, amphibolitic and metapelitic gneisses, mylonites, phyllonites, migmatites, and leucogranites (Socquet & Pubellier, 2005; Wang et al., 2006; Zhang et al., 2012b; Li & Ji, 2020). In the sampling localities, the metamorphic rocks developed subvertical foliation and subhorizontal stretching lineation. Zircon U-Pb dating revealed that the gneisses formed initially at 1053-635 Ma and 547-470 Ma (Song et al., 2010; Xu et al., 2015). The metapelitic gneisses were equilibrated successively at the T-P conditions of 700-750 MPa and 600-650 °C, 650-700 MPa and 700-750 °C, and 400-500 MPa and 500-600 °C (Ding, 1991; Zhong, 2000; Ji et al., 2000).

The geochnological data including zircon U/Pb, amphibole, muscovite and biotite $^{40}Ar/^{39}Ar$, and zircon and apatite (U-Th)/He ages (e.g., Ji et al., 2000; Song et al., 2010; Lin et al., 2009; Wang et al., 2013; Xu et al., 2015; Zhang et al., 2017, 2020; Tang et al., 2020) suggest that the dextral (with a minor component of reverse) shear occurred under first the amphibolite- and then greenschist-facies metamorphic conditions at 32-10 Ma with an average cooling rate of 33.41 °C/Ma. The P-T path was interpreted as an evolutional history of exhumation and cooling of the metamorphic terrane after initial crustal thickening (Zhong, 2000; Song et al., 2010; Zhang et al., 2012b; Xu et al., 2015). The GPS (longitude, latitude and altitude), lithology and structural data (foliation and lineation) of each locality where samples were collected are listed in Table 2.2

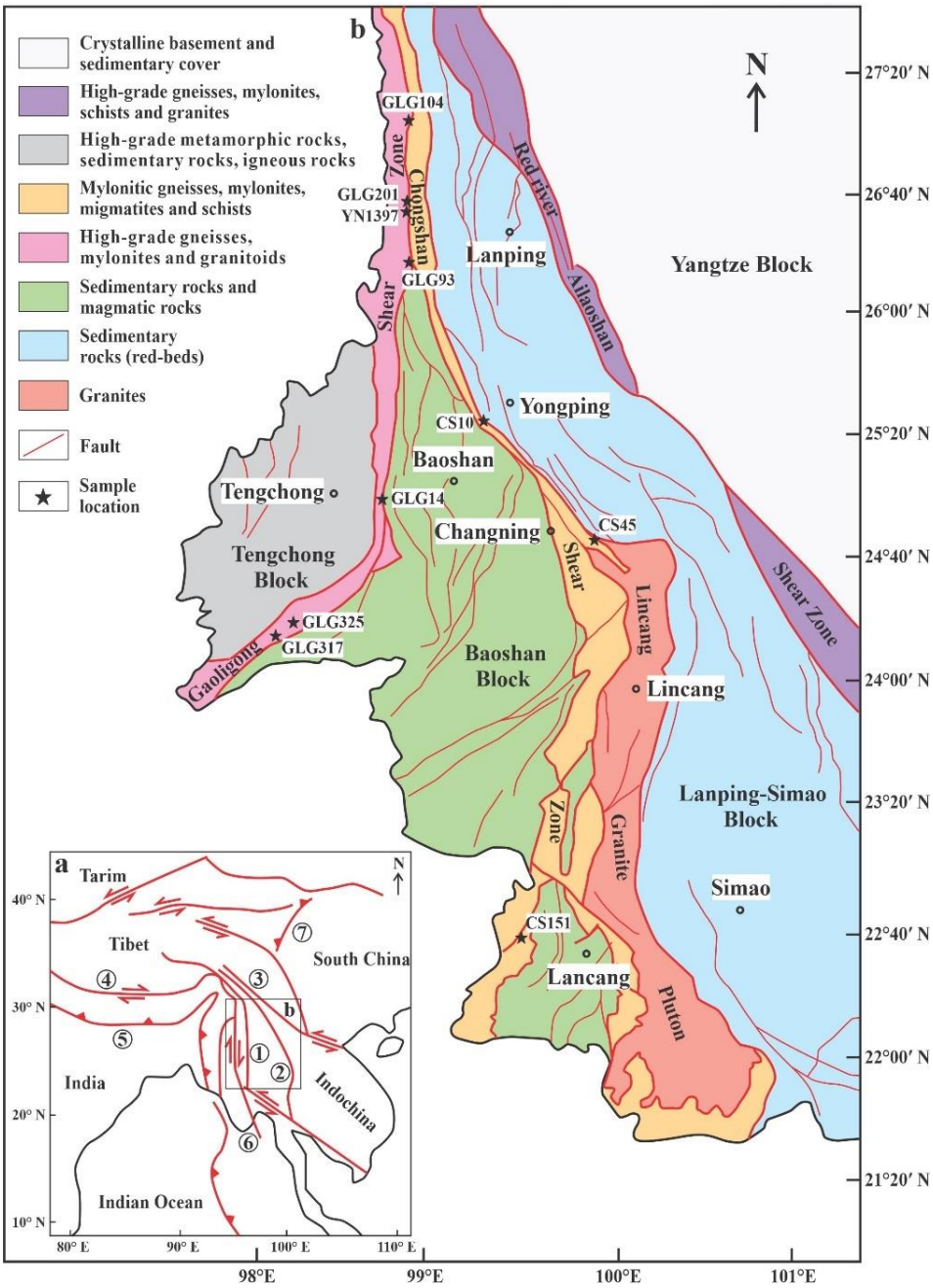

Figure 2.8 (a) Simplified geological map of the Tibetan plateau and surrounding regions. Red lines show main shear zones or fault zones: (1) Gaoligong shear zone; (2) Chongshan shear zone; (3) Ailao Shan-Red River shear zone; (4) Indus-Tsangpo suture zone; (5) Main boundary thrust; (6) Sagaing Fault; and (7) Longmen Shan fault; Box refers to Figure 2.8b. (b) Sampling locations (black stars) within the Gaoligong and Chongshan shear zones, west Yunnan, China. Modified from Zhang et al. (2012a and b).

.

Table 2.2 Localities of tourmaline-bearing rock samples from the Gaoligong and Chongshan shear zone, west Yunnan, China

		Locality				
Sample	**Longitude (°, E)**	**Latitude (°, N)**	**Altitude (m)**	**Lithology**	**Foliation (°)**	**Lineation (°)**
YN1397	98.9045278	26.5559167	1320	Felsic mylonite	(005,54)	(031, 31)
GLG14	98.7289444	24.9795278	1995	Dioritic mylonite	(340, 80)	(160, 05)
GLG93	98.8662500	26.2664167	683	Granitic mylonite	(175, 84)	(177, 20)
GLG104	98.8733056	27.0665556	1226	Phyllonite	(356, 74)	(166, 14)
GLG201	98.9113889	26.6119444	1181	Felsic mylonite	(336, 65)	(352, 31)
GLG317	98.1108056	24.2421944	875	Granitic mylonite	(222, 42)	(222, 00)
GLG325	98.2108611	24.3109722	1331	Granitic mylonite	(221, 24)	(260, 16)
CS10	99.3401750	25.4121750	-	Granitic mylonite	(190, 55)	(000, 14)
CS45	99.8681583	24.7790528	-	Granitic mylonite	(330, 55)	(140, 14)
CS151	99.4719917	22.6649056	-	Granitic mylonite	(015, 80)	(020, 25)

The Chongshan shear zone crops out between the Baoshan Block to the west and the Lanping-Simao Block to the east (Akciz et al., 2008; Zhang et al., 2010, 2011; Fig. 2.8). According to the orientation of the CS shear zone, it can be subdivided into three segments: the N-S trending northern segment extended from the Eastern Himalayan Syntaxis, the NW-SE trending middle segment along the Langcang river, and the NNE-SSW trending southern segment converging with the Lincang granite pluton (Wang & Burchfiel, 1997; Wang et al., 2006; Akciz et al., 2008; Zhang et al., 2010). This pluton, which is about 370 km-long, was intruded syntectonically into the collisional zone between the Baoshan Block and the Lanping-Simao Block during closure of the Palaeo-Tethyan Ocean (~230 Ma, Peng et al., 2006; Catlos et al., 2017). The CS shear zone is composed of felsic (granitic and granodioritic) mylonites, schists and migmatites, which have deformed under amphibolite- to greenschist-facies metamorphic conditions (Akciz et al., 2008; Zhang et al., 2010, 2011; Wang et al., 2006). The deformed rocks developed moderately dipping to subvertical foliation with sub-horizontal lineation (Zhang et al., 2010, 2012a). Shear sense indicators including S-C fabrics, asymmetric folds, rotated porphyroclasts and crystallographic preferred orientations of quartz suggest that dextral strike-slip movements have been dominant in the northern segment whereas sinistral strike-slip events dominant in the middle and southern segments (Zhang et al., 2010, 2012a). Data of zircon U-Pb, monazite (U-Th)/Pb, muscovite and biotite $^{40}Ar/^{39}Ar$, and zircon and apatite (U-Th)/He ages from the CS shear zone are available (e.g., Akciz et al., 2008; Zhang et al., 2010, 2012a; Wang et al., 2018). These data yields an

average cooling rate of ~37.52 °C/Ma during the time interval from ~26.1 Ma (~750 °C, zircon U-Pb ages) to ~6.9 Ma [65 °C, Apatite (U-Th)/He ages]. The $^{40}Ar/^{39}Ar$ plateau ages of muscovite (~400 °C) and biotite (~300 °C) display average ages of 16.62 and 13.96 Ma, respectively. The exhumation mechanisms of the mylonites and metamorphic rocks have been dealt with in Akciz et al. (2008), Zhang et al. (2010, 2012a), Wang et al. (2018) and Ge et al. (2020).

2.5 Microstructural observations

The observation and measurements were performed on the XZ section cut parallel to the lineation (X) and perpendicular to the foliation (XY-plane). For the samples from the Gaoligong shear zone, the tourmaline crystals are essentially aligned parallel to the principal foliation and stretching lineation of the rock (Fig. 2.9). The microboudins of tourmaline do not show pinch and swell structures or ductile deformation at the edges, indicating that little ductile deformation has taken place in the columnar grains before and after fracturing (Fig. 2.9). The fractures are remarkably straight rather than curvilinear, and form mutually parallel arrays. There is no evidence the fracture surfaces have been eroded or modified by dissolution. Furthermore, the fractures show ideal rectangular forms and sharp planar breaks perpendicular to the lineation and the separation between adjacent microboudins is parallel to the lineation (Fig. 2.9). There is no evidence for rotation of the microboudins, indicating that the fracturing took place likely in a local quasi-coaxial strain regime. The fractures are confined to tourmaline crystals and do not propagate into the surrounding quartz or felsic matrix. Interboudin gaps are generally filled with quartz which were extruded into the pull-apart gaps from the surrounding flowing matrix. This fact indicates that microboudinage took place during the ductile deformation of the quartzofeldspathic matrix. For each tourmaline crystal, large and smaller gaps are interpreted as the sites of earlier and later fractures, respectively (Ferguson & Lloyd, 1982; Ferguson, 1987; Masuda & Kuriyama, 1988; Ji & Zhao, 1993).

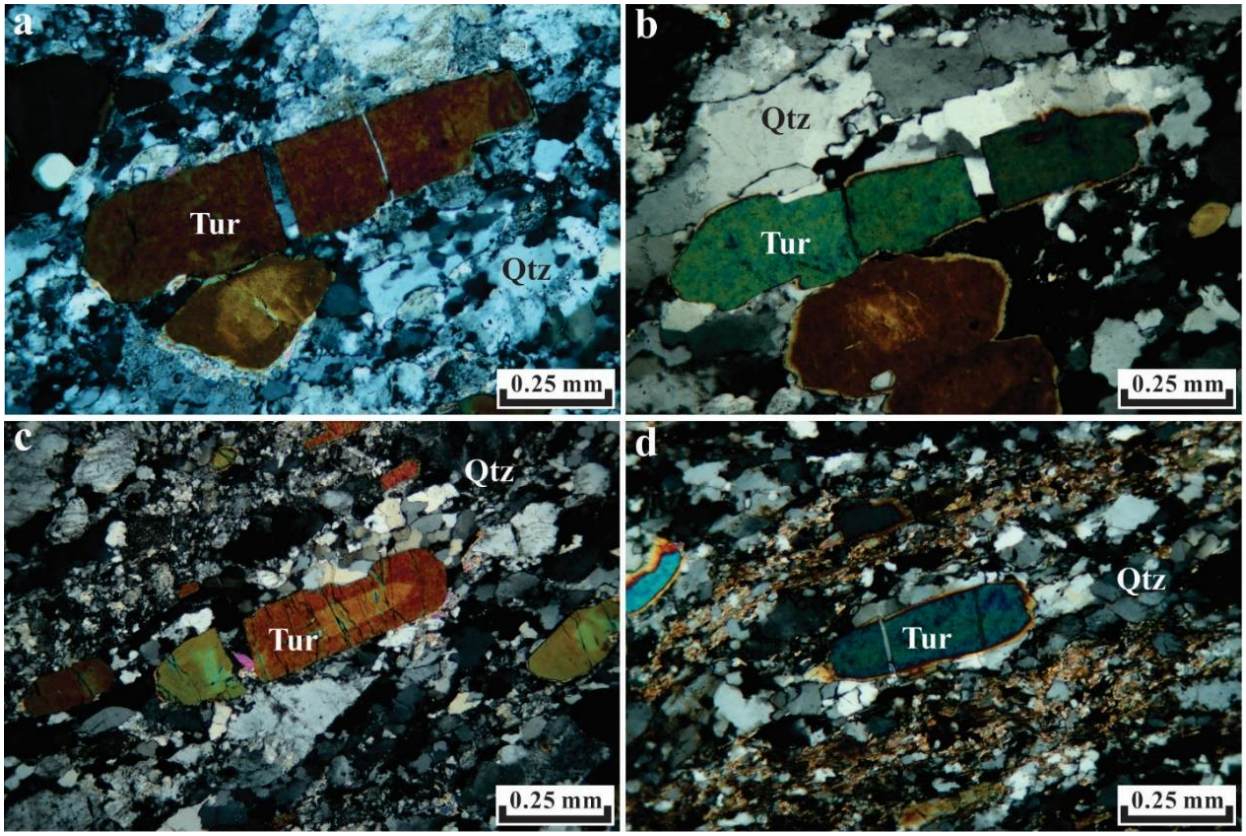

Figure 2.9 Tensile fracture microboudins of tourmaline in mica-bearing quartzofeldspathic mylonites from the GLG shear zone, Yunnan Province, China. Note that tourmaline grains were broken into fragments of different lengths.

For samples from the Chongshan shear zone, microboudins of large tourmaline crystals can easily be recognized on hand specimen scale (Fig. 2.10). In each sample, tourmaline crystals deformed in the same manner of brittle fracturing (Fig. 2.11). The rock-forming minerals of each sample are mainly quartz and feldspar (Figs. 2.10-2.12). Quartz were plastically deformed with subgrains and dynamically recrystallized neograins along the grain boundaries, while the feldspar acts as porphyroclasts with brittle factures (Figs. 2.11-2.12). The tourmaline crystals (≤0.5-1.0%) are scattered in the quartz-flowing matrix with their long axis parallel to the stretching lineation (Figs. 2.10-2.11). Tourmaline crystals were broken into microboudins, and the gaps between the microboudins were filled essentially with ductile polycrystalline quartz from the surrounding flowing matrix. Fracture planes of tourmaline are also consistently sharp and straight, and the microboudins show no pinch-and-swell structures. Evidently, tourmaline is a mineral with brittle behavior under the regional metamorphic condition.

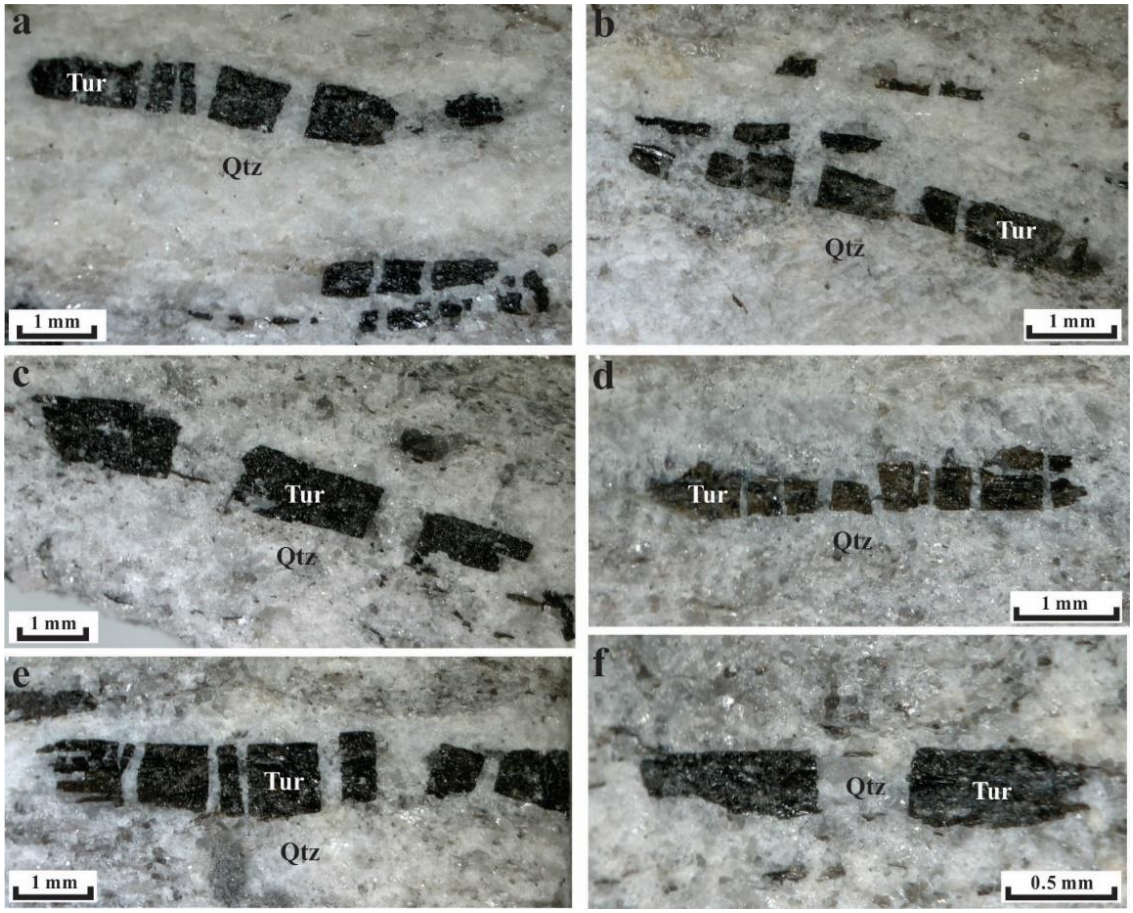

Figure 2.10 Reflected light micrographs of typical fractured tourmaline crystals (black) in felsic gneisses and mylonites from the CS shear zone, west Yunnan, China. Tensile fractures are approximately perpendicular to the foliation and stretching lineation.

Furthermore, the fracture planes in tourmaline (Figs. 2.10-2.11) and feldspar (Fig. 2.12) are mutually parallel, and aligned perpendicular to the stretching lineation and foliation, indicating that little rotation has taken place at least in the scale of samples. Thus, the samples representative of the CS shear zone have relative simple tectonic history.

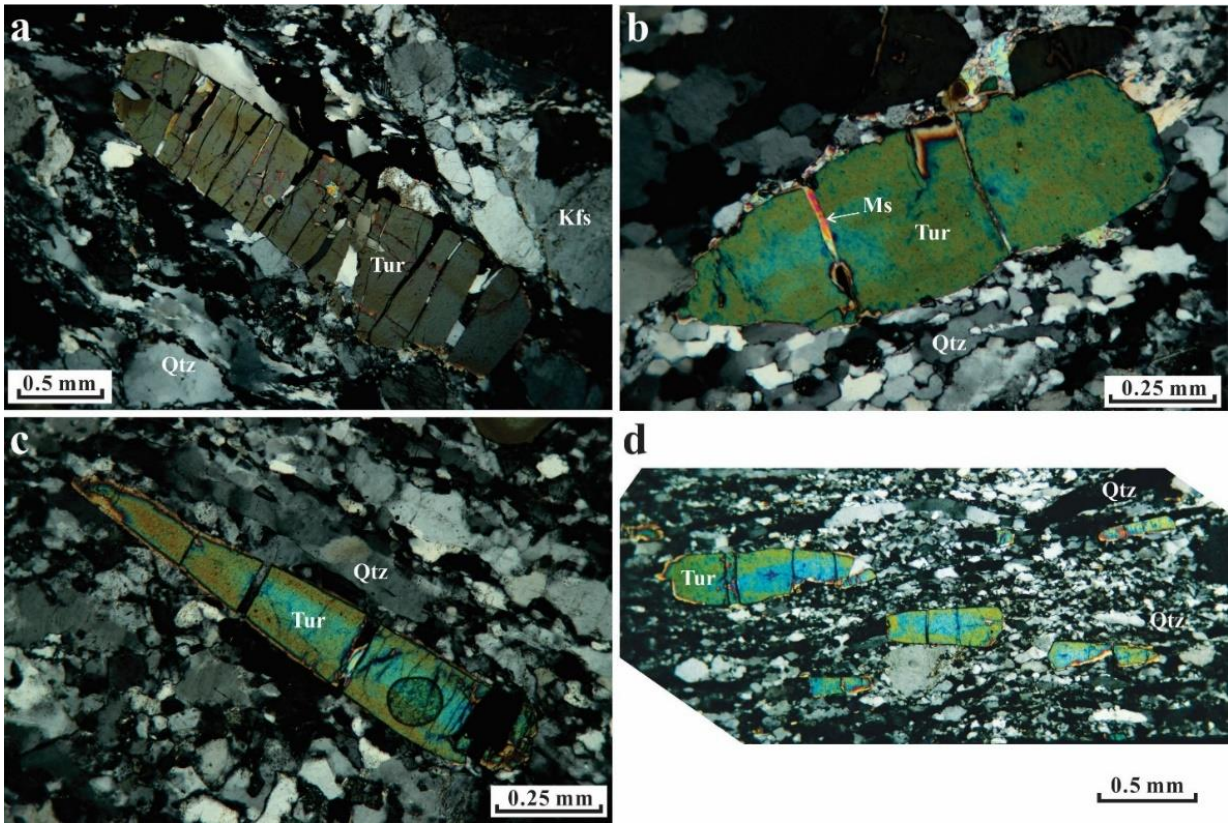

Figure 2.11 Photomicrographs of fractured tourmaline (Tur) in plastically deformed quartz (Qtz) matrix of felsic gneisses and mylonites from the CS shear zone, west Yunnan, China. The interboudin gaps are filled with quartz and muscovite (Ms).

The microstructural observations also reveal that the tourmaline microboudins could not be formed during the magmatic stage, for if the tourmaline microboudins were formed during the magmatic stage, the microboudins should be more likely to evenly oriented in the matrix (Bouchez & Nicolas, 2021), rather than aligned along the long-axis of original tourmaline crystals like observed in the samples (Figs. 2.9-2.11). Another argument is that magma commonly has relatively low viscosity and cannot be able to transfer the far-field stress to break the tourmaline crystals.

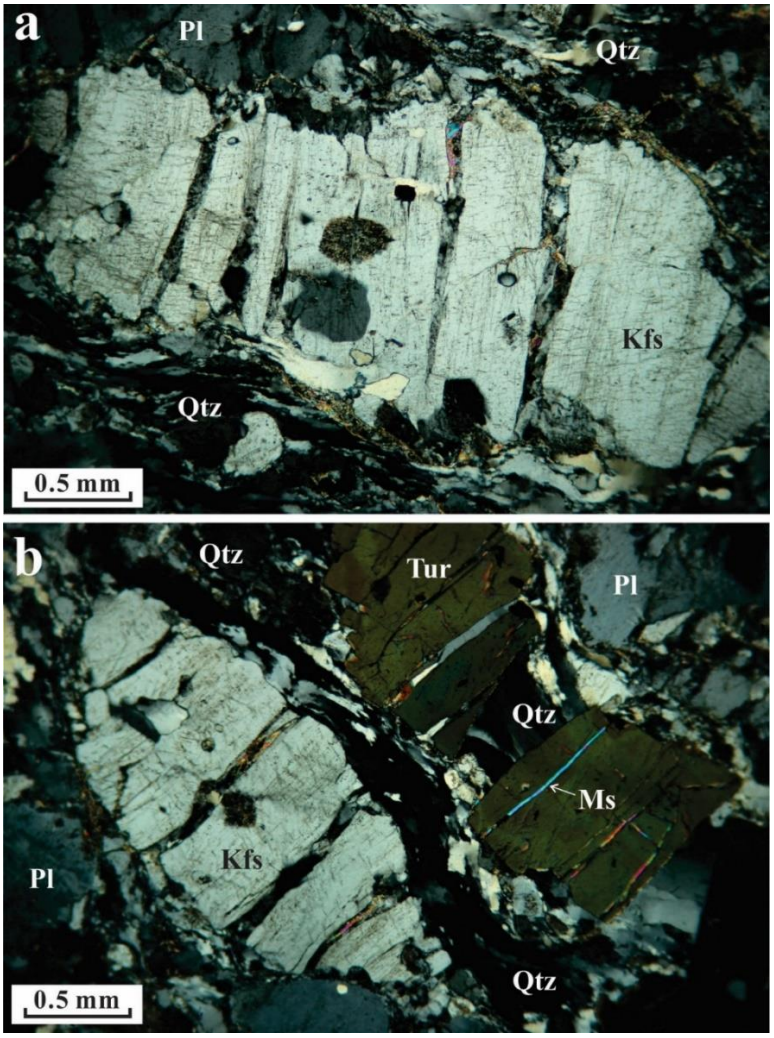

Figure 2.12 Photomicrographs showing brittle deformation of feldspar and tourmaline in which tensile fractures are mutually parallel. Samples from the CS shear zone, west Yunnan, China.

2.6 Methodology

In order to apply the tourmaline microboudin piezometer to estimate the shear stress that deformed the mylonite samples and to recover the deformation process, the geometric features of tourmaline microboudins (length and width) and the strain recorded by the microboudins were measured and the tensile strength of tourmaline crystals were also estimated. Furthermore, to improve the understanding on the rheological properties of the shear zones, the temperature for each fracture breaking the tourmaline crystals into microboudins were also estimated.

2.6.1 Measurements of tourmaline microboudins and strain

The width and length of each tourmaline microboudin and the length of gaps between microboudins were measured from each thin petrographic section with an optical microscope. The process of multiple fracturings of tourmaline crystals then can be recovered with the strain reversal method (Fig. 2.13), and at the same time the geometric features (*L* and *W*) of the recovered microboudins formed in each generation of fracturing can be calculated.

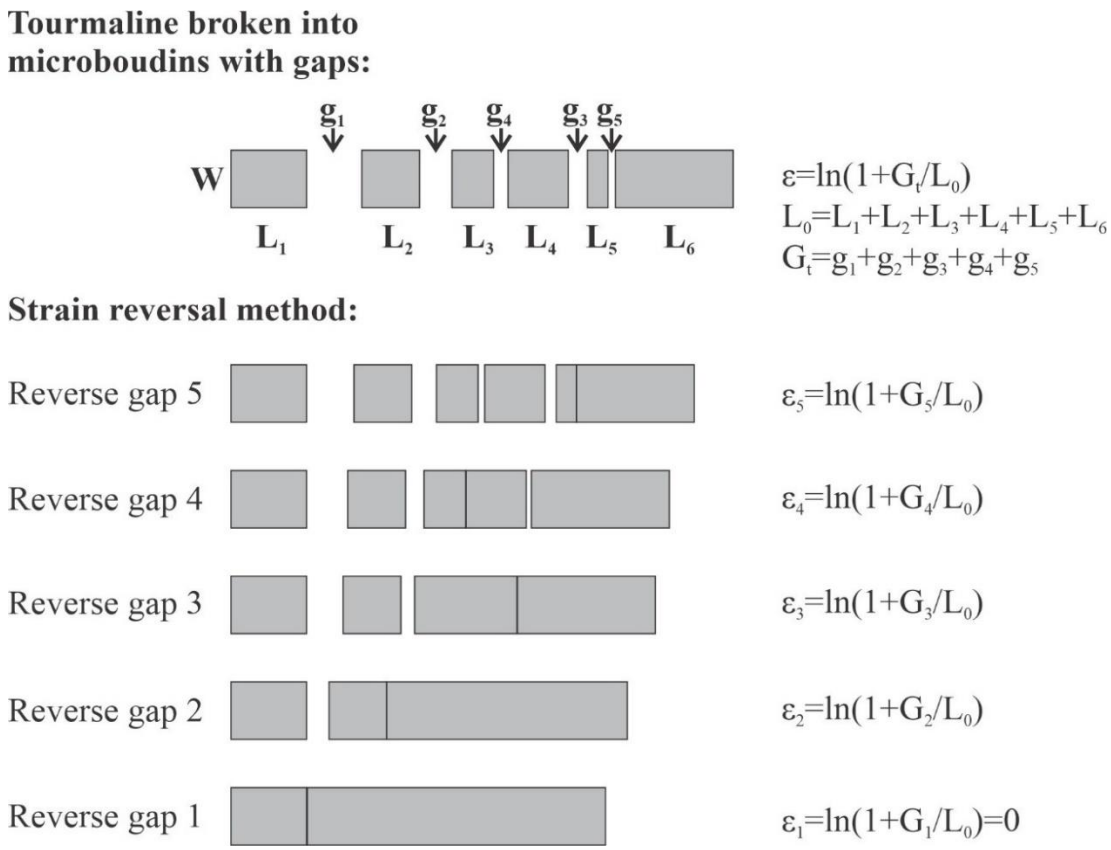

Figure 2.13 Schematic illustration of the strain reversal method (Ferguson, 1981; Lloyd & Ferguson, 1981, 1989; Lloyd & Condliffe, 2003) which has been used to recover the fracturing history of each tourmaline crystal. The gaps are ordered according to their lengths from large to small, indicating the sequence of fracturing. In each reversal stage, the remaining smallest gap is closed, while the length of the rest gaps is reduced by the length of the smallest gap. The natural strains (ε_n) of different reversal stages are calculated from the equations listed alongside, where L_0 is the sum length of all the microboudin segments, which is equal to the initial length of the original crystal before fracturing, G_t is the total length of the gaps before reverse, and G_n is the sum length of all the remaining gaps after the reversal of the nth gap (n = number of gaps).

The strain reversal method is based on the origin of sequential fracturing and separation of microboudins with larger interboudin gaps corresponding to earlier fracture sites while smaller gaps to later ones. The microboudins are treated as rigid segments, so that strain is derived by progressive closure of the interboudin gaps with smaller gaps being closed earlier and reduction in the same amount of gap distance in all the others (Fig. 2.13).

In this study, because of the difference between fracturing generations and strain recorded by the samples from the GLG and CS shear zones, the measured microboudin data are processed in different manners. For samples from the GLG shear zone which we investigated at first, the length and width of each microboudin were measured, while the lengths of gaps between microboudins were just estimated and compared to determine the fracture sequence. For samples from the CS shear zone, however, both the geometric features (length and width) of each microboudin and gaps between microboudins were measured together.

2.6.2 Estimates of tensile strength of tourmaline

As pointed by Etheridge (1983), tensile strength of geological materials such as minerals is among the most difficult mechanical properties to measure in great part due to technical problems in the laboratory. The measurements are extremely sensitive to any small variations in the conditions of the test samples (e.g., degree of crystal quality, microcracks, inclusions, cleavage orientation, and surface roughness) and in the environmental parameters (e.g., loading rates, confining pressure, and temperature). The tensile strengths of mineral single crystals can be significantly higher than those of granular polymineralic rocks because the presence of microcracks and altered grain boundaries makes the rocks incapable to support high tensile effective stresses.

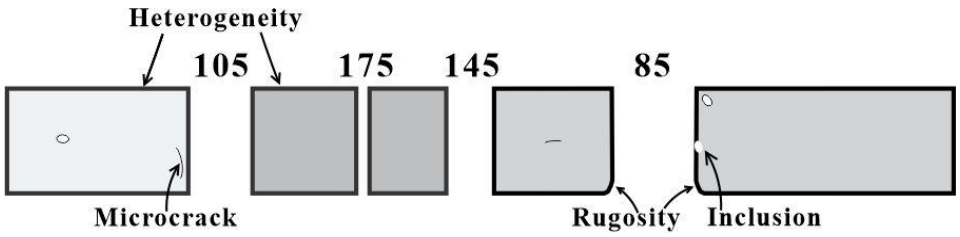

Figure 2.14 Schematic illustration of estimating the tensile strength (*C* value) of tourmaline crystals. The *C* value is affected by the degree of crystal quality and internal flaws, such as microcracks, inclusions, heterogeneities, and surface rugosity.

In order to apply the tourmaline microboudin piezometer to the measured microboudin data from the study samples, the tensile strength (*C* value) of tourmaline has been settled to be 145 MPa as explained in Section 2.3 (there is a dearth of experimentally measured tensile strength data for natural tourmaline crystals). For samples from the GLG shear zone, most of the tourmaline crystals were broken by less than 4 generations of fracturing and the strain recorded by the microboudins are rather small. The microboudin data were measured and then classified by fracturing generations to obtain the average aspect ratios (*L*/*W*) for each generation. In this case, the mean tensile strength of tourmaline could be taken as a constant value (145 MPa) when using the piezometer to calculate the average shear stress for each fracturing generation. For samples from the CS shear zone, tourmaline crystals broken by more than 4 generations of fracturing are rather common, and the total strains recorded by tourmaline microboudins are relatively large. In this case, in order to extract more information from the tourmaline microboudins formed by multiple generations of fracturing. The tensile strength of tourmaline where each fracture formed was estimated by taking the affecting factors (degree of crystal quality, microcracks, inclusions, heterogeneities, and surface rugosity) (e.g., Fig. 2.14) into consideration. If the microboudins on both sides of a gap are in good crystal quality, the estimated *C* value could be greater than 145 MPa, but will also be no greater than the flexure fracture strength of tourmaline crystal of good quality (283 and 198 MPa, Kimura et al., 2006; Masuda et al., 2008). If the microboudin on one side or both sides of a gap are of less good crystal quality, that is, microcracks, inclusions, compositional heterogeneities or surface rugosities occur, the estimated *C* value could be smaller than 145 MPa (Fig. 2.14). Previous theoretical studies (Weibull, 1951; Paterson & Wong, 2005; Dodson, 2006) reveal that the tensile strength values of materials usually follow a Weibull distribution. Therefore, after estimation of the *C* values of the measured tourmaline crystals, distribution test will be applied to determine whether the *C* values follow a Weibull distribution.

2.6.3 Estimates of the temperature

Experiments on tourmaline crystallization temperature (Weisbrod et al., 1986; Wolf & London, 1997; London, 2011, 2016) provide constraints on the upper limit of temperature conditions at which tourmaline deformed in the study rocks. These experiments illustrated that the critical concentration of B_2O_3 needed for crystallization of tourmaline is significantly lower in granitic melts than in aqueous fluids at each given temperature and that the solubility of B_2O_3 decreases

rapidly with decreasing temperature (Fig. 2.15). For example, the amount of B_2O_3 needed to maintain tourmaline saturation is ~2.50 wt% at 800 °C, ~0.67 wt% at 700°C, and ~0.10 wt% at 600°C, respectively (London, 2011). As tourmaline, which is dispersed uniformly throughout the volume of the granitic mylonites, is less than 0.5 wt%, the crystallization temperature of intact tourmaline grains should be below 600 °C in undercooled granitic melts or at 450-500 °C in hydrothermal fluids. This conclusion is consistent with the results of London (2008) and London et al. (2012) who documented that tourmaline in pegmatite-forming undercooled melts started to crystallize at 450-500°C. Thus, tourmaline boudinage developed below 450-500°C regardless of how its intact crystals formed from granitic melts or hydrothermal fluids.

The deformation temperature for each sequential fracture was estimated based on results of combing microstructural observations, geochronological data and paleostrain estimates. The rock samples exhibit crystal plasticity of quartz and brittle deformation of feldspar, indicating that deformation took place at temperatures between 450-300 ºC (Snoke & Tullis, 1998; Scholz, 2019). All the tourmaline fractures across which microboudins are separated by plastically flowing quartz rather than feldspar occurred at 450-300 ºC or mostly 400-300 ºC. In contrast, the tourmaline fractures in which no quartz has filled should take place at temperatures below 300 ºC, where quartz can no longer flow into the interboudin gaps and both tourmaline and quartz matrix deformed elastically (Ji et al., 1997; Ji & Xia, 2002). Microstructures of quartz-filled interboudin gaps also provide useful hints about approximate temperature of deformation after each stage of fracturing. For example, the quartz fillings in the older fractures developed subgrains and subgrain rotation recrystallization, indicating dynamic recovery occurred at relatively high temperatures (≥400 °C, Stipp et al., 2002, 2006; Jeřábek et al., 2007). However, the quartz fillings in the younger gaps exhibit undulose extinction and small-scale serration of grain boundaries, indicating that limited dislocation climb and grain boundary bulging recrystallization took place at low temperatures (300-400 °C, Stipp et al., 2002, 2006; Jeřábek et al., 2007). No grain boundary migration recrystallization has been observed in any fracture-filled quartz, suggesting that the fracturing took place below 500 °C (Stipp et al., 2002, 2006; Jeřábek et al., 2007).

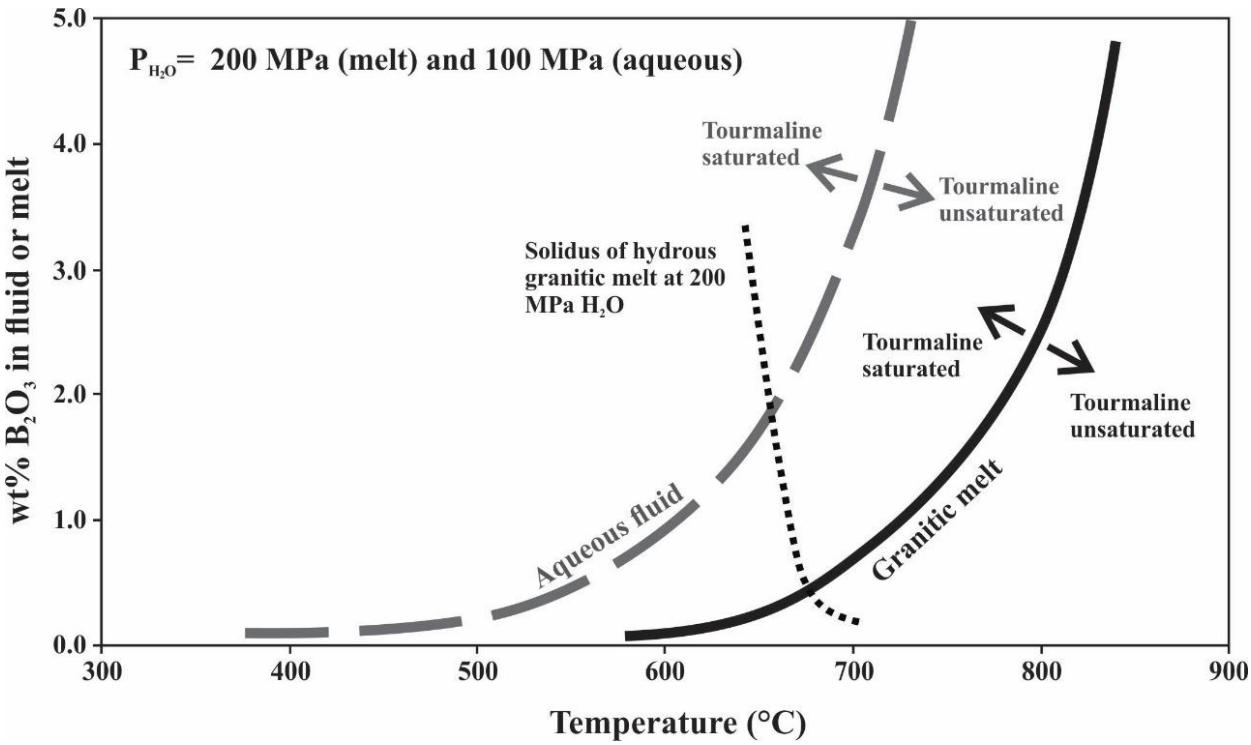

Figure 2.15 The solubility of tourmaline in granitic melt (black solid line) and in aqueous solutions (grey dashed line) as functions of temperature and of the B_2O_3 content of the melt or fluid. Modified from London (2016). See the text for discussion.

In this study, in order to extract information on rheological properties of shear zones, the temperature when each fracture formed should be approximately estimated. As verified before, the fracturing of tourmaline crystals commonly occurred between the temperature interval of 450-300 °C. If it is assumed that the temperature decreases along with the increasing strain in a linear manner, the temperature corresponding to formation of each fracture in the interval of 450-300 °C can be calculated by connecting the cooling process to the strain increasing process, as indicated in Fig. 2.16. For simplicity, it is also feasible to estimate the temperature corresponding to each sequential fracturing in a manner of subdividing the temperature interval of deformation (e.g., 450-300 °C) by the number of fractures. For example, if 5 fractures occurred in an original tourmaline crystal between the temperature interval of 450-300 °C, each fracture then corresponds to a temperature interval of 30 °C. In addition, barren fractures without infillings are regarded to be formed after the plasticity of the matrix had ceased, thus between the temperature interval of 300-250 °C. The temperature estimation for each fracturing event is subject to the

largest uncertainties of about 30 °C. It is hoped that the precision of temperature estimates will be improved by using new methods and techniques in the future.

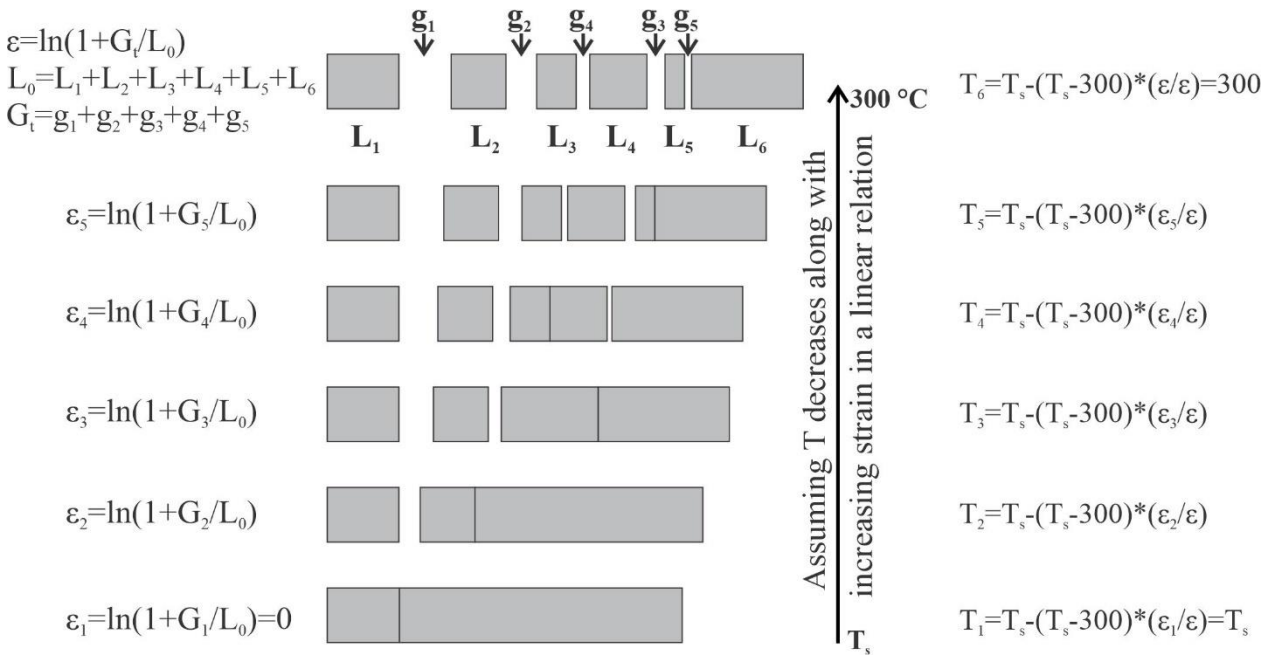

Figure 2.16 Schematic illustration of estimating the temperatures when each fracture formed with the strain reversal method assuming that the temperature (*T*) decreases along with the increasing strain in a linear relation. The meanings of the symbols are the same as those in Fig. 2.13. The starting temperature (T_s) is commonly taken as 450 °C according to the microstructural observation and corresponds to the opening of the first fracture. This starting temperature can also be adjusted, if minerals form at lower temperature are observed to occur in the first gap (g_1). The cease of the plasticity or the finite strain (ε) of the matrix mainly consisting of quartz corresponds to the temperature of 300 °C.

2.7 Analysis of measured data

2.7.1 Measurements of the geometric features of tourmaline microboudins

The results of the measured data from the GLG and CS shear zones are listed in Table 2.3 and Appendix A and B, respectively. In the following, the measurement and calculation results of three samples (YN1397 and GLG325 from the GLG shear zone and CS45 from the CS shear zone) will be described in detail for demonstrating the principles and methods.

Table 2.3 Summary of the parameters measured for tourmaline microboudins from GLG shear zone in Yunnan

Samples	Description	Average Values		
		L_0 (mm)	W_0 (mm)	L_0/W_0
GLG14	Total number of tourmaline grains (N = 44)	0.62±0.26	0.16±0.06	4.05±1.59
	Broken grains (N = 36; 81.8%)	0.64±0.28	0.16±0.07	4.16±1.70
	(N = 36): First generation of shorter segments	0.22±0.12	0.14±0.06	1.72±0.86
	First generation of longer segments	0.42±0.19	0.16±0.07	2.74±1.16
	(N = 14): Second generation of shorter segments	0.18±0.08	0.17±0.05	1.12±0.53
	Second generation of longer segments	0.33±0.17	0.17±0.04	1.97±0.89
	Unbroken grains (N = 8; 18.2%)	0.51±0.08	0.15±0.04	3.53±0.91
GLG93	Total number of tourmaline grains (N = 10)			
	Broken grains (N = 10; 100%)	0.79±0.42	0.20±0.12	4.07±1.10
	(N = 10): First generation of shorter segments	0.27±0.17	0.19±0.10	1.54±0.70
	First generation of longer segments	0.52±0.28	0.20±0.12	2.67±0.71
	(N = 2): Second generation of shorter segments	0.30±0.14	0.24±0.04	1.25±0.41
	Second generation of longer segments	0.43±0.11	0.25±0.06	1.70±0.04
GLG104	Total number of tourmaline grains (N = 4)			
	Broken grains (N = 4; 100%)	0.92±0.58	0.36±0.11	2.40±0.87
	(N = 4): First generation of shorter segments	0.29±0.21	0.35±0.11	0.76±0.30
	First generation of longer segments	0.63±0.39	0.34±0.14	1.75±0.54
GLG201	Total number of tourmaline grains (N = 126)	0.41±0.16	0.12±0.04	3.41±1.06
	Broken grains (N = 110; 87.3%)	0.44±0.15	0.13±0.04	3.51±1.09
	(N = 110): First generation of shorter segments	0.16±0.07	0.12±0.04	1.35±0.47
	First generation of longer segments	0.28±0.10	0.13±0.04	2.28±0.85
	(N = 10): Second generation of shorter segments	0.11±0.06	0.14±0.06	0.76±0.26
	Second generation of longer segments	0.26±0.11	0.15±0.06	1.91±0.72
	Unbroken grains (N = 16; 12.7%)	0.22±0.08	0.08±0.02	2.75±0.34
GLG317	Total number of tourmaline grains (N = 4)			
	Broken grains (N = 4; 100%)	1.31±0.48	0.37±0.21	3.77±1.05
	(N = 4): First generation of shorter segments	0.41±0.10	0.37±0.21	1.31±0.58
	First generation of longer segments	0.88±0.41	0.37±0.21	2.46±0.62
	(N = 3): Second generation of shorter segments	0.27±0.07	0.38±0.26	0.83±0.27
	Second generation of longer segments	0.77±0.29	0.40±0.20	2.00±0.35
	(N = 1): Third generation of shorter segments	0.15	0.625	0.24
	Third generation of longer segments	0.95	0.625	1.52

Table 2.3 Summary of the parameters measured for tourmaline microboudins from GLG shear zone in Yunnan (continued)

Samples	Description	Average Values		
		L_0 (mm)	W_0 (mm)	L_0/W_0
GLG325	Total number of tourmaline grains (N = 195)	0.62±0.30	0.26±0.13	2.55±0.83
	Broken grains (N = 173; 88.7%)	0.64±0.30	0.26±0.13	2.60±0.86
	(N = 173): First generation of shorter segments	0.22±0.11	0.24±0.13	0.98±0.40
	First generation of longer segments	0.43±0.22	0.26±0.13	1.76±0.68
	(N = 46): Second generation of shorter segments	0.19±0.08	0.29±0.14	0.72±0.34
	Second generation of longer segments	0.38±0.21	0.31±0.16	1.26±0.47
	(N = 5): Third generation of shorter segments	0.26±0.12	0.45±0.18	0.59±0.24
	Third generation of longer segments	0.36±0.09	0.41±0.17	1.00±0.37
	Unbroken grains (N = 22; 11.3%)	0.44±0.18	0.21±0.07	2.16±0.38
YN1397	Total number of tourmaline grains (N = 228)	0.70±0.30	0.27±0.12	2.72±0.89
	Broken grains (N = 191; 83.8%)	0.73±0.31	0.28±0.13	2.80±0.92
	(N = 191): First generation of shorter segments	0.25±0.12	0.24±0.11	1.10±0.49
	First generation of longer segments	0.49±0.23	0.27±0.13	1.87±0.64
	(N = 49): Second generation of shorter segments	0.21±0.12	0.26±0.11	0.84±0.33
	Second generation of longer segments	0.41±0.17	0.27±0.11	1.62±0.62
	(N = 4): Third generation of shorter segments	0.23±0.08	0.29±0.07	0.81±0.36
	Third generation of longer segments	0.40±0.09	0.28±0.09	1.47±0.39
	Unbroken grains (N = 37; 16.2%)	0.55±0.19	0.25±0.10	2.32±0.52

In a thin section cut parallel to the XZ plane of sample YN1397, for example, 228 tourmaline grains were measured. Their average length (L_0) and width (W_0) are 0.70 ± 0.30 mm and 0.27 ± 0.12 mm, respectively, with an average aspect ratio of 2.72 ± 0.89 (Fig. 2.17a). A linear relationship occurs between length L_0 and width W_0: $L_0 = 2.44*W_0$ ($R^2 = 0.40$, Fig. 2.17b). Among these 228 grains, 191 (83.8%) were broken to two segments (Figs. 2.18a-c), whereas the other 37 grains (16.2%) survived fracturing (Figs. 2.19a-b). The average aspect ratios of the broken and unbroken grains are 2.80±0.93 (Fig. 2.18a) and 2.32 ±0.52 (Fig. 2.19a), respectively. The broken 191 grains had originally an average length of 0.73 ± 0.31 mm, an average width of 0.28 ± 0.13 mm, and a relationship $L_0=2.48*W_0$ ($R^2 = 0.36$, Fig. 2.20a). The unbroken 37 grains have an average length of 0.55 ± 0.19 mm, an average width of 0.25 ± 0.10 mm, and a relationship $L_0=2.14*W_0$ ($R^2 = 0.61$, Fig. 2.19b).

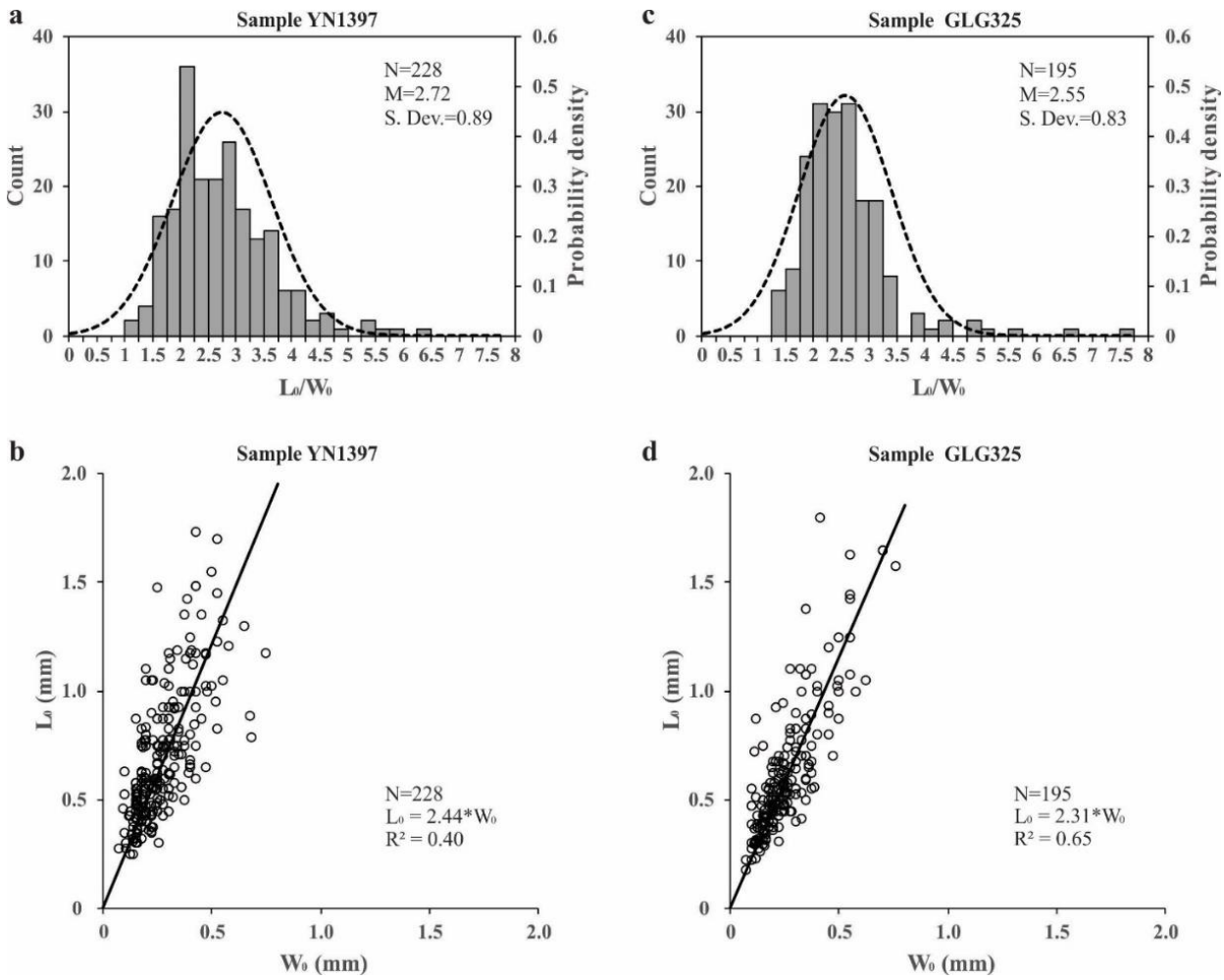

Figure 2.17 Histograms for initial aspect ratios (L_0/W_0) and plots of length L_0 versus width W_0 of the original tourmaline grains prior to fracturing. (a-b) and (c-d) for samples YN1397 and GLG325, respectively. N: number of grains; M: Mean; S. Dev.: Standard deviation.

As shown in Figs. 2.18b-c, two segments separated by the first generation of tensile fracture in each of the 191 original tourmaline crystals are statistically unequal in length. The shorter segments display an average length of 0.25 ± 0.12 mm (Fig. 2.20b) and an average aspect ratio of 1.10 ± 0.49 (Fig. 2.18b). However, the longer segments have an average length of 0.49 ± 0.23 mm (Fig. 2.20c) and an average aspect ratio of 1.87 ± 0.64 (Fig. 2.18c).

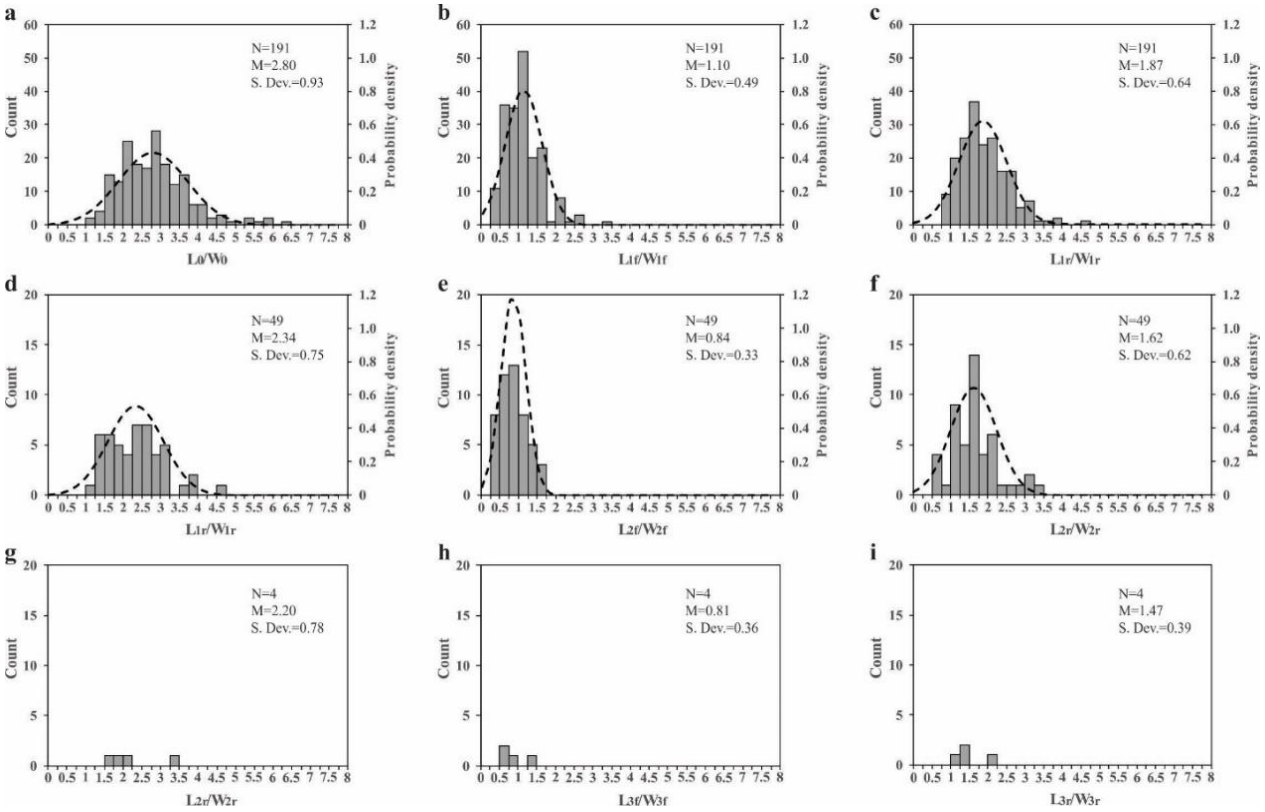

Figure 2.18 Histograms for the length/width ratios of tourmaline microboudins formed by each generation of fracture in sample YN1397. (a) 191 grains prior to fracturing; (b) and (c) shorter and longer segments divided by the first generation of fracture, respectively; (d) 49 among the 191 longer segments were broken by the second generation of fracture; (e) and (f) shorter and longer segments divided by the second generation of fracture, respectively; (g) only 4 among the 49 longer segments were broken by the third generation of fracture; (h) and (i) longer and shorter segments divided by the third generation of fracture, respectively.

Among the 191 long segments, 49 were broken again (Fig. 2.18d), yielding the average aspect ratios of 0.84±0.33 (Fig. 2.18e) and 1.62±0.62 (Fig. 2.18f) for their shorter and longer segments, respectively. Finally, only 4 of the 49 long segments were broken by the third generation of tensile fracturing (Fig. 2.18g), forming a group of short microboudins (L/W=0.81±0.36, Fig. 2.18h) and a group of long segments (L/W=1.47±0.39, Fig. 2.18i). The above microstructural observations suggest that each generation of fracturing forms two segments of unequal length, the shorter of which has an aspect ratio of 0.81-1.10 (Figs. 2.18b, e and h) and will no longer be fragmented. Successive fracturing occurs only within a longer segment with relatively large aspect ratio (L/W>1.47). Clearly, the assumption of mid-point fracturing is not valid in the case of

sample YN1397. Furthermore, there is a linear correlation between fracture spacing and tourmaline width (Fig. 2.20b, e).

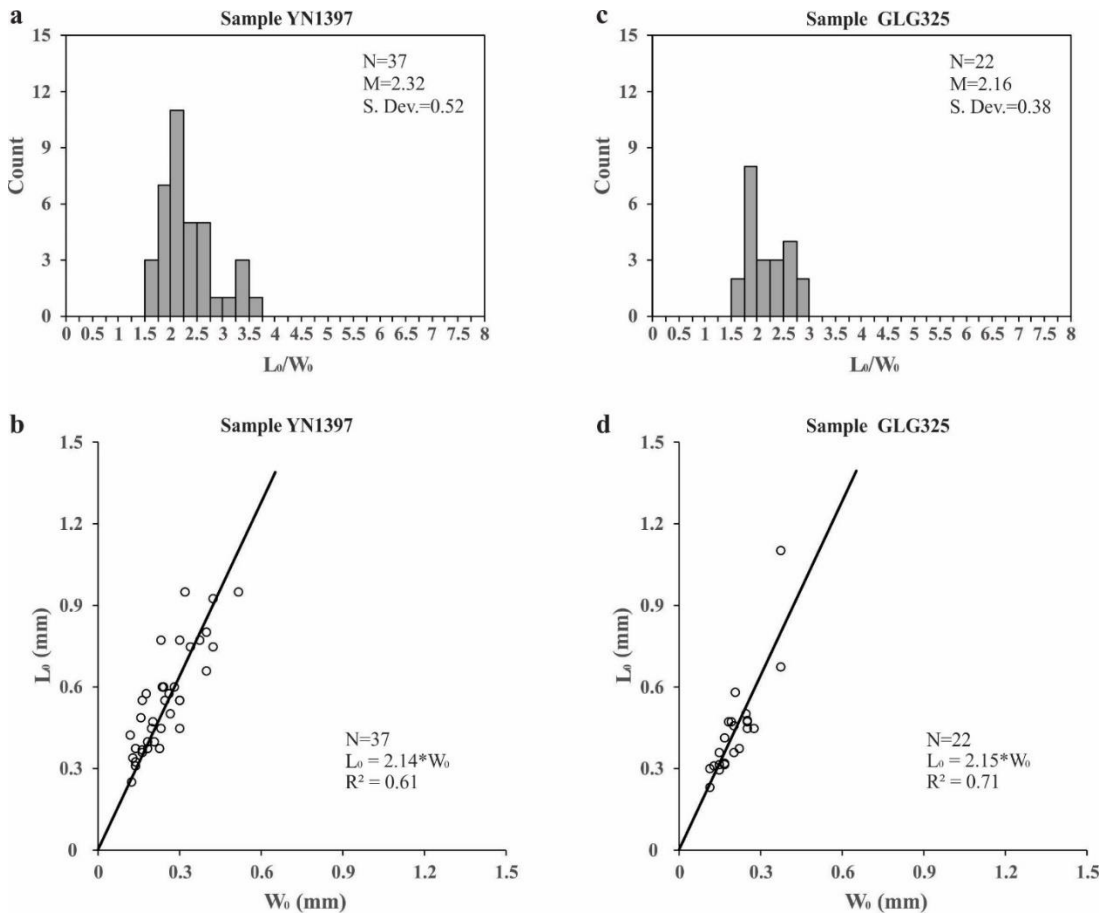

Figure 2.19 Histograms for length/width (L_0/W_0) ratios and plots of length L_0 versus width W_0 of the unbroken tourmaline grains in samples YN1397 (a-b) and GLG325 (c-d). N: number of grains; M: Mean; S. Dev.: Standard deviation.

In a XZ section cut from sample GLG325, 195 tourmaline grains measured show a length and a width of 0.62 ± 0.30 mm and 0.26 ± 0.13 mm, respectively. The average aspect ratio of the grains (L/W) is 2.55 ± 0.83 (Fig. 2.17c), and the linear relationship between the length and width is L_0 = 2.31*W_0 (R^2 = 0.65, Fig. 2.17d). Among the 195 grains, 173 were broken by the first generation of tensile fracturing (Figs. 2.21a-c), and the rest 22 grains were intact. The broken grains had initially an aspect ratio of 2.60 ± 0.86 (Fig. 2.21a) with the average length and width of 0.64 ± 0.30 mm and 0.26 ± 0.13 mm, respectively. The unbroken grains, however, had relatively a smaller aspect ratio (L/W=2.16 ± 0.38) and smaller length and width (L_0=0.44 ± 0.18 mm and W_0=0.21 ± 0.07 mm).

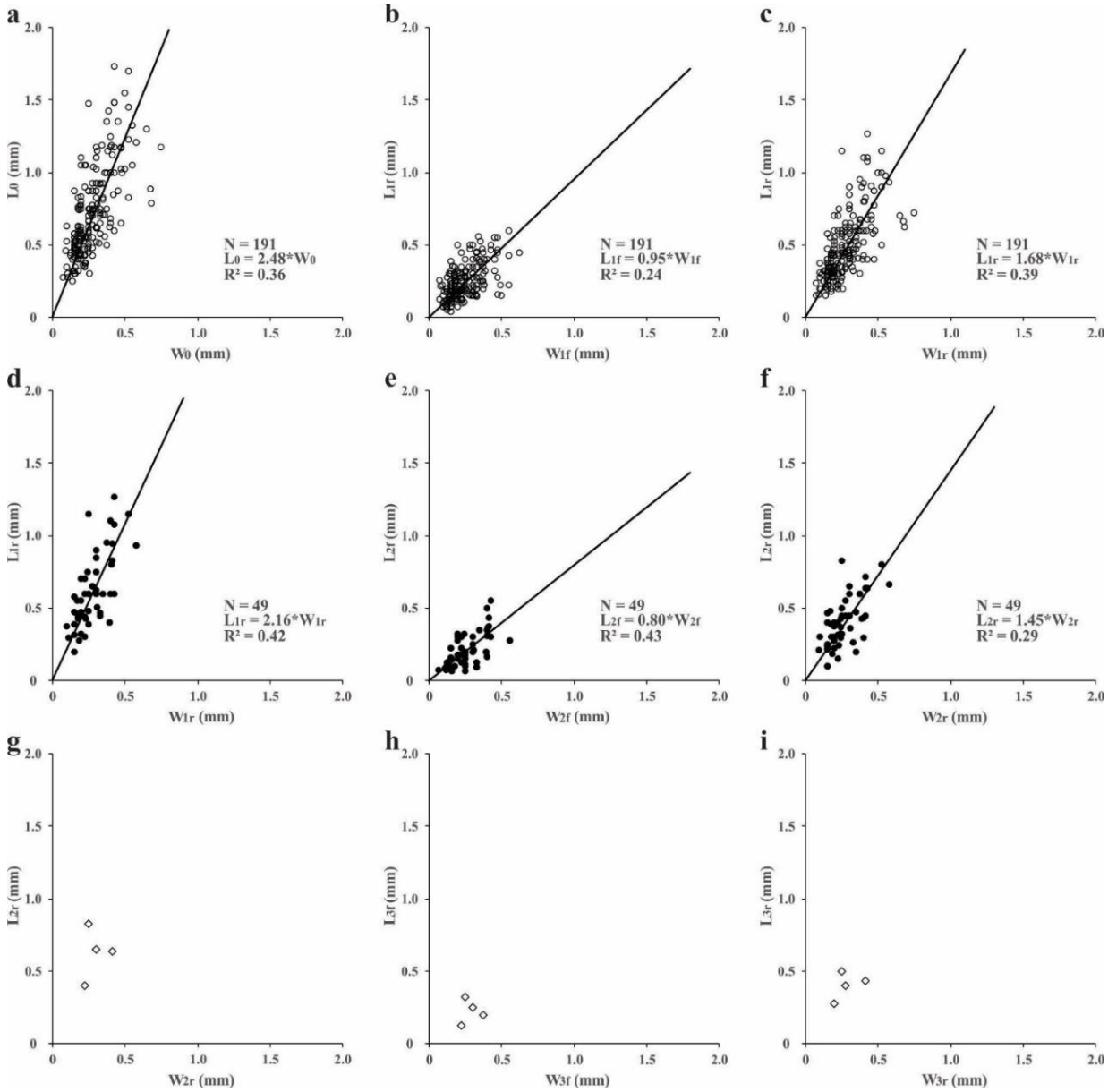

Figure 2.20 Plots of length versus width of the tourmaline microboudins formed by the first (a-c), second (d-f) and third (g-i) generations of tensile fracturing in samples YN1397. Each tensile fracture formed two fragments of unequal lengths. A linear correlation between fracture spacing and tourmaline width is observed (b and e).

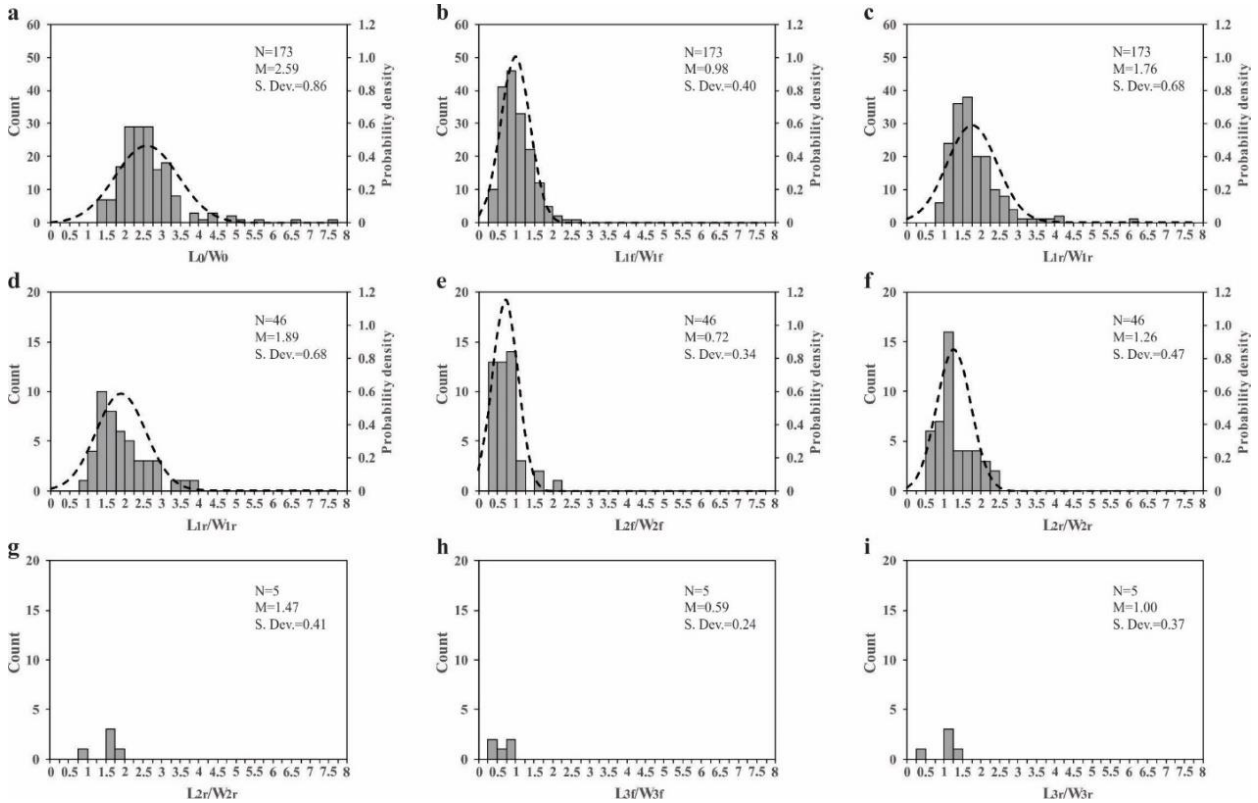

Figure 2.21 Histograms for the aspect ratios of tourmaline microboudins formed by each generation of fracture in sample GLG325. (a) 173 grains prior to fracturing; (b) and (c) shorter and longer segments divided by the first generation of fracture, respectively; (d) 46 among the 173 longer segments were broken by the second generation of fracture; (e) and (f) shorter and longer segments divided by the second generation of fracture, respectively. (g) 5 among the 46 longer segments were broken by the third generation of fracture; (h) and (i) shorter and longer segments divided by the third generation of fracture, respectively.

The first generation of tensile fracturing broke each of the 173 tourmaline crystals into two segments with unequal length (Figs. 2.21b-c). The shorter segments displays an aspect ratio of 0.98 ± 0.40 (Fig. 2.21b) with a length of 0.22 ± 0.11 mm and a width of 0.24 ± 0.13 mm. The longer segments are 0.43 ± 0.22 mm in length and 0.26 ± 0.13 mm in width and have an aspect ratio of 1.76 ± 0.68 (Fig. 2.21c). Among the 173 longer segments, 46 with a length of 0.57 ± 0.28 mm, a width of 0.32 ± 0.16 mm, and an aspect ratio of 1.89 ± 0.68 (Fig. 2.21d) were re-broken. This second generation of tensile fracturing produces shorter and longer segments with aspect ratios of 0.72 ± 0.34 (Fig. 2.20e) and 1.26 ± 0.47 (Fig. 2.21f), respectively. Finally, only 5 of the 46 long segments were broken by the third generation of tensile fracturing (Fig. 2.21g), forming a

group of short microboudins (L/W=0.59±0.24, Fig. 2.21h) and a group of long segments (L/W=1.00±0.37, Fig. 2.21i).

For the samples from the CS shear zone, take sample CS45 for example, 47 original tourmaline crystals have their mean length (L_0) and width (W_0) of 1.65±0.96 mm and 0.60±0.28 mm, respectively, with a mean length/width ratio of 2.82±1.02 (Fig. 2.22). However, the 250 microboudins of tourmaline from the 47 crystals have their average final length (L_f) of 0.31±0.25 mm and average length/width ratio of 0.64±0.39 (Fig. 2.22).

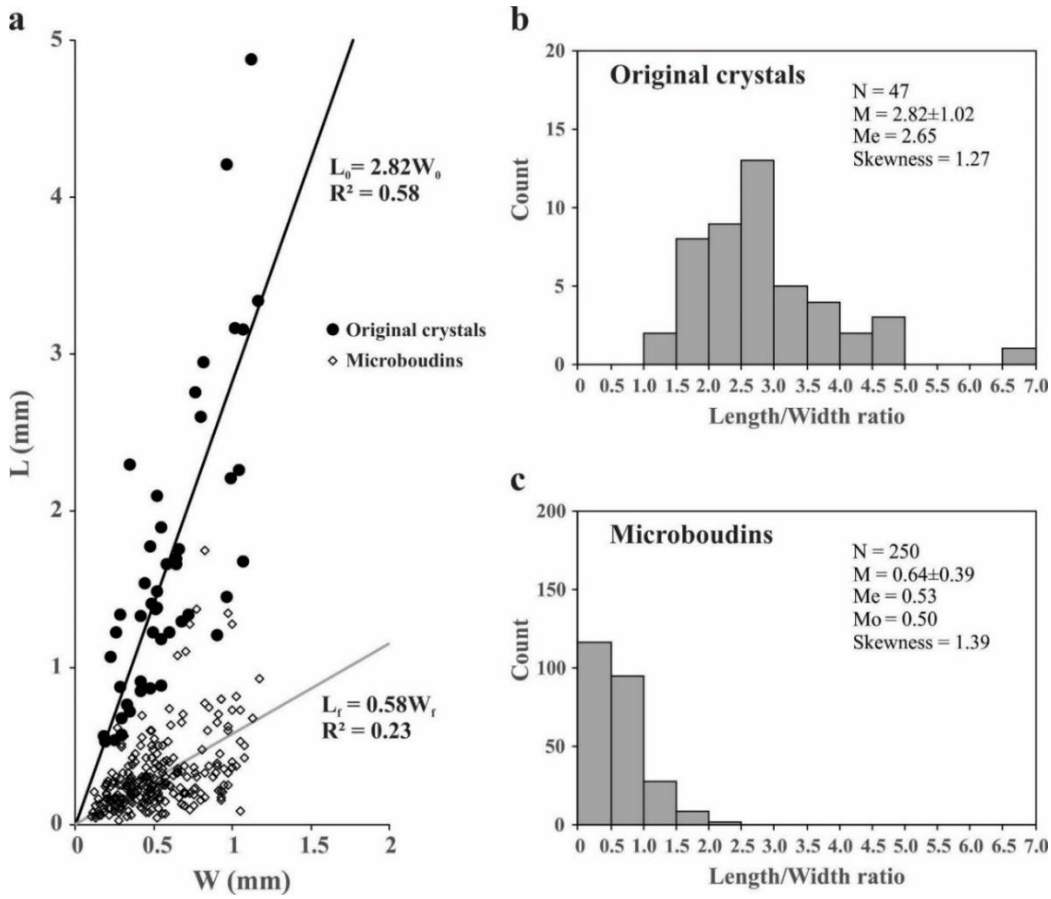

Figure 2.22 Data measured from sample CS45. (a) Plots of length versus width of 47 original grains before fracturing (solid circle) and their 250 microboudins after fracturing (open circle). (b) and (c) Histograms of length/width (aspect) ratios for the intact grains before fracturing and their microboudins after fracturing, respectively. Fracturing results in decreasing length/width ratios of tourmaline fragments. N: number of measurements; M: mean; Me: median.

The studied samples from the Gaoligong and Chongshan shear zone show that tensile fracturing in columnar tourmaline crystals within the flowing matrix was successive and each event made the tourmaline fragmented into two segments of unequal length, the shorter of which generally has an aspect ratio less than 1. The phenomenon, contrary to the mid-point fracturing predicted by the conventional shear-lag model (Ji & Zhao, 1993, 1994; Zhao & Ji, 1997; Masuda & Kuriyama, 1988; Masuda et al., 1989, 1990, 2003; 2004; 2007, 2008, 2011; Masuda & Kimura, 2004; Kimura et al., 2006, 2010; Matsumura et al., 2017), is referred to as near-end fracturing (Ji et al., 1998). The shear-lag model predicts that the tensile stress reaches first a maximum at the center of the mechanically homogeneous fiber (Fig. 2.1d), based on the assumptions that no slip occurs along the fiber-matrix interface (Fig. 2.1c). Actually, the shear strength of the interface cannot be infinitely large and thus slip will occur along the interface if the interfacial shear stress reaches its shear strength. The maximum tensile stress, which cannot exceed the tensile strength of the fiber mineral (C), is controlled primarily by the shear strength of the fiber/matrix interface. Furthermore, the highest interfacial shear strength cannot exceed the shear flow strength of the matrix. In the ductile regime, we can reasonably assume that the interfacial shear strength is equal to the shear flow strength of the matrix.

2.7.2 Measurements of strains and estimates of strain rates

The length of each gap between adjacent microboudins were also estimated (for samples from the GLG) and measured (for samples from the CS) from each thin petrographic section. Taking the samples from the CS shear zone as an example, the largest interboudin gap observed is ~2.7 mm while the smallest interboudin gap is only ~0.5 μm. The measured data were also used to calculate the finite extension strain using the strain reversal method (Fig. 2.13, Appendix B).

Figure 2.17 shows the distribution of finite extension strains estimated from 85 tourmaline crystals from the Chongshan shear zone using the strain reversal method described above. The estimated finite extension (natural) strain varies from 0.01 to 0.57 with an average of 0.18 (standard deviation: 0.12) for the fractured tourmaline grains within the granitic gneisses and mylonites from the CS shear zone. With the measured strain and combined with the geochronological data from the CS shear zones, the strain rate of the deformed mylonite samples can be estimated.

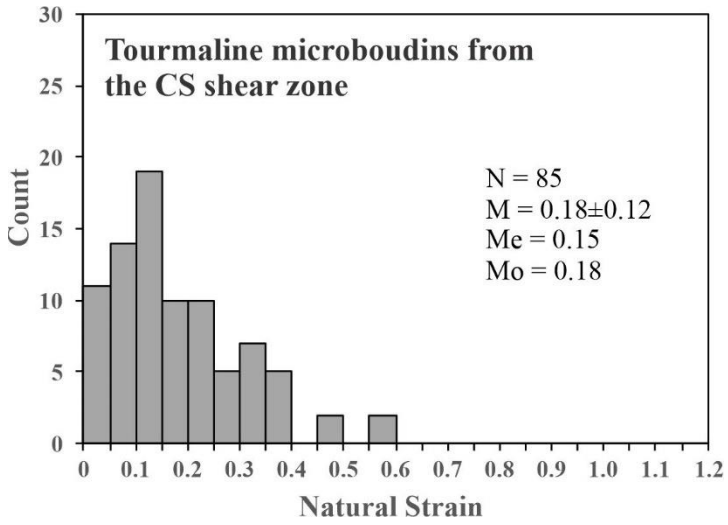

Figure 2.23 Extension strains measured from microboudins of 85 tourmaline grains using the strain reversal method. N: number of intact grains; M: mean; Me: median; Mo: mode.

Figure 2.18 summarized available accurate data of zircon U-Pb, monazite U-Th/Pb, muscovite and biotite $^{40}Ar/^{39}Ar$, and zircon and apatite (U-Th)/He ages for the CS shear zone (Akciz et al., 2008; Zhang et al., 2010, 2012a; Wang Y. et al., 2018). The closure temperatures of zircon U/Pb, monazite U-Th/Pb, muscovite and biotite $^{40}Ar/^{39}Ar$, and zircon and apatite (U-Th)/He thermochronometric systems are taken to be ≥750, 700±50, 400±50, 300±40, 180±25, and 65±5 °C, respectively (Harrison et al., 1985; Hames & Bowring, 1994; Parrish, 2001; Reiners, 2005; Flowers et al., 2009; Guenthner et al., 2013). The data suggest that rapid cooling started at ~21.6 Ma with a mean cooling rate of ~62.9 °C/Ma during the time interval from 21.6 Ma to 13.0 Ma. Such a rapid cooling rate corresponds to quartz microstructural quenching that occurred during this period. The results are consistent with previous geochronological data from the southeastern Himalayan syntaxis (e.g., Jiali and Gaoligong shear zones), which show similar cooling history between 22 Ma and 13 Ma (Lee et al., 2003; Lin et al., 2009; Wang Y. et al., 2016, 2018). In the CS shear zone, the $^{40}Ar/^{39}Ar$ plateau ages of muscovite and biotite display average ages of 16.0 and 14.5 Ma, respectively, which corresponds to a mean exhumation rate of 3.33 mm/yr assuming a geothermal gradient of 20 °C/km. The low-temperature thermochronological data (i.e., zircon and apatite (U-Th)/He ages, Wang Y. et al., 2018) suggest the cooling rate increased again during 12-5 Ma, corresponding to brittle faulting-related exhumation.

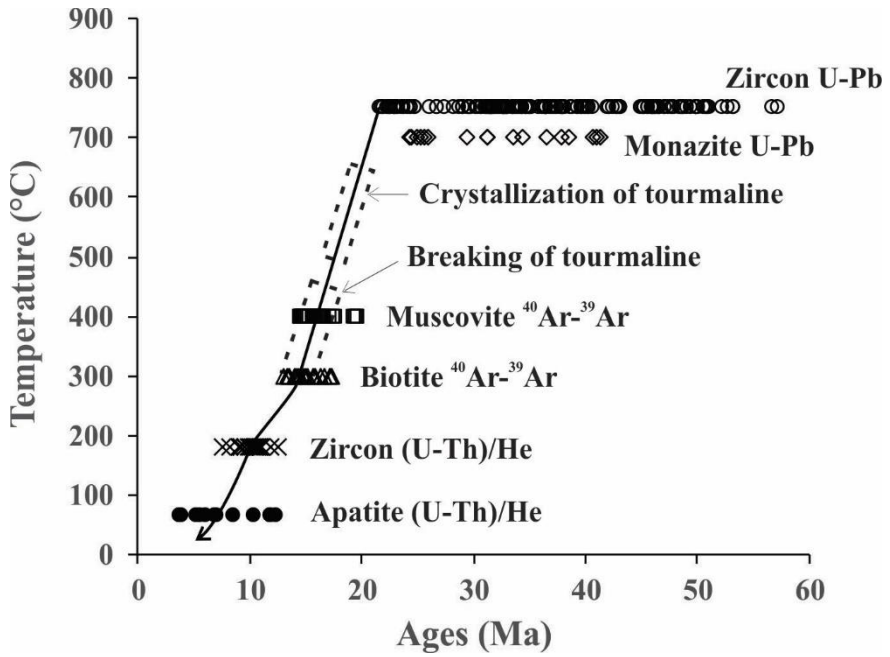

Figure 2.24 A compilation of available accurate data of zircon U-Pb, monazite U-Th/Pb , muscovite and biotite $^{40}Ar/^{39}Ar$, and zircon and apatite (U-Th)/He ages for the CS shear zone (Akciz et al., 2008; Zhang et al., 2010, 2012a; Wang Y. et al., 2018). Conditions where tourmaline crystallized and broke are indicated.

Microstructures suggest that tourmaline crystals were broken successively into microboudins in the temperature range of 450-300 °C (16.8-14.5 Ma, Fig. 2.24) or mostly 400-300 °C (16.0-14.5 Ma) because quartz and feldspar crystal plasticity onsets occur at ~300 and ~450 °C, respectively (e.g., Snoke & Tullis, 1998; Scholz, 2019). According to the extensional strains recorded by the microboudins (Fig. 2.23) and the thermochronological data (Fig. 2.24), the strain rates of the microboudins are estimated to vary from 1.06×10^{-16} s^{-1} to 7.59×10^{-15} s^{-1} with a mean value of $(2.38\pm1.64)\times10^{-15}$ s^{-1} and from 1.59×10^{-16} s^{-1} to 1.14×10^{-14} s^{-1} with a mean value of $(3.56\pm2.46)\times10^{-15}$ s^{-1} if the deformation presumably took place at 450-300 °C (Fig. 2.25a) and 400-300 °C (Fig. 2.25b), respectively. However, these strain rates must be regarded as minimum estimates because the deformation recorded by interboudin gaps of tourmaline should be substantially smaller than those of the flowing quartz matrix or that of the bulk rock (Ferguson & Lloyd, 1982). On this basis, we settle for a strain rate of 10^{-14} s^{-1} as the 'best' strain rate estimate for the metamorphic rocks in which the tourmaline microboudins formed. The strain rate of ~s^{-1} is consistent with those values estimated for other metamorphic terranes such as the Ruby Gap

duplex, Central Australia (Hirth et al., 2001) and the Ailaoshan-Red River and Karakorum shear zones (Boutonnet et al., 2013).

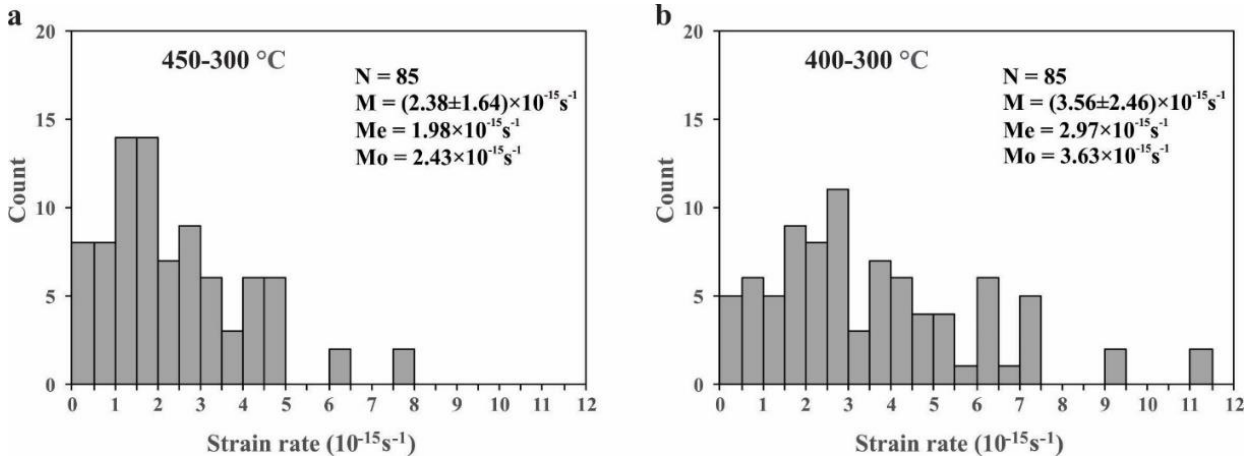

Figure 2.25 Extension strain rates estimated for 85 tourmaline grains, assuming the fracturing took place at 450-300 ºC (a) and 400-300 ºC (b). N: number of intact grains; M: mean; Me: median; Mo: mode.

The mean strain rates from (2.38±1.64) $\times 10^{-15}$ s^{-1} to (3.56±2.46)$\times 10^{-15}$ s^{-1}, estimated from the tourmaline microboudins are close to the value (1.1×10^{-15} s^{-1}) obtained from Rb-Sr darting of fibrous fringes around pyrite grains from a thrust-type Pyrenean shear zone near Lourdes, France (Müller et al., 2000). In the latter case, the fibrous fringes of cogenetic calcite, quartz and chlorite grew through dissolution-precipitation mechanism in carbonate-rich slates at temperatures below 300 ºC. The fibrous growth, which spanned over a time interval of about 37 Ma (87-50 Ma), could be discontinuous and cyclic (e.g., crack-seal mechanism) rather than continuous in such a semi-brittle regime. In other words, deformation can hardly homogeneous in either space or time within a period over 37 Ma documented by Müller et al. (2000). The strain rates that we obtained from a time span of only 2.3 Ma, which is much shorter than that documented by Müller et al. (2000). Thus, the tourmaline microboudins provide likely a good constraint on natural strain rates associated to a-few-million-years-long processes.

2.8 Estimates of paleostresses

With the estimated tensile strength of tourmaline, Eq. (2.14) will permit to estimate the shear flow strength of the felsic or quartz matrix. The stress magnitude calculated from Eq. (2.14) can be considered as the upper limit for the shear flow stress in the ductile matrix. The applications of the new microboudinage piezometer (Eq. 2.14) will be presented in Sections 2.8.1 and 2.8.2.

2.8.1 Paleostresses in the Gaoligong shear zone

According to Eq. (2.14), with the tensile strength of tourmaline taken as 145 MPa, the tourmaline microboudins (the shorter segments formed by each generation of near-end fracturing) measured from the Gaoligong shear zone yields shear flow stresses varied from 21 MPa (sample GLG14) to 61 MPa (sample GLG325) in the Gaoligong shear zone (Table 2.4).

Table 2.4 **S**hear flow stress estimated using the tourmaline microboudinage piezometer for each sample from the Gaoligong shear zone

Sample No.	**Fracturing**	***L/W***	**Shear flow stress (MPa)***	**Differential stress (MPa)**
GLG14	First generation	1.72	21	37
	Second generation	1.12	32	56
GLG93	First generation	1.54	24	41
	Second generation	1.25	29	50
GLG104	First generation	0.76	48	83
GLG201	First generation	1.35	27	47
	Second generation	0.76	48	83
GLG317	First generation	1.31	28	48
	Second generation	0.83	44	76
GLG325	First generation	0.98	37	64
	Second generation	0.72	50	87
	Third generation	0.59	61	106
YN1397	First generation	1.10	33	57
	Second generation	0.84	43	75
	Third generation	0.81	45	78

* Calculated assuming C=145 MPa for tourmaline

Interestingly, multiple generations of fracturing display a progressive increase in shear flow stress: from 21 MPa to 32 MPa in sample GLG14, from 27 MPa to 48 MPa in sample GLG201, and from 37 MPa to 61 MPa in sample GLG325. The sequential fracturing is interpreted to have taken place during a process of uplift-induced hardening. In sample YN1397, for example, the

shear flow stress continued to increases from 33 MPa (first generation of fracturing), to 43 MPa (second generation of fracturing) and then reached to 45 MPa during the third generation of fracturing. Finally, the microboudinage structures were frozen after the matrix of quartz could not plastically flow any more at temperatures below ~300 °C due to tectonic exhumation and cooling (Masuda et al., 1990; Omori et al., 2016).

2.8.2 Paleostresses in the Chongshan shear zone

Taking the tourmaline grains from the CS shear zone as an example, *C* value was estimated for each of the 365 tensile fractures in 85 tourmaline grains from the study samples according to the degree of crystal quality and internal flaws (e.g., microcracks, inclusions, heterogeneities, and surface rugosity) (Fig. 2.26, Appendix B). On this basis, we settle for *C*=145±35 MPa as the "best" tensile strength estimate for the tourmaline from the CS shear zone, although further experimental measurements are needed.

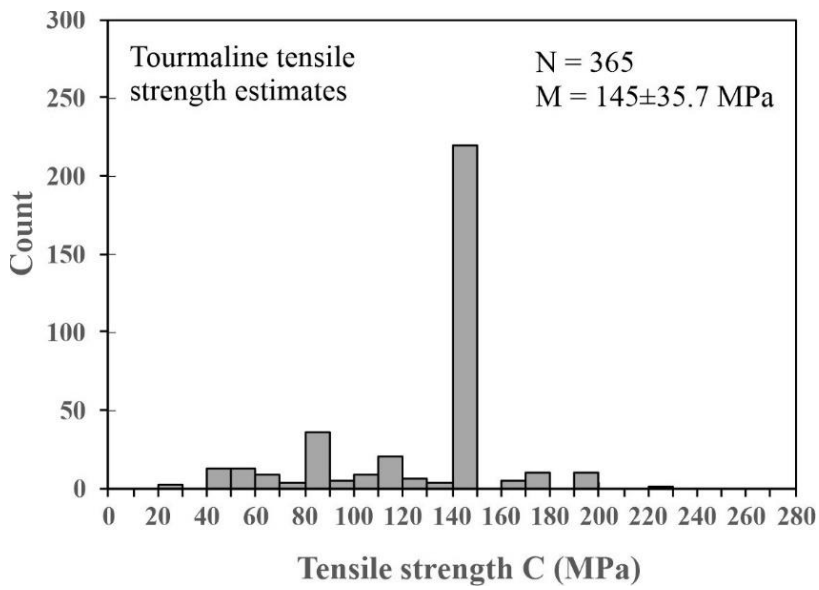

Figure 2.26 "Best" tensile strength estimates for the tourmaline grains from the CS shear zone according to their crystal quality and internal flaws such as microcracks, inclusions, heterogeneities, and surface rugosity. N: number of fractures; M: mean.

We then performed the Kolmogorov–Smirnov (KS) statistical test on the estimated *C* values for five distribution models. The computed statistic values are as follow: exponential distribution (0.380), Log-normal distribution (0.352), Gamma distribution (0.351), normal distribution (0.335), and Weibull distribution (0.328). The KS statistics measure how well the measured data

is fitted by a given theoretical distribution model. The smaller the KS value is, the better the given model fits the measured data. The results reveal that the best-fit distribution function for the estimated *C* values is the Weibull distribution, which agrees with the previous theoretical studies (Weibull, 1951; Paterson & Wong, 2005; Dodson, 2006).

The shear flow stress corresponding to each tourmaline microboudin embedded in the plastically deformed matrix in the samples from the Chongshan shear zone has been estimated (Appendix B). Plots of estimated quartzite shear flow stress as a function of estimated deformation temperature are shown in Fig. 2.27.

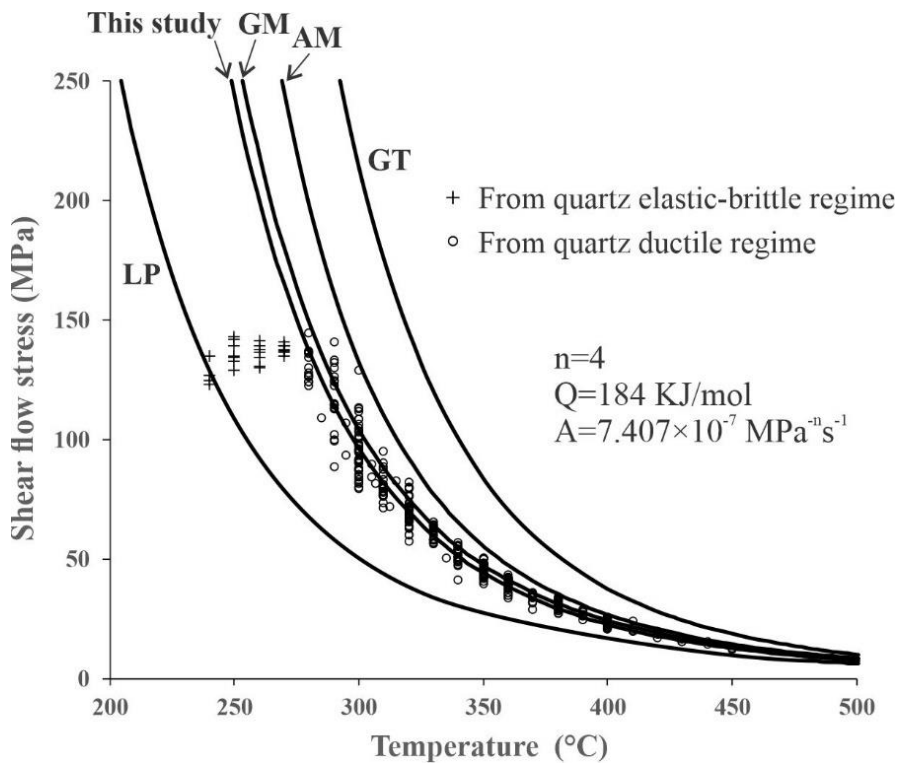

Figure 2.27 Plots of shear flow stress versus temperature for the quartz matrix surrounding the tourmaline microboudins. Largest uncertainties in deformation temperature and shear flow stress are ±20 °C and ±15 MPa, respectively. The data in the ductile regime yields a flow law defined by Eq. (2.19) with n=4, Q=184 kJ/mol and A=7.180×10^{-7} MPa^{-n}s^{-1}. Results calculated from extrapolation of quartzite flow laws assuming a strain rate of 10^{-14} s^{-1} (LP: Luan & Paterson, 1992; GT: Gleason & Tullis, 1995), and their arithmetic and geometric means (AM and GM) are also shown.

The fracturing of tourmaline took place sequentially with larger gaps formed earlier whereas the microboudins with smaller length/width ratios formed later, indicating an increase in flow strength, which is caused by a decrease in temperature or burial depth. Thus, the sequential fractures correspond to decreasing temperatures during the progressive exhumation upward the brittle-ductile transition. Furthermore, microstructures of quartz filled in the interboudin gaps can provide some information about approximate temperature of deformation after each stage of fracturing. The quartz filled in the older gaps exhibit optically visible subgrains and recrystallized neograins along grain boundaries, which are characteristic of the mechanism that recovery is dominated by dislocation climb and subgrain rotation recrystallization (Hirth & Tullis, 1992). However, the quartz filled in the younger gaps exhibit optically uneven extinction and highly fine neograins along the grain boundaries. The microstructural features suggest that the deformation occurs at so low temperatures that dislocation climb is limited and the recrystallization takes place by grain boundary bulging (Hirth et al., 2001). Biotite and muscovite are observed in some gaps formed at high and moderate temperatures, respectively. Sericite is present in the tensile fractures across which microboudins are not separated, indicating that fracturing occurred at very low temperatures (≤280-290 ºC) which were insufficient to permit ductile deformation of quartz. The uncertainties in the temperature estimates are ±30 °C.

2.9 Discussion

2.9.1 Exhumation-induced hardening in the Gaoligong shear zone

Multiple generations of tensile fracturing to form successively smaller aspect ratios of microboudins indicate a tectonic environment of hardening where temperature drops, strain rate rises or a combined situation is also possible. As the flow strength of the quartz-rich crust below the brittle-ductile transition increases with decreasing depth and temperature, the hardening was likely caused by progressive tectonic uplift and exhumation. As the interboudins should cease to being pulled further apart after the matrix material lose its plasticity and entered into the brittle regime due to tectonic cooling (<300 ºC), the observed microboudinage structures accordingly recorded the shear flow stresses of the rock within the upper layer of the ductile crustal regime, which below the brittle-ductile transition depth (Fig. 2.28).

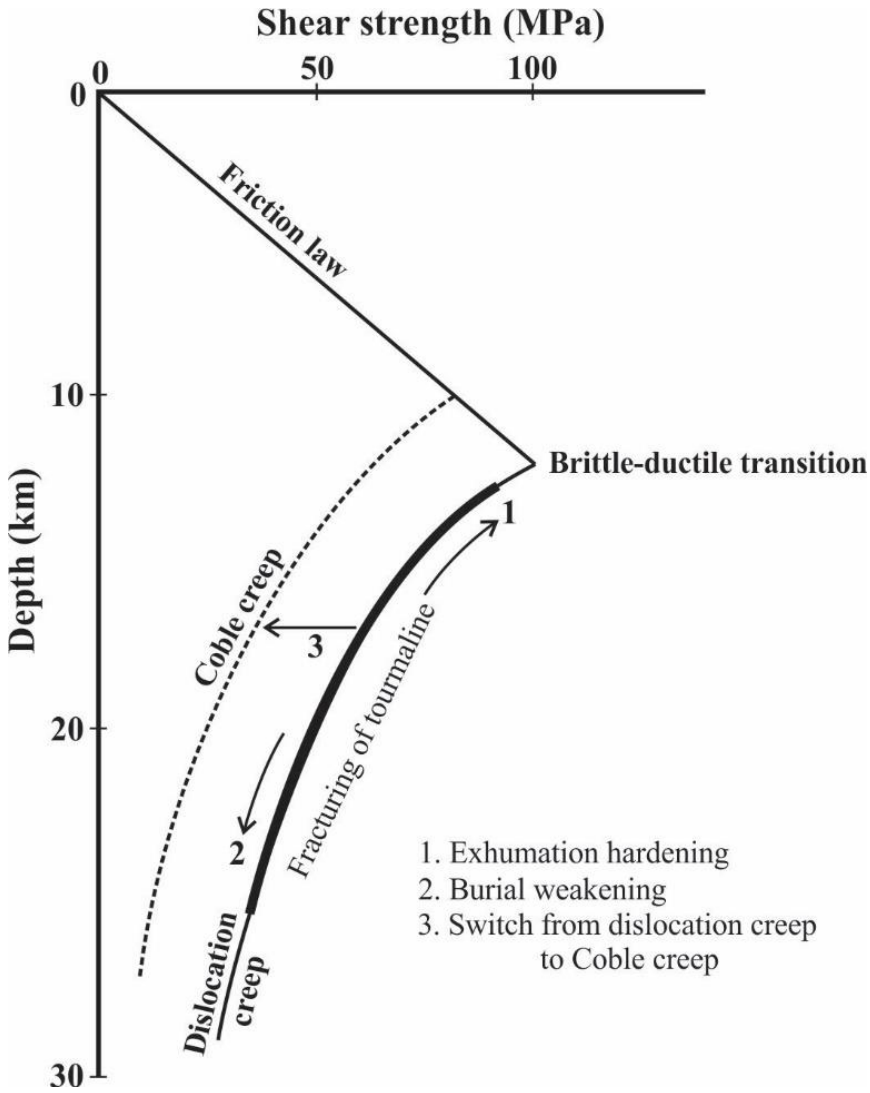

Figure 2.28 Schematic strength profile for the quartz-rich part of the continental crust. The strength is controlled by the Byerlee friction law down to the brittle-ductile transition, and then decreases non-linearly with depth following a power flow law of wet quartz below the transition. Smaller length/width ratios of microboudins form successively when the ductile rock becomes stronger due to cooling caused by tectonic exhumation until the brittle-ductile transition is reached (path 1). In contrast, greater length/width ratios of microboudins are sequentially produced when the ductile rock becomes warmer and weaker due to burial and temperature increase (path 2). A switch from dislocation creep to Coble creep due to grain size reduction (dynamical recrystallization or retrogressive metamorphic reactions) induces a weakening and thus forms greater length/width ratios of microboudins (path 3).

Rheological weakening is also common in localized deformation belts within the crust. The processes that result in rheological weakening include temperature rises (e.g., shear heating, and thrust-induced burial and temperature increase, Platt, 2015a), grain size reduction (e.g., dynamic recrystallization, Tullis & Yund, 1985), compositional change (e.g., hydration, retrogressive metamorphic reactions, Rubie, 1990; Hirauchi et al., 2016) and preferred orientation of weak phyllosilicate minerals (Collettini et al., 2009; Niemeijer et al., 2010). The grain size reduction in the matrix can substantially contribute to weakening by leading to a switch from dislocation creep to grain boundary diffusion creep (Nicolas & Poirier, 1976). The sequential formation of greater length/width ratios of microboudins by near-end fracturing may be served as evidence for operation of the weakening processes (Fig. 2.28).

2.9.2 Rheological properties of the Chongshan shear zone

In the following, we take the CS shear zone as an example to show how the application of the microboudinage piezometer, combined with microstructural observations and independent estimates of deformation temperature, accurate geochronological ages and regional geophysical data improves the understanding of the rheological properties of study area.

2.9.2.1 Flow law of quartz derived from the Chongshan shear zone

As shown in Fig. 2.27, shear flow stresses for the ductile quartz matrix range from 13 to 148 MPa with an obvious increase with decreasing temperature. At temperatures lower than 280-290 ºC where quartz deforms in the elastic-brittle regime, however, there is a trend that shear flow stresses decrease gently with decreasing temperature. A clear peak in shear flow stress occurs at 280-300 °C, which we interpret to correspond to the brittle-ductile transition of quartz.

Neither the flow law of Luan and Paterson (1992) for silicic acid origin synthetic specimens nor that of Gleason and Tullis (1995) for Black Hill quartzites (Table 2.5) can fit well with our data in the range of 450-300 ºC and at the strain rate of 10^{-14} s^{-1}. This strain rate has been regarded as a typical one for continental shear zones (e.g., Pfiffner & Ramsay, 1982; Christensen et al., 1989; Twiss & Moores, 2001; Boutonnet et al., 2013). The steady-state flow behavior of quartz polycrystalline aggregates by dislocation creep has a power law stress dependency and is of the form (e.g., Ji & Xia, 2002):

$$\dot{\varepsilon}=A\sigma^{n}exp(-Q/RT) \qquad (2.19)$$

where $\dot{\varepsilon}$ is the steady-state strain rate, A is the pre-exponential factor, σ is the differential stress, n is the stress exponent, Q is the apparent activation energy, R is the gas constant, T is the absolute temperature (K). The deformation experiments of Luan and Paterson (1992) and Gleason and Tullis (1995), which were used to determine the flow law parameters (n, Q and A, Table 2.5), are believed to have had the highest stress resolution because a gas or molten confining medium was used (e.g., Hirth et al., 2001; Ji & Xia, 2002; Lu & Jiang, 2019). The stresses obtained directly from the flow laws of both Hirth et al. (2001) and Lu and Jiang (2019) are differential stresses (σ_1-σ_3), which should be divided by $\sqrt{3}$ (Paterson & Olgaard, 2000; Behr & Platt, 2014) to obtain the shear flow stress values comparable to those estimated by tourmaline microboudinage paleopiezometer. As illustrated in Fig. 2.27, the rheological data from the study samples are distributed consistently between the upper and lower bounds defined by Gleason and Tullis (1995) and Luan and Paterson (1992), respectively, which bracket the plausible range of the quartzite shear flow strengths (Lu & Jiang, 2019). It is also noted that the estimated results are better described by the geometrical mean than the arithmetic average of the bounds (Fig. 2.27).

Table 2.5 Dislocation creep law parameters of quarztites

Reference	***n***	***Q* (KJ/mol)**	***A* (MPa^{-n}/s)**
Luan and Paterson (1992)	4	152	1.198×10^{-8}
Gleason and Tullis (1995)	4	223	1.095×10^{-4}
This study	4	184	7.407×10^{-7}

The rheological data obtained from the study samples (Fig. 2.27) can be best fit by the flow law defined by Eq. (2.19) with n=4, Q=184 kJ/mol and A=7.180×10^{-7} MPa^{-n}s^{-1}. Similar to those of Luan and Paterson (1992) and Gleason and Tullis (1995), our natural quartzite flow law does not include the term of water fugacity. The stress data below 280-290 ºC are notably lower than those described by this flow law (Fig. 2.27), where quartz can no longer deform by dislocation creep but goes into the elastic-brittle regime. This new quartzite flow law derived from the naturally deformed rocks may provide more reasonable estimations of quartzite flow strength than the extrapolation of experimentally determined flow laws from either Luan and Paterson (1992) or Gleason and Tullis (1995). At 300 ºC, for example, quartz deformed plastically by dislocation creep, our quartzite flow law yields a flow strength of 168 MPa, which is significantly lower than the value (374 MPa) given by that of Gleason and Tullis (1995).

2.9.2.2 Application of the quartz flow law to the Chongshan shear zone

In the following, we will take the CS shear zone as an example to show how the flow law of quartzite deformed at natural strain rates (n=4, Q=184 kJ/mol, and A=7.180×10^{-7} MPa^{-n}s^{-1}) can be applied to constrain the rheological properties of the present-day crust. In order to do so, we first need to determine the lithological composition-depth and temperature-depth profiles for the CS shear zone.

Linear geothermal gradients were assumed in many previous investigations of depth-dependent rheological properties (Ranalli & Murphy, 1987; Hirth et al., 2001; Lu & Jiang, 2019). However, such practices unavoidably overestimates the temperatures in the deep crust because the geothermal gradient ($\partial T/\partial z$) decreases generally non-linear with increasing depth. Here we calculate the temperature-depth and geothermal gradient-depth profiles for the study region, based on the data of surface heat flow values (Q_0), thermal conductivity (k) and radioactive heat productivity (A) of rocks, the crustal lithological structure (Fig. 2.29), and the equilibrium heat conduction equation of a steady regime (Carslaw & Jaeger, 1959; Fowler, 1992). A state of steady thermal equilibrium is assumed to be reached. For simplicity, no erosion or deposition has been taken into consideration.

The following boundary conditions were used in the calculation of the temperature-depth profile which is also called an equilibrium geotherm:

T=20 ℃, when z=0 km;

$Q_0 = k\frac{\partial T}{\partial z}$, when z=0.

Each compositional layer was considered separately, and temperatures and heat flows were matched across the boundaries:

At $z=z_1$, $T_{\text{layer1}}= T_{\text{layer2}}$, and $Q_{\text{layer1}}= Q_{\text{layer2}}$;

At $z=z_2$, $T_{\text{layer2}}= T_{\text{layer3}}$, and $Q_{\text{layer2}}= Q_{\text{layer3}}$.

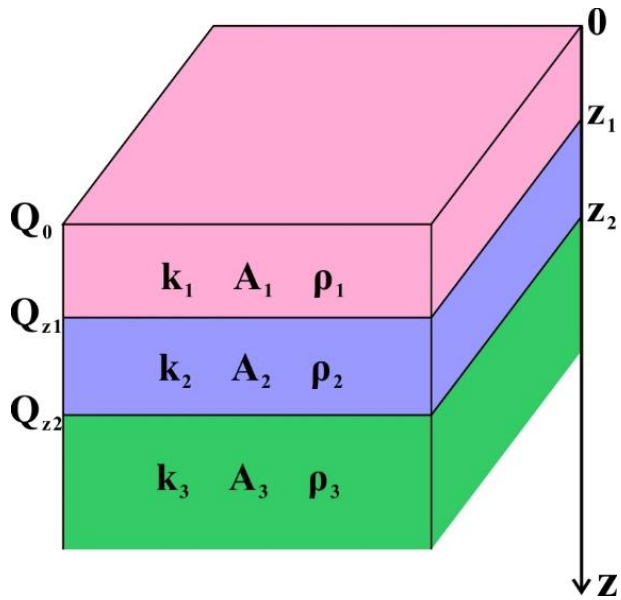

Figure 2.29 Three-layer model lithosphere of the Chongshan region, western Yunnan China: 20 km-thick granitic upper crust (k=3.1 $Wm^{-1}°C^{-1}$, A=1.0×10^{-6} Wm^{-3}, ρ=2600 kg/m^3), 18 km-thick dioritic lower crust (k=4.0 $Wm^{-1}°C^{-1}$, A=7.0×10^{-7} Wm^{-3}, ρ=2650 kg/m^3), and peridotitic upper mantle (k=2.5 $Wm^{-1}°C^{-1}$, A=0 Wm^{-3}, ρ=3300 kg/m^3), where k is the thermal conductivity, A is the radioactive heat productivity, and ρ is the density. The lithological structure derived from regional seismic data (e.g., He et al., 2009; Sun et al., 2012; Hu et al., 2013; Zha & Lei, 2013; Deng et al., 2014; Sun et al., 2014; Wang F. et al., 2018).

For layer 1 ($0<z< z_1$),

$$\frac{\partial^2 T}{\partial z^2} = -\frac{A_1}{k_1} \qquad (2.20)$$

This second-order differential equation is solved according to the above boundary conditions. Integrating Eq. (2.20) once yields:

$$\frac{\partial T}{\partial z} = -\frac{A_1}{k_1} z + c_1 \qquad (2.21)$$

where c_1 is the constant of intergration. Based the boundary conditions, we obtained

$$c_1 = \frac{Q_0}{k_1} \qquad (2.22)$$

Putting Eq. (2.22) into Eq. (2.21), and then intergrating the second time yields:

$$T = -\frac{A_1}{2k_1} z^2 + \frac{Q_0}{k_1} z + c_2 \qquad (2.23)$$

In Eq. 2.23, c_2 is the constant of integration for layer 1. c_2=20 °C because T=20 °C at z=0 km.

For layer 2 (z_1<z< z_2),

$$\frac{\partial T}{\partial z} = -\frac{A_2}{k_2} z + c_3 \qquad (2.24)$$

As Q_{layer1}= Q_{layer2} on the interface between layer 1 and layer 2,

$$k_1\left(-\frac{A_1}{k_1} z_1 + \frac{Q_0}{k_1}\right) = k_2(-\frac{A_2}{k_2} z + c_3) \qquad (2.24)$$

with

$$c_3 = \frac{1}{k_2}(Q_0 + z_1(A_2 - A_1)) \qquad (2.25)$$

$$T = -\frac{A_2}{2k_2} z^2 + c_3 z + c_4 \qquad (2.26)$$

At z=z_1,

$$-\frac{A_1}{2k_1} {z_1}^2 + \frac{Q_0}{k_1} z_1 = -\frac{A_2}{2k_2} {z_1}^2 + c_3 z_1 + c_4 \qquad (2.27)$$

with

$$c_4 = \left(\frac{A_2}{k_2} - \frac{A_1}{k_1}\right)\frac{{z_1}^2}{2} + (c_1 - c_3) z_1 \qquad (2.28)$$

Both c_3 and c_4 are the constants of integration for layer 2.

For layer 3 (z_2<z< z_3),

$$\frac{\partial^2 T}{\partial z^2} = -\frac{A_3}{k_3} \qquad (2.29)$$

$$\frac{\partial T}{\partial z} = -\frac{A_3}{k_3} z + c_5 \qquad (2.30)$$

As Q_{layer2}= Q_{layer3} on the interface between layer 2 and layer 3, we have

$$k_2\left(-\frac{A_2}{k_2} z_2 + c_3\right) = k_3(-\frac{A_3}{k_3} z_2 + c_5) \qquad (2.31)$$

with

$$c_5 = \frac{k_2}{k_3} c_3 + \frac{(A_3 - A_2)}{k_3} z_2 \qquad (2.32)$$

$$T = -\frac{A_3}{2k_3} z^2 + c_5 z + c_6 \qquad (2.33)$$

At z=z_2,

$$-\frac{A_2}{2k_2}{z_2}^2 + c_3 z_2 + c_4 = -\frac{A_3}{2k_3}{z_2}^2 + c_5 z_2 + c_6 \qquad (2.34)$$

then

$$c_6 = \left(\frac{A_3}{k_3} - \frac{A_2}{k_2}\right)\frac{{z_2}^2}{2} + (c_3 - c_5)z_2 + c_4 \qquad (2.35)$$

Both c_5 and c_6 are the constants of integration for layer 3.

The available Q_0 data from the region, which are listed in Table 2.6 (Wang & Huang, 1990; Xu et al., 1992), range from 61.3 to 66.0 mW/m^2 with a mean of 63.5 mW/m^2. As shown in Fig. 2.29, the one-dimensional lithospheric column consists of three layers: 20 km-thick granitic upper crust (k=3.1 Wm^{-1}°C^{-1}, A=1.0×10^{-6} Wm^{-3}, ρ=2600 kg/m^3), 18 km-thick dioritic lower crust (k=4.0 Wm^{-1}°C^{-1}, A=7.0×10^{-7} Wm^{-3}, ρ=2650 kg/m^3), and peridotitic upper mantle (k=2.5 Wm^{-1}°C^{-1}, A=0 Wm^{-3}, ρ=3300 kg/m^3), where k is the thermal conductivity, A is the radioactive heat productivity, and ρ is the density. The calculated temperature-depth profile is given in Fig. 2.30a. The temperatures at depths of 5, 10, 15, 20, 25, 30, and 35 km are, respectively, 118, 209, 291, 365, 433, 497 and 556 °C. The temperature at the Moho (38 km) is ~589 °C, which is consistent with the Moho temperature as a function of crustal thickness, modeled by Mareschal and Jaupart (2013) for orogenic belts. As shown in Fig. 2.30b, the geothermal gradient decreases gradually from 19.77 °C/km at the Earth's surface to 9.95 °C/km at the Moho.

Table 2.6 Heat flow data measured from the study region

Hole	Latitude (North)	Longitude (East)	Depth range of measurements (m)	Heat flow (mW/m^2)	Thermal gradient (°C/km)	Thermal Conductivity W/(m K)	Reference
Lancang-1	22.80944	99.71722	50-180	66.0	25.19	2.62	Wang and Huang (1990)
Lancang-2	22.51361	99.91222	110-130	61.4	16.51	3.72	Wang and Huang (1990)
Mohei-1	23.14083	101.15694	40-108	63.2	21.57	2.93	Wang and Huang (1990)
Lancang-1010	22.80944	99.71722	50-180	66.0	25.19	2.62	Xu et al. (1992)
Lancang-SHK1	22.51361	99.91222	100-135	61.3	16.48	3.72	Xu et al. (1992)
Puer-ZK207	23.14083	101.15694	40-110	63.2	21.57	2.93	Xu et al. (1992)
Mean				**63.5**	**22.20**	**2.61**	

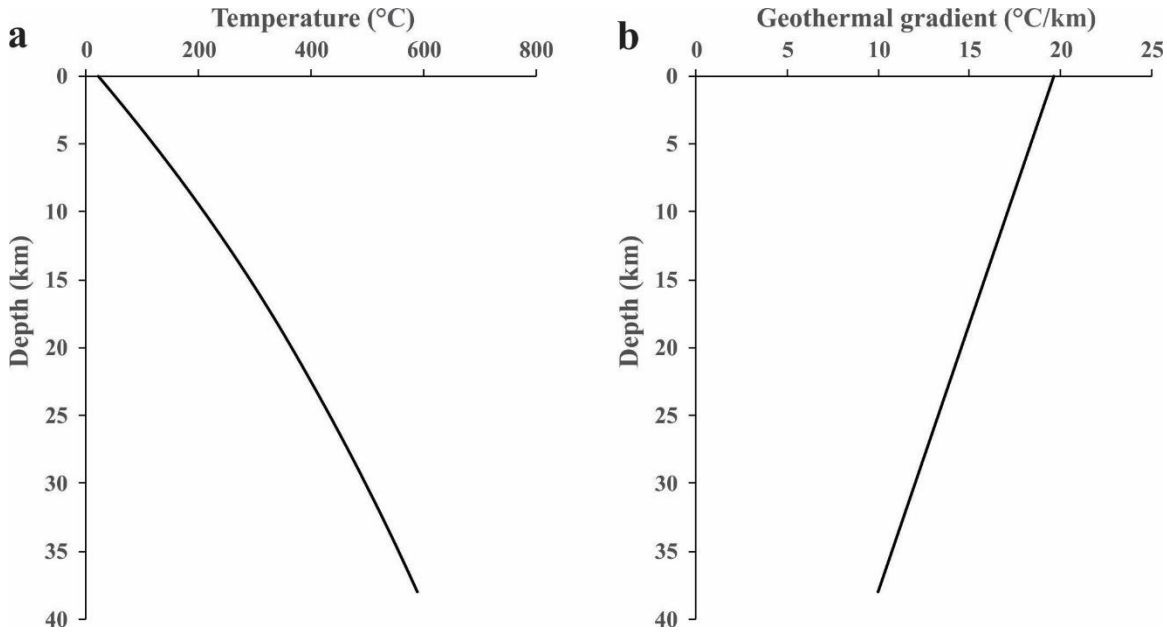

Figure 2.30 Temperature-depth (a) and geothermal gradient-depth (b) variations, computed from the surface heat flow, thermal conductivity and radioactive heat generation, for the Chongshan shear zone (Yunnan, Southwest China).

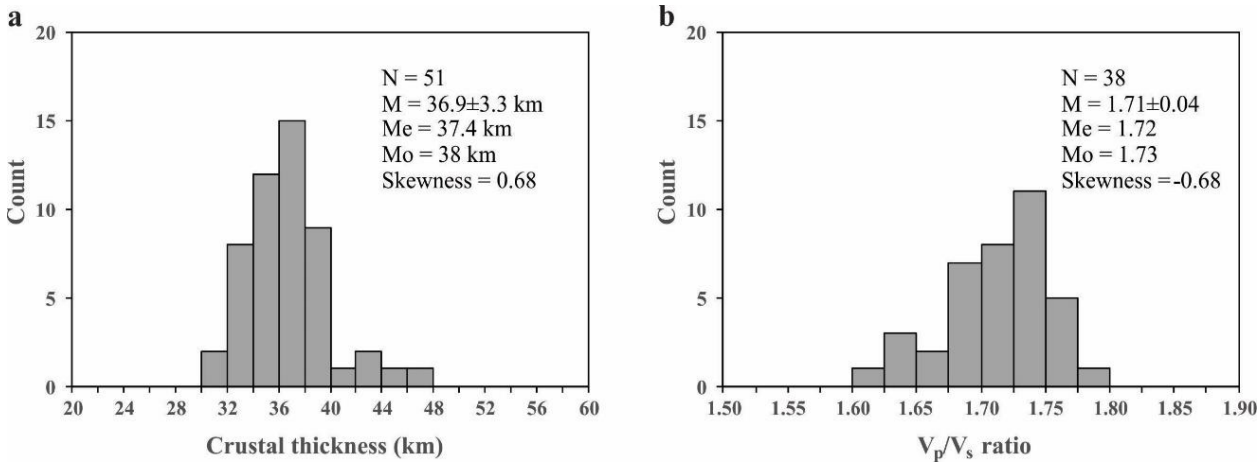

Figure 2.31 Histograms for the crustal thickness (a) and V_p/V_s ratio (b), measured for the Chongshan shear zone (Yunnan, Southwest China) using the method of function analysis (He et al., 2009; Sun et al., 2012; Hu et al., 2013; Zha & Lei, 2013; Deng et al., 2014; Sun et al., 2014; Wang F. et al., 2018). N: number of measurements; M: mean; Me: median; Mo: mode.

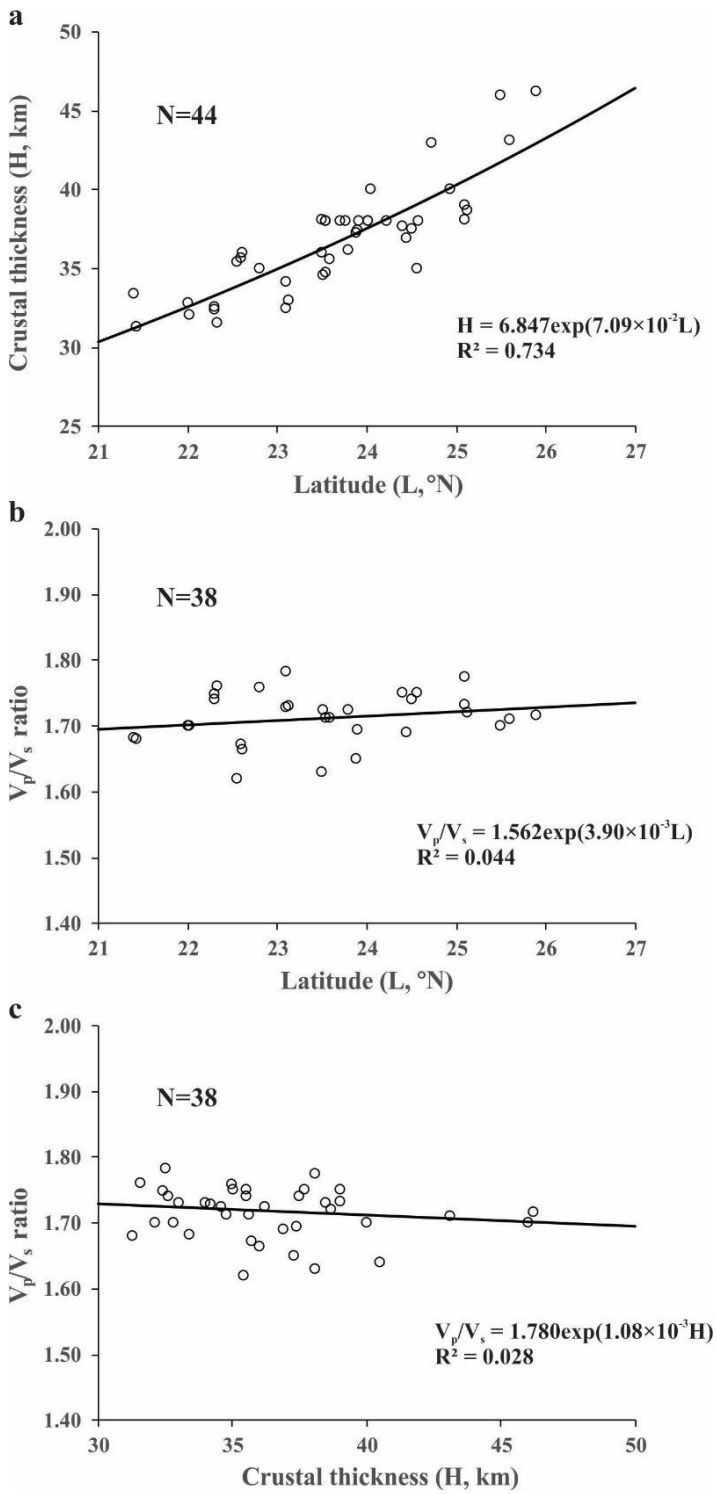

Figure 2.32 Variations of the crustal thickness (a) and V_p/V_s ratio (b) with latitude, and plots of V_p/V_s ratio versus the crustal thickness (c) for the Chongshan shear zone (west Yunnan, China). N: number of measurements.

The crustal thicknesses (H) and average V_p/V_s ratios beneath 38 seismic stations in the

Chongshan shear zone have been determined using the receiver function analysis (Hu et al., 2013; He et al., 2009; Sun et al., 2012; Zha & Lei, 2013; Deng et al., 2014; Sun et al., 2014; Wang F. et al., 2018). In addition, Gao et al. (2008) obtained the crustal thicknesses beneath 6 teleseismic stations from the study area using the transform function method that detects S-wave velocity jump across the Moho discontinuity. Figure 2.31 shows the histograms of H and V_p/V_s distributions obtained from the study region. The crusts beneath the region has an average thicknesses of 36.9±3.3 km (Fig. 2.31a) and an average V_p/V_s ratio of 1.71±0.04 (Fig. 2.31b). The V_p/V_s ratios suggest an average composition of felsic rocks including granites, granodiorites and diorites and their deformed and metamorphosed counterparts (Zandt & Ammon, 1995; Owens & Zandt, 1997; Ji et al., 2009, 2016). The crustal thickness displays a clear trend to increase from the south to the north (Fig. 2.32a), indicating that the crustal thickening is more pronounced nearer the eastern Himalayan syntaxis due to southeastward extrusion of the Tibetan Plateau (Tapponnier et al., 1990, 2001). Nevertheless, the V_p/V_s ratio has no systematical correlation with either latitude (Fig. 2.32b) or the crustal thickness (Fig. 2.32c), implying that the crust has an identical average composition equivalent to that of felsic igneous or metamorphic rocks (e.g., Ji et al., 2002, 2009; 2015, 2018; Hacker et al., 2015).

Figure 2.33 shows the plots of P-wave velocities as a function of depth, based on the results of seismic tomography across the region (Xu et al., 2013). There is a gentle increase in V_p with increasing depth, for example, 5.6, 6.0 and 6.6 km/s at depths of 3, 20 and 35 km, respectively. Below ~44 km, P-wave velocities reach to 8.0 km/s, typical of the peridotites in the upper mantle (Ji et al., 2002). At the depths between 38 and 44 km, a continuous, abrupt rise in V_p from 6.8 to 8.0 km/s is observed, which is interpreted as the crust-mantle transition zone related to underplating of mafic materials from the upper mantle.

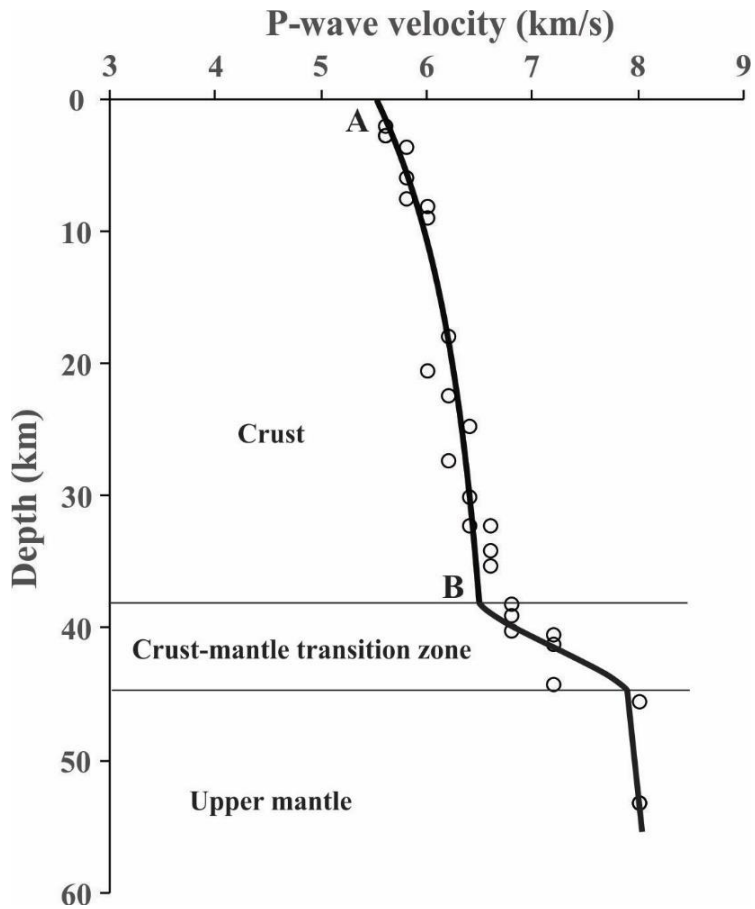

Figure 2.33 P-wave velocities as a function of depth (circles), measured by seismic tomography across the Chongshan shear zone (Data from Xu et al., 2013), and comparison with the V_p-depth curve calculated from extrapolation of experimentally measured data for felsic gneiss (solid line AB).

The crustal P-wave velocity (V) variation with depth (z) can be interpreted by the extrapolation of laboratory velocity data of a typical felsic gneiss to crustal P-T conditions at a given depth (Ji et al., 2007):

$$V(z)=V_0+(dV/dT)[T(z)-20]+DP(z)-B\exp[-kP(z)] \qquad (2.36)$$

where V_0 is the intrinsic velocity of the crack-free rock at room temperature (20 ºC) and pressure (0.1 MPa), T is the temperature, dV/dT is the temperature derivative of velocity, T(z) is given in Fig. 2.30a; D is the pressure derivative of velocity in the linear elastic regime; P is the confining pressure, B is the velocity descent caused by pores and microcracks at room pressure, k is the decay constant of velocity descent in the poroelastic regime. For typical felsic gneisses, V_0=6.45 km/s, D=2.744×10^{-4} km/s/MPa, B_0=0.922 km/s, k=2.364×10^{-2} /MPa, and dV/dT=5.214 ×10^{-4}

km/s/°C (Handbook of Seismic Properties of Minerals, Rocks and Ores, Ji et al., 2002). A good agreement between the measured and extrapolated results (line AB in Fig. 2.33) suggest that the crust is dominated by the felsic composition and the V_p-depth variation is caused by combined effects of progressive increase in both confining pressure and temperature. Increasing pressure leads to increasing velocities, in contrast to the temperature dependence.

Recently, Yang et al. (2018) carried out analyses of travel time curve based on 7412 earthquake data during 2009-2014 in the Yunnan region, acquired from 10 permanent seismic stations. Their analyses show that the crustal V_p changes with increasing depth from 6.0 to 6.6 km/s and V_s from 3.53 to 3.86 km/s, yielding an average V_p/V_s ratio of 1.71. Their results agree with the data illustrated in Figs. 2.31b and 2.32b-c. All the seismic data documented above indicate that the Chongshan shear zone crust is dominated by felsic composition, and thus its rheology is controlled by quartz deformation.

The rheological profiles calculated using different quartzite flow laws (Luan & Paterson, 1992; Gleason & Tullis, 1995; Hirth et al., 2001; Lu & Jiang, 2019; this study) for the Chongshan shear zone deformed at strain rates of 10^{-12}-10^{-16} s^{-1} are compared in Figs. 2.34-2.35. The quartzite flow strength under the geothermal conditions of the Chongshan shear zone, calculated from our flow law, is substantially higher than the value from the flow law obtained by Hirth et al. (2001) for the Ruby Gap duplex and used by other authors (e.g., Behr & Platt, 2011, 2014; Platt, 2015b), assuming that the water partial pressure equals to lithostatic pressure (Figs. 2.34-2.35). Hirth et al. (2001) analyzed the rheological behavior of quartzite using the flow law:

$$\dot{\varepsilon}=Bf_w^m\sigma^n exp(-Q/RT) \qquad (2.37)$$

where B is the pre-exponential factor, f_w is the water fugacity and m is the water fugacity exponent. They obtained that m=1, n=4, Q=135 kJ/mol, and B=$10^{-11.2}$ MPa^{-n}/s for quartzite. The water fugacity in an experimentally deformed sample can be calculated using the state equation of water (Pitzer & Sterner, 1994) if the partial pressure of water is known. In naturally deformed crustal rocks at different depths from different tectonic environments, however, the partial pressure of water cannot be determined directly in most cases, and is often assumed to be equal to lithostatic pressure due to water saturation (e.g., Lu & Jiang, 2019).

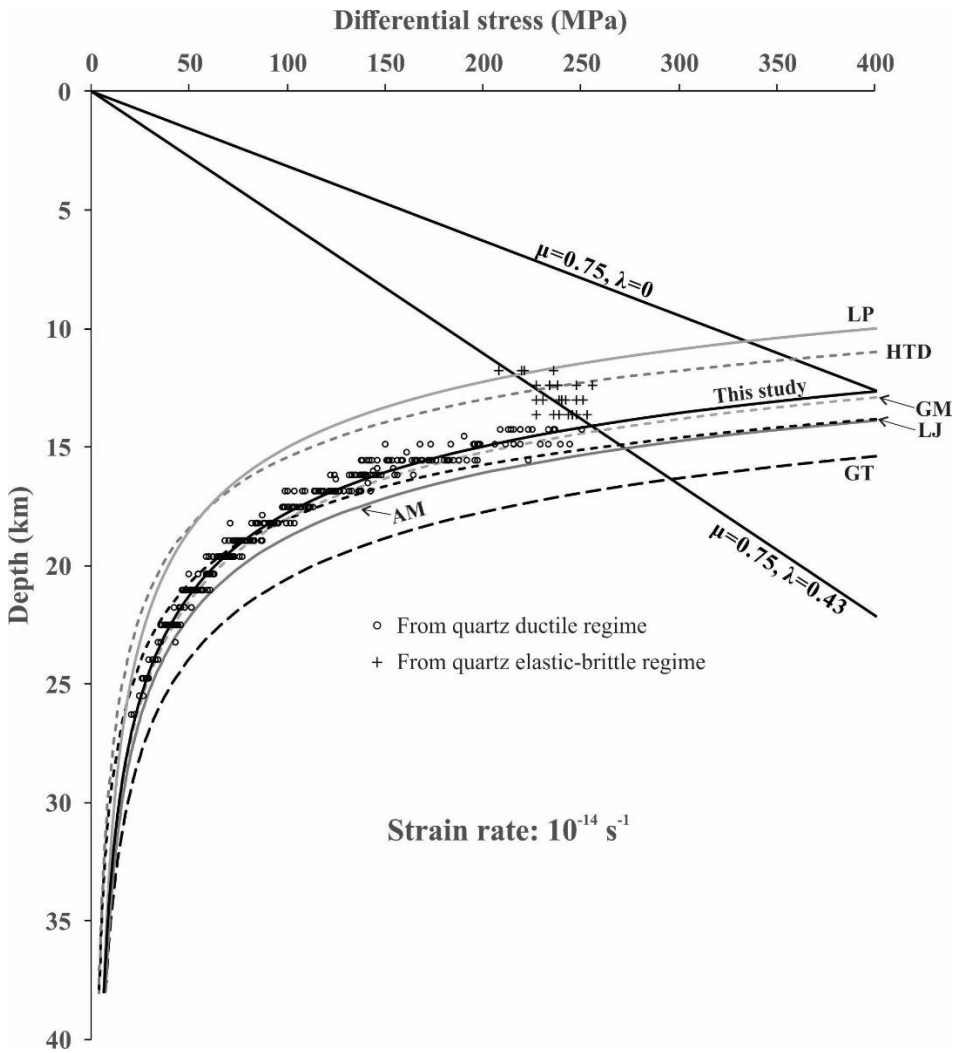

Figure 2.34 Rheological strength (differential stress) of quartzite as a function of depth, estimated for the Chongshan shear zone (west Yunnan, China) at a typical strain rate of 10^{-14} s^{-1}. The frictional strengths (differential stresses) are obtained from multiplying the frictional shear stresses of the Byerlee's law (μ=0.75, λ=0; μ=0.75, λ=0.43) by a factor of $\sqrt{3}$ (Paterson & Olgaard, 2000; Behr & Platt, 2014). Results estimated using the tourmaline microboudinage piezometer for quartzite in ductile and elastic-brittle regimes are represented by open circles and crosses, respectively. Previous flow laws (LP: Luan & Paterson, 1992; GT: Gleason & Tullis, 1995; HTD: Hirth et al., 2001; LJ: Lu & Jiang, 2019) are also shown for comparison. AM and GM represent for the arithmetic and geometric means of the LP and GT flow strengths, respectively.

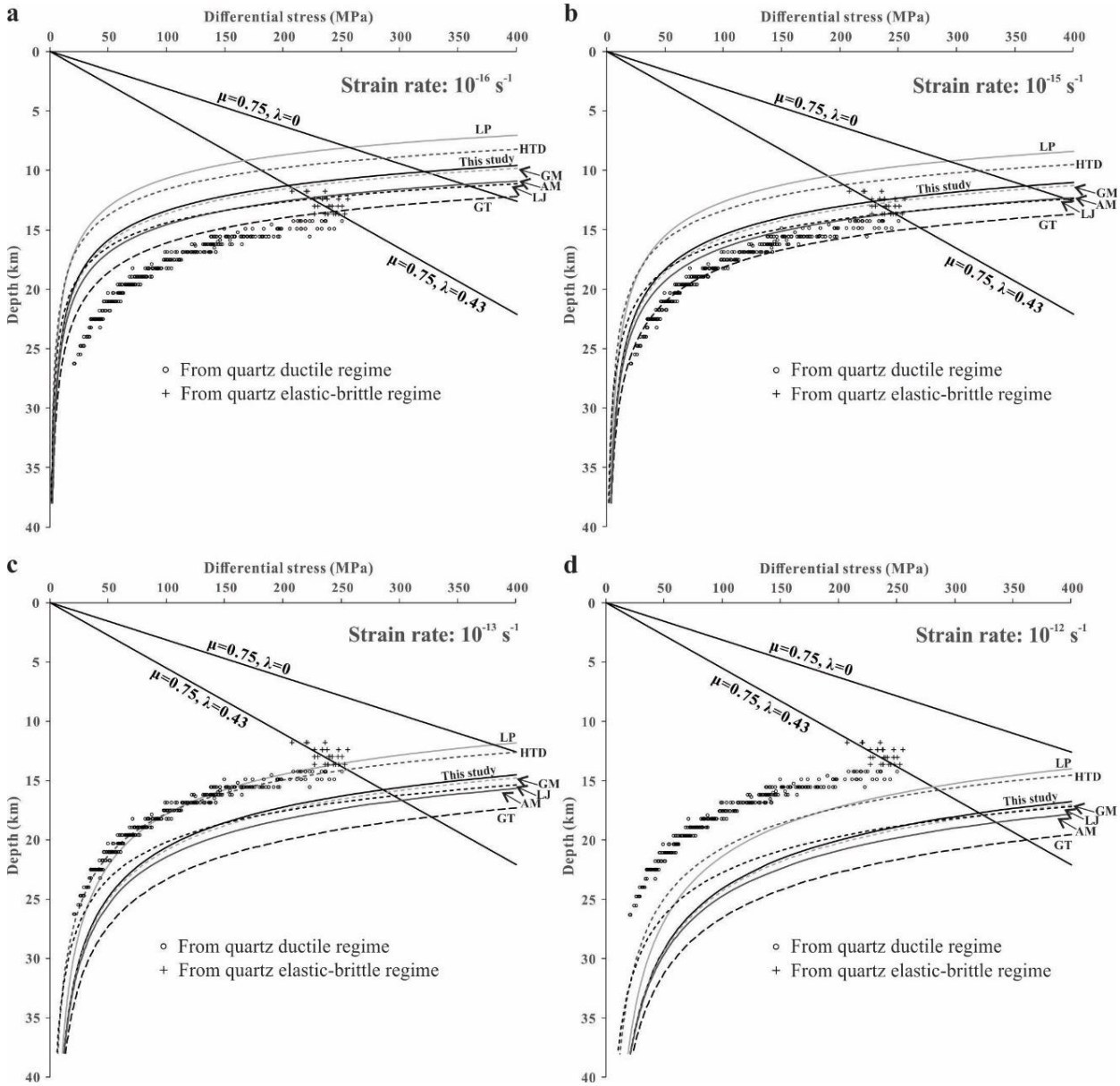

Figure 2.35 Effects of strain rates on the rheological strength-depth profile in the crust dominated by quartz (example of the CS shear zone). Strain rates for (a), (b), (c) and (d) are 10^{-16} s^{-1}, 10^{-15} s^{-1}, 10^{-13} s^{-1}, 10^{-12} s^{-1}, respectively. Results estimated using the tourmaline microboudinage piezometer for quartzite in ductile and elastic-brittle regimes are represented by open circles and crosses, respectively. LP: Luan and Paterson (1992); GT: Gleason and Tullis (1995); HTD: Hirth et al. (2001); LJ: Lu and Jiang (2019). AM and GM represent for the arithmetic and geometric means of the LP and GT flow strengths, respectively.

By taking into account the potential influence of confining pressure (*P*), Lu and Jiang (2019)

used the following flow law to analyze the rheological properties of quartzite:

$$\dot{\varepsilon}=Df_w^m\sigma^n exp(-(Q+P\Delta V)/(RT)) \qquad (2.38)$$

where ΔV is the activation volume, and D is the pre-exponential factor. They suggest that D=6.0×10^{-15} MPa^{-n}/s, m=2.7, n=4, Q=132 kJ/mol, ΔV=35.3 cm^3/mol. In the case where the water partial pressure equals to lithostatic pressure as these authors assumed, this flow law yields a flow strength very close to the arithmetic mean of the bounds defined by Gleason and Tullis (1995) and Luan and Paterson (1992). As shown in Fig. 2.34, the flow law proposed by Lu and Jiang (2019) provides a good agreement with our data only when temperatures are higher than 350 ºC (≥19 km depth).

In Figs. 2.34-2.35, the differential stress in the brittle regime, which is controlled by the strength of faults, is calculated by Byerlee's friction law (Byerlee, 1978; Sibson et al., 1988):

$$\sigma=\beta\rho gz(1-\lambda) \qquad (2.39)$$

where σ is the differential stress (σ_1- σ_3), ρ is the average density of the overlying rocks from the surface to depth z, g is the gravitational acceleration, λ is pore fluid factor (i.e., ratio of pore fluid pressure to overburden pressure), and β is a parameter varying with the type of faulting. β=1.2 for strike-slip faulting assuming μ=0.75 (Byerlee, 1978; Sibson et al., 1988), which is the case in the study region. Our calculated results suggest that λ=0.43 provides an optimal interpretation for the stresses estimated from tourmaline microboudinage paleopiezometer (Figs. 2.34-2.35).

The influence of strain rates is evident on the flow strengths of quartzite in the crust with the same geothermal gradient (Figs. 2.34-2.35). The strain rate of 10^{-14} s^{-1} offers the best prediction to the flow strength estimated from the tourmaline microboudin piezometer (Fig. 2.34). Our paleostrain rate estimates are consistent with the values assessed by Pfiffner and Ramsay (1982), Christensen et al. (1989), Twiss and Moores (2001) and Boutonnet et al. (2013), but are inconsistent with the range between 10^{-12} to 10^{-11} s^{-1} suggested by Lu and Jiang (2019) for naturally deformed rocks. At a strain rate of 10^{-12} s^{-1}, for example, the flow stress should be higher by a factor of 3.16 (i.e., 10$^{1/2}$) than the value appraised at each temperature for the Chongshan shear zone. In addition, the slow strain rates of 10^{-15} - 10^{-16} s^{-1} correspond to neither the measured crustal flow strength profile nor those built by the extrapolation of experimentally determined quartzite flow laws (Luan & Paterson, 1992; Gleason & Tullis, 1995; Hirth et al.,

2001). Thus, the rheological data derived from the tourmaline microboudinage piezometer suggest that 10^{-14} s^{-1} is an optimal estimate for quartz in the granitic mylonites from the Chongshan shear zone (Yunnan, Southwest China). It should be kept in mind that a softer rheology zone in the crust will unavoidably develop a higher strain zone. The rocks which deformed less than the study samples might deform at smaller strain rates than 10^{-14} s^{-1} in the same metamorphic complex (e.g., Platt, 2015b).

As shown in Fig. 2.34, the flow law of Luan and Paterson (1992) offers a quartzite flow strength of only 88.0 MPa at 300 ºC or at the depth of 15.6 km, and predicts that quartzite can deform plastically by dislocation creep at temperatures as low as 242 ºC. On the other hand, the quartzite flow law of Gleason and Tullis (1995) predicts that the critical temperature above which quartz is able to deform plastically by dislocation creep should be higher than 375 ºC. These predictions are in contradictory with abundant geological observations that crystalline plasticity of quartz occurs at ~300 ºC (lower green-schist grade conditions, Snoke & Tullis, 1998; Scholz, 2019). Figures 2.34-2.35 display that the extrapolation of the flow laws determined experimentally by Luan and Paterson (1992) and Gleason and Tullis (1995) predicts too low and too high flow strengths for quartzite deformed at natural strain rates. In contrast, our quartzite flow law derived from the results of combing microstructural observations, thermochronological data, and paleostress and paleostrain rate estimates based on tourmaline microboudins does offer highly reliable constraints on the rheological properties of quartzite in the continental crust.

Seismicity is essentially confined to brittle levels in the lithosphere, so the distribution of focal depths is closely linked with rock rheological properties in the crust (Ranalli & Murphy, 1987; Chen et al., 2012; Scholz, 2019). Figure 2.36 is a compilation of the focal depths of earthquakes with magnitudes larger than 2.7 in the study area (i.e., Lincang, Puer and Sishuangbana cities) during the last 40 years. Almost all seismicity is confined to the upper crust of depths between 5 and 15 km, but occur rarely at depths larger than ~15 km. This can be readily interpreted by the seismic-aseismic transition or the brittle-ductile transition at the depth of ~15 km, which is predicted by the intersection of the quartzite flow law and Byerlee's friction law (Fig. 2.34). The depth of ~15 km corresponds to a temperature of ~300 ºC at which the onset of quartz plasticity occurs (Fig. 2.30a, Snoke & Tullis, 1998; Behr & Platt, 2011; Scholz, 2019).

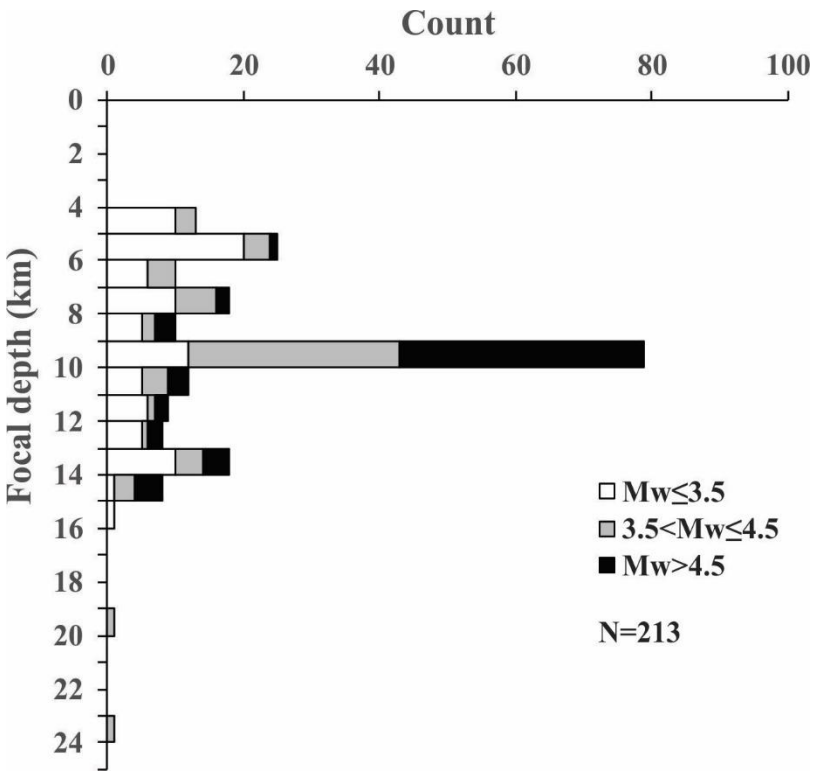

Figure 2.36 Depth distribution of seismicity (Mw≥2.7) in the Chongshan shear zone (west Yunnan, China) during a period of 40 years (1978-2018). Mw: Moment magnitude of earthquake; N: number of earthquakes.

Magnetotelluric imaging across the study area reveals a low electrical resistivity (<10 Ωm) zone at depths between 15 and 38 km (Bai et al., 2010; Tang et al., 2012; Li et al., 2014; Yu et al., 2017). High resistivities (>100-1000 Ωm) occur above and below the low resistivity zone. Possible causes for the elevated crustal conductivities include the presence of aqueous fluids, partial melt, and graphite (e.g., Mareschal et al., 1995). Whatever the dominant mechanism of the increase in electrical conductivity, the low resistivity zone is an indication of rock ductility because plasticity-induced foliation, stretching lineation and compositional layering enhance considerably the continuity and interconnectivity of aqueous fluids, partial melt or graphite. Thus, the available data of the deep electrical resistivity structure also suggest that the crust between the depths of 15-38 km beneath the study region is indeed in the ductile regime.

2.10 Conclusions

The present study of tourmaline microboudins from the Gaoligong and Chongshan shear zones (Yunnan, China) yields the following principal conclusions:

1. The tensile fracturing successively fragmented the columnar tourmaline crystals embedded in the flowing matrix of felsic materials into two segments of unequal length. Thus, the application of the microboudin piezometers established previously on the mid-point fracturing predicted by the conventional shear-lag model, which assumes perfectly welded interfaces, must be questionable. In addition, the shear-lag model cannot explain the linear correlation between fracture spacing and fiber mineral width. The previous estimates of far-field differential stresses obtained from the no interfacial slip shear-lag model should be doubtful too.
2. The new, simple microboudin piezometer has been developed: $\tau=0.25C/(L/W)$, where τ is the shear flow stress of the ductile matrix, C is the tensile fracture strength of the columnar mineral, and L/W is the length/width ratio of the microboudins formed by near-end fracturing. It provides a straightforward method of estimating the magnitude of shear flow stresses responsible for ductile deformation of natural rocks. This piezometer is easiest to apply because it does not require the use of TEM (dislocation density), SEM-EBSD or the identification of deformation mechanism (e.g., dislocation creep, diffusion creep, subgrain rotation recrystallization, grain boundary migration recrystallization). Unlike the recrystallized grainsize piezometer, which can be applied into only a steady state regime of dislocation creep, the microboudin piezometer can be used to calibrate the stress magnitudes in any ductile regimes with whatever prevailing deformation mechanism (dislocation creep, diffusion creep, hardening or weakening).
3. The study samples from the Gaoligong shear zone (Yunnan, China) display that the earlier formed microboudins had consistently a larger mean length/width ratio than the later formed ones, indicating that the rocks recorded a geological history of continuous hardening prior to the cessation of quartz plasticity. The rheological hardening was most likely caused by tectonic exhumation and cooling up progressively to the brittle-ductile transition where temperature was about 300 ºC. For

the felsic gneisses from the Gaoligong shear zone, the shear flow stresses is estimated to be in the range of 21 MPa to 61 MPa when taking the tensile strength of tourmaline as 145 MPa.

4. Whether laboratory-derived flow laws can be reliably extrapolated to crustal rocks deformed at natural strain rates remains debated (e.g., Ranalli, 2003; Burov, 2003). Such an extrapolation need be constrained by independent determination of natural strain rates, flow stresses and their correlations with temperature and corresponding depth for in-situ or exhumed crustal rocks. A valuable method in which the newly developed microboudinage paleopiezometry has been combined with microstructural observations and independent estimates of deformation temperature, accurate ages of zircon U-Pb, monazite U-Th/Pb, muscovite and biotite $^{40}Ar/^{39}Ar$, and zircon and apatite (U-Th)/He systematics, and regional geophysical data (e.g., surface heat flow, focal depths, seismic velocity-depth profile, crustal V_p/V_s ratios, and electrical resistivity structure) have been applied to determine the strain rate ($\dot{\varepsilon}$), flow stress (σ) and their correlations with temperature and corresponding depth for the polycrystalline quartz matrix in which columnar tourmaline grains have been fractured into microboudins.
5. The application of the method to the felsic mylonites and gneisses from the Chongshan shear zone, Yunnan, Southwest China, yields a flow law of $\dot{\varepsilon}=A\sigma^n exp(-Q/RT)$ with n=4, Q=184 kJ/mol and A=7.180×10^{-7} MPa^{-n}s^{-1} for the natural quartz deformed plastically below the brittle-ductile transition. The flow stresses described by this flow law do not coincide with those values given by either Luan and Paterson (1992) or Gleason and Tullis (1995), but lie between the extrapolations of these experimentally derived flow laws. The naturally derived flow stress-temperature profile is very close to the geometrical mean of the bounds defined by Luan and Paterson (1992) and Gleason and Tullis (1995). A strain rate of 10^{-14} s^{-1} is an optimal estimate for the study rocks, whereas the high strain rates (10^{-12}-10^{-11} s^{-1}) assumed by previous workers (e.g., Lu & Jiang, 2019) will result in a crustal rheology that is far too strong and thus is impossible at least for the study region. The results also offers a reliable interpretation for the distribution of focal depths and electrical resistivity structure in the Chongshan shear zone, which are actually controlled by the brittle-

ductile transition and the peak stress at a depth of ~15 km below which the onset of quartz plasticity occurs.

6. As tourmaline microboudins are ubiquitous in deformed crustal rocks such as granitic and pegmatitic mylonites and metasediments, both flow stress and strain rate can now be estimated from fracture and separation history of tourmaline with an unprecedented accuracy although uncertainties related to the tensile strength of tourmaline as a function of temperature and pressure remain to be resolved. The method presented in this chapter provides natural constraints on long timescale rheological properties of the felsic crust in west Yunnan (China), which may be used widely in other orogenic belts.

CHAPTER 3 MICROBOUDINAGE PALEOPIEZOMETER OF FELDSPAR AND ITS APPLICATIONS

3.1 Introduction

As discussed in Chapter 2, tensile fractures and resultant microboudins of brittle, elongate minerals [e.g., tourmaline, amphibole, epidote (e.g., piemontite), pyroxene, garnet, glaucophane, andalusite, apatite, quartz and chromite, Fig. 3.1) are often observed in a ductile granular matrix of deformed crustal and mantle rocks (e.g., Allison & Latour, 1977; Ji & Zhao, 1993; Holtzman, 2000; Masuda et al., 2003; Fazio et al., 2020; Li & Ji, 2020). The columnar or elongate minerals are generally aligned parallel to the overall foliation and stretching lineation of the rock, whereas the tensile fractures are commonly normal to the long axes of the crystals, that is, the stretching lineation. The plastically flowing matrix is usually recrystallized quartz or fine-grained quartz-mica aggregate in deformed felsic rocks, olivine-pyroxene or serpentine aggregate in deformed ultramafic rocks. The boudinage structure has been used to estimate finite strains (e.g., Ferguson, 1981; Ferguson & Lloyd, 1982; Lloyd & Ferguson, 1981, 1989; Lloyd & Condliffe, 2003), strain rates (Li et al., 2020), paleostresses (e.g., Masuda et al., 1995, 2003; Holtzman, 2000; Li & Ji, 2020; Li et al., 2020) and exhumation history (e.g., Ji et al., 1997).

In deformed crustal rocks such as granitic mylonites, optical microstructures of ductile quartz and mica have received much more attention than those of brittle feldspar (e.g., Zhao et al., 1997; Gueydan et al., 2005; Jeřábek et al., 2007; Behr & Platt, 2011; Fazio et al., 2017). In these research papers, most descriptions about brittle deformation microstructures of feldspar are shear fractures and relative displacements between broken feldspar fragments (e.g., bookshelf structures) as an indicator of shear sense (e.g., Simpson & Schmid, 1983; Andrews, 1984; Hanmer & Passchier, 1991; Hippertt, 1993; Duebendorfer & Christensen, 1998; Passchier & Trouw, 2005). The microfaults, which can be either synthetic or antithetic with respect to the overall shear sense, developed along fractures aligned at low to moderate angles to the foliation and stretching lineation (e.g., Mandal et al., 2001; Samanta et al., 2002). The fragments of broken feldspar have undergone offsetting and occasionally rigid rotation.

In this chapter, we will characterize the deformation microstructures of granitic rocks from the Red River, Chongshan, and Gaoligong shear zones, Yunnan, Southwest China, in which quartz

and mica deformed plastically while sodic plagioclase (albite) and particularly K-feldspar deformed by multiple cycles of extensional fracturing with only subordinate dislocation glide. The application of the modified microboudinage piezometer (see Chapter 2) to feldspar permits us to assess the magnitude of paleodifferential stresses during the activity of crustal shear zones.

3.2 Microboudin piezometer for feldspar

Previous microboudinage piezometers of tourmaline (See Chapter 2), which were derived on an assumption that this type of columnar minerals has a cylindrical shape, cannot be directly applied to the feldspar porphyroclasts which display ellipsoidal shapes. A feldspar microboudin can be approximately considered as a segment cut along two separated, parallel planes normal to the long axis of the ellipsoid (Fig. 3.1a). The mechanical analysis of such a system requires calculating both the base and lateral surface areas of each truncated ellipsoidal segment. However, such calculations, which are complex [see Tee (2005) for the mathematical treatment], can be performed only by numerical integration for each specific case with given values of a, b, c, h_1 and h_2 (Fig. 3.1). Thus, there are no simple analytical expressions (Tee, 2005). For simplicity, in the following (Fig. 3.2), we will treat each of the feldspar microboudin as a circular-truncated-conical fiber of length (L) and diameters of the smaller end (D_1) and the larger end (D_2). The fiber, whose symmetry axis is parallel to the extension direction (X), is embedded in a weaker solid matrix (e.g., quartz or quartz-mica aggregate). The presence of rheological contrast between strong feldspar and its surrounding weak matrix redistributes the stresses and strains within the composite system, and results in transferring load from the weak matrix to the strong feldspar (Ji & Zhao, 1993; Zhao & Ji, 1997).

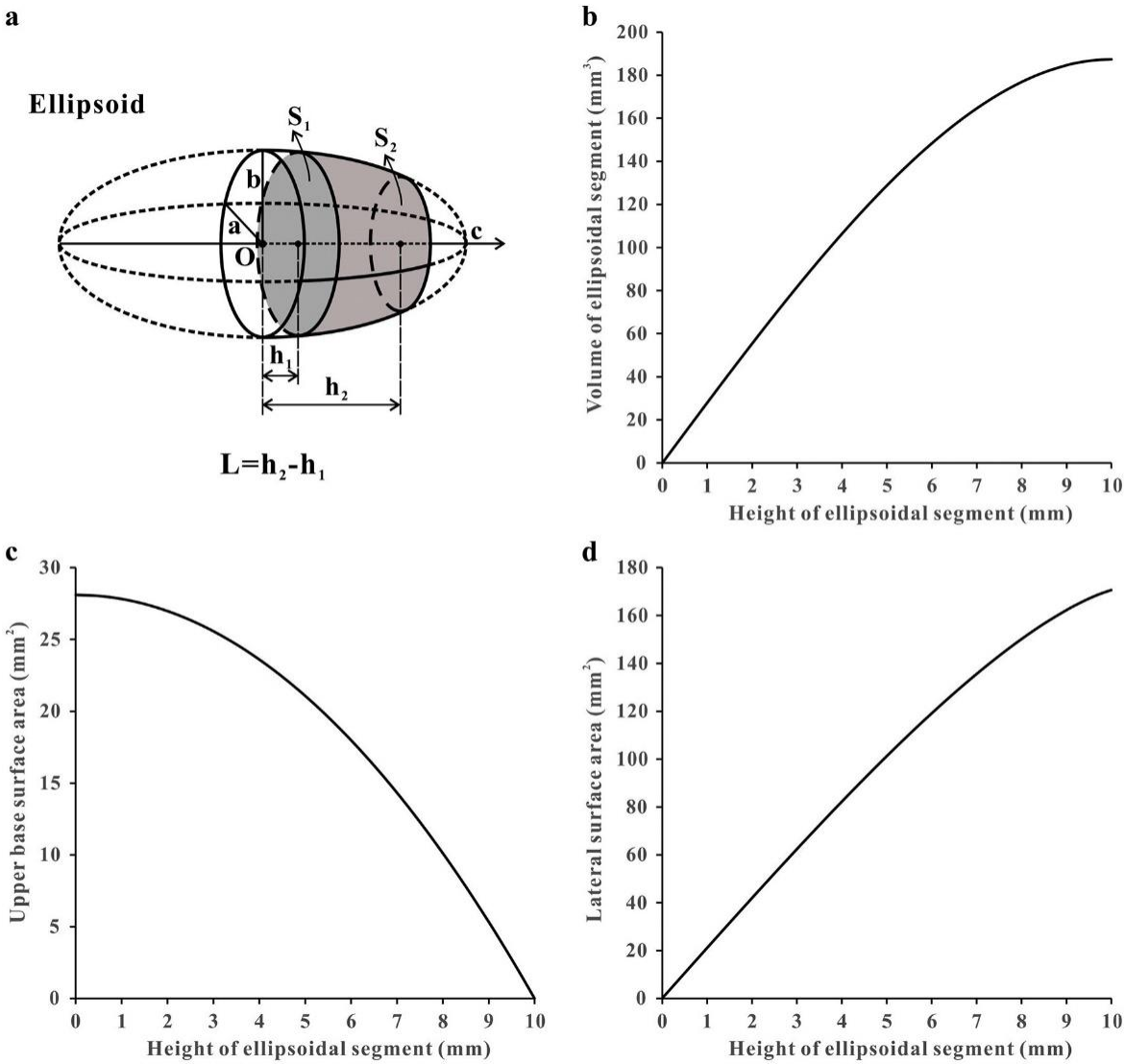

Figure 3.1 Schematic diagram to illustrate an ellipsoidal segment (a) and its volume (b), base surface area (c) and lateral surface area (d) as a function of h_2. The numerical calculations were based on the data (a=2 mm, c=10 mm, b=$2\sqrt{5}$ mm, h_1=0 mm). The mathematic equations were given in Tee (2005).

A shear stress occurs at the feldspar-matrix interface because the matrix deforms faster than the feldspar porphyroclast. A tensile fracture forms when the tensile effective stress exceeds or equals the material tensile strength. The mechanic equilibrium of such a system can be described by the following equation:

$$S_L \tau \cos\theta = \pi \left(\frac{D_2}{2}\right)^2 C \qquad (3.1)$$

where τ is the interfacial shear stress between the feldspar and the matrix, C is the tensile strength of the feldspar, θ is the angle between the generator and the symmetry axis (Fig. 3.2), D_2 is the diameter of the larger end, and S_L is the lateral surface area of the segment. The flow stress of the matrix material is equal to τ if no slip occurs on the phase interface.

$$S_L = \pi L \left(\frac{D_2+D_1}{2}\right) \qquad (3.2)$$

and

$$\cos\theta = \frac{L}{[L^2+0.25(D_2-D_1)^2]^{0.5}} \qquad (3.3)$$

Substituting Eqs. (3.2) and (3.3) into Eq. (3.1), we have

$$\tau = \frac{D_2^2}{2L(D_2+D_1)} C \qquad (3.4)$$

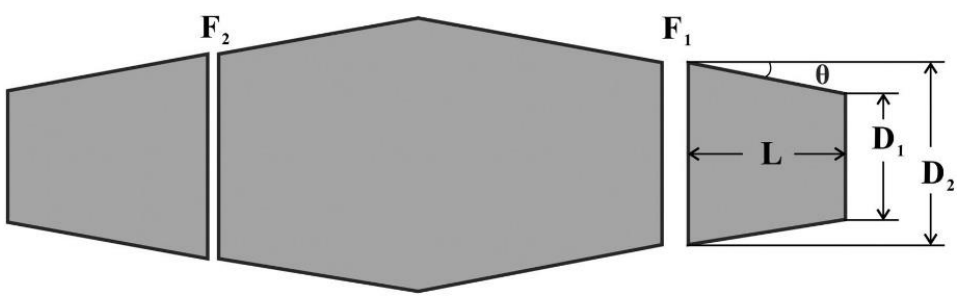

Figure 3.2 Schematic representation for the longitudinal section of a fractured porphyroclast, cut parallel to the XZ plane. Larger and smaller gaps occur at the sites of earlier (F_1) and later (F_2) fractures, respectively. The length (L), diameters of the smaller and larger ends (D_1 and D_2), and the angle between the generator and the symmetry axis (θ) are indicated for the microboudin resulted from fracture F_1.

Then, the differential stress ($\sigma=\sigma_1-\sigma_3$) can be obtained by multiplying the shear stress (τ) from Eq. (3.4) by $\sqrt{3}$ (Paterson & Olgaard, 2000; Rybacki & Dresen, 2004; Behr & Platt, 2014).

$$\sigma = \frac{\sqrt{3}\, D_2^2}{2L(D_2+D_1)} C \qquad (3.5)$$

For a cylindrical prism such as elongated tourmaline, $D_1=D_2=D$, Eq. (3.5) becomes

$$\sigma = \frac{\sqrt{3}\,\mathrm{D}}{4L} C \qquad (3.6)$$

Equation (3.6) is exactly the same as that used in Chapter 2 as the tourmaline boudinage piezometer.

The tensile strength of various feldspars including K-feldspar and plagioclase have not been experimentally measured at controlled temperatures and confining pressures. As pointed by Etheridge (1983), tensile strength of geological materials such as minerals is among the most difficult mechanical properties to measure in great part due to technical problems in the laboratory. The measurements are extremely sensitive to any small variations in the conditions of the test samples (e.g., degree of crystal quality, microcracks, inclusions, cleavage orientation, and surface roughness) and in the environmental parameters (e.g., loading rates, confining pressure, and temperature). The tensile strengths of mineral single crystals can be significantly higher than those of granular polymineralic rocks because the presence of microcracks and altered grain boundaries makes the rocks incapable to support high tensile effective stresses.

As discussed in Chapter 2, a perfect crystal has an ideal tensile strength of about $E/10$, where E is Young's modulus (e.g., Idrissi et al., 2016). E=68.87 and 73.07 GPa for K-feldspar and albite (An9), respectively (Fig. 3.3), which yield ideal tensile strengths of ~6.9 and ~7.3 GPa for K-feldspar and albite, respectively. As documented by Li et al. (2020), the actual tensile strength of an engineering material is statistically only about 0.2324% of its Young's modulus (Fig. 3.3a). For natural crystals (e.g., tourmaline from the GLG and CS shear zones), however, their tensile strengths are estimated to be only about 0.072% of their Young's moduli (Kimura et al., 2010; Li et al., 2020). The application of the same inference (Fig. 3.3b) gives estimated C values of 50-53 MPa for K-feldspar and sodic plagioclase in the granitic mylonites although further experimental measurements under well-controlled temperature and pressure conditions are exigently needed.

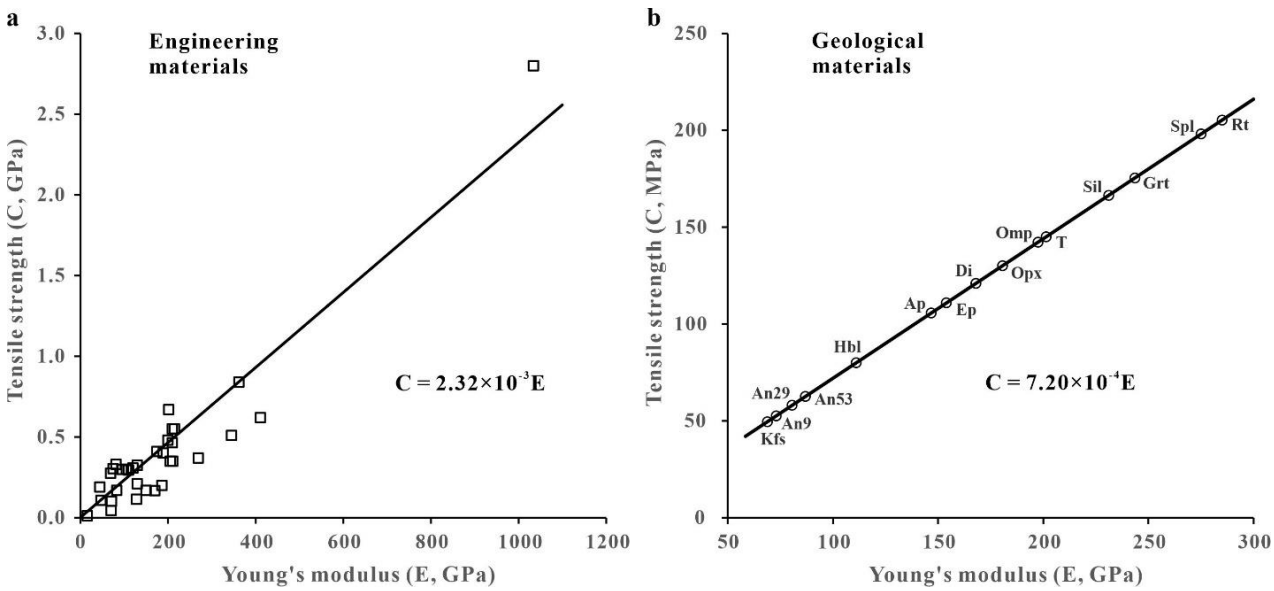

Figure 3.3 Tensile strength (*C*) versus Young's modulus (*E*) for engineering and geological materials. $C = 2.32 \times 10^{-3}$*E for the engineering materials (a, squares, measured, Ashby, 2016; Howatson, 2012, Table 2.1 and Table 3.1), and $C = 7.20\times10^{-4}$*E for natural minerals (b, circles, predicted). Abbreviations: An, anorthite; Ap, apatite; Di, diopside; Ep, epidote; Grt, garnet; Hbl, hornblende; Kfs, K-feldspar; Omp, omphacite; Opx, orthopyroxene; Rt, rutile; Sil, sillimanite; Spl, spinel; T, tourmaline.

Table 3.1 Young's moduli and estimated tensile strength of 15 common minerals

Mineral	Young's modulus (GPa) E (GPa)*	Estimated tensile strength C (MPa)
K-feldspar	69	50
Plagioclase (An9)	73	53
Plagioclase (An29)	81	58
Plagioclase (An53)	87	63
Hornblende	111	80
Apatite	147	106
Epidote	154	111
Diopside	168	121
Orthopyroxene	181	130
Omphacite	198	142
Tourmaline	201	145
Sillimanite	231	166
Garnet	244	175
Spinel	275	198
Rutile	285	205

* Calculated from the data in Handbook of Seismic Properties of Minerals, Rocks and Ores (Ji et al., 2002)

With the estimated tensile strength of feldspar, we can then apply the piezometer to estimate the shear flow stress recorded by feldspar microboudins in felsic mylonite samples from the Gaoligong, Chongshan and Red River shear zones in Yunnan, Southwest China.

3.3 Geological setting

The study samples are granitic mylonites collected from three important crustal-scale, strike-slip shear zones in west Yunnan (China): 31 from the Red River (RR) shear zone, 6 from the Chongshan (CS) shear zone, and 19 from the Gaoligong (GLG) shear zone (Fig. 3.4). The GPS coordinates (longitude, latitude and altitude) of each sampling locality are listed in Table 3.1. These shear zones, which lie to the southeast of the eastern Himalayan syntaxis, are believed to have played an important role in the southeastward lateral extrusion of the Indochina composite block and even the formation of the South China Sea in response to the Indo-Asian continental collision (e.g., Tapponnier et al., 1986; 1990; Briais et al., 1993; Leloup et al., 1995). The geodynamic implications of these shear zones in the region has been greatly debated in the literature (e.g., Davy & Cobbold, 1988; Dewey et al., 1989; England & Molnar, 1997; Searle, 2006; Searle et al., 2010; Burchfiel et al., 2008). The tectonic evolution history of the Gaoligong (GLG) and Chongshan (CS) shear zones has been introduced in Chapter 2. Therefore, only the Red River (RR) shear zone will be introduced in detail in this chapter.

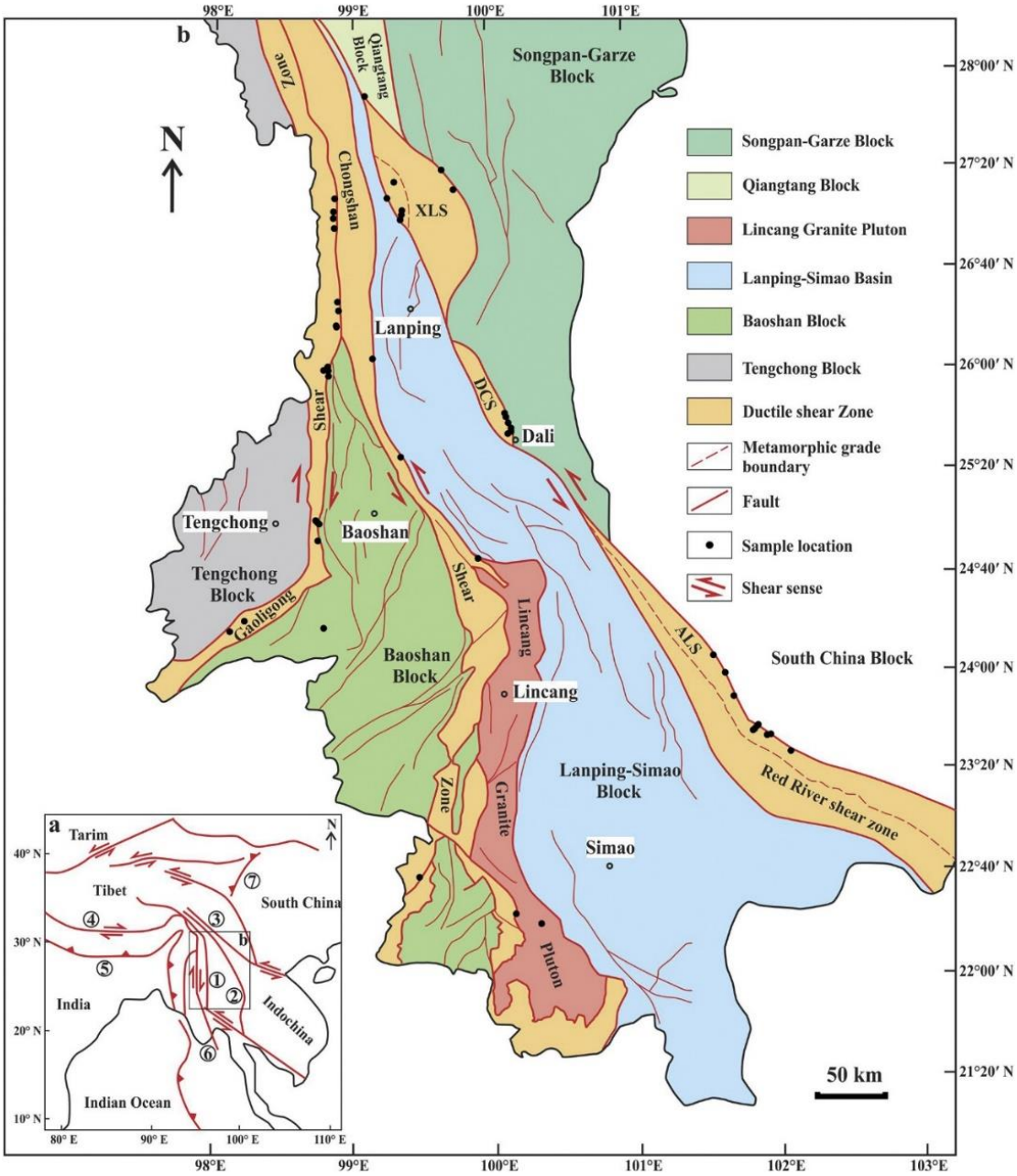

Figure 3.4 (a) Simplified geological map of the southeastern Tibetan plateau and the surrounding regions. Red lines represent the main shear or fault zones: (1) Gaoligong shear zone; (2) Chongshan shear zone; (3) Ailao Shan-Red River shear zone; (4) Indus-Tsangpo suture zone; (5) Main boundary thrust; (6) Sagaing Fault; and (7) Longmen Shan fault; Box refers to Figure 3.2b. (b) Sample locations (black dots) within the Gaoligong, Chongshan and Red River shear zones, Yunnan, China. Abbreviations: ALS: Ailao Shan; DCS: Diancang Shan; XLS: Xuelong Shan. Modified from Zhang et al. (2012a and b).

Table 3.2 Localities of granitic mylonite samples from the Gaoligong, Chongshann and Red River shear zones, Yunnan, China

Sample No.	Locality	Latitude	Longitude	Altitude (m)
CS10	Chongshan	25.41218	99.34018	1309
CS154	Chongshan	22.66491	99.47199	1262
CS45	Chongshan	24.77905	99.86816	1230
LS4	Chongshan	22.34528	100.14194	1453
LS6	Chongshan	22.28778	100.28611	1202
YN1372	Chongshan	26.04233	99.12575	1459
GLG104	Gaoligong	27.06656	98.87331	1226
GLG11	Gaoligong	24.93261	98.76061	2307
GLG13	Gaoligong	24.95292	98.74403	2303
GLG131	Gaoligong	27.02264	98.86661	1183
GLG136	Gaoligong	26.43492	98.89211	988
GLG14	Gaoligong	24.9795	98.7289	1995
GLG203	Gaoligong	26.9579	98.8676	1174
GLG23	Gaoligong	24.84556	98.74061	1933
GLG251	Gaoligong	27.12492	98.881	1240
GLG317	Gaoligong	24.24219	98.11081	875
GLG325	Gaoligong	24.31097	98.21086	1331
GLG42	Gaoligong	24.30469	98.79625	1772
GLG75	Gaoligong	25.98114	98.80683	2068
GLG77	Gaoligong	25.97167	98.79464	2007
GLG79	Gaoligong	25.97303	98.78808	1998
GLG86	Gaoligong	25.94139	98.81633	1018
GLG92	Gaoligong	26.26556	98.87122	988
GLG93	Gaoligong	26.26642	98.86625	683
YN1384	Gaoligong	26.37186	98.89172	1001
AY21	Ailaoshan	23.5725	101.94361	824
AY22	Ailaoshan	23.55767	101.91771	691
AY24	Ailaoshan	23.84111	101.65361	2045
AY25	Ailaoshan	23.58667	101.78278	2045
GR35	Ailaoshan	23.44222	102.05278	1837
GR4	Ailaoshan	24.10439	101.51225	945
GR8	Ailaoshan	24.00806	101.61722	722
R82	Ailaoshan	23.6313	101.82383	975
R84	Ailaoshan	23.62546	101.81741	1372
R85	Ailaoshan	23.5968	101.79409	1057

Table 3.2 Localities of granitic mylonite samples from the Gaoligong, Chongshann and Red River shear zones, Yunnan, China (continued)

Sample No.	Locality	Latitude	Longitude	Altitude (m)
D10	Diancangshan	25.57214	100.14261	2017
D13	Diancangshan	25.57378	100.17192	1936
D19	Diancangshan	25.564	100.13211	2229
D3	Diancangshan	25.68431	100.10139	2311
D30	Diancangshan	25.57469	100.08414	2275
D4	Diancangshan	25.70086	100.103	2472
D9	Diancangshan	25.69622	100.10925	3030
GR35	Ailaoshan	23.44222	102.05278	1837
GR4	Ailaoshan	24.10439	101.51225	945
GR8	Ailaoshan	24.00806	101.61722	722
R82	Ailaoshan	23.6313	101.82383	975
R84	Ailaoshan	23.62546	101.81741	1372
R85	Ailaoshan	23.5968	101.79409	1057
SH17	Shigu	27.28528	99.63111	1934
SH9	Shigu	27.15806	99.76083	1984
YN1318	Xuelongshan	27.24567	99.27008	2519
YN1327	Xuelongshan	27.00083	99.35653	2319
YN1328	Xuelongshan	26.99106	99.35206	2321
YN1329	Xuelongshan	26.97758	99.34322	2080
YN1343	Xuelongshan	27.80189	99.03914	1988
YN1361	Xuelongshan	27.09408	99.25064	2798

The Red River (RR) shear zone, which is the boundary fault separating the South China Block to the northeast and the Indochina Block to the southwest, is marked by 4 narrow (10-40 km wide) metamorphic ranges: Xuelongshan (XLS), Diancangshan (DCS), Ailaoshan (ALS) in China (Fig. 3.4) and Day Nui Con Voi (DNCV) in Vietnam. The metamorphic rocks (e.g., ortho- and paragneisses, schists, mylonites, marbles and amphibolites) are characterized by subvertical foliation and subhorizontal stretching lineation, and left-lateral shear indicators such as asymmetrical folds and boudins, rolling porphyroclasts, S-C structure, mica fishes and quartz fabrics (e.g., Wu et al., 1989; Tapponnier et al., 1990; Leloup et al., 1995; Cao et al., 2017). Zircon U/Pb ages of 216 samples range from 37.0 Ma to 20.5 Ma with a mean value of 28.64 Ma. Monazite (U-Th)/Pb ages from 89 samples range from 34.3 Ma to 18.9 Ma with an average value of 26.45 Ma, whereas the ages of xenotime and titanite from 44 samples range from 33.3 Ma to 22.0 Ma with a mean of 25.80 Ma. These thermochronological data (≥650 ºC) indicate that partial

melting (leucocratic dykes) associated with high temperature metamorphism occurred synkinematically during the period of 37.0-20.5 Ma in the RR shear zone (e.g., Schärer et al., 1990; Zhang & Schärer, 1999; Sassier et al., 2009; Tang et al., 2013; Zhang et al., 2014). $^{40}Ar/^{39}Ar$ age data of amphibole from 39 samples, muscovite from 20 samples, biotite from 67 samples and K-feldspar from 64 samples, apatite fission track ages from 24 samples and apatite (U-Th)/He ages from 32 samples yield a mean cooling rate of 39.27 ºC/Ma for the RR shear zone although the cooling and exhumation of the metamorphic rocks started at different ages from 35 Ma to 20 Ma for different parts of the shear zone (e.g., Harrison et al., 1996; Gilley et al., 2003; Cao et al., 2011; Chen et al., 2015). The closure temperatures of zircon U/Pb, monazite U-Th/Pb, xenotime and titanite U/Pb, amphibole, biotite and muscovite $^{40}Ar/^{39}Ar$, apatite fission track and (U-Th)/He) systems are ≥750, 700±50, 650±50, 500±50, 400±50, 300±40, 110±25, and 65±5 ºC, respectively (Harrison et al., 1985; Hames & Bowring, 1994; Parrish, 2001; Reiners, 2005; Flowers et al., 2009; Guenthner et al., 2013). Left-lateral strike-slip deformation with which dip-slip components (transpressional or transtentional) were associated, is coeval with cooling and exhumation of the metamorphic rocks. The exhumation mechanisms were discussed in Leloup et al. (1995), Viola and Anczkiewicz (2008) and Wang et al., (2018, 2020).

3.4 Optical microstructures

The microstructural observations were performed, under an optical microscope, on the petrographic thin sections cut parallel to the XZ plane of each sample (X is parallel to the stretching lineation, and Z is normal to the foliation). Tensile fractures are confined to each single crystal of feldspar, and do not extend into the matrix of fine-grained quartz, mica or quartz-mica aggregate (Figs. 3.5-3.7). This suggests that the matrix was plastically flowing while the feldspar porphyroclasts deformed essentially by brittle fractures. In each fragmented feldspar grain, the fractures are roughly parallel to each other, and aligned approximately perpendicular to the long axis of the porphyroclast (Figs. 3.5-3.8). Little lateral displacement along the fracture walls (i.e., parallel pull-aparts) has been discerned, indicating that the fractures were tensile (Mode I) and no rotation of the segments separated by the fracture.

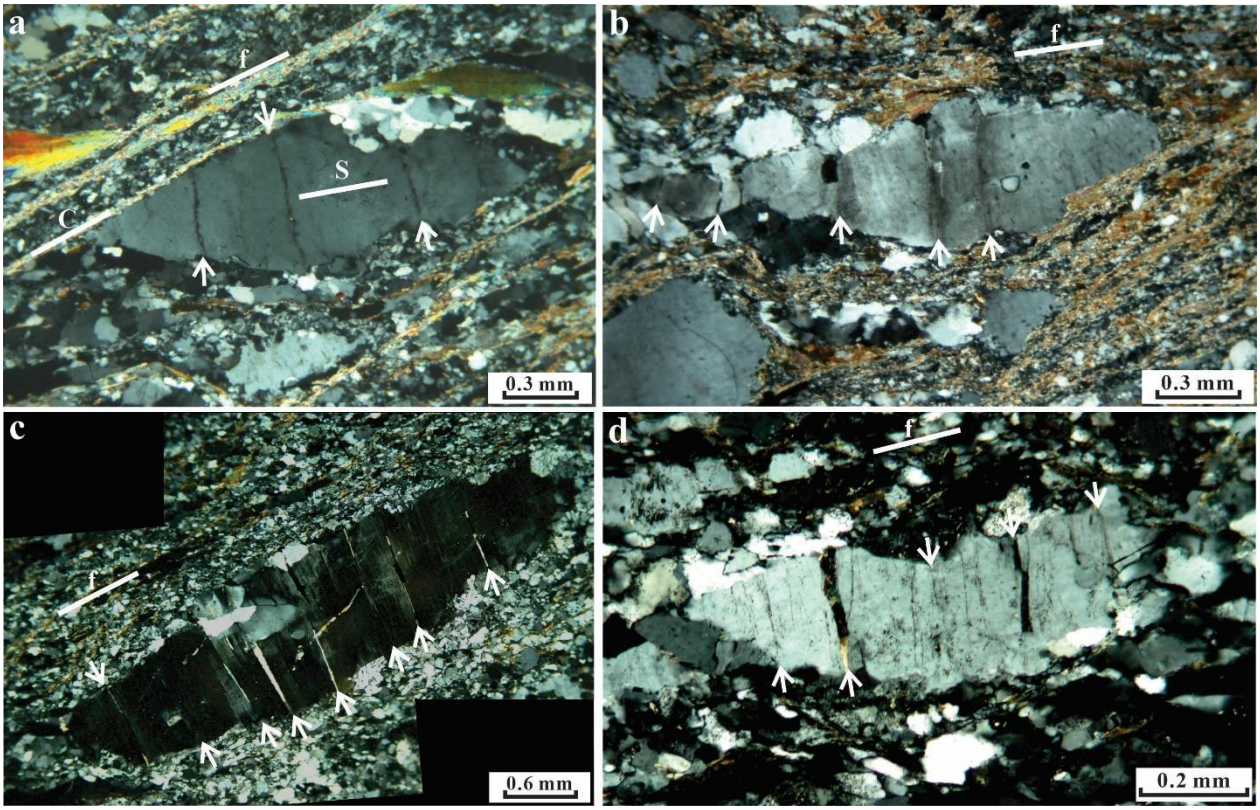

Figure 3.5 Extensional fractures and resultant microboudinage of feldspar porphyroclasts in fine-grained muscovite-quartz aggregates from granitic mylonites of the Gaoligong shear zone (Yunnan, China). (a), (b), (c) and (d) from samples GLG11A, GLG 317, GLG14B and GLG14A, respectively. Abbreviation: f, foliation; S, S plane; C, C plane.

These pull-apart fractures and subsequent separation of broken segments produced microboudinage structures of feldspar. The fracture walls are generally well preserved and have not been obscured by retrograde reaction or recrystallization. The feldspar grains do not show pinch and swell structures, remarkably plastic deformation or extensive dynamic recrystallization (Figs. 3.5-3.7). Optical, irregular, patchy extinction was observed adjacent to fractures and grain boundaries. These microstructural features suggest that no large crystalline plasticity has occurred in the feldspar porphyroclasts immediately before and after fracturing because effective dislocation climb and recovery are difficult due to sluggish diffusion at relatively low temperatures (e.g., Ji & Mainprice, 1987; Tullis & Yund, 1987; Tullis, 2002). The tensile fractures occur generally along cleavage planes (010) or (001) of feldspar although such coincidence does not always appear in each grain. Most of the tensile fractures initiated at grain boundaries and propagated inwards presenting “V” shape and implying (1) the stress transferred

from the surrounding ductile matrix, and/or (2) the surface flaws favor the initiation of cracks. The patchy undulatory extinction adjacent to fractures or grain boundaries of some feldspar porphyroclasts is interpreted to be resulted from the presence of microscopic, densely distributed, intragranular microcracks. The above microstructural features suggest that the feldspar boudinage formed at temperatures of 300-450 °C where feldspar and quartz deformed in brittle and ductile manners, respectively (e.g., Snoke & Tullis, 1998; Tullis, 2002; Scholz, 2019). This conclusion is consistent with petrologic studies showing that main deformation of these shear zones in Yunnan, which was coeval with cooling and exhumation, took place under greenschist facies conditions (e.g., Leloup et al., 1995, 2001; Zhang et al., 2010; 2012b, 2014; Searle et al., 2010; Cao et al., 2011; 2017; Wang et al., 2020).

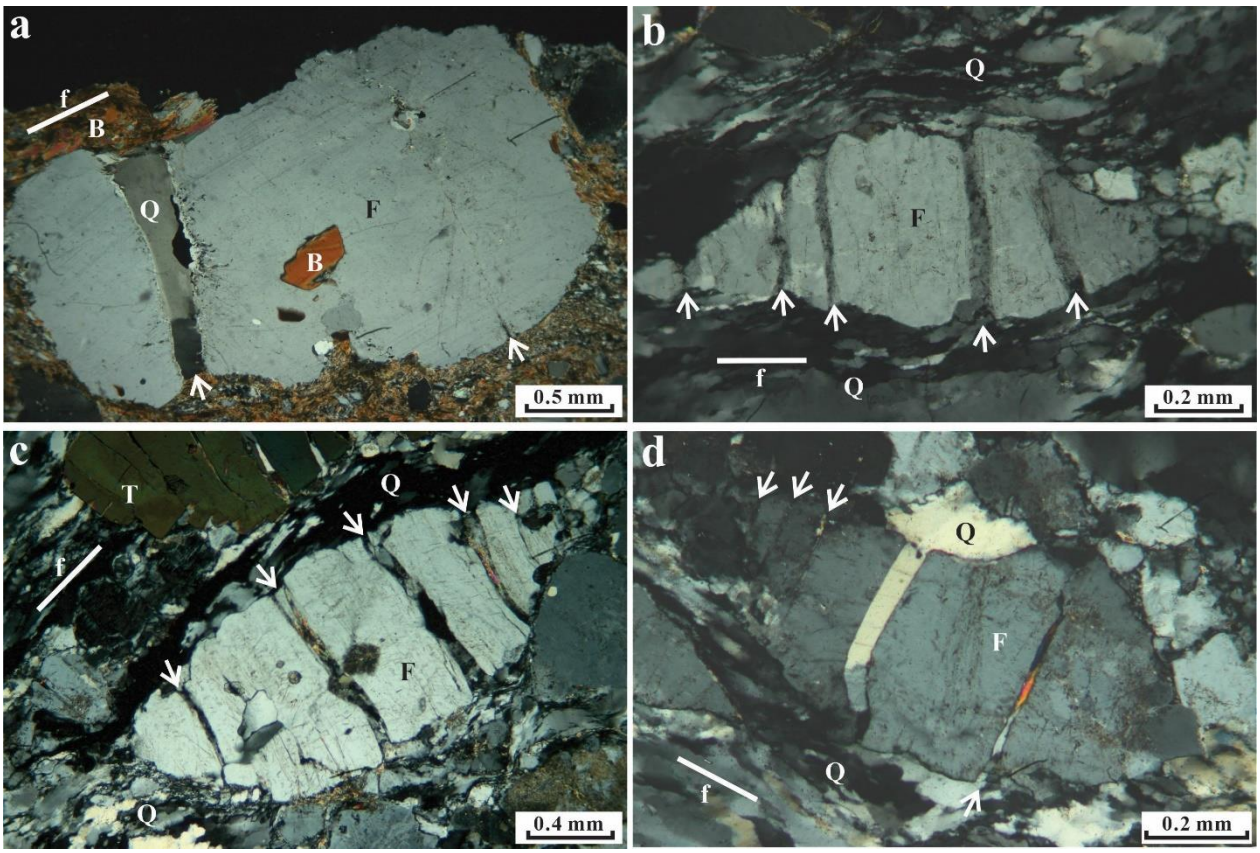

Figure 3.6 Tensile fractures and resultant pull-apart structures of feldspar porphyroclasts in granitic mylonites from the Chongshan shear zone (Yunnan, China). (a) and (d) from samples LS4 and CS10E, respectively, and (b)-(c) from samples CS45E. Abbreviations: B, biotite; F, feldspar; f, foliation; Q, quartz; T, tourmaline.

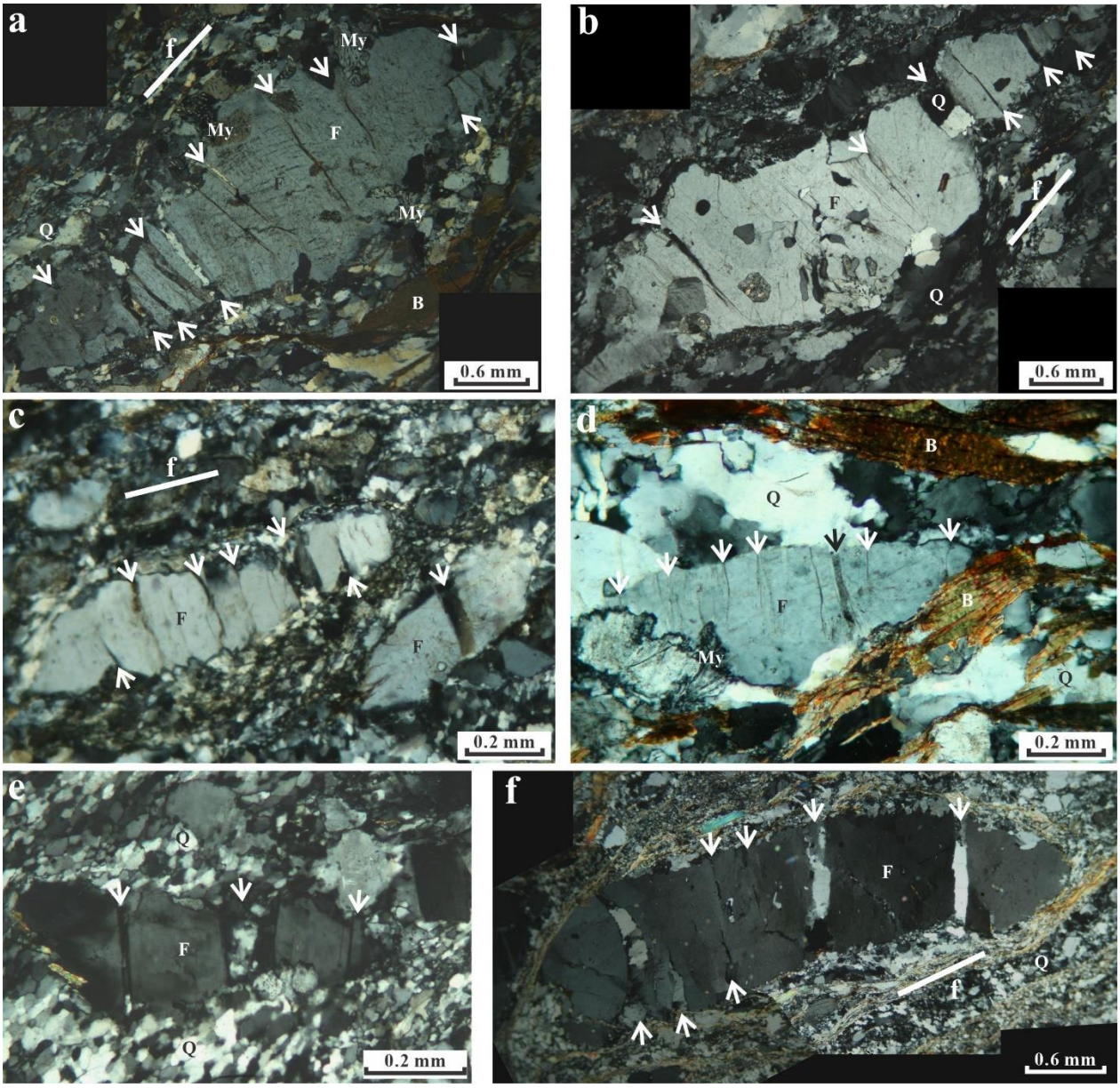

Figure 3.7 Microstructures of fragmented feldspar porphyroclasts in granitic mylonites from Ailaoshan (e, sample R82), Diancangshan (c, sample D10; f, sample D9) and Xuelongshan (a, sample YN1361D; b, sample YN1329C; d, sample YN1328) in the Red River shear zone (Yunnan, China). Abbreviations: B, biotite; F, feldspar; f, foliation; My, myrmekite; Q, quartz.

As illustrated in Figs. 3.5-3.7, fracturing process in feldspar is dominated by the near-end or off-centered fracturing (e.g., Ji & Zhao, 1993; Ji et al., 1998, Samanta et al., 2002; Li & Ji, 2020), although the mid-point or centered fracturing (Lloyd et al., 1982; Ferguson & Lloyd, 1984; Michibayashi, 1996) occasionally occurred in some samples. Either centered or off-centered

fractures produced parallel pull-aparts. In Figs. 3.5, 3.6a, d, and 3.7e, for example, the first tensile fracture in each feldspar porphyroclast does not occur at the center of the feldspar. It is also interesting to note that tensile fractures have not cut through myrmekitic patches (vermicular intergrowth of quartz and sodic plagioclase) located at rims of K-feldspar (e.g., Fig. 3.7d). This phenomenon was previously reported in deformed granitic rocks from the Kashio shear zone, central Honshu, Japan (Michibayashi, 1996). This phenomenon suggests that myrmekite occurred at earlier high temperatures (≥500 °C, Simpson & Wintsch, 1989; Ceccato et al., 2018) while tensile fracturing of feldspar took place at later low temperatures (≤450 °C). The myrmekites consisting abundant of fine-grained quartz was able to deform plastically when fractures initiated and propagated in feldspar at 300-450 °C (e.g., Tullis, 2002).

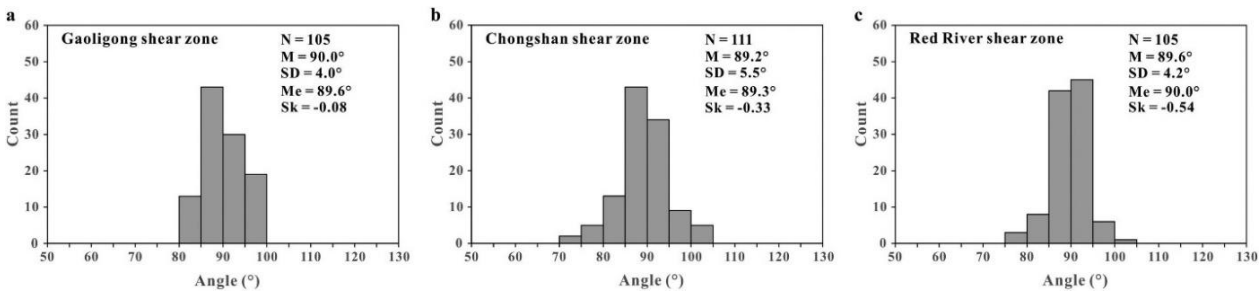

Figure 3.8 Preferred orientation of tensile fractures with respect to the long axes of feldspar porphyroclasts. (a), (b), and (c) measured from the Gaoligong, Chongshan and Red River shear zones, respectively. N: number of measurements; M: mean; Me: median; Sk: skewness.

The gap between adjacent feldspar microboudins has been filled with ductile quartz (Figs. 3.5-3.7), muscovite (Figs. 3.5c, 3.6d) or their fine-grained composite aggregates. Most of the quartz grains within the opening fractures of feldspar show undulatory extinction, subgrains and serrated boundaries, indicating that they have deformed by dislocation creep since their infilling. The microcracks without infill of quartz or muscovite from the adjacent matrix obviously formed when the matrix was no longer ductile (Figs. 3.5a, c, and 3.7a, d). These microcracks formed at low temperatures (<300 °, even lower than 250 °C) are filled with extremely fine-grained sericite and opaque materials due to infiltration of fluids.

In the studied samples where feldspar crystals were deformed by extensional fracturing and boudinage, soft minerals such as mica and muscovite deformed by non-coaxial shear as evidenced by the presence of mica fishes with typical lens (Figs. 3.9a-b) or lozenge (Figs. 3.9c-d)

shapes. The lens-shaped mica fishes (Figs. 3.9a-b) belong to group 1 of Passchier and Trouw (2005) and formed by slip on (001) in each mica fish and extensional shear separating each fish-shaped microboudin of mica from its neighbors. The lozenge shapes (Figs. 3.9c-d) are classified into group 4 of Passchier and Trouw (2005) and formed by antithetic slip on (001) in a mica grain whose (001) planes were initially oriented at high-angle to the foliation and lineation. These two types of microstructures (Fig. 3.9) indicate that mica deformed plastically by intracrystalline slip in the right-lateral shear zone of the GLG shear zone.

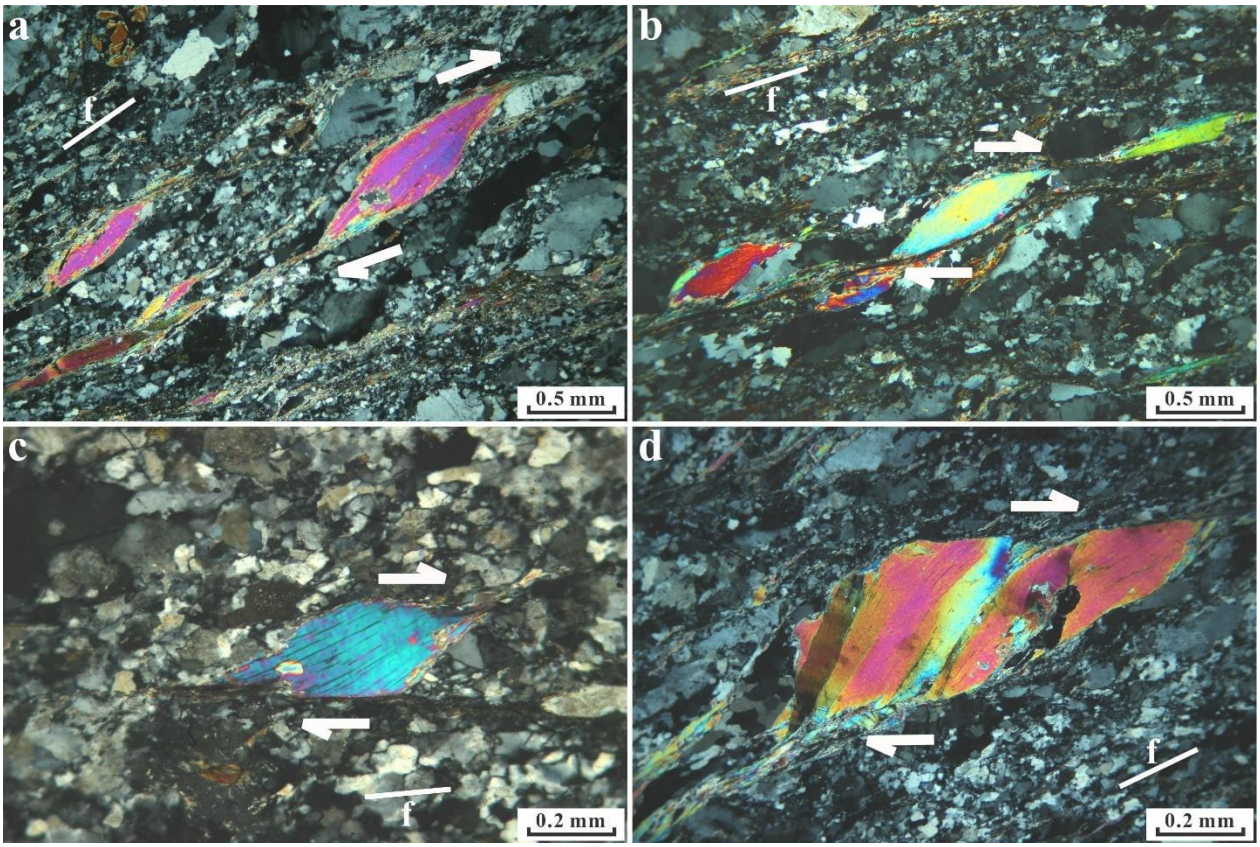

Figure 3.9 Typical mica fishes in granitic mylonites from the Gaoligong shear zone (right-lateral strike slip). (a), (b), (c), and (d) from granitic mylonite samples GLG11A, GLG45B, GLG86B and GLG86C, respectively. Abbreviation: f, foliation.

Throughout the protomylonitic and mylonitic rocks, which were derived from granitic protoliths of Triassic age (Indosinian), quartz and mica define the high strained C-plane while elongate porphyroclasts of feldspar define the local foliation (S-plane). Figure 3.6b-d show such an example that a feldspar porphyroclast is embedded in a fine-grained matrix consisting of quartz and occasionally muscovite. The geometrical relationship between the S- and C-planes, which are

respectively defined by elongated feldspar porphyroclasts and intensively sheared quartz or quartz-mica aggregate is also observed (Fig. 3.5a). The parallel, open mode, tensile fractures are perpendicular to the long axis of the porphyroclast. The relative widths of these intermicroboudin gaps suggest that the fractures were sequentially formed. The fractures with the large, moderate and smallest separations are the earliest, medium and latest ones. Such microstructures are typical in augen gneisses and felsic mylonites in the study region and show a dextral shear sense for strike-slip GLG shear zone and a sinistral shear sense for strike-slip CS and RR shear zones.

3.5 Methodology

The methods applied in this Chapter is similar to the methods used in Chapter 2. Therefore, the methodology will be introduced in brief.

3.5.1 Measurements of feldspar microboudins and strain

The geometric features (L, D_1 and D_2 in Fig. 3.2) of each feldspar microboudin and the length of gaps between microboudins were also measured from each thin petrographic section with an optical microscope. The process of multiple generations of fracturing then can be recovered with the strain reversal method (Fig. 3.10), and meanwhile the geometric features (L, D_1 and D_2) of the recovered microboudins formed in each generation of fracturing can be easily calculated.

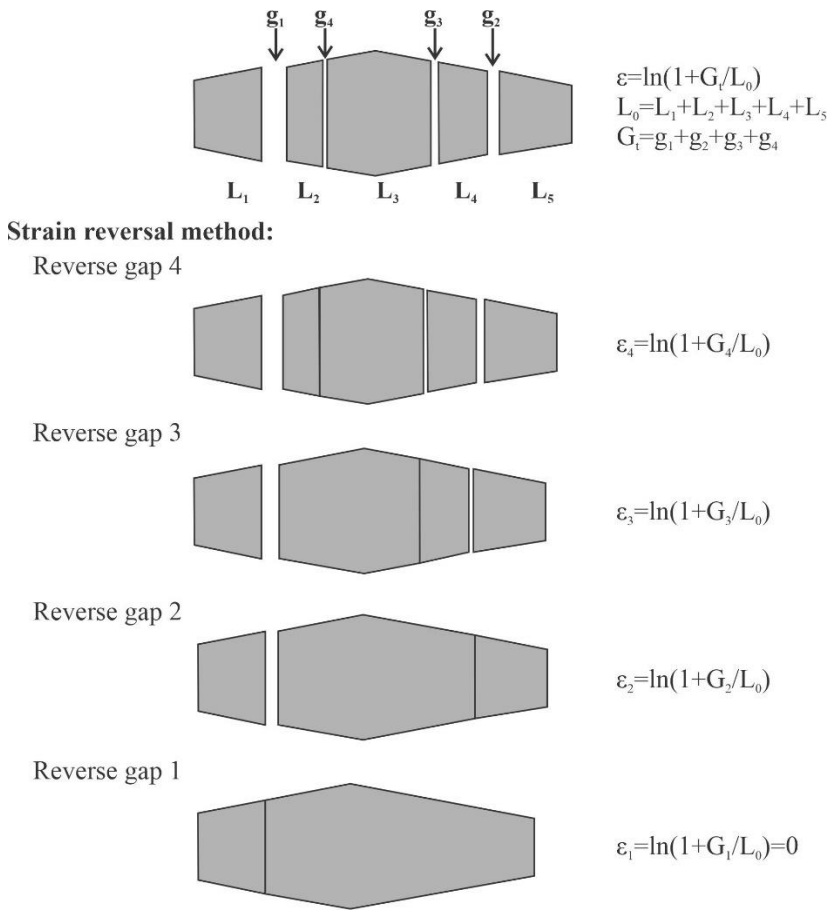

Figure 3.10 Schematic illustration of the strain reversal method used to recover the fracturing history of each feldspar porphyroclast. The gaps are ordered according to their lengths from large to small, indicating the sequence of fracturing. In each reversal stage, the remaining smallest gap is closed, whereas the length of the rest gaps is reduced by the same amount of the smallest gap. The natural strain (ε_n) after each reversal stage is calculated from the equation listed on the right side, where L_0 is the sum length of all the microboudin segments or the initial length of the original crystal before fracturing, G_t is the total length of the gaps before reverse, and G_n is the sum length of all the remaining gaps after the reversal of the nth gap (n = gap number).

3.5.2 Estimates of tensile strength of feldspar

Figure 3.3b gives the estimated tensile strength (*C* value) of 50-53 MPa for K-feldspar and sodic plagioclase. To extract information on rheological properties of the shear zones from the feldspar microboudins formed by multiple generations of fracturing, the *C* value of feldspar where each fracture formed was estimated based on factors such as degree of crystal quality, cleavage

orientation and the distribution of internal flaws. The detailed method is similar to that used in Chapter 2, with one more factor, the cleavage orientation, to be considered. The distribution of the estimated *C* values of the feldspar microboudins should also follow a Weibull distribution.

3.5.3 Estimates of the temperature

The deformation temperature for each sequential fracture of the feldspar porphyroclasts was approximately estimated based on results of combining microstructural observations, thermochronological data and paleostrain estimates (e.g., Behr & Platt, 2011; Li et al., 2020). The feldspar fractures across which microboudins are separated by plastically flowing quartz (Snoke & Tullis, 1998; Tullis, 2002; Scholz, 2019; Li et al., 2020). Those fractures without quartz infillings occurred below ~300 ºC, where both feldspar and quartz deformed in a brittle manner (Ji et al., 1997; Li & Ji, 2020). The fracturing of feldspar took place sequentially with larger gaps formed earlier at higher temperature whereas the microboudins with smaller interboudin gaps formed later at lower temperature, which can be verified by microstructures of quartz-filled interboudin gaps (higher *T* subgrains and subgrain rotation recrystallization occurred in earlier gaps while lower *T* bulging recrystallization took place in younger gaps). Biotite, muscovite and chlorite (Figs. 3.5c-d, 3.6c-d) occur in gaps formed at high, moderate and low temperatures, respectively, while sericite is observed in the tensile fractures across which microboudins are not separated at temperatures lower than ~300 ºC. These observation reveals that the overall range of deformation temperature is limited between 300 ºC and 450 ºC. The detailed process of determining the specific value of deformation temperature for each fracture or the temperature interval corresponding to each fracture is the same as that in Chapter 2.

3.6 Analysis of measured data

3.6.1 Measurements of feldspar microboudins

The length (L) and end widths (D_1 and D_2) of each feldspar microboudin (Fig. 3.2) were measured from each thin section (Table 3.3). No stereographic correction has been made.

The strain reversal method proposed by Ferguson (1981) and successfully applied by Ferguson and Lloyd (1982, 1984) and Lloyd and Ferguson (1989) permits us to construct the original shape (length/width ratio, L_0/W_0) and grain size [$d=(L_0W_0)^{0.5}$] of each feldspar grain prior to fracturing

by fully closing all the pull-apart fractures. The mean grain sizes of feldspar are 0.94 (SD=0.56), 0.84 (SD=0.64) and 0.99 (SD=0.61) mm for the GLG, CS and RR shear zones, respectively (Figs. 3.11a-c). The mean length/width ratios of the measured feldspar are 2.12 (SD=0.84), 1.65 (SD=0.84) and 1.82 (SD= 0.66) from the GLG, CS, and RR shear zones, respectively (Figs. 3.11d-f). Its maximum L_0/W_0 value is 5.80, 3.13 and 3.61 for the samples from the GLG, CS and RR shear zones, respectively. There is a miraculous linear relationship between L_0 and W_0 for each of the three shear zones (Fig. 3.11g-i).

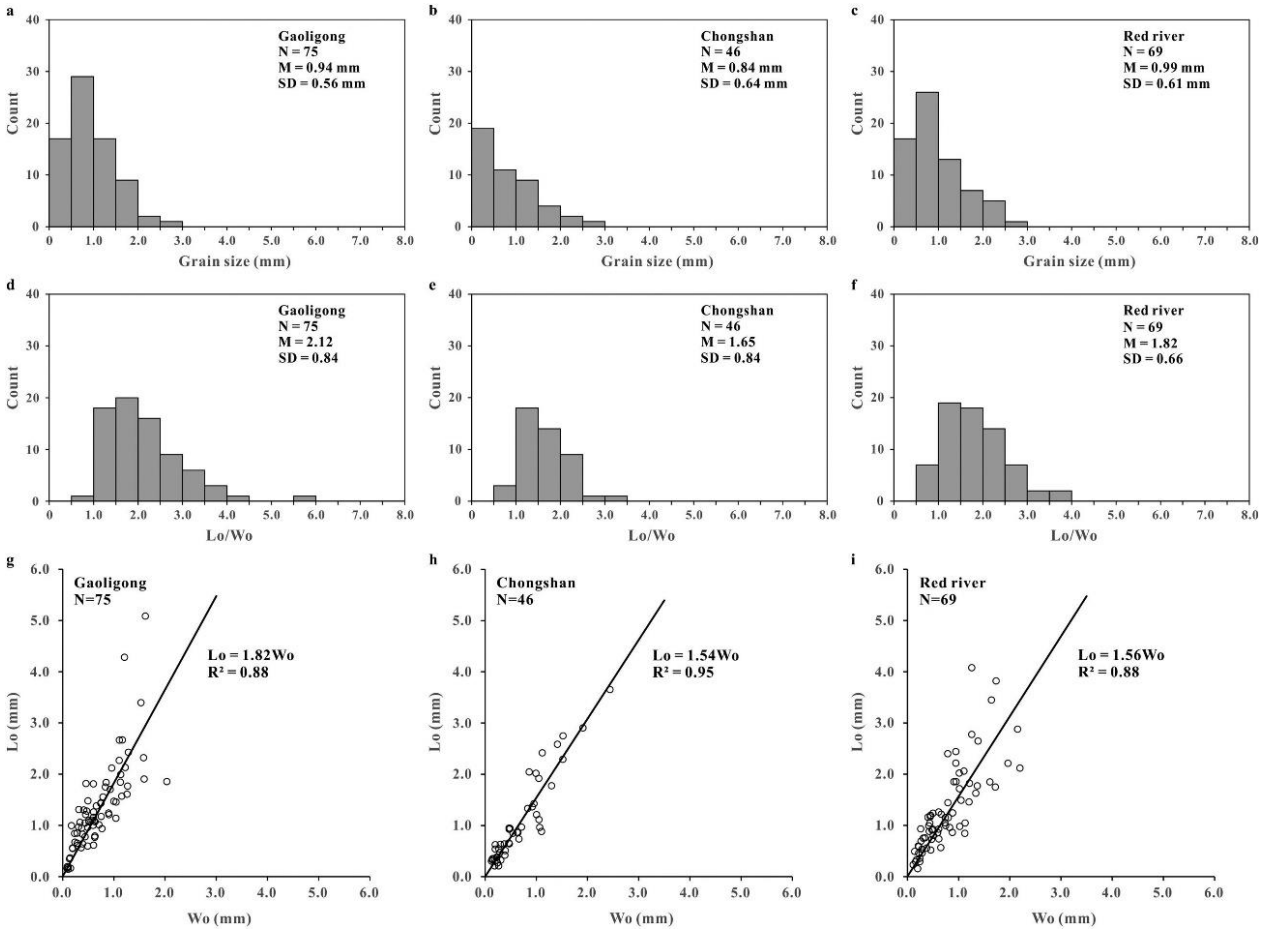

Figure 3.11 Distributions of intact grain size (a-c), aspect ratio (length/width, d-f), and length-width plots (g-i) for feldspar porphyroclasts measured from the Gaoligong (left column), Chongshan (middle column) and Red River (right column) shear zones. N: number of intact grains; M: mean; SD: standard deviation.

Table 3.3 Representative data of feldspar microboudins measured and estimated from optical observations of petrographic thin sections for samples CS10 and CS45 (Chongshan Shear Zone) from which recrystallized grain sizes of quartz have been measured for comparison

No.	*L* (mm)	D_2 (mm)	D_1 (mm)	Estimated *T* (°C)	Natural strain	*C*-value	Differential stress
Sample CM10							
CM10E-Grain 1	0.50	0.70	0.48	400	0.034	53	38
CM10E-Grain 1	0.14	0.56	0.48	310	0.060	53	100
CM10E-Grain 1	0.14	0.74	0.61	280	0.092	53	129
CM10E-Grain 10	0.67	1.11	0.58	360	0.073	53	50
CM10E-Grain 10	0.30	0.92	0.76	320	0.096	53	78
CM10E-Grain 12	0.49	0.51	0.10	380	0.067	53	40
CM10E-Grain 12	0.14	0.25	0.10	340	0.079	53	58
CM10E-Grain 12	0.16	0.46	0.34	320	0.221	53	77
CM10E-Grain 13	0.17	0.26	0.04	340	0.020	53	61
CM10E-Grain 14	0.16	0.31	0.21	350	0.021	53	52
CM10E-Grain 15	0.28	0.33	0.02	360	0.064	53	51
CM10E-Grain 15	0.24	0.28	0.02	360	0.101	53	52
CM10E-Grain 16	0.14	0.10	0.06	450	0.166	53	22
CM10E-Grain 17	0.55	0.76	0.46	380	0.140	53	40
CM10E-Grain 18	0.28	0.37	0.11	360	0.028	53	48
CM10E-Grain 18	0.37	0.47	0.01	340	0.061	53	58
CM10E-Grain 19	0.26	0.47	0.32	360	0.071	53	50
CM10E-Grain 19	0.29	0.59	0.32	340	0.255	53	60
CM10E-Grain 2	0.38	0.82	0.34	430	0.011	25	33
CM10E-Grain 2	0.77	0.77	0.47	400	0.019	53	28
CM10E-Grain 2	0.47	0.76	0.47	370	0.085	53	46
CM10E-Grain 4	0.09	0.27	0.21	330	0.178	53	73
CM10E-Grain 5	0.42	0.64	0.50	380	0.018	53	40
CM10E-Grain 5	0.24	0.51	0.50	360	0.046	53	50
CM10E-Grain 6	0.27	0.13	0.04	450	0.051	53	16
CM10E-Grain 6	0.06	0.07	0.04	400	0.110	53	37
CM10E-Grain 6	0.08	0.09	0.08	380	0.194	53	25
CM10E-Grain 7	0.08	0.22	0.16	330	0.046	53	72
CM10E-Grain 8	0.21	0.33	0.16	370	0.014	53	48
CM10E-Grain 8	0.20	0.37	0.19	350	0.043	53	55
CM10E-Grain 9	0.12	0.19	0.07	380	0.022	53	55
CM10E-Grain 9	0.13	0.20	0.17	360	0.042	53	38
CM10E-Grain 9	0.11	0.13	0.01	340	0.087	53	53
Sample CM45							
CM45C-Grain 1	0.24	0.58	0.26	320	0.039	53	77
CM45E1-Grain 1	0.23	0.22	0.18	440	0.010	53	25
CM45E1-Grain 1	0.08	0.15	0.10	360	0.041	53	49
CM45E1-Grain 10	0.51	0.50	0.01	390	0.005	53	44
CM45E1-Grain 10	0.29	0.85	0.72	320	0.042	53	72

Table 3.3 Representative data of feldspar microboudins measured and estimated from optical observations of petrographic thin sections for samples CS10 and CS45 (Chongshan Shear Zone) from which recrystallized grain sizes of quartz have been measured for comparison (continued)

No.	*L* (mm)	D_2 (mm)	D_1 (mm)	Estimated *T* (°C)	Natural strain	*C*-value	Differential stress
CM45E1-Grain 11	0.16	0.27	0.13	360	0.012	53	51
CM45E1-Grain 12	0.12	0.20	0.16	400	0.011	53	42
CM45E1-Grain 12	0.14	0.27	0.23	360	0.109	53	47
CM45E1-Grain 13	0.59	0.92	0.70	380	0.259	53	40
CM45E1-Grain 14	0.16	0.19	0.14	440	0.021	53	31
CM45E1-Grain 14	0.15	0.13	0.09	430	0.072	53	23
CM45E1-Grain 14	0.02	0.14	0.13	300	0.136	53	135
CM45E1-Grain 15	0.05	0.13	0.11	380	0.029	53	64
CM45E1-Grain 15	0.13	0.18	0.17	360	0.117	53	32
CM45E1-Grain 15	0.06	0.17	0.15	330	0.153	53	69
CM45E1-Grain 2	0.09	0.09	0.07	440	0.126	53	25
CM45E1-Grain 3	0.29	0.29	0.15	400	0.041	53	30
CM45E1-Grain 4	0.89	0.92	0.03	380	0.071	53	46
CM45E1-Grain 4	0.27	0.35	0.17	360	0.083	53	39
CM45E1-Grain 4	0.16	0.54	0.30	310	0.107	53	97
CM45E1-Grain 5	0.45	0.97	0.77	350	0.050	53	55
CM45E1-Grain 5	0.30	0.79	0.40	320	0.084	53	80
CM45E1-Grain 6	0.27	0.36	0.14	400	0.023	53	44
CM45E1-Grain 6	0.20	0.35	0.14	360	0.029	53	57
CM45E1-Grain 6	0.15	0.36	0.26	350	0.034	53	64
CM45E1-Grain 6	0.15	0.32	0.16	340	0.044	53	62
CM45E1-Grain 6	0.06	0.31	0.26	290	0.088	53	122
CM45E1-Grain 7	0.24	0.37	0.24	370	0.159	53	43
CM45E1-Grain 7	0.14	0.35	0.24	330	0.180	53	67
CM45E1-Grain 8	1.16	1.45	0.76	390	0.003	53	38
CM45E1-Grain 8	0.69	1.22	0.76	360	0.017	53	50
CM45E1-Grain 9	0.25	0.42	0.42	380	0.003	53	39
CM45E1-Grain 9	0.21	0.45	0.32	340	0.095	53	59
CM45E2-Grain 1	0.67	1.46	1.30	430	0.014	25	25
CM45E2-Grain 1	0.80	1.07	0.99	410	0.021	53	32
CM45E2-Grain 1	0.59	1.05	0.99	370	0.038	53	42
CM45E2-Grain 1	0.42	1.52	1.49	320	0.090	53	83
CM45E2-Grain 1	0.13	1.05	0.98	290	0.128	53	193
CM45E2-Grain 2	1.13	0.71	0.50	450	0.034	53	17
CM45E2-Grain 2	0.41	0.98	0.71	360	0.056	53	64
CM45E2-Grain 2	0.37	1.00	0.85	330	0.096	53	68
CM45E2-Grain 3	0.19	0.53	0.33	320	0.079	53	77
CM45E2-Grain 4	0.64	0.91	0.06	360	0.006	40	46
CM45E2-Grain 4	0.47	0.98	0.96	360	0.025	53	49
CM45E2-Grain 4	0.34	0.58	0.06	330	0.049	40	53

Table 3.3 Representative data of feldspar microboudins measured and estimated from optical observations of petrographic thin sections for samples CS10 and CS45 (Chongshan Shear Zone) from which recrystallized grain sizes of quartz have been measured for comparison (continued)

No.	*L* (mm)	D_2 (mm)	D_1 (mm)	Estimated *T* (°C)	Natural strain	*C*-value	Differential stress
CM45E2-Grain 4	0.28	0.51	0.25	320	0.100	53	55
CM45E2-Grain 4	0.16	0.25	0.06	300	0.116	73	77
CM45E2-Grain 5	0.33	0.44	0.13	390	0.008	53	47
CM45E2-Grain 5	0.20	0.29	0.13	370	0.027	53	47
CM45E2-Grain 5	0.29	0.35	0.06	350	0.049	53	47

3.6.2 Measurements of strains and assessment of strain rates

The length of each gap between adjacent microboudins were measured from each thin section (Table 3.3). The largest interboudin gap observed is ~1.0 mm and filled essentially with quartz from the flowing matrix. In contrast, there is almost not separation across a tensile fracture that formed when the matrix became no longer ductile at temperatures below the brittle-ductile transition (<300 ºC, Snoke et al., 1998).

The strain reversal method were used to calculate the finite extension strain for each measured feldspar grain. The strain was computed by progressive closure of the interboudin gaps with smaller gaps being closed earlier and reduction in the same amount of gap distance in all the others. This method is valid because fracturing is sequential and separation of microboudins with smaller interboudin gaps corresponding to later fracture sites while larger gaps to earlier ones. Using this method, we obtained the L, D_1 and D_2 data of each fragment at the moment of each fracturing event and the extension strain that formed the gap after formation of each fracture. Figure 3.12 shows the distribution of finite extension strains estimated from 56, 43 and 61 feldspar grains from the GLG, CS, and RR shear zones. The maximum extensional finite strains recorded by feldspar boudinage are 35.4%, 26.9%, and 46.7% in the samples from the GLG, CS and RR shear zones, respectively. The mean finite strains, however, are significantly smaller (4.5% for GLG, 9.5% for CS, and 13.6% for RR). It is evident that the stronger feldspar with little ductile deformation takes much smaller part of strain than the softer strongly recrystallized quartz and mica in the same rocks (Ji & Xia, 2002).

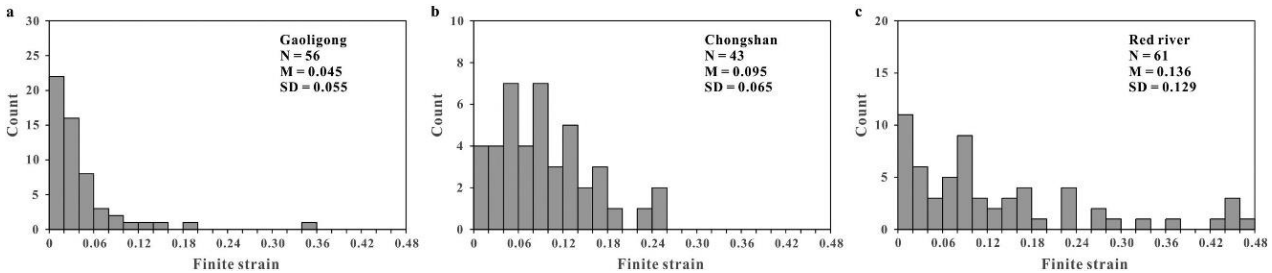

Figure 3.12 Histograms for the extensional finite strains recorded by feldspar boudinage in the granitic mylonites from the Gaoligong, Chongshan and Red River shear zones. N: number of intact grains; M: mean; SD: standard deviation.

Paleostrain rates can be roughly estimated for the feldspar grains that developed ≥2 generations of pull-apart fractures. The strain accumulated between two adjacent fracturing events was measured using the strain reversal method (Ferguson, 1981; Ferguson & Llyod, 1982, 1984; Lloyd & Ferguson, 1989). The time interval between the adjacent events was calculated according to the data of feldspar fracture temperatures and the thermochronological results (i.e., the average cooling rate for each shear zone). The average cooling rates are 33.41, 37.52 and 39.27 ºC/Ma for the GLG, CS, and RR shear zones, respectively. As illustrated in Fig. 3.13, the strain rates of the feldspar microboudinage vary from 1.726×10^{-18} s^{-1} to 6.263×10^{-15} s^{-1} with a mean value of 8.24×10^{-16} s^{-1} for the GLG shear zone, from 1.716×10^{-16} s^{-1} to 1.094×10^{-14} s^{-1} with a mean value of 1.861×10^{-15} s^{-1} for the CS shear zone, and 1.022×10^{-16} s^{-1} to 7.416×10^{-15} s^{-1} with a mean value of 1.895×10^{-15} s^{-1} for the RR shear zone. These strain rates recorded by feldspar microboudinage, which yield the lower limit, assuredly cannot be representative of the overall strain rates of the shear zones because the measured strains associated with feldspar interboudin gaps are considerably smaller than those of the flowing matrix of quartz or quartz-mica aggregate. The fastest strain rate among the data of the three shear zones is 1.094×10^{-14} s^{-1}, which can be taken, to a first approximation, as the strain rates for the shear zones during the feldspar boudinage formed. The value is lower than the strain rate (3 to 4 $\times10^{-14}$ s^{-1}) estimated by Sassier et al. (2009) based on the deformation and monazite U-Th/Pb ages of three sets of synkinematic leucocratic dykes (22.55, 26.81 and 29.89 Ma) from a large outcrop at Yuanjiang's Huashiban Hydraulic Station in the central RR shear zone. These ages are the crystallization ages of monazite in partial melt and represent the ages of dike emplacements. Most of the strains recorded by the dykes were accumulated during the high temperature stage (550-700 ºC, Leloup

et al., 1995). For this reason, we assume that the mean strain rate in the study rocks is about 10^{-14} s^{-1} at temperatures of 300-450 ºC. This temperature interval of 150 ºC corresponds to a time span of 4.0, 4.5, and 3.8 Ma during the cooling and exhumation of metamorphic rocks from the GLG, CS and RR shear zones, respectively.

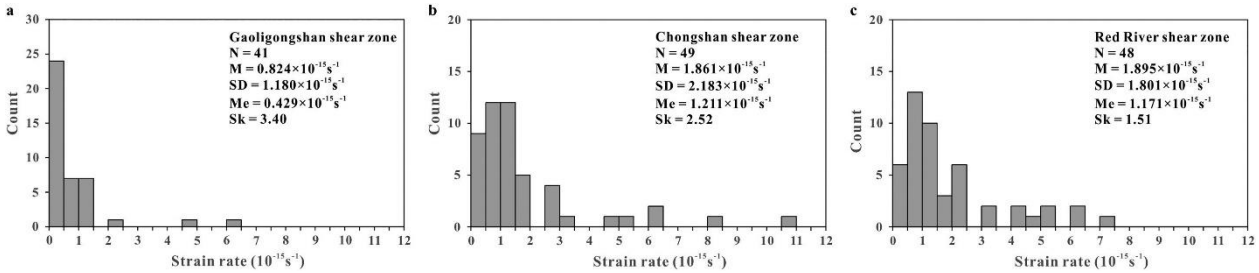

Figure 3.13 Histograms for the extensional strain-rates estimated by combining feldspar boudinage piezometer results and thermochronological data from the granitic mylonites in the Gaoligong (a), Chongshan (b), and Red River (c) shear zones. N: number of measurements; M: mean; SD: standard deviation; Me: median; Sk: skewness.

3.6.3 Estimates of temperature

The deformation temperature for each fracture was estimated based on microstructural observations, thermochronological data and paleostrain. The estimated results of deformation temperature are displayed in Table 3.3. The temperature estimation for each fracturing event is subject to the largest uncertainties of ±30 °C.

3.7 Assessment of differential stresses

As shown in Fig. 3.14, the estimated tensile strength of feldspar (Table 3.3), which cannot be a constant value due to the apparent quality of crystals observed under the microscope, shows a probability distribution with a mean of 53 MPa and a standard deviation (SD) of 6 MPa. We computed the Kolmogorov–Smirnov (KS) statistic value for each of the five distribution models: exponential distribution (0.541), Log-normal distribution (0.450), Gamma distribution (0.444), normal distribution (0.430), and Weibull distribution (0.424). The KS statistics measure how well a given theoretical model fits the measured data. The smaller the KS value is, the better the fitting is. The calculations reveal that the best-fit distribution function for the estimated *C* values is the Weibull distribution whose scale and shape parameters are equal to 55.1 MPa and 8.2,

respectively. This agrees with previous theoretical analyses (e.g., Weibull, 1951; Paterson & Wong, 2005; Dodson, 2006), reflecting that the tensile strength varies with the degree of crystal quality, cleavage orientation and particularly the distribution of internal flaws (e.g., microcracks, inclusions, heterogeneities, and surface roughness). The "guideline" tensile strength and its variation of feldspar, assessed above, will be subject to verification by laboratory experiments at high temperatures and high pressures.

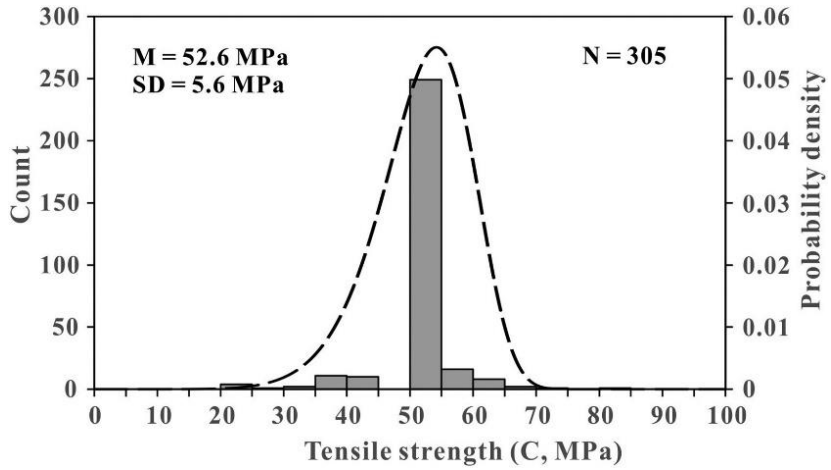

Figure 3.14 "Best" or "guideline" values of the tensile strength estimated for the feldspar porphyroclasts of granitic mylonites according to their crystal quality and internal flaws (e.g., microcracks, inclusions, cleavage orientation, and surface roughness) observed under the microscope. N: number of fractures; M: mean; SD: standard deviation. The estimated tensile strengths follow a Weibull distribution with a scale parameter of 55.1 MPa and a shape parameter of 8.2.

The differential stress (σ) of the polycrystalline matrix surrounding each feldspar porphyroclast is estimated according to Eq. (3.5). The result can be the magnitude of differential stress in the brittle or ductile regime whether the tensile fracture is barren or quartz-filled. The histograms (Fig. 3.15) illustrate distributions of estimated paleostresses in both the ductile and brittle regimes of each shear zone. 97 measurements from the GLG shear zone show that the estimated paleodifferential stresses in the ductile regime range from 12.5 MPa to 124.7 MPa with the mean (M) of 45.9 (SD=19.6) MPa (Fig. 3.15a). In the brittle regime, however, the differential stresses in the same shear zone vary in the range of 13.1-158.5 MPa with M=70.7 (SD=33.6) MPa (Fig. 3.15d). The ductile and brittle regimes of the CS shear zone show their mean differential stresses

of 52.2 (SD=26.3) MPa (Fig. 3.15b) and 82.8 (SD=41.8) MPa (Fig. 3.15e), respectively. In the ductile regime of the RR shear zone, the differential stresses vary in the range of 16.3-185.9 MPa with M=51.6 (SD=26.3) MPa (Fig. 3.15c). This shear zone has its differential stresses of 12.6-162.8 MPa (M=69.4 MPa, SD=44.3 MPa) in the brittle regime (Fig. 3.15f). The differential stress magnitudes estimated from the feldspar microboudinage piezometer agree largely with the stresses determined for other crustal shear zones in the world using other independent methods (e.g., Gueydan et al., 2005; Behr & Platt, 2011; 2014; Kidder et al., 2012).

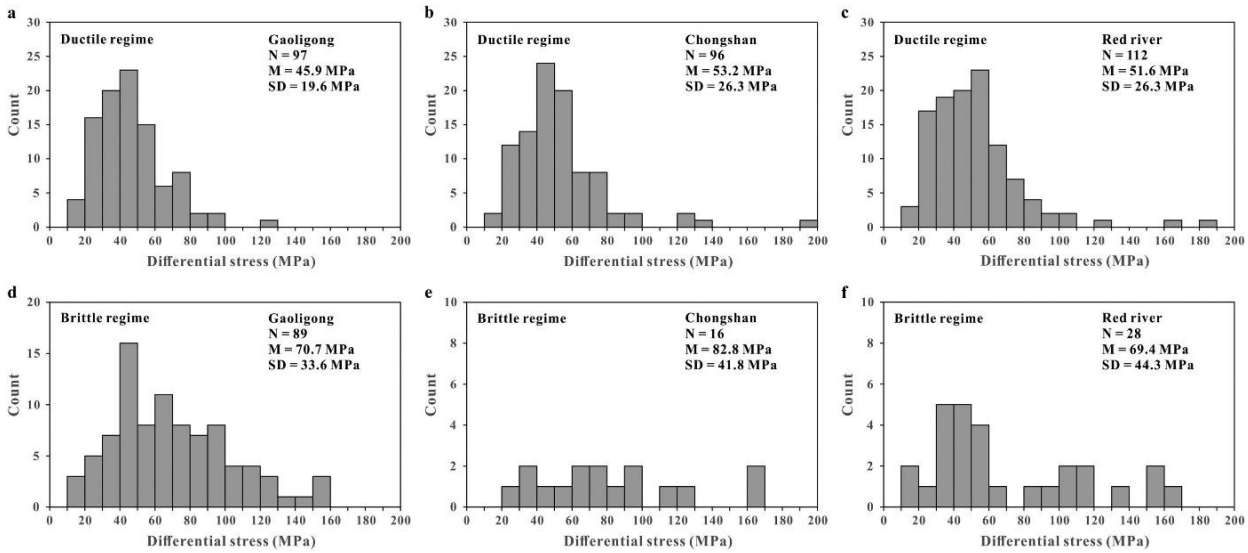

Figure 3.15 Distributions of the differential stresses estimated from the feldspar microboudinage piezometer in the ductile (a-c) and brittle (d-f) matrixes of granitic mylonites from the Gaoligong (left column), Chongshan (middle column) and Red River (right column) shear zones.

Plots of assessed matrix flow stress as a function of estimated deformation temperature are shown in Figure 3.16a-c for the three shear zones. The sequential fractures led to an increase in the end surface areas (S_2, Fig. 3.2) and a decrease in the aspect-ratio [$2L/(D_1+D_2)$] of fractured segment. Accordingly, the sequential fracturing is observed to have occurred during an increase flow strength of the matrix and accordingly a decrease in environmental temperature due to progressive exhumation upward the brittle-ductile transition (e.g., Leloup et al., 1995, 2001; Wang et al., 2018, 2020; Zhang et al., 2010, 2011, 2012a, b; Tang et al., 2013, 2020).

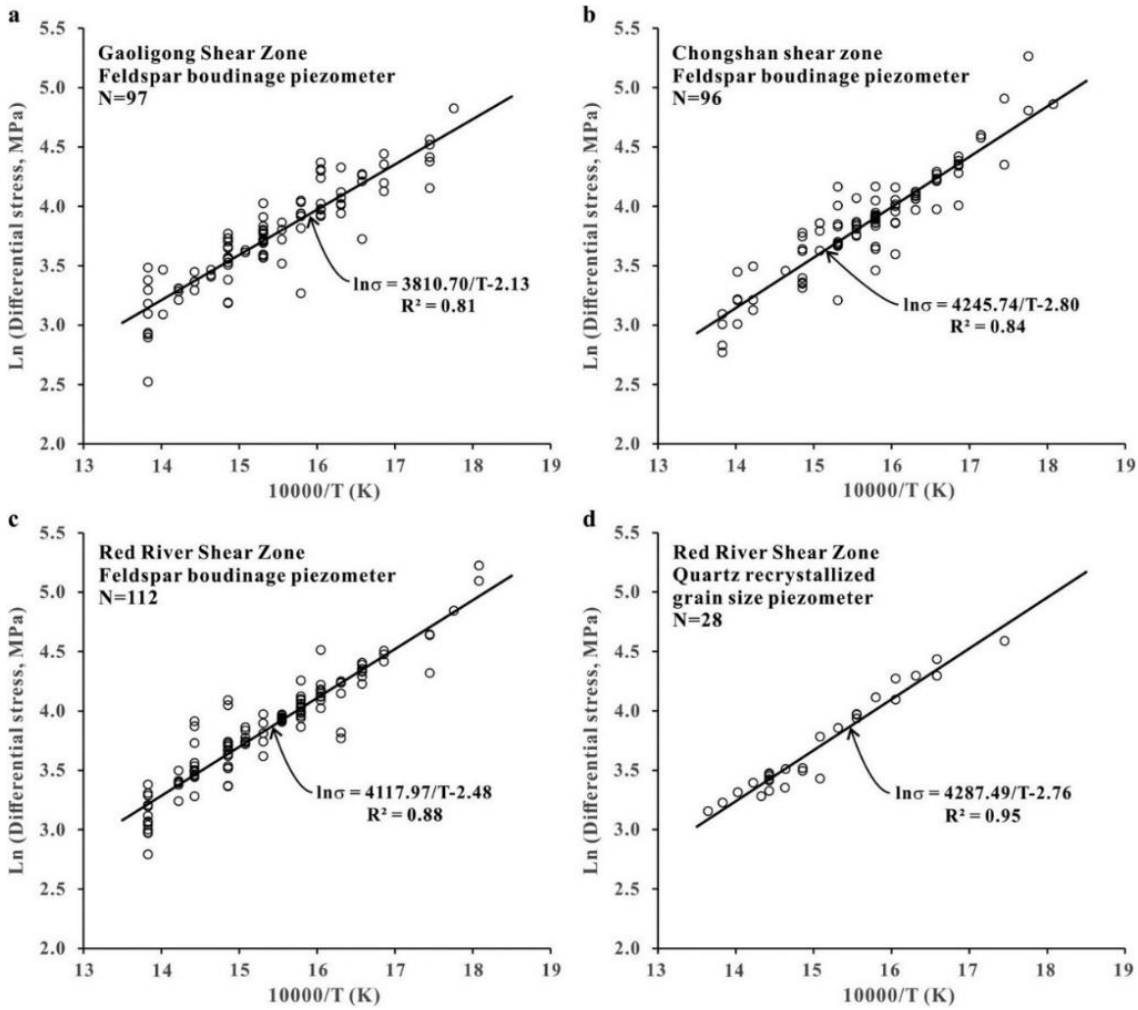

Figure 3.16 Plot of lnσ versus 10^4/T for the Gaoligong (a), Chongshan (b) and Red River (c-d) shear zones. Data in (a-c) from the estimates of feldspar microboudinage piezometer while those in (d) from quartz recrystallized grain size piezometer of Stipp and Tullis (2003), with data compiled from An and He, (1987), Zhang et al. (2008) and Boutonnet et al. (2013).

As shown in Fig. 3.16, the variation of flow stress as a function of temperature for each of the three shear zones can be described by the following equation:

$$ln\sigma = a/T - b \qquad (3.7)$$

where σ is in MPa, T in K, and a and b are two empirical parameters. The parameters obtained from the best fit of 97 feldspar microboudins from the GLG shear zone are: a=3810.70 and b=2.13 (Fig. 3.16a). Ninety-six feldspar microboudins from the CS shear zone give: a=4245.74

and b=2.80 (Fig. 3.16b). For the RR shear zone, a=4117.97 and b=2.48, determined from 112 feldspar microboudins (Fig. 3.16c).

3.8 Discussion

The GLG, CS and RR shear zones are well-known, extensively studied, crust-scale, non-coaxial ductile shear zones in the southeastern Tibetan plateau (e.g., Tapponnier et al., 1990; Leloup et al., 1995; Searle et al., 2010). However, in the granitic mylonite samples collected from these shear zones, extensional fractures (e.g., pull-apart structure) are much more common than shear fractures (e.g., bookshelf structure characterized by rotation and offset of fragments) in feldspars (Figs. 3.5-3.7). The predominance of extension fractures in the scale of the porphyroclasts is largely due to the fact that the tensile strength of geological material such as feldspar is appreciably lower than its shear strength. It is possible that tensional fracturing of feldspar has been underestimated during previous investigations due to the emphasis of shear-sense determination. Furthermore, in the same mylonite sample, soft minerals such as recrystallized quartz and mica deformed by non-coaxial shear whereas the tensile fractures within feldspar porphyroclasts suggest that they deformed by local quasi-coaxial deformation with extensional and compressional directions parallel to the long and short axes, respectively, at the moment of fracturing (Hippertt, 1993; Michibayashi, 1996; Hentschel et al., 2019). Thus, the strain is particularly partitioned into different materials with contrasting rheological properties.

The steady-state flow behavior of polycrystalline quartz by dislocation creep can be described by the following equation:

$$\dot{\varepsilon}=A\sigma^{n}exp(-Q/RT) \qquad (3.8)$$

where $\dot{\varepsilon}$ is the steady-state strain rate, A is the pre-exponential factor, σ is the differential stress, n is the stress exponent, Q is the activation energy, R is the gas constant, T is the absolute temperature (K).

Equation (3.8) can be rewritten as:

$$ln\sigma=(ln\dot{\varepsilon}-lnA)/n+Q/(nRT) \qquad (3.9)$$

Comparing Eq. (3.7) with Eq. (3.9) allows us to determine the activation energy Q for each shear zone.

$$a=Q/(nR) \quad (3.10)$$

or

$$Q=a\times n\times R \quad (3.11)$$

According to Paterson and Luan (1990), Luan and Paterson (1992), Gleason and Tullis (1995), Hirth et al. (2001), and Lu and Jiang (2019), the stress exponent is equal to 4 for quartz, and R=8.314 J/mol/K. Then, we obtain Q=126.738, 141.205 and 136.948 kJ/mol for quartz from the GLG, CS and RR shear zones, respectively, based on the feldspar microboudinage piezometer results shown in Figs. 3.16a-c. The quartz recrystallized grain size piezometer data yield that Q=142.585 kJ/mol for quartz from the RR shear zone. These results together give a mean Q value of 136.864±7.170 kJ/mol for naturally deformed quartz.

$$b = -(ln\dot{\varepsilon}-lnA)/n \quad (3.12)$$

or

$$lnA= ln\dot{\varepsilon}+bn \quad (3.13)$$

The b value for each shear zone is given in Fig. 3.16. Obviously, the A value depends on the estimated strain rate. Deformed leucocratic dykes at Yuanjiang's Huashiban Hydraulic Station in the central RR shear zone yield a mean strain rate of ~3.5×10^{-14} s^{-1} between 22 and 23 Ma (Sassier et al., 2009) when the rocks were at 550-700 ºC (Leloup et al., 1995). The strain rates recorded by feldspar boudinage in the granitic mylonites from the same shear zone range from 1.022×10^{-16} s^{-1} to 7.416×10^{-15} s^{-1} with a mean value of 1.895×10^{-15} s^{-1} for the RR shear zone at 300-450 ºC. Laboratory experiments show that quartz deforms at strain rates of about one order of magnitude faster than feldspar under the same conditions (e.g., Tullis, 2002). For the above reasons, we judicially assume an average strain rate of 10^{-14} s^{-1} for the shear zones under the greenschist facies conditions, in view of many uncertainties involved. Then we obtained a mean A=(4.020 ± 3.269)×10^{-10} s^{-1} for quartz deformed naturally in the temperature range of 300-450 ºC where feldspar microboudinage formed. The choice of the strain rate is consistent with the previous results from Pfiffner and Ramsay (1982), Christensen et al. (1989, 1994), and Fagereng and Biggs (2019) who concluded that the crustal shear zones has a typically average strain rate of ~10^{-14} s^{-1}. The data of feldspar microboudinage piezometer, together with those of quartz

recrystallized grain size piezometer permit us to obtain a best-fit flow law for the polycrystalline quartz deformed at natural strain rates by dislocation creep:

$$\dot{\varepsilon}=4.020\times10^{-10}\,\sigma^{4}\exp(-136.864/RT) \qquad (3.14)$$

where $\dot{\varepsilon}$ is in s^{-1}, σ in MPa, and T in K.

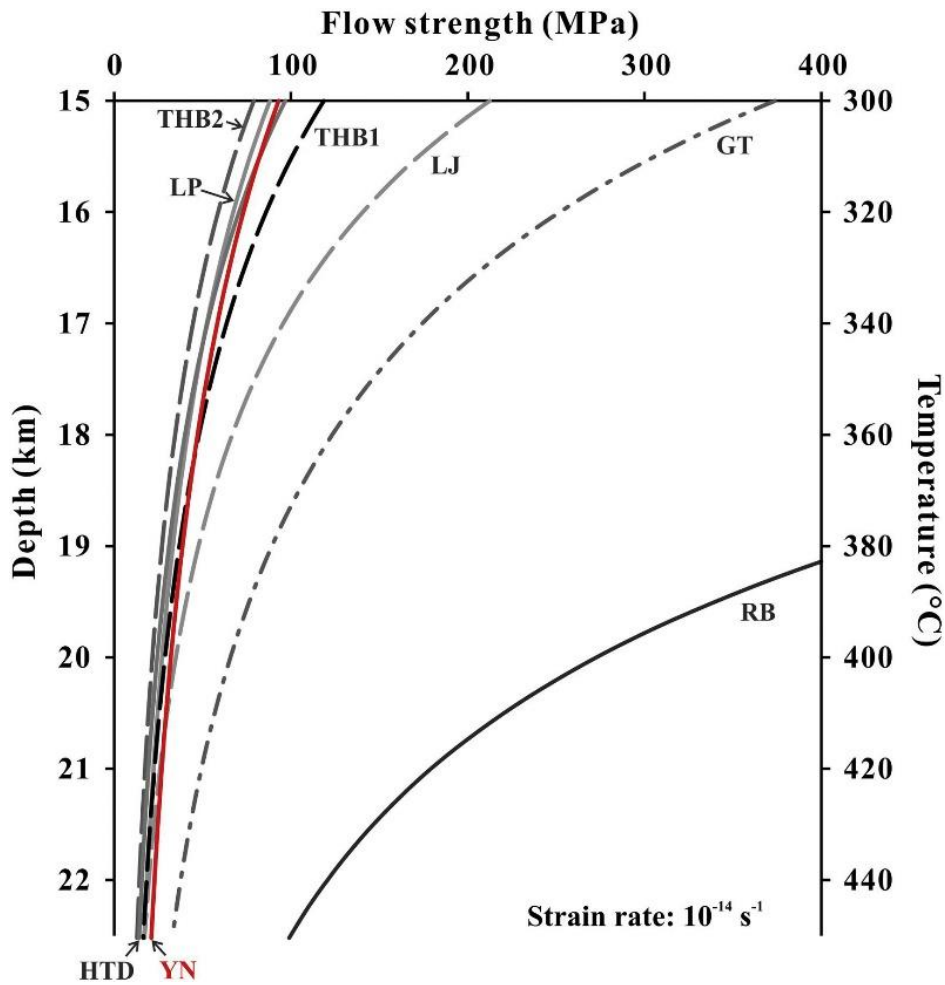

Figure 3.17 Flow strength-depth profiles calculated using various polycrystalline quartz flow laws for a continental crust (20 °C/km) deformed at strain rates of 10^{-14} s^{-1}. GT (Gleason & Tullis, 1995), HTD (Hirth et al., 2001), LJ (Lu & Jiang, 2019), LP (Luan & Paterson, 1992), RB (Rutter & Brodie, 2004), THB1 (laboratory fit) and THB2 (extrapolation fit) of Tokle et al. (2019), and YN (Yunnan, this study).

Figure 3.17 shows the differential stresses calculated from Eq. (3.14) with existing quartz flow laws (Luan & Paterson, 1992; Gleason & Tullis, 1995; Hirth et al., 2001; Rutter & Brodie, 2004;

Lu & Jiang, 2019; Tokle et al., 2019) in the range of 300-450 ºC, which corresponds to the depth range of 15.0-22.5 km assuming a geothermal gradient of 20 ºC/km. Equation (3.14) derived from the feldspar microboudinage and quartz recrystallized grain size piezometer data agree consistently with those flow laws of Luan and Paterson (1992) and Hirth et al. (2001). The extrapolation of the flow laws from Lu and Jiang (2019), Gleason and Tullis (1995) and particularly Rutter and Brodie (2004) overestimates the quartz flow strengths at temperatures of 300-450 ºC. The quartz flow strength given by Eq. (3.14) lie between the laboratory fit (THB1) and extrapolation fit (THB2) flow laws of Tokle et al., (2019) below ~360 °C. The calculations of the flow laws (Hirth et al., 2001; Lu & Jiang, 2019) are based on an assumption that the water partial pressure is equal to the lithostatic pressure. The flow strengths predicted by these flow laws will substantially increase if the actual water partial pressure becomes significantly lower than the lithostatic pressure. Thus, we believe that Eq. (3.14) derived from microstructural-piezometrical data of naturally deformed rocks gives a more realistic flow strength of quartz aggregates at natural strain rates, comparing to previous models.

3.9 Conclusions

Pull-apart microboudinage formed by multiple cycles of tensile fractures is a common microstructure observed in feldspar porphyroclasts embedded in ductile flowing matrix of quartz in felsic mylonites deformed under the greenschist facies (300-450 °C). As shown by the granitic mylonites from the Red River, Chongshan and Gaoligong shear zones, Yunnan, China, the valuable information which can be extracted from the feldspar microboudins includes the magnitudes of finite strains and differential stresses and their evolutions during the cooling and exhumation of the mylonites upwards the brittle-ductile transition. The feldspar microboudinage piezometer is applicable when the quartz matrix deforms in either ductile or brittle regime. In the ductile regime, for example, the Red River, Chongshan and Gaoligong shear zones (Yunnan, Southwest China) display the paleodifferential stresses varying in the ranges of 16.3-185.9, 16.0-193.0 and 12.5-124.8 MPa, and increasing with progressively decreasing temperature from 450 °C to 300 °C.

Combined with the estimates of deformation temperature and thermochronological data [i.e., amphibole, muscovite and biotite $^{40}Ar/^{39}Ar$, and zircon and apatite (U-Th)/He ages], the feldspar piezometrical results allow us to establish an empirical flow law: $\dot{\varepsilon}=A\sigma^{n}exp(-Q/RT)$ with n=4,

Q=137 kJ/mol and A=4.02×10^{-10} MPa^{-n}s^{-1} for polycrystalline quartz deformed at natural strain rates under the greenschist-facies conditions. This microstructure-based flow law yields a flow strength close to the values extrapolated from experimentally determined quartz flow laws of Luan and Paterson (1992), Hirth et al. (2001) and Tokle et al. (2019). The method developed in this chapter is viable for felsic mylonites where feldspar porphyroclasts imbedded in a ductile matrix of quartz or quartz-mica aggregate deform in the brittle pull-apart manner. However, the method may be directly used or adapted to a wide range of geological problems, for example, fractured pebbles in an unlithified matrix (Eidelman & Reches, 1992), chromite pods in the mantle rocks (Holtzman, 2000), and strong boudins in a soft material on any scale (e.g., Fagereng & Sibson, 2010).

CHAPTER 4 CHARACTERIZATION AND INTERPRETATION FOR FORMATION OF ORTHOGONAL JOINTS IN SEDIMENTARY ROCKS

4.1 Introduction

Sedimentary rocks are typically layered composites in which brittle fractures occur in competent beds (e.g., limestone and sandstone) while apparent ductile deformation takes place in incompetent layers (e.g., mudstone and shale). The existence of rock fractures or joints changes physical properties of sedimentary rock layers (e.g., strength, stability and permeability), and thus has significant influences on the formation of landforms and practical engineering problems such as underground water modeling, hydrocarbons exploitation and nuclear waste disposal (e.g., Barton & Larsen, 1985; Lorenz et al., 1991; Narr & Suppe, 1991; Ji & Saruwatari, 1998; Ji et al., 1998; Bahat et al., 2005; Van Noten & Sintubin, 2010; Hassanpour et al., 2011; Wong et al., 2018; Ji & Li, 2020). Thus, the knowledge of joints is important to rock engineering and hydrologic applications (excavations of underground openings and chambers, open pits of mines, quarrying operations, slope stability, and groundwater and toxic waste leakage and flow) and fundamental geological research (e.g., determination of paleostress field, and structural control on landforms and drainage patterns). For these reasons, joints in sedimentary rocks have received extensive researches since the 1940s (Bogdanov, 1947; Lachenbruch, 1961; Sowers, 1973; Roberts, 1974; Ramsay, 1980; Huang & Angelier, 1989; Narr & Suppe, 1991; Captuo & Hancock, 1999; Bai & Pollard, 2000; Gillespie et al., 2001; Van Noten & Sintubin, 2010; Tan et al., 2014).

In layered sedimentary rocks, tensile fractures, such as joints and veins, cut through competent beds (e.g., limestone or sandstone) and terminate at the interfaces with adjacent incompetent layers (e.g., shale or mudstone). The spacing (s), which is defined as the perpendicular distance between two adjacent joints or veins of the same set, is one of the primary geometric characteristics for the fractures (Dershowitz & Einstein, 1988). It has been reported that joint spacings have a linear relationship with mechanical bed thicknesses (t) in sedimentary rocks (e.g., Harris et al., 1960; Huang & Angelier, 1989; Narr & Suppe, 1991; Gross et al., 1995; Ji & Saruwatari, 1998; Ji et al., 1998; Tindall & Davis, 2003; Jiang et al., 2013; Rustichelli et al., 2013; Guerriero et al., 2015; Saein & Riahi et al., 2017; Bao et al., 2019). However, nonlinear relationships between s and t were also documented by other studies (Norris, 1966; Mastella,

1972; McQuillan, 1973; Ladeira & Price, 1981; Mandal et al., 1994). Some workers argued that there is a critical value of bed thickness (t_c), above and below which the *s*-*t* relation can be presented by linear relationships with smaller and larger slope values, respectively (Angelier et al., 1989; Price & Cosgrove, 1990). Therefore, if a generalized functional relation being able to describe the *s*-*t* variation in the full range of measured bed thickness exists, it will help to reconcile the previous contrasting models for joint spacing (*s*) in layered sedimentary rocks.

Orthogonal joints, which consist of two sets of nearly vertical, opening mode, brittle fractures aligned at almost right angles, are very common in folded or flat-lying sandstones on platforms (e.g., Hancock, 1985; Gauthier & Angelier 1986; Hancock et al., 1987; Bahat, 1989; Dunne & North, 1990; Rives et al., 1994; Caputo, 1995) or the external zones of the orogenic belts (e.g., Ji et al., 2021a). Orthogonal joints with a variety of abutting and cross-cutting relationships result in a characteristic landform named as 'tessellated pavement', because the sandstone bedding surface is fractured into more or less regular rectangular blocks that resemble tiles of a mosaic floor or tessellations (e.g., Branagan, 1983). Famous examples of tessellated pavement (Fig. 4.1) are observed at the Eaglehawk Neck (Tasmania, Australia) and St. Mary's Chapel (Caithness, Scotland) which are geological wonders attracting tourists. The origin of orthogonal joints are worth studying (e.g., Hancock, 1987; Dunne & North, 1990; Rives et al., 1994; Caputo, 1995), not only because of their important role in forming fabulous landscapes, but also because they tremendously influence permeability of fluid (e.g., water, gas, oil, and pollutants, Bear et al., 1993; Thunvik & Braester, 1990), rock mass strength and mechanical stability (e.g., Einstein et al., 1983; Shang et al., 2016, 2018), and erosion rate of the uppermost crustal rocks (e.g., Ji & Saruwatari, 1998; Ji et al., 1998; Rawnsley et al., 1998; Bahat, 1989; Tang et al., 2008).

Orthogonal joints viewed on a bedding-parallel surface can be geometrically classified as two types:

(a) Ladder-pattern network in which cross joints extending across intervals between long, parallel joints but do not cut across these joints (e.g., Gross, 1993; Rives et al., 1994; Rawnsley et al., 1998);

(b) Fracture grid-lock system in which both orthogonal joints systematically abut and cross-cut each other (e.g., Hancock et al., 1987; Dunne & Hancock, 1994; Rives et al., 1994).

For the ladder-pattern network, cross joints extend across intervals between long, parallel, systematic joints but generally do not cut across these joints (e.g., Gross, 1993; Rives et al., 1994; Rawnsley et al., 1998). According to linear elastic fracture mechanics (e.g., Jaeger & Cook, 1979), an extension or mode I fracture forms perpendicularly to the minimum principal stress (σ_3) trajectory and parallel to the principal stress plane containing the maximum principal stress σ_1 and intermediate principal stress σ_2 directions (e.g., Hancock, 1985; Gross, 1993; Ji & Saruwatari, 1998; Ji et al., 1998; Jain et al., 2007; Tang et al., 2008). As each of the orthogonal joint sets is extension fractures, the presence of orthogonal joints has been argued due to rotation of the local or regional σ_3 direction by about 90º. The local stress rotation is presumably caused by stress release on newly formed systematic fractures (e.g., Simón et al., 1988; Caputo, 1995; Dunne & North, 1990; Rives et al., 1994; Tang et al., 2006) or reduction in joint spacing to bed thickness ratio (e.g., Bai et al., 2002; Boersma et al., 2018). Do the systematic and cross joints, which formed by different mechanisms, have different s-t relationships although they developed in the same lithological layers?

Although the existent models may explain some features of ladder-pattern of systematic and cross joints, it is difficult for the workers to convincingly interpret the formation of grid-lock-type orthogonal joints that mutually abut and intersect (Fig. 4.1). Is there an alternative interpretation for formation of fracture grid-lock system? Does the fracture grid-lock system arise as a consequence of roughly simultaneous extension along two orthogonal directions along the layer? In flat-lying sandstone terrains, for example, whether does the presence of orthogonal joints indicate a stress field where effective σ_1^* (compressive) is vertical whereas both σ_2^* and σ_3^* are horizontal and tensile ($\sigma_3^* \leq \sigma_2^* < 0$)?

In this chapter, we summarize the results of anatomic investigations on ladder-pattern of orthogonal joints in sandstone beds of the Tourelle Formation in the Sainte-Anne des Monts area (the Gaspé Peninsula, Quebec, Canada) (Figs. 4.2-4.3) and grid-lock-pattern of orthogonal joints in quartz sandstone from the Potsdam Group at the Ausable Chasm (New York State, USA) and Beauharnois (Quebec, Canada) (Fig. 4.4). The systematic and cross joints from the Tourelle Formation show that the best-fit relationship for the *s-t* is a power law ($s=mt^n$) in the full range of measured bed thicknesses. In addition, the physical implications of the parameters in this power law relationship are examined. It is found that *m*, the pre-exponential parameter, is related to the ratio between the tensile strength (C_0) of the competent bed to the shear strength (τ) of the

interfaces between the competent and incompetent beds, whereas *n*, the exponent, is a measure of the Weibull modulus (*k*) of the jointed beds. The Weibull modulus is a parameter, which describes the frequency of brittle failure of materials (Weibull, 1939, 1952). We also propose a new, alternative interpretation that the formation of grid-lock-type orthogonal joints in the Potsdam Group may result from auxetic effects of quartz sandstone rather than the rotation of the maximum tensile stress direction by about 90º. The flat-lying sandstone layers had presumably negative values of Poisson's ratio at the time of joint formation so that, when deformed by compression of the overburden, transverse contraction-induced horizontal tensile stresses in the bedding plane, producing two roughly orthogonal sets of vertical, opening-mode fractures that initiate at various flaws.

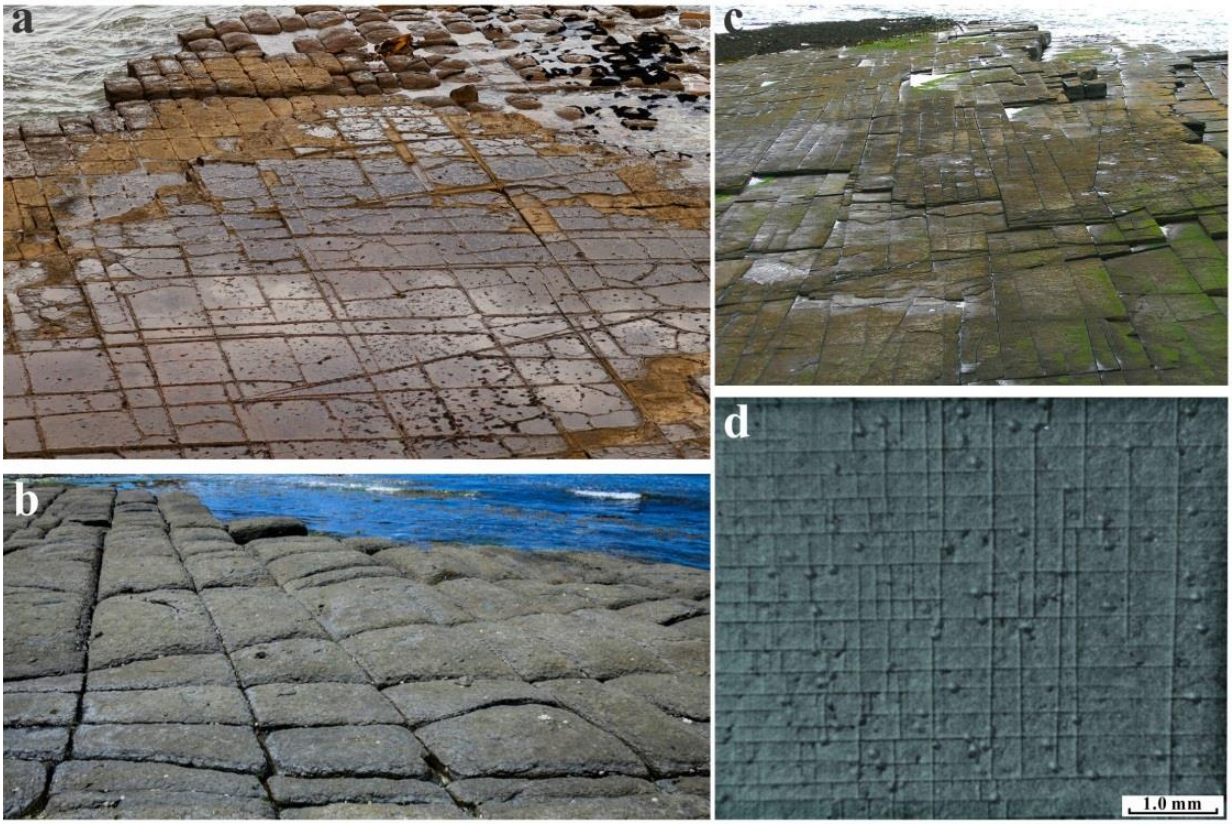

Figure 4.1 Traces of orthogonal systematic joints defining a grid-lock pattern. (a-c) Views on a bedding surface of quartz sandstone from Eaglehawk Neck, Tasmania, Australia (a-b) and St. Mary's Chapel, Caithness, Scotland (c). (d) Orthogonal fractures produced in brittle varnish by orthogonal loadings (Rives et al., 1994). Courtesy Carolyn Bell, Stephanie Sykora, and Mike Norton for pictures (a), (b) and (c), respectively.

The present study has produced two research papers: (1) A new interpretation for formation of orthogonal joints in quartz sandstone (Journal of Rock Mechanics and Geotechnical Engineering, 13, 289-299, 2021), and (2) Power-law relationship between joint spacing and bed thickness in sedimentary rocks and implications for layered rock mechanics (Journal of Structural Geology, 15, 104413, 2021).

4.2 Geological setting

Field observations and measurements were performed on the Tourelle Formation in the Sainte-Anne-des-Monts area (Fig. 4.2) and the Potsdam Group at the Ausable Chasm and Beauharnois (Fig. 4.4). The high quality outcrops provide an excellent opportunity for us to measure and statistically analyze different types of orthogonal joints.

4.2.1 Geological setting of the Tourelle Formation

The Tourelle Formation, which consists of interlayered sandstone, siltstone and shale beds, crops out from the region of Rivière-du-Loup to the eastern tip of the Gaspé Peninsula, and lies above the Logan's line (Cousineau, 1998, Fig. 4.2). Studies on the provenance of detrital components and depositional environment of the Tourelle Formation reveal that the flysch sedimentary rocks in the formation were turbidites deposited in the marginal basin south to the North American Craton during the Early Ordovician (Hiscott, 1978, 1980; Hiscott & Middleton 1980). The sedimentary rocks in this formation were then intensively folded and deformed in the lowest allochthonous thrusting nappe in the Humber zone during the Taconic orogeny (St-Julien & Hubert, 1975; Hiscott & DeVries, 1995; Cousineau, 1998). Little metamorphism occurred in the sedimentary rocks of this formation and the estimated maximum burial depth for the sedimentary rocks is about 4-5 km.

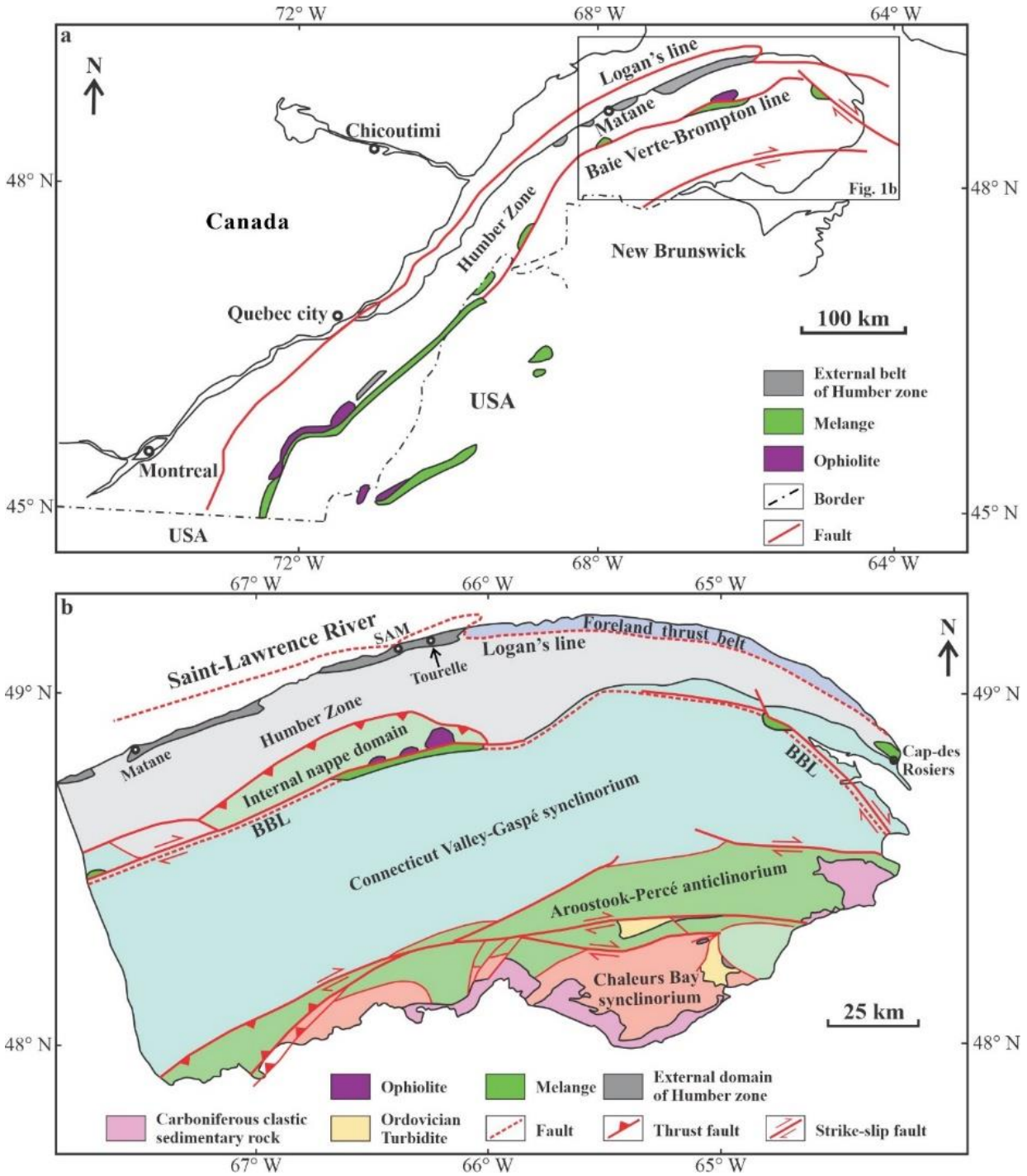

Figure 4.2 Simplified geological map displaying the study area. (a) and (b) are modified from Cousineau (1998), Malo et al. (2001) and Ji et al. (2021).

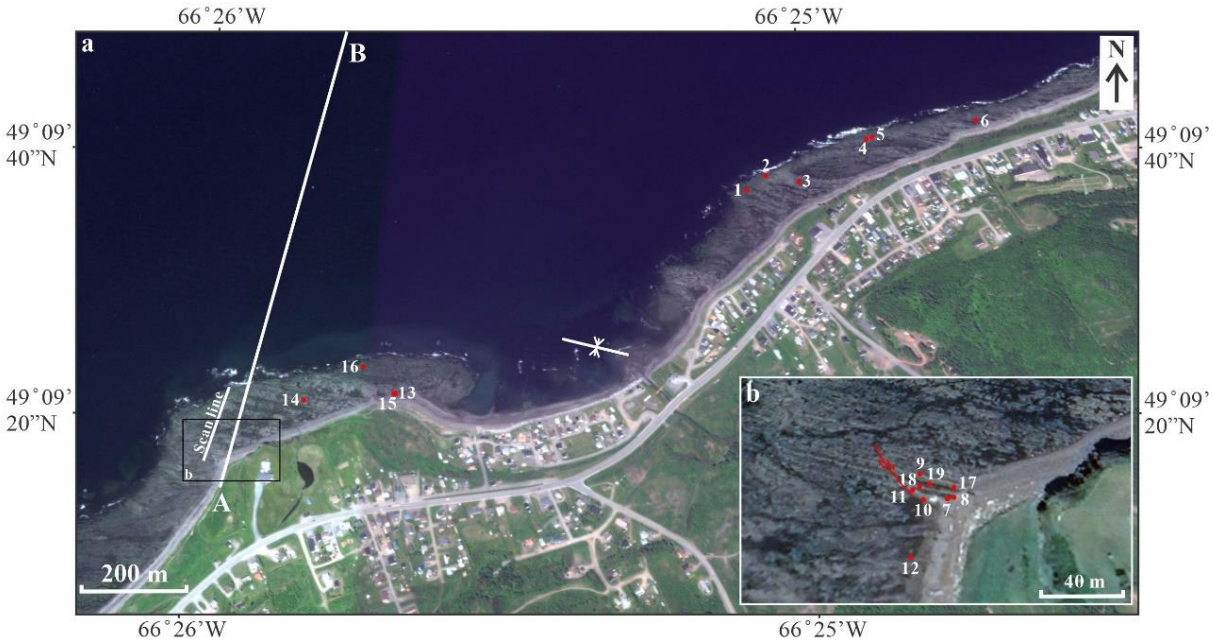

Figure 4.3 (a-b) Satellite images showing the sites of measurements on the rocky beaches of Saint-Joachin-de-Tourelle, Quebec, Canada. Modified from Ji et al. (2021a).

4.2.2 Geological setting of the Potsdam Group

The Potsdam sandstone, which is bedded in moderately thick, uniform layers, was deposited along the edge of Ottawa Embayment and Quebec Basin on the Laurentian margin during the Cambrian period (~520-500 Ma, Landing et al., 2009; Sanford & Arnott, 2009). Rivers located on the northwestern continental shoreline flowed into the shallow sea and deposited deltas of sand. Fisher (1968) reported a cumulative stratigraphic thickness of 450 m for the Potsdam sandstone in the northern Champlain Lowland just between sites 1 and 2 in Fig. 4.4b. In the northeastern Adirondack margin, however, the Potsdam sandstone has a thickness of nearly 300 m (Chiarenzelli & Selleck, 2016). The sandstone exposed at the sites consists of clean washed quartz sand cemented by silica (e.g., Globensky, 1987), and some beds contain a little clay and other impurities (Sanford & Arnott, 2009). The quartz-rich sandstone of the Potsdam Group, which contains a porosity between 3.0% and 3.5%, displays abundant ripple marks caused by tide on sandy beach (Fig. 4.5) and cross beds and dewatering structures formed by the migration of subaqueous dunes during sand deposition. The tide-dominant shallow marine quartz arenite of the Potsdam Group overlies non-conformably on the Precambrian metamorphic basement

consisting of gneisses and intrusive rocks such as anorthosite, granite and tonalite of 1.35-1.00 Ga, Chiarenzelli & Selleck, 2016). The Potsdam group is conformably but abruptly overlain by dolostone, dolomitic limestone, sandstone and shale of lower Ordovician age (the Beekmantown Group, about 305 m thick), which were deposited in a shallow sea environment (Selleck, 1993; Globensky, 1987; Salad Hersi et al., 2002, 2003; Dix et al., 2004; Lavoie, 2008).

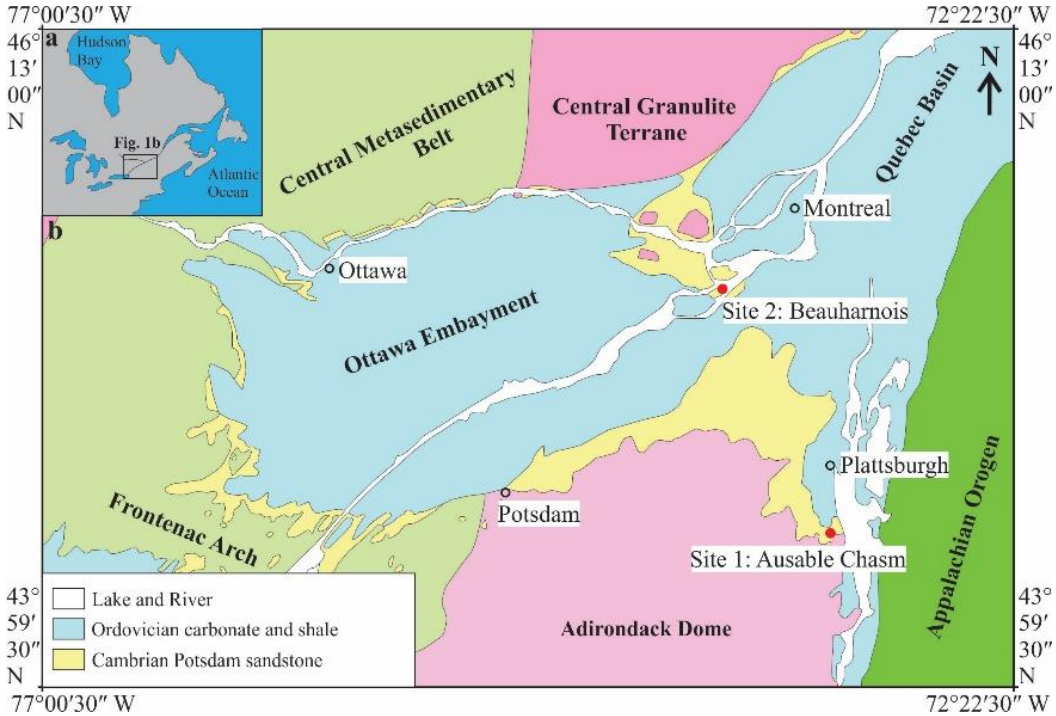

Figure 4.4 Simplified geological map showing the distribution of the Potsdam sandstone and the sites of study. Modified from Lowe et al. (2015). Stratigraphic column of the study region can be found from Globensky (1987) and Salad Hersi et al. (2003).

Figure 4.5 Tide-formed ripple marks observed on the upper bedding surface of quartz sandstone at the Ausable Chasm (New York State, USA). The mechanical pencil is 14.5 cm.

Site 1 is located at the Ausable Chasm which is a gorge developed in the Potsdam sandstone. Through this gorge, the Ausable River runs for several kilometers from the area just northeast of Keeseville (New York State) toward Lake Champlain. The gorge is as deep as 90-150 m in places and only 6-15 m wide for narrow parts. The occurrence of such high vertical side walls indicates that the quartz arenites of the Potsdam Group are mechanically strong and chemically stable; otherwise the walls should be broken down and form a valley with the normal V-shaped profile. Since it was first seen by non-native Americans in 1765, the Ausable Chasm has been regarded as among the natural wonders of eastern North America and presents an important tourist attraction for geological heritage (Resser, 1942). Like many canyons and gorges in the world (e.g., the Grand Canyon carved by the Colorado River in Arizona, USA), the Ausable Chasm results from erosion of running water of a swift river along well-developed joints in flat-lying sandstones. Site 2 is a large continuous outcrop located near the Dam of Beauharnois Power Plant of Hydroquebec, Canada (Fig. 4.4).

4.3 Field observations

In this chapter, the attitudes of planes (beds or joints) are described by strike and dip according to the right-hand rule. The strikes are represented by three numbers, whereas the dips are represented by two numbers (SSS/DD). The maximum uncertainties of measurements for the strikes and dips are ±2°.

4.3.1 Observation on the systematic and cross joints (Sainte-Anne-des-Monts)

In the Sainte-Anne-des-Monts region, two sets of orthogonal tensile joints (Fig. 4.6) developed in the sandstone beds of the Tourelle Formation and are nearly normal to the bedding surfaces (S_0). The two joint sets are referred to as the gently-dipping set J1 and steeply-dipping set J2, which display average attitudes of (148º, 22º) and (018º, 78º), respectively (Fig. 4.7). The combination of sets J1 and J2 joints forms saw-teeth-shaped landforms of small-scale (Fig. 4.6c and d). Observation reveals that the Set J1 is more persistent than the Set J2 (Figs. 4.6, 4.8 and 4.9), making a typical ladder-pattern network. Joints of Set J2 commonly extend between and abut their adjacent joints of Set J1, forming the "T" and "H" shapes of trace (Fig. 4.8, Hancock, 1985). Thus, Set J1 is the systematic joint while Set J2 is the cross joint. A cross joint forms always later than the systematic joints that it abuts. The upper limit for the length of a cross joint is thus controlled by the distance between the two systematic joints that contains it.

Figure 4.6 Photographs of the typical outcrops (a and b, NE to SW) of interlayered sandstone (siltstone) and shale in the study area. Saw-teeth-shaped small-scale landforms (c and d) created by gently-dipping (J1) systematic joints and steeply dipping (J2) cross joints in thin beds of sandstone.

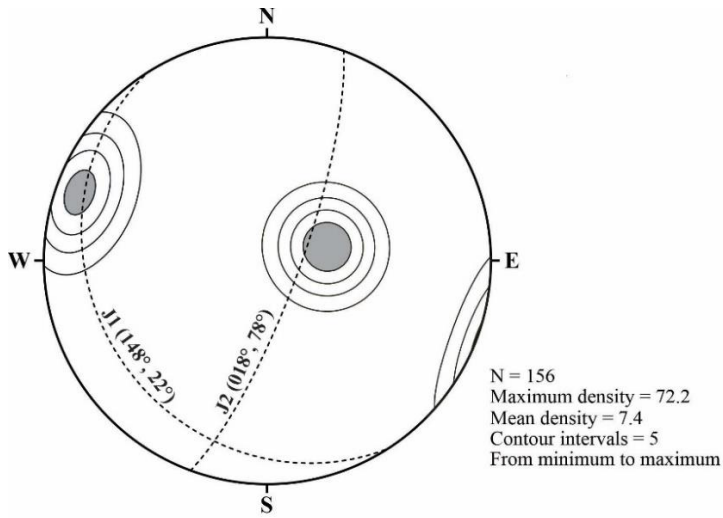

Figure 4.7 Preferential orientations of J1 and J2 joints in sandstone layers in the study area. 156 measurements (N(J1)=77 and N(J2)=79). The average attitudes of J1 and J2 joints are (148º, 22º) and (018º, 78º), respectively.

Figure 4.8 Ladder-pattern of orthogonal joints (sets J1 and J2) observed on sandstone bedding surfaces. J2 joints, which are less persistent than J1, extend across intervals between J1 joints and abut J1 joints at ~90º angles. Scale in (a) is 1 m.

Plumose structures were observed in joint surfaces of both sets J1 (Fig. 4.10) and J2 (Fig. 4.11) in uniform fine-grained siltstones. Analyses of these plumose structures indicate that the joints initiated and propagated, in the direction perpendicular to the maximum tensile stress (σ_3), away from stress-concentrated point defects at the interfaces between sandstone and mudstone (Fig. 4.11a) and somewhere within the sandstone beds (Figs. 4.10, 4.11b-c).

Figure 4.9 Steeply-dipping J2 joints observed on the J1 joint surfaces in thick sandstone layers. The joint spacing of J2 and particularly that of J1 are significantly smaller than the bed thickness.

Figure 4.10 Plumose structures observed on the J1 joint surface in a fine-grained sandstone. The propagation direction of the fracture is indicated by arrow.

Figure 4.11 Plumose structures observed on the J2 joint surface in sandstone layers. The plumose diverges from a point on (a) and near (b) the lithological interface and within the layer (c). The propagation direction of the fracture is indicated by arrow.

It is noted that the initiation of tensile fractures is more common at lithological interfaces than in the central portion of the competent layers, which is consistent with previous observations documented in McConaughy and Engelder (2001), Cooke et al. (2006), and Simón et al. (2006). In addition, no joint contain detectable mineral fill (Figs. 4.6, 4.8-4.11), indicating that brittle fracturing occurred at relatively shallow depths where temperature was so low that the solubility of quartz or calcite was too low to form veins along the joints (e.g., Dunne & North, 1990; Van Noten & Sintubin, 2010). The unmineralized joints may also indicate that fluid pressure was relatively low during the joint formation (Rawnsley et al., 1998; Van Noten & Sintubin, 2010).

4.3.2 Observation on the grid-lock type orthogonal joints (Ausable Chasm and Beauharnois)

The bedding in the Potsdam quartz arenite gently dips northwestward with an attitude (314°, 05°) at Ausable Chasm (Figs. 4.12-4.13). Two sets of planar, vertical joints (one set aligned at ~140° and the other set at ~050°, which will be referred to as set J1 and set J2, respectively; Fig. 4.14) at almost right angles to each other cut systematically the sandstone so that almost everywhere the rock can be taken out in more or less rectangular cuboidal blocks (Fig. 4.15). The blocks bounded by orthogonal joints and bedding surface more readily fall down and then are carried away by running water along the stream. The channel has formed by removal of block after block since the end of the Pleistocene Epoch ice age (which ended up there around 15,000 years ago, Resser, 1942).

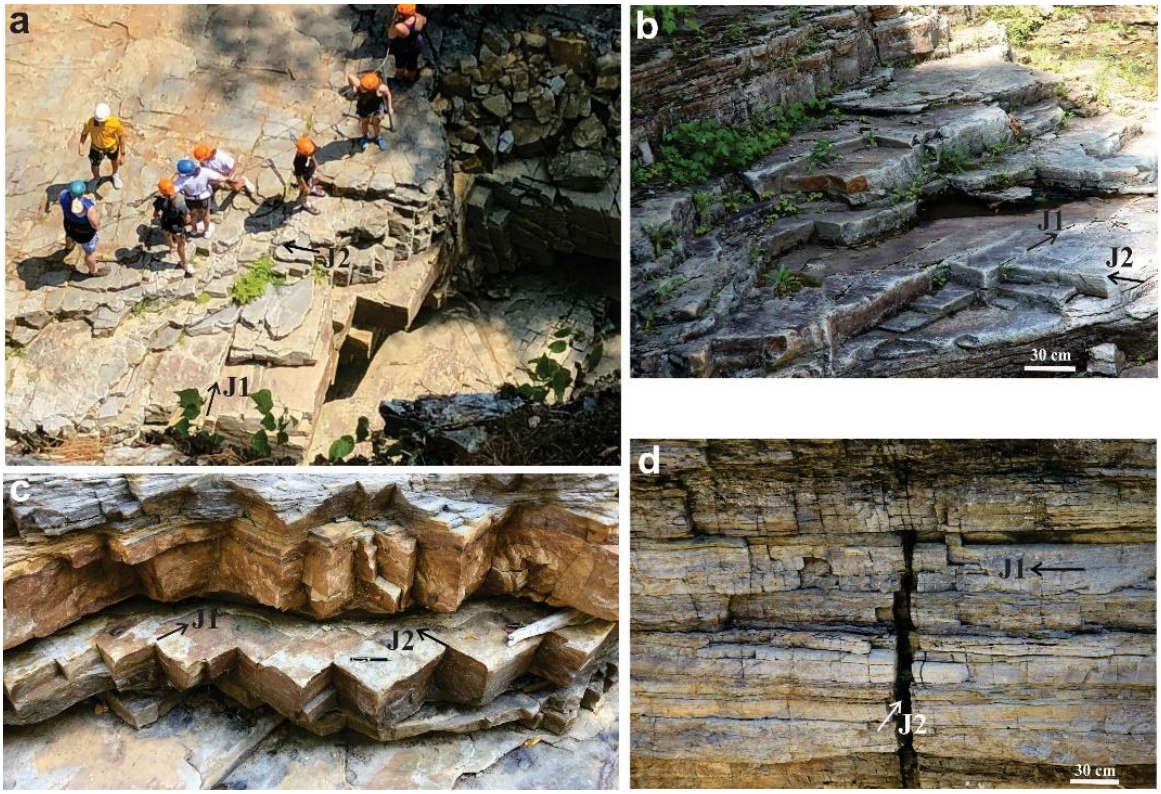

Figure 4.12 Characteristics of orthogonal joints (set J1 and J2) observed in quartz sandstone at Ausable Chasm (New York State, USA). Set 1 is generally more persistent than set 2. Note that the observation surface in (d) is parallel to joint plane of set 1. In central part of (d), a throughgoing open fracture developed late by coalescence and linkage of joint J2 across bed boundaries. The pen is 13.5 cm.

Field observations display that NW-SE trending joint set 1 is more persistent than NE-SW trending joint set 2, although both sets are interpreted to be systematic joints. These orthogonal joints are organized essentially in grid-lock pattern (Figs. 4.12-4.13; Gauthier & Angelier, 1986; Hancock et al., 1987; Caputo, 1995) rather than ladder pattern (Gross, 1993; Bai et al., 2002). Mutual abutting/cutting relationships (e.g., both sets abut each other) indicate that the orthogonal joints are geologically coeval extension (Haccock et al., 1987; Caputo, 1995). Furthermore, these joints are opening-mode fractures and display no detectable shear displacement along them (Figs. 4.12-4.13). No joints contain detectable mineral fill (Figs. 4.12-4.13), indicating that brittle fracturing occurred at shallow depths where temperature was so low that the solubility of quartz or calcite was too low to form veins along the joints (e.g., Dunne & North, 1990; Van Noten &

Sintubin, 2010). Rawnsley et al. (1998) took this phenomenon as an indicator that fluid pressure was relatively low during the joint formation.

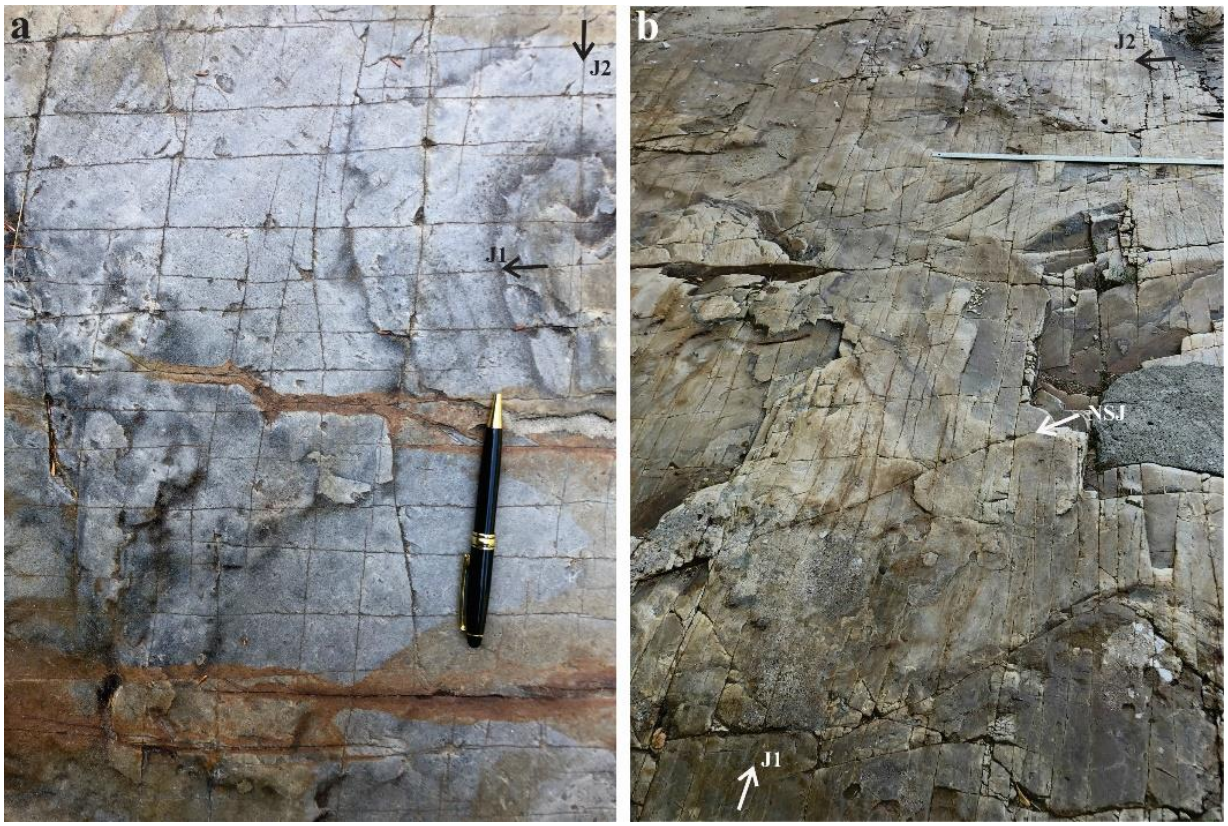

Figure 4.13 Geometrical relationships between two sets of orthogonal systematic joints (set J1 and J2), observed on bedding-parallel surface of quartz sandstone at Ausable Chasm (New York State, USA). Mutual intersecting and abutting suggest that the orthogonal joints are geologically coeval. NSJ: Non-systematic joint.

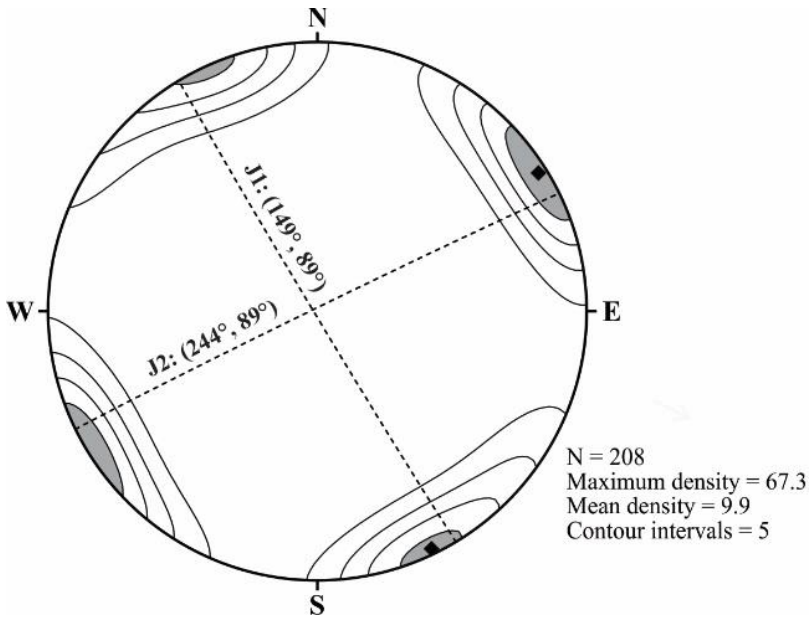

Figure 4.14 Preferential orientations of orthogonal joints in quartz sandstone at Ausable Chasm (New York State, USA). N: number of measurements.

It is interesting to note that the Ausable River at site 1 is not straight and makes a right-angle turn from the northwest direction to the northeast direction near the highway bridge (Fig. 4.16a) and the Whirlpool basin (Fig. 4.16b). The northwest- and northeast-oriented stream segments are roughly parallel to vertical joints of J1 and J2, respectively. The chasm walls stand vertical, straight and smooth because the walls are parallel to one set of the orthogonal joints. Thus, the Ausable Chasm provides a good example of the control of systematic vertical joints on orientation of gorge.

Figure 4.15 Rectangular cuboidal sandstone blocks bounded by vertical orthogonal joints and horizontal bedding surface at Ausable Chasm (New York State, USA).

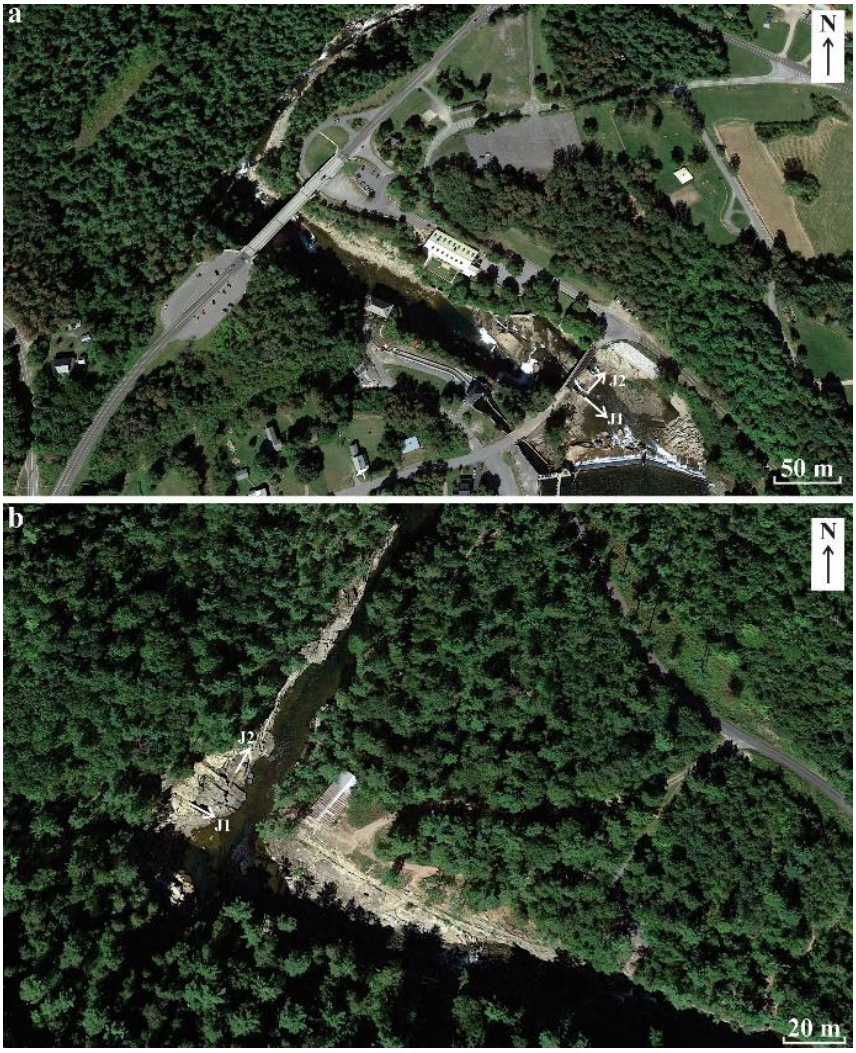

Figure 4.16 Orthogonal joints control on gorge orientation at Ausable Chasm (New York State, USA). The Ausable River makes a right-angle turn from the northwest direction (joint set J1) to a northeast direction (joint set J2) near the highway bridge (a) and the Whirlpool basin (b).

At site 2, the bedding in the Potsdam quartz arenite gently dips southwestward with an attitude (236°, 03°) and vertical orthogonal joints can be clearly seen on the Google map (Fig. 4.17a) with one set striking about 301° and the other set striking about 212° (Fig. 4.17b).

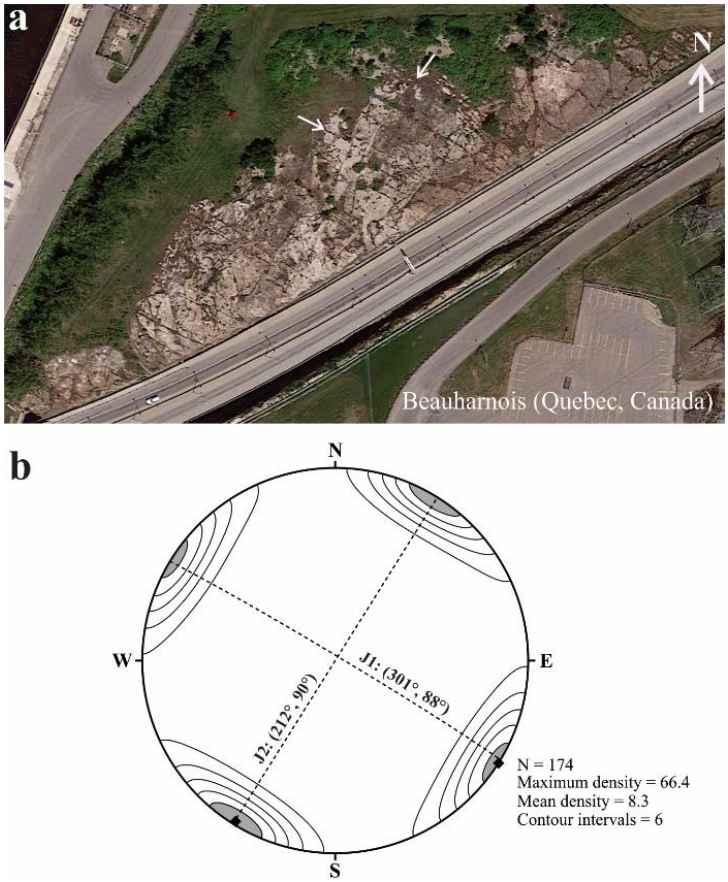

Figure 4.17 Orthogonal joints (a) and their preferential orientations (b) in sandstone at Beauharnois. Quebec, Canada. N: number of measurements.

4.4 Methodology

Joint spacings were measured from 109 sandstone beds along the scanline perpendicular to the bedding (S_0) (Fig 4.3a) and 14 sandstone beds (Fig. 4.3b). In addition, the thicknesses (*t*) of each measured fractured bed and its immediately adjacent incompetent layers (i.e, mudstone or shale) were also measured. The selected sandstone beds display uniform lithology and thickness along its strike. All the fractures cutting through the whole bed were taken into account. Short fracture spacings were carefully identified and recorded in order to avoid potential bias (Huang & Angelier, 1989). As the joint sets are nearly vertical to the bedding planes, the measurements of joint spacing were performed on the bedding plane, and in this case no more correction need to be done.

4.5 Results of measurements

4.5.1 Joint spacing of the systematic and cross joints (Sainte-Anne-des-Monts)

Joint spacing measurement was performed on 109 sandstone beds along the scanline perpendicular to the bedding (S_0) (the location of the scanline in Fig 4.3a) and 14 sandstone beds (Fig. 4.3b, Table 4.1), respectively. The number of measurement on each bed of the 14 sandstone beds was greater than that of the 109 sandstone beds. The uncertainties of measurement for either bed thickness or joint spacing are ±0.2 cm.

Table 4.1 Statistical analyses of joint spacing data measured from sandstone layers of the Tourelle Formation in the region of Ste-Anne-des-Monts (Quebec, Canada)

		Bedding	*t*	*d1*	*d2*	Joint		Mean	Median	Mode	SD	
Bed No.	**Joint set**	**attitude**	**(cm)**	**(cm)**	**(cm)**	**Attitude**	**N**	**M (cm)**	**Me (cm)**	**Mo (cm)**	**(cm)**	**M_o/M**
3	J2	105, 64	99.0	22.5	33.5	005, 85	10	43.3	42.8	N/A	17.0	N/A
4	J2	085, 61	93.5	16.0	51.5	179, 88	45	33.9	35.5	53.5	21.6	1.6
5	J2	079, 71	25.0	19.0	15.0	005, 86	34	20.0	20.9	22.5	9.7	1.1
7	J2	285, 74	20.5	11.4	51.8	195, 88	97	26.4	23.8	11.5	14.8	0.4
8	J2	280, 65	2.8	49.0	53.5	023, 63	143	9.8	8.5	7.8	6.3	0.8
8	J1	280, 65	2.8	49.0	53.5	148, 21	100	4.1	3.5	2.9	2.3	0.7
9	J2	289, 66	10.5	3.1	8.5	222, 82	139	21.0	19.2	19.2	9.5	0.9
9	J1	289, 66	10.5	3.1	8.5	163, 16	90	9.6	9.1	9.5	4.1	1.0
10	J2	287, 69	8.4	84.0	-	025, 66	83	18.6	17.5	3.5	10.9	0.2
10	J1	287, 69	8.4	84.0	-	171, 27	67	8.0	6.7	4.2	4.8	0.5
11	J2	292, 73	9.2	11.5	7.2	031, 81	143	16.5	15.0	10.2	8.9	0.6
11	J1	292, 73	9.2	11.5	7.2	170, 36	73	9.3	8.9	8.9	4.0	1.0
12	J2	285, 66	5.2	36.6	5.8	029, 85	223	8.4	7.4	7.2	4.7	0.9
12	J1	285, 66	5.2	36.6	5.8	125, 24	103	5.1	4.9	4.5	2.3	0.9
14	J2	286, 72	129.0	24.5	72.5	026, 82	80	52.9	46.8	59.0	31.1	1.1
14	J1	286, 72	129.0	24.5	72.5	110, 11	29	18.2	19.0	19.0	9.7	1.0
16	J2	278, 72	18.2	-	83.8	002, 89	324	25.0	17.7	9.2	22.5	0.4
16	J1	278, 72	18.2	-	83.8	161, 05	52	17.0	16.4	12.2	7.6	0.7
17	J2	280, 82	3.0	5.8	6.0	014, 75	130	12.8	11.7	7.6	6.6	0.6
17	J1	280, 82	3.0	5.8	6.0	177, 18	120	6.0	5.7	3.6	2.7	0.6
18	J2	286, 68	6.2	1.0	11.1	022, 60	162	17.9	16.1	7.2	12.6	0.4
18	J1	286, 68	6.2	1.0	11.1	148, 29	179	4.0	3.6	3.2	2.0	0.8
19	J2	286, 82	3.0	1.0	6.1	014, 80	139	14.4	12.9	14.2	9.6	1.0
19	J1	286, 82	3.0	1.0	6.1	183, 17	106	5.5	5.5	6.2	2.5	1.1

Table 4.1 Statistical analyses of joint spacing data measured from sandstone layers of the Tourelle Formation in the region of Ste-Anne-des-Monts (Quebec, Canada) (continued)

Bed No.	Joint set	SD/M	*s/t*	Max (cm)	Min (cm)	Skewness	Kurtosis	Geomean	Weibull distribution ShP	Weibull distribution ScP	Gamma distribution ShP	Gamma distribution ScP
3	J2	0.39	0.43	76.5	14.0	0.30	1.04	39.8	2.90	48.53	6.16	7.03
4	J2	0.64	0.38	83.0	1.2	0.39	-0.76	25.2	1.55	37.51	1.83	18.49
5	J2	0.49	0.84	42.0	5.2	0.50	-0.50	17.6	2.23	22.63	4.06	4.92
7	J2	0.56	1.16	85.0	4.3	1.62	3.60	22.9	1.92	29.89	3.71	7.12
8	J2	0.65	3.04	34.2	2.2	1.41	2.07	8.1	1.67	11.03	2.74	3.57
8	J1	0.55	1.25	11.3	0.6	1.00	0.89	3.5	1.95	4.67	3.40	1.21
9	J2	0.45	1.83	55.8	3.6	0.51	0.23	18.7	2.36	23.74	4.40	4.77
9	J1	0.43	0.86	22.6	2.1	1.09	1.50	8.7	2.46	10.79	5.77	1.66
10	J2	0.59	2.08	53.5	2.2	1.09	1.46	15.4	1.80	21.00	2.82	6.60
10	J1	0.59	0.80	20.1	1.0	0.81	0.05	6.6	1.78	9.04	2.69	2.98
11	J2	0.54	1.63	54.6	3.1	1.04	1.55	14.2	1.99	18.66	3.55	4.64
11	J1	0.43	0.97	23.0	2.9	0.71	0.70	8.4	2.49	10.49	5.30	1.75
12	J2	0.55	1.44	25.8	1.1	1.22	1.85	7.2	1.93	9.55	3.46	2.44
12	J1	0.45	0.95	12.2	1.3	0.64	0.18	4.6	2.39	5.80	4.82	1.06
14	J2	0.59	0.36	-	4.5	0.88	0.73	43.6	1.80	59.65	2.75	19.24
14	J1	0.53	0.15	42.0	2.5	0.79	0.44	15.6	2.02	20.59	3.36	5.42
16	J2	0.90	0.97	-	1.1	1.86	4.33	17.3	1.22	26.78	1.52	16.43
16	J1	0.44	0.90	39.0	4.6	0.52	-0.05	15.3	2.44	19.26	4.84	3.52
17	J2	0.52	3.95	31.0	1.9	0.80	0.28	11.1	2.06	14.50	3.62	3.54
17	J1	0.45	1.93	14.1	2.0	0.74	0.13	5.4	2.40	6.82	5.11	1.18
18	J2	0.70	2.60	58.5	1.2	0.72	-0.07	13.1	1.42	19.70	1.74	10.31
18	J1	0.49	0.58	16.1	1.2	1.98	7.66	3.6	2.13	4.56	4.95	0.81
19	J2	0.67	4.30	55.6	0.9	1.36	2.71	11.3	1.57	16.10	2.20	6.56
19	J1	0.45	1.82	16.3	1.1	0.80	2.17	5.0	2.38	6.25	4.69	1.18

Abbrebations: *d1* and *d2* are the shale bed thicknesses below and above the jointed sandstone layer measured; SD: Standard deviation; ShP: Shape parameter; ScP: Scale parameter; CV: Coefficient variation

Figure 4.18 displays the relationship between joint spacing (*s*) and bed thickness (*t*) of sets J1 and J2 for the 109 measured sandstone beds. The best-fit relation for the data follows a power law:

$$s=2.18t^{0.66}; \quad (R^2=0.83) \qquad (4.1)$$

and

$$s=6.66t^{0.57}; \quad (R^2=0.77) \qquad (4.2)$$

for both Set J1 and Set J2, respectively, in the range of *t* from 0.9 to 760 cm. In Fig. 4.18, it is obvious that a rapid and nonlinear rise of *s* with increasing *t* occurs when *t* is less than ~300 cm, and then an approximate linear increase of *s* along with increasing *t* appears when *t* is greater than ~300 cm, for both both Set J1 and J2. Similar trend has been reported in previous studies (Norris,

1966; McQuillan, 1973; Ladeira & Price, 1981; Mandal et al., 1994; Van Noten & Sintubin, 2010). It's also clear that, for each given value of *t*, the corresponding value of *s* of Set J2 is strikingly greater than that of Set J1.

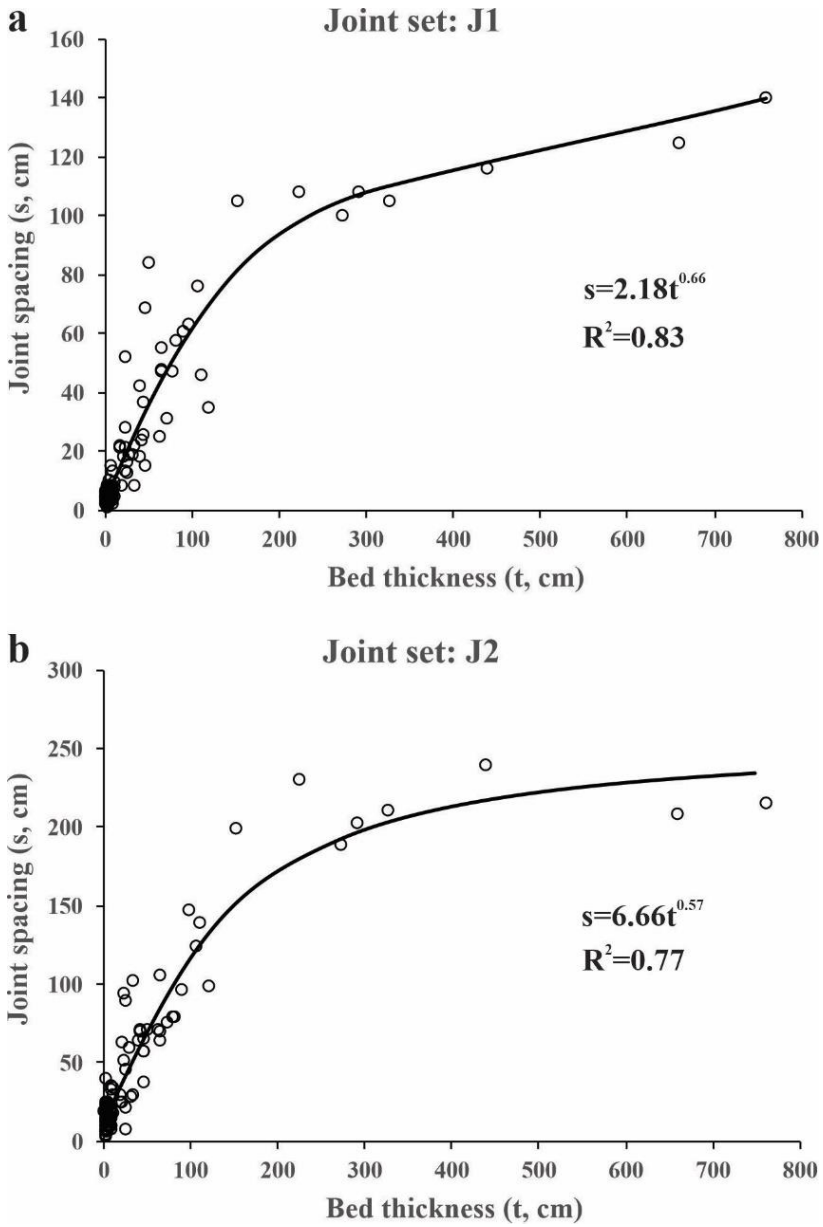

Figure 4.18 Plots of joint spacing (s) versus bed thickness (t) for 109 layers of sandstone measured along a bedding-perpendicular scanline on the beach of Saint-Joachin-de-Tourelle, Quebec, Canada. (a) joint set J1, and (b) joint set J2.

In Fig. 4.19, the median joint spacing of sets J1 and J2 in the 14 sandstone beds were plotted against their bed thicknesses (Table 4.1). In the range of *t* from 2.8 to 129.0 cm, the *s-t*

relationships for sets J1 and J2 of the 14 measured sandstone beds both follow a power law: s=2.86$t^{0.43}$ (R^2=0.73) and s=6.64$t^{0.39}$ (R^2=0.87), respectively.

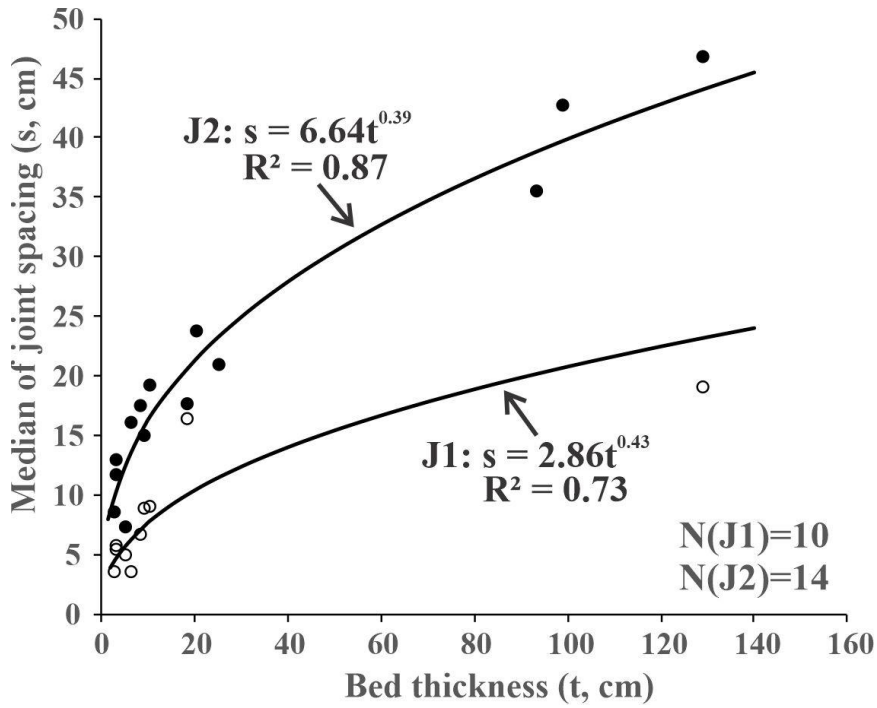

Figure 4.19 Plots of median joint spacing versus bed thickness for joints of sets 1 and 2 in sandstone layers. Data measured collected from 14 sandstone layers of the Tourelle Formation.

Figure 4.20 illustrates the plots of joint spacing as a function of the thicknesses of the incompetent layers (shale) below and above the jointed bed (*d1*and *d2*) for joint sets J1 and J2. The influences of *d1* and *d2* on the joint spacing are less obvious, for the effects of the thicknesses of adjacent incompetent layers (i.e., mudstone) are rather complex on the joint spacing of competent bed (i.e., sandstone) (Ji & Saruwatari, 1998; Ji et al., 1998).

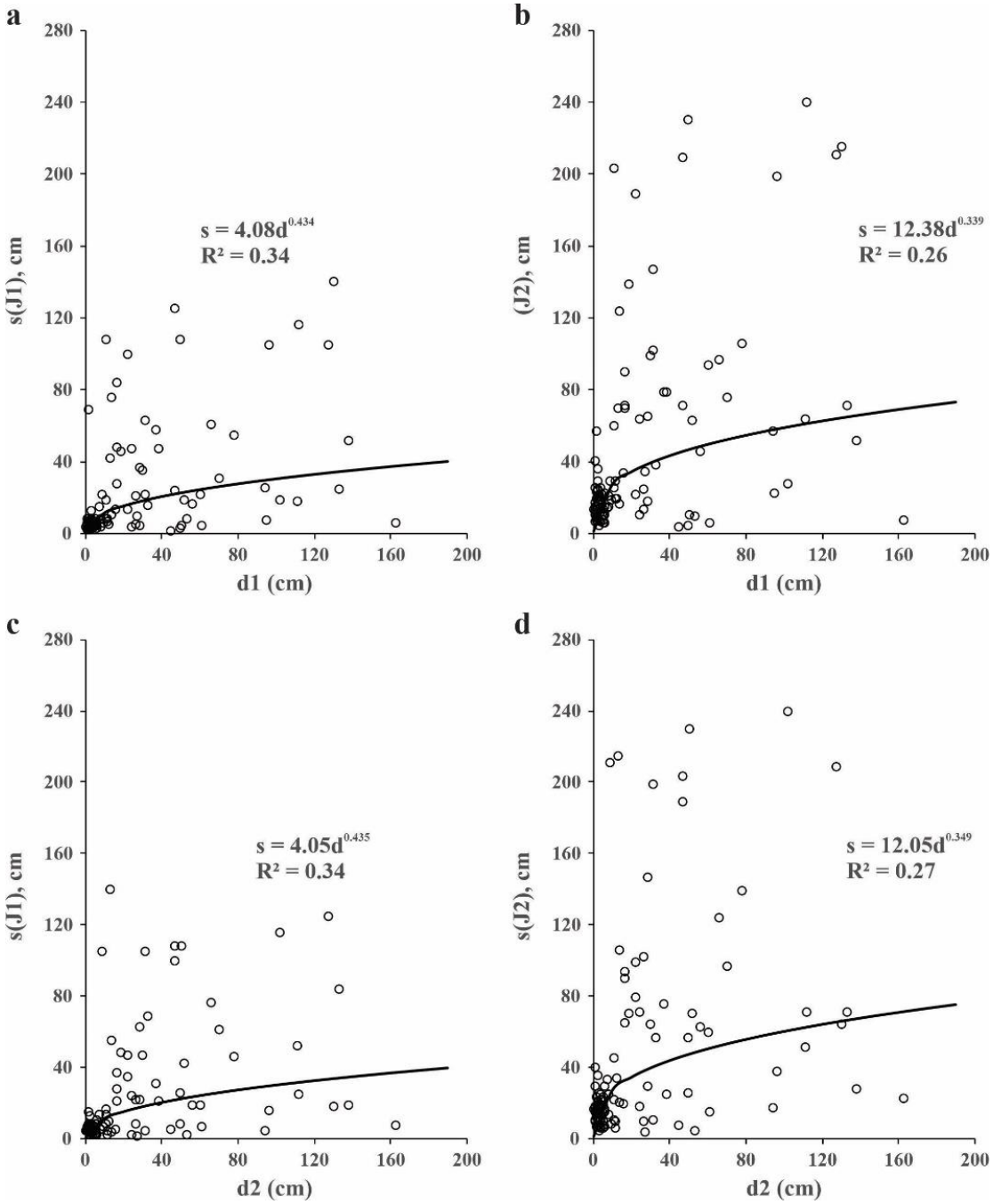

Figure 4.20 Plots of joint spacing versus thickness of shale layer below (*d1*) and above (*d2*) the jointed sandstone bed. (a)-(c) joints of set 1, and (b)-(d) joints of set 2.

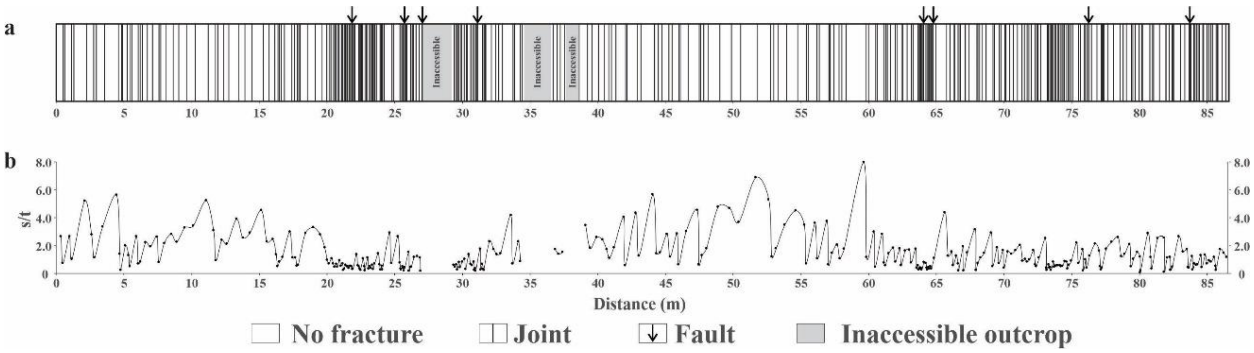

Figure 4.21 Data of joint set J2 (attitude: 002º, 89º), measured from a continuous sandstone layer with a quasi-constant thickness (18.2 ± 0.5 cm), at site 16 (49.15645°N, 66.42905°). 324 measurements. (a) Distribution of joints, and (b) Variation of *s/t* ratio along the layer. Joint spacing and *s/t* ratio systematically decrease near each fault. Arrow: the location of minor fault.

Figure 4.21 show typical features for the distribution of 324 opening-model joints of set J2 and their *s/t* ratios along a 80.7 m-long sandstone layer (No. 16) with an attitude (278°, 72°) and a quasi-constant thickness (18.2±1.0 cm). The measurements yield an average joint spacing (s) of 24.9 cm, and an average *s/t* ratio of 1.37 (standard deviation of 1.24). Eight minor faults group into two conjugate sets based on orientation, one with a mean attitude of (030°, 75°) and the other with (154°, 76°). The mean orientations of slickenlines in the fault planes for the first and second sets are (036°, 25°) and (328°, 26°), respectively. The features shown in Fig. 4.21 indicate that the joint spacing is not regularly spaced even in a lithogically homogeneous layer with a nearly constant thickness. Irregularly alternated high and low values of *s/t* ratios occur over the entire outcrop. The pattern displays no symmetry about the planes of faults. The mean *s/t* ratio near the faults is only 0.38, which is significantly lower near each fault than the mean value (1.37) for the whole sandstone layer. In other words, the joints, which are significant more closely spaced near the faults, have been perturbed by faulting, indicating that faults are post-formation of orthogonal systematic joints. Nevertheless, not all places with closely spaced joints are cut by faults, but the places cut by faults show commonly reduced *s/t* ratios. The interaction between joint and fault can be mutual. On one hand, faulting causes a localized strain concentration that results in high joint densities and thus low *s/t* ratios around faults (Rives et al., 1992; Gross et al., 1997; Ji & Saruwatari, 1998; Ji et al., 1998). On the other hand, the occurrence of densely spaced joints results in locally mechanical weakening, favorable for development of a fault. Hence, faults and

their adjacent closely spaced joints anomalously increase reservoir rock permeability and thus often damage traps and seals for hydrocarbons.

4.5.2 Joint spacing of the grid-lock type orthogonal joints (Ausable Chasm)

Each set of orthogonal joints in the Potsdam Group at Site 1 displays a uniform strike, and is straight and continuous over several meters. As shown in Fig. 4.22, the joint spacing for the NW-SE-oriented set (J1) is statistically about 1/3 of that for the NE-SW-oriented set (J2).

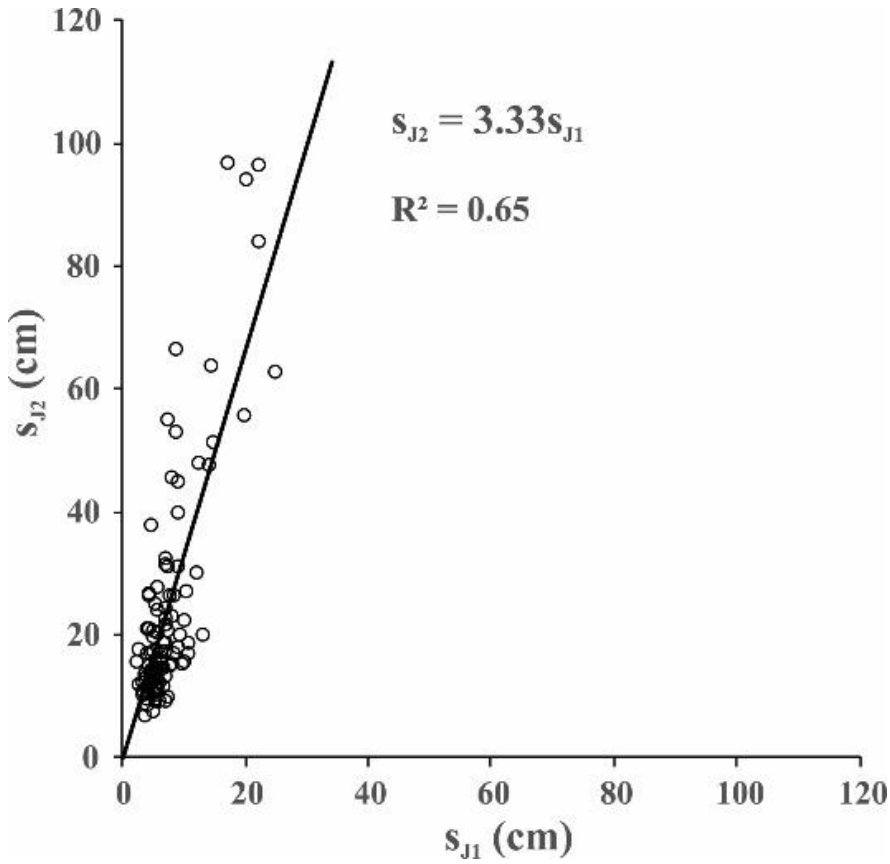

Figure 4.22 Plot of joint spacing for set 1 (s_{J1}) versus joint spacing for set 2 (s_{J2}) for quartz sandstone at Ausable Chasm (New York State, USA). Spacing s_{J1} and s_{J2} are the length and width of each rectangle bounded by joint set J1 and J2, measured on the bedding-parallel surface.

4.6 Discussion

4.6.1 Relationship between joint spacing and layer thickness

Both sets J1 and J2 joints in the Tourelle Formation are confined in the competent sandstone beds and terminate at their boundaries with adjacent mudstone beds, indicating that stratigraphic bed thickness of sandstone defines the mechanical layer thickness in the study area.

It is found that the *s*-*t* data reported in the literature (e.g., Ladeira & Price, 1981; Angelier et al., 1989; Huang & Angelier, 1989; Aydan & Kawamoto, 1990; Gross, 1993; Gross et al., 1995, 1997; Ji & Saruwatari, 1998; Ji et al., 1998; Ruf et al., 1998; Gross & Eyal, 2007; Iyer & Podladchikov, 2009; Van Noten & Sintubin, 2010; Guerriero et al., 2015; Cilona et al., 2016; Saein & Riahi, 2019; Bao et al., 2019) can be equally fitted by a power law over the range of bed thicknesses measured (Ji et al., 2021a).

$$s=mt^n \qquad (4.3)$$

where m is the pre-exponential parameter, and n is the exponent. The m and n values, which can be obtained from the regression of each set of measured *s*-*t* data. In the following, we explain why a power law function can offer an ideal description for the *s*-*t* relationship.

The relation between joint spacing (s) and the bed thickness (t) of fractured layer are commonly described by the equation:

$$2\tau s = Ct \qquad (4.4)$$

where τ is the interfacial shear stress along the competent and incompetent beds, and C is the tensile strength of the competent bed (Kelly & Tyson, 1965; Lloyd et al., 1982; Price & Cosgrove, 1990; Ji et al., 1998; Morrison et al., 1988; Tripathi & Jones, 1998; Li & Ji, 2020).

Eq. (4.4) describes the mechanical equilibrium when a new segment is formed in the competent beds bounding by plastically deformed incompetent beds. The tensile stress in the competent bed is induced by the interfacial shear stresses (τ) along the boundaries between the competent and incompetent beds. According to Eq. (4.4), the relation between s and t should be linear. However, experiments reveal that the tensile strength C of materials can not be a constant, and it commonly varies along with the size of materials (e.g., Bažant, 2000; Paterson & Wong, 2005; Askeland et al., 2010). The size effect on the tensile strength of competent bed then can be described by the expression:

$$C=C_0 t^{-1/k} \quad (4.5)$$

where C_0 is the tensile strength of the competent layer with a reference thickness, and k is the Weibull modulus of materials (Paterson & Wong, 2005; Kimura et al., 2006; Askeland et al., 2010). Based on this, Ji et al. (2021) modified Eq. (4.4) into a new form:

$$2\tau s = C_0 t^{1-1/k} \quad (4.6)$$

Eq. (4.6) indicates that the relation between s and t should follow a power law, which is verified by regression results between s of sets J1 and J2 and t in sandstone beds (Figs. 4.18-4.19). Comparing Eqs. (4.3) and (4.6), it is obvious that $m=C_0/(2\tau)$ and $n=1-1/k$.

4.6.2 Estimation of the interfacial shear stress

Equation (4.6) also allows us to estimate the shear stress on the interfaces between the sandstone and mudstone beds (τ), as long as the value of C_0 of the sandstones is available. As the maximum interfacial shear stress cannot be larger than the shear strength of the matrix, τ given by Eq. (4.6) can be approximately considered as the shear stress applied to the matrix: $\tau=C_0/(2m)$. Take the data of the 109 sandstone beds measured along the bedding-perpendicular scanline as an example. We have obtained that m=2.18 for the J1 joints (systematic joints) and m=6.66 for the J2 joints (cross joints). The matrix shear stress in the direction normal to the J1 joints ($\tau=C_0/4.36$) is higher than that along the direction normal to the J2 joints ($\tau=C_0/13.32$), by a factor about 3.1, during their formations. The C_0 is needed to be experimentally measured in the future. If we know the the value of C_0, it becomes possible to calculate the stress that caused the formation of the joints and compare it to the stress measured in this region nowadays (Konstantinovskaya et al., 2012). Clearly, the shear stress in the mudstone matrix is direction-dependent and thus anisotropic.

4.6.3 Formation of orthogonal joints

As orthogonal joints provide pathways for underground flow of water and hydrocarbons (e.g., Bear et al., 1993; Thunvik & Braester, 1990), and the joint spacing controls sizes of rock blocks and in turn affects rock mass stability and permeability (e.g., Einstein et al., 1983; Shang et al., 2016, 2018), the origin of the orthogonal joints has received considerable attention (e.g., Hancock et al., 1987; Rives et al., 1994; Caputo, 1995; Bai et al., 2002). These two sets of joints cannot be interpreted as a conjugate shear fracture system formed by a stress field because the dihedral angle between the two joint sets are approximately 90º, which yields a unrealistic frictional

coefficient $\mu \approx 0$ for the quartz arenite. Two sets of coeval shear joints in a system commonly form an acute angle (θ) described by the following equation:

$$\theta = 90^{o} - \arctan(\mu) \qquad (4.7)$$

Taking μ=0.60 (Byerlee, 1978), for example, θ=59º. Furthermore, these orthogonal joints show no evidence of shear displacement.

4.6.3.1 Existent models

It is generally accepted that each of orthogonal, opening-mode joint sets forms perpendicular to the least principal stress (σ_3) when the effective tensile stress ($\sigma_3^* = \sigma_3 - P_f$, where P_f is the pore fluid pressure) exceeds the tensile fracture strength of the rock (C) at the time of failure (e.g., Jaeger & Cook 1979; Dunne & Hancock, 1994; Tang et al., 2006). Opening mode fractures develop when $\sigma_1 - \sigma_3 \leq 4C$ (Price & Cosgrove, 1990), otherwise only shear fractures form. In the Potsdam sandstone studied, the two orthogonal sets of joints are roughly perpendicular to the bedding plane that is approximately horizontal. Thus, the stress field at the time of joint formation was characterized by vertical orientation of σ_1 and layer-parallel alignment of σ_2 and σ_3. Previous workers proposed that the vertical orthogonal joints could be formed by temporary rotation of the σ_3 direction by 90º in the horizontal plane but the maximum principal stress σ_1 remained vertical (Hancock et al., 1987; Caputo, 1995; Stewart & Hancock, 1990; Dunne & North, 1990; Rives et al., 1994). Such swapping of σ_2 and σ_3 repeatedly occur to form mutually abutting of joint sets, which were roughly coeval in a geological time scale (Caputo, 1995). Accordingly, geometrical relationships display that some numbers of one joint set are older than those in the other set, and vice versa.

The 90º rotation of σ_3 direction can be caused by various processes:

(1) A switch between σ_2 and σ_3 in the horizontal plane normal to vertical σ_1 is caused by some kind of stress release on newly formed systematic fractures (Simón et al., 1988; Caputo, 1995; Stewart & Hancock, 1990; Dunne & North, 1990; Rives et al., 1994). Joints formed in this manner are most probably cross joints that extend across the intervals between existing systematic sets. In other words, cross joints initiate at an existing systematic joint, then propagate laterally, and finally terminate at an adjacent systematic joint (Fig. 4.23a). Cross joints generally do not cut across the systematic joints, forming so-called T and H shapes of joint traces (Hancock,

1985). Thus, their maximum lengths are limited by the separation distance between the two adjacent initial joints. The above process may be periodically repeated.

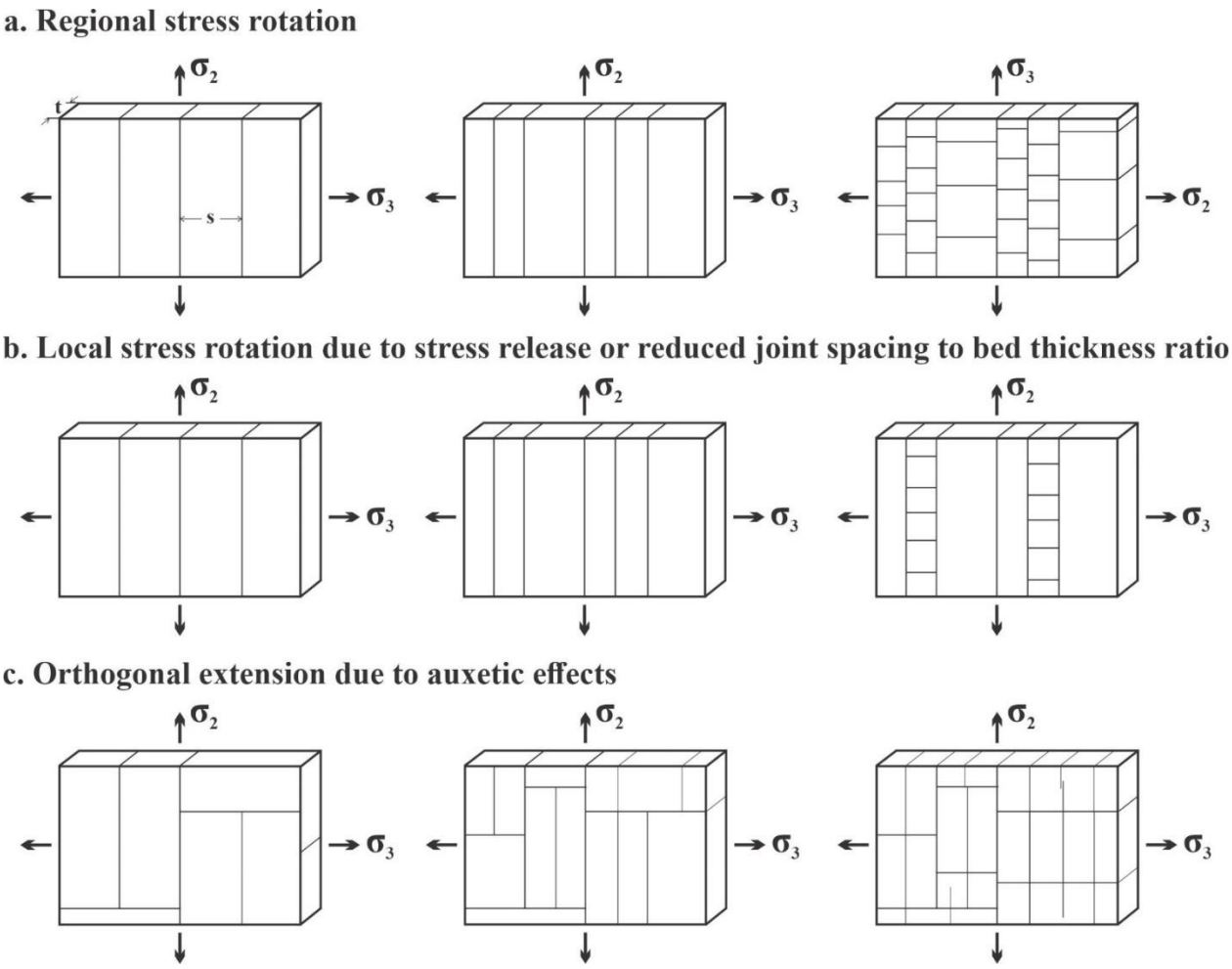

Figure 4.23 Schematic illustration of different models to interpret the development of ladder-pattern (cross joints, a and b) and grid-lock pattern (c) orthogonal joints in a flat-lying sandstone bed. (a) Cross joints develop perpendicular to the systematic joints due to regional stress rotation. (b) Cross joints form laterally between adjacent systematic joints due to stress rotation caused by local stress release or reduced joint spacing to bed thickness ratio (*s*/*t*). (c) Grid-lock joints formed by repeated extension along two orthogonal directions in sandstone due to the auxetic effects (negative Poisson's ratio). The effective maximum principal stress σ_1^* (overburden) is compressive and normal to the sandstone layer, whereas both effective immediate and minimum principal stresses (σ_2^* and σ_3^*) are tensile and perpendicular to widely spaced and narrowly spaced joint sets, respectively, at the time of fracturing. Joint set J1 and J2, which are normal to σ_3^* and σ_2^*, respectively, display spacings of s_{J1} and s_{J2}. Different joints nucleated at flaws with

varying shape and size, where the materials had different tensile strengths and stress concentration factors. A new joint could crosscut healed or partially sealed fractures.

(2) A switch between σ_2 and σ_3 is due to changes in local or regional stress field (Hancock et al., 1987; Dunne & North, 1990). Mechanisms to cause the local stress switch comprise folding, faulting and erosion (e.g., Isachsen, 1975; Rives et al., 1994). The orthogonal joints formed by the regional stress rotation are systematic joints over a broad region (e.g., in orogenic forelands). If the regional stress rotation takes a few million years as inferred from previous results (e.g., Mercier et al., 1987; Tapponnier et al., 1990), one set of joints may be readily distinguishable to have formed prior to the other based on their intersecting and abutting relationships. Joint spacing of each set after the fracture saturation has been reached, depends mainly on the magnitudes of σ_3^* during the brittle deformation before and after stress rotation. The higher magnitude of σ_3^* in one direction is, the closer the joints perpendicular to this direction are. According to Dunne and Hancock (1994), the square-shaped fracture grid-lock system (e.g., Rawnsley et al., 1992) may result from 90º switching of σ_2^* and σ_3^* axes of approximately equal magnitude. However, independent field evidence such as orthogonal pairs of stylolitic structures to support the rotation of regional stress field is often absent.

Bai et al. (2002) proposed a critical joint spacing to bed thickness ratio $(s/t)_c$ for the local tensile stress (σ_3) switch from being perpendicular to parallel to the strike of the systematic joints in a brittle layer. When $s/t>(s/t)_c$, the local stress (σ_3) is perpendicular to the systematic joints, sequential infilling of systematic joints occur. When $s/t<(s/t)_c$, the local tensile stress (σ_3) becomes parallel to the systematic joints, orthogonal cross joints form across the intervals between two adjacent systematic joints (Fig. 4.23b). As a result, the systematic joints formed prior to the cross joints. Numerical computations of Bai et al. (2002) suggested that $(s/t)_c$ ranges from 1 to 2 considering the stress field within the sedimentary rocks. However, their model cannot explain our field observations.

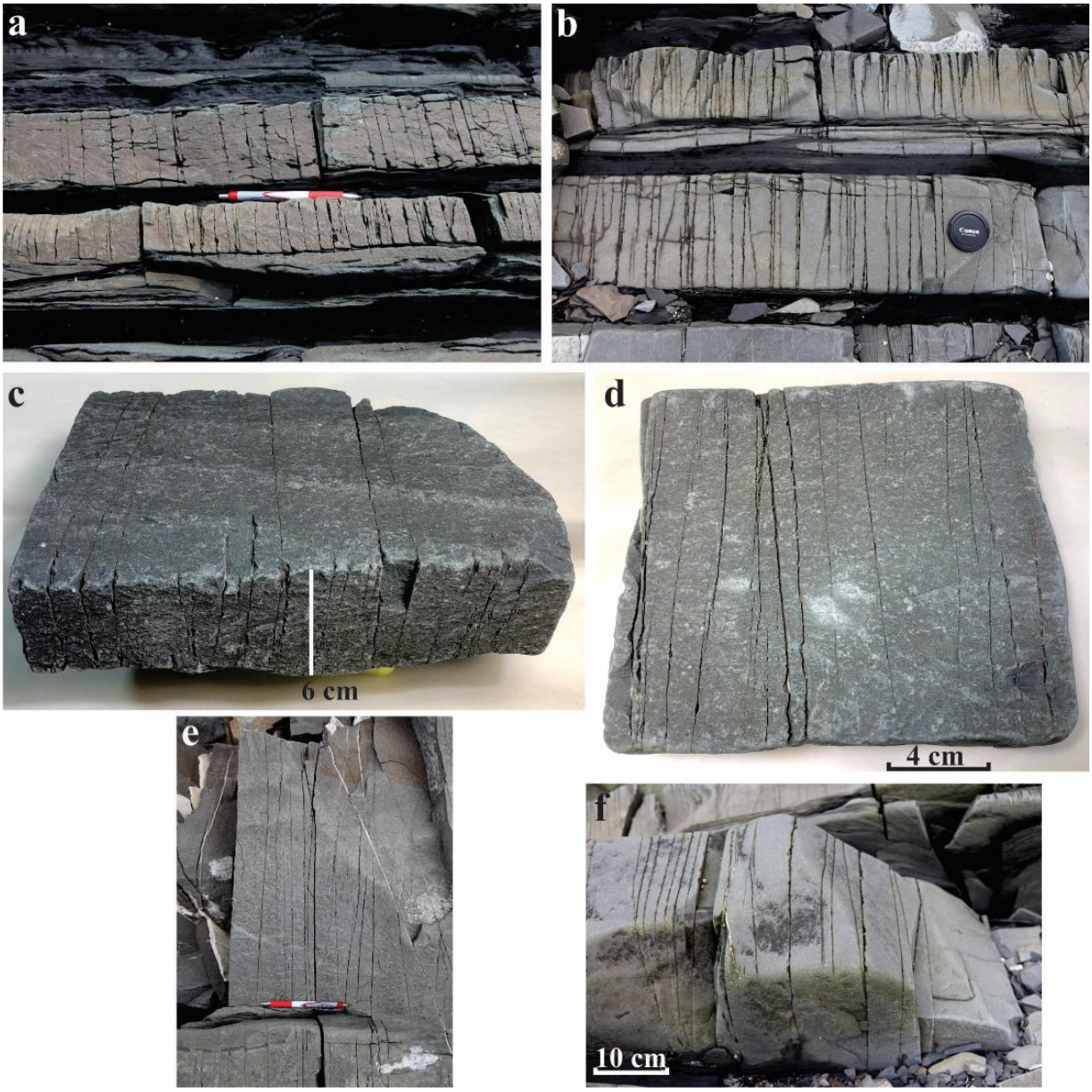

Figure 4.24 Examples of jointed calcareous greywacke beds with joint spacing to bed thickness ratio $s/t \leq 0.2$ but without cross joints developed as predicted by numerical models of Bai et al. (2002). Calcareous greywacke consisting of quartz, feldspar, calcite and clay has a positive Poisson's ratio (Ji et al., 2002). Samples collected from the External Humber Zone of the Appalachian orogen at Petite Vallée, Quebec, Canada (GPS coordinates 49.22133° N, 65.03569° W). (a-b) View from a plane perpendicular to the bedding surface and to the systematic joints. (c and f) Jointed sandstone resembling a sliced-up loaf of bread. (d-e) View from the bedding surface.

As shown in Fig. 4.24, no orthogonal cross joints have formed between the systematic joints in greywacke layers consisting of quartz, feldspar and clay, even though the joint spacing to bed thickness ratio is as low as 0.1-0.2. Bai et al. (2000) proposed s/t=1.0 as the critical-spacing-to-layer-thickness ratio for joint saturation after which no new tensile fractures can form between two existing fractures because the stress becomes compressive rather than tensile. Wu and Pollard (1995) performed a series of extension experiments using a brittle coating material (methylene chloride) on a polymethyl methacrylate substrate and found that the critical-spacing-to-layer-thickness ratio for joint saturation ranges from 7.4 to 11.7. These values are much higher than that proposed by Bai et al. (2000) from numerical modeling. The numerical modeling of Bai and his coworkers assumed that an isotropic, homogeneous, elastic whole space with equally spaced fractures are elastically deformed under tensile horizontal principal stresses (i.e., both σ_2 and σ_3 are tensile). Whether their input rock mechanical parameters (e.g., tensile strength, Young's modulus E=30 GPa, and Poisson's ratio ν=0.25) are representative of in-situ sedimentary rocks during the formation of the orthogonal joints remains uncertain (e.g., Freund, 1992; Van der Pluijm & Marshak, 2004; Ji et al., 2002, 2018; Bandyopadhyay & Abdullah, 2013; Mahmourd et al., 2019). More critically, Bai and his coworkers assumed that the opening-mode fractures have a zero tensile strength, disregarding the effects of 'rock bridges' in natural rocks (Zheng et al., 2015; Shang et al., 2018). With this in mind, it is not surprising that the numerical results from oversimplified models are not necessarily applicable to real rocks in nature.

4.6.3.2 A new interpretation

Previous workers observed that orthogonal tensile joints formed by a strain field with $\varepsilon_1 \geq \varepsilon_2 > 1$ and $\varepsilon_3 \leq 1$ (e.g., Simón et al., 1988). Analogue experiments of Rives et al. (1994) using PVC plates demonstrated that two orthogonal extension loadings could induce an orthogonal fracture pattern with abutting and intersecting relationships. How do the tensile stresses appear simultaneously along two orthogonal direction in a sandstone layer within the Earth's upper crust?

Here we propose alternatively that the two sets of mutually abutting and crosscutting orthogonal joints formed due to auxetic behavior of in-situ quartz arenite layers that possessed negative values of Poisson's ratio during horizontal contraction caused by overburden pressure (Fig. 4.23c). Such an auxetic material is so fascinating that, when placed under layer-normal compression, it becomes shortened in the layer-parallel direction (Lakes, 1987; Alderson &

Alderson, 2007; Greaves et al., 2011; Ren et al., 2018). In the case of flat-lying Potsdam sandstone, the effective σ_1^* is vertical and given by:

$$\sigma_1^*=\rho gz(1-\lambda) \qquad (4.8)$$

where ρ is the average density of the overlying rocks from the surface to depth z (e.g., ρ=2500 kg/m^3 for sandstone), g is the gravitational acceleration, λ is pore fluid factor (i.e., ratio of pore fluid pressure to overburden pressure, λ<1 and λ=1/2.5=0.4 for hydrostatic conditions). Assuming the elastic strain in the direction along the horizontal layer is fully constrained, the effective least principal stress σ_3^* can be estimated from the following equation (Jaeger et al., 2009):

$$\sigma_3^*= \rho gz(1-\lambda)v/(1-v) \qquad (4.9)$$

where v is the Poisson's ratio.

As shown in Fig. 4.25, σ_3^* becomes tensile (negative) only when the Poisson's ratio is negative regardless the λ value (λ=0 and λ=0.4 for lithostatic and hydrostatic conditions, respectively). Furthermore, the absolute magnitude of σ_3^* decreases with raising the pore fluid pressure. Superposing a horizontal tectonic stress ($\Delta\sigma$) over the gravity-induced horizontal stress will slightly change the calculated σ_3^* value, depending on whether the tectonic stress is compressive or tensile within the shallow crust (≤5 km depth). For the same reason, an auxetic (negative Poisson's ratio) quartz arenite layer becomes expanded in the direction of σ_2^* when stretched in the direction of σ_3^*, where both σ_2^* and σ_3^* are parallel to the layer. The layer-parallel tectonic stress ($\Delta\sigma$) can result from tectonic uplift, flexure due to folding, or updoming of sandstone body by underlying magmatic intrusion or salt diapirism (e.g., Isachsen, 1975; Rives et al., 1994).

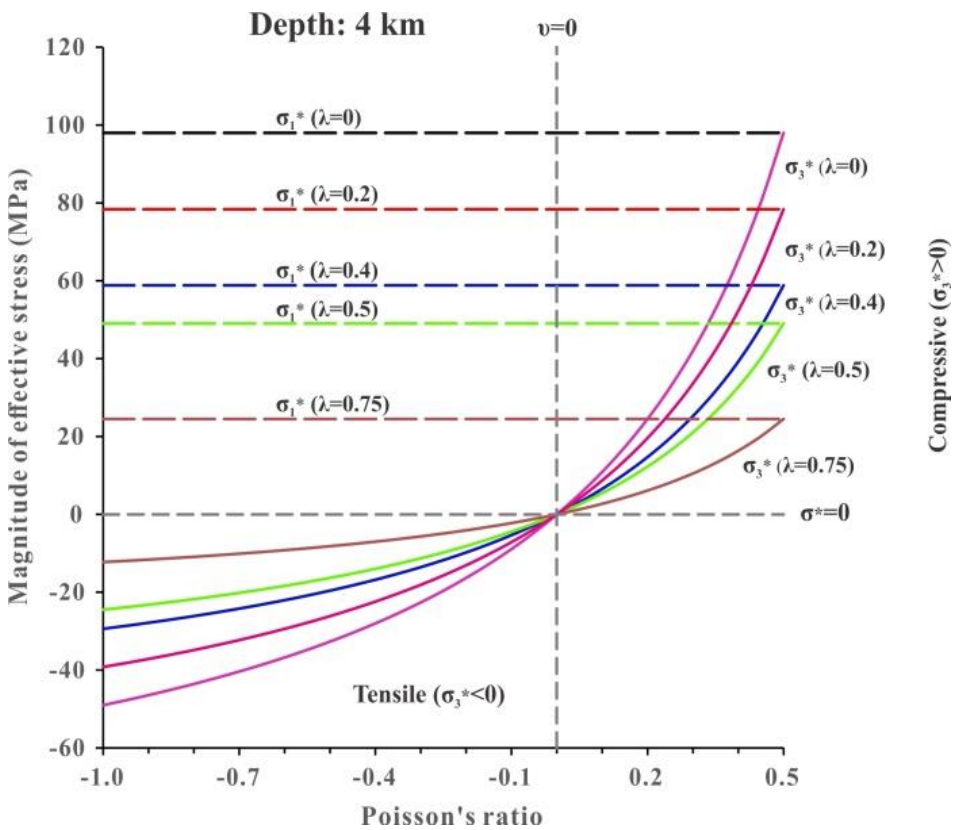

Figure 4.25 Horizontal effective stress (σ_3^*) within a flat-lying layer due to the vertical overburden (σ_1^*) at a depth of 4 km. Conditions with different pore fluid factors (λ) have been considered. λ=0 and λ=0.4 represent lithostatic and hydrostatic conditions, respectively. Tensile σ_3^* occurs only when the material is auxetic with negative Poisson's ratios or $P_f > \sigma_3$ (not shown). The density is taken to be 2.5 g/cm^3.

A conventional material or rock with a positive Poisson's ratio become thinner in directions orthogonal to the applied extension. However, an auxetic material with a negative Poisson's ratio show a 'counterintuitive' behavior: it becomes stretched in directions orthogonal to the applied extension (Lakes, 1987; Ren et., 2018). The transverse stretching results in transverse deformations with tensile stresses in the directions both parallel and perpendicular to σ_3 due to its unusual mechanical response caused by the auxetic effects (Alderson & Alderson, 2007; Evans & Alderson, 2000; Greaves et al., 2011). Natural rock layers such as the Potsdam sandstone were abundant in flaws (e.g., microcracks, microcavities, defects, inhomogeneity, and irregularity on bedding or fracture plane). Each extension fracture nucleated preferentially at such a flaw where the material had locally a low tensile strength or stress concentration occurs. Not all flaws could initiate tensile fractures. Only those whose long axes were aligned perpendicular or high angles to

tensile σ_3 or σ_2 were preferentially chosen and successfully propagate to become continuous joints. In addition, the materials at different flaws of varying size and shape had different tensile strengths. A younger joint could crosscut a healed or partially sealed one. Repeated failure events, which were related to cyclic accumulation-relaxation of stresses, eventually generated grid-lock pattern orthogonal joints in each auxetic sandstone layer subjected to vertical compression and horizontal extension under elastic-brittle conditions.

The proposed process explains reasonably the formation of the vertical orthogonal joints in flat-lying sandstone. The major and subordinate sets of systematic joints are roughly normal, respectively, to σ_3 and σ_2; both are tensile (Fig. 4.23c). Furthermore, the ratio of joint spacing of J1 to J2 is correlated with the value of negative Poisson's ratio. The sandstone exposed at Ausable Chasm shows a typical s_{J2}/s_{J1} ratio of 3.3 (Fig. 4.22), suggesting that a Poisson's ratio ($\nu = -\varepsilon_2/\varepsilon_3$) of -0.30, which corresponds to - s_{J2}/s_{J1} assuming reasonably an average tensile strength of sandstone in the bedding plane. This value is consistent with the experimental data of sandstones measured at confining pressures of below ~100 MPa (Fig. 4.26) or at depths of less than about 4.5 km.

Poisson's ratios illustrated in Fig. 4.26 are the dynamic values obtained by measuring velocities of P- and S-waves (V_p and V_s) propagating through the rock. The method is non-destructive, cost effective, and time efficient (e.g., Ji et al., 2002; Yu et al., 2016). In a static test of Poisson's ratio measurements, however, the strain is larger and a non-elastic deformation of the sample (e.g., microcrack-induced transverse dilatation) occurs (e.g., Simmons & Brace, 1965; Cheng & Johnston, 1981; Li & Fjær, 2012). The static and dynamic Poisson's ratios are roughly equal in magnitude if the effects of crack-induced dilatancy have been eliminated or corrected in the static deformation tests (e.g., Ciccotti et al., 2004; Xu et al., 2016; Ji et al., 2019). Thus, there is generally no significant dependence of the Poisson's ratio on either frequency or strain amplitude because it depends on only the ratios of E/G (E and G are the Young's and shear moduli, respectively) or V_p/V_s rather than their absolute values (Ciccotti & Mulargia, 2004). Recently, Tinni et al. (2019) conducted experimental measurements on acrylic blocks and reported that propagation velocities of hydraulic fractures are as high as 45-96 m/s. Thus, it would be reasonable to use dynamic rather than static properties when dealing with problems such as initiation and propagation of fractures in materials and rocks.

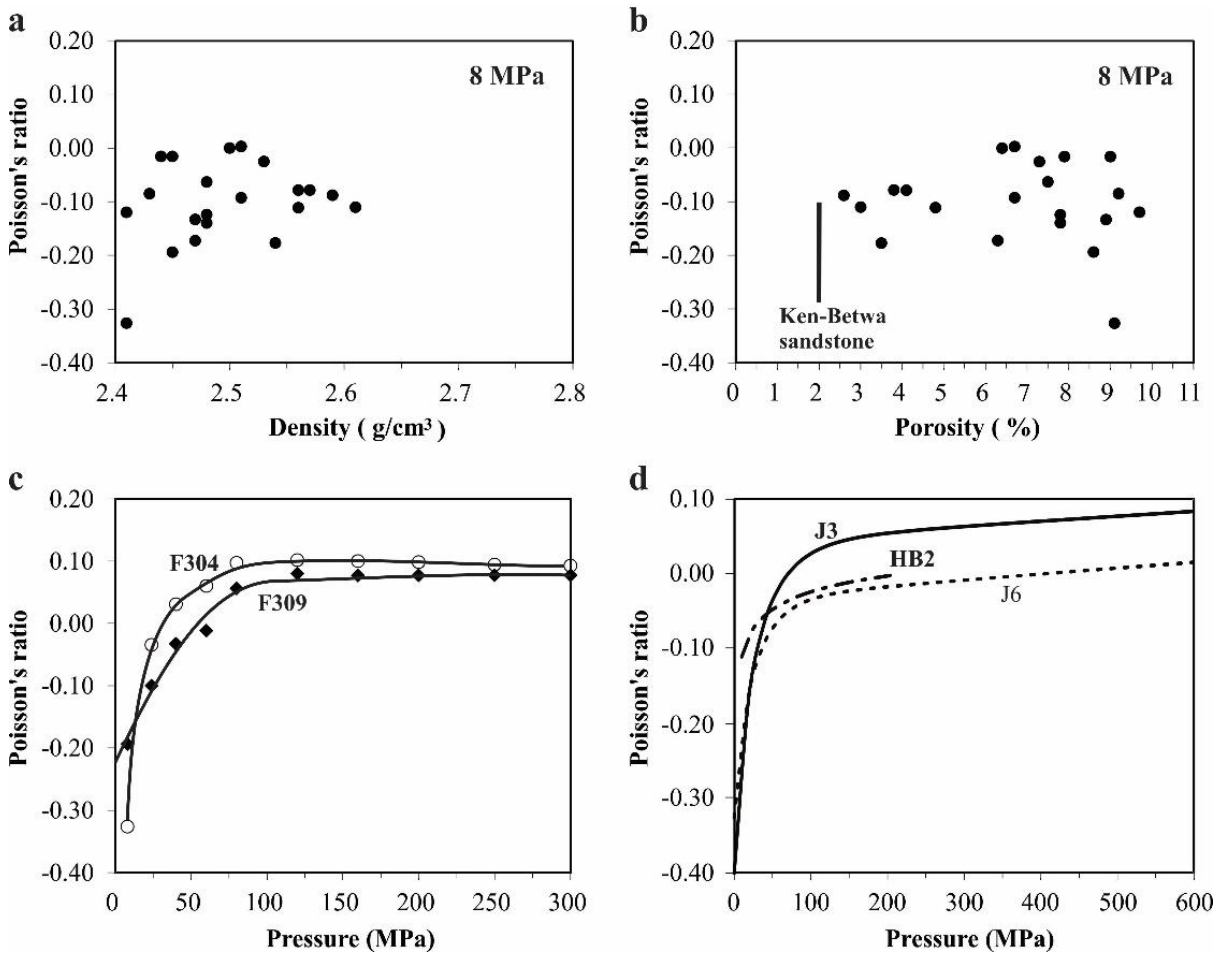

Figure 4.26 Sandstones with zero or negative values of Poisson's ratio. Poisson's ratio as a function of density (a), porosity (b), and confining pressure (c-d). Experimental data in (a-c) from Freund (1992) and (d) from Ji et al. (2018). Samples numbers are also indicated in (c-d). Data of Ken-Betwa sandstone from Bandyopadhyay and Abdullah (2013) are indicated in (b).

Isotropic aggregates of α-quartz with zero porosity has extremely low Poisson's ratio (0.06, Heyliger et al., 2003). Laboratory measurements (Fig. 4.26) showed that quartz-rich sandstone and siltstone containing microcracks and micropores display negative Poisson's ratios (ranging between -0.4 and -0.1) at low confining pressures (<150-200 MPa, Freund, 1992; Ji et al. 2018). For the same reason, the in-situ sandstones, which presumably possessed negative Poisson's ratios, acted as auxetic materials at the time of fracturing by vertical burial compression and horizontal NE-SW extension (Fig. 4.16). The sandstone beds were stretched not only in the direction parallel to but also in the direction perpendicular to the maximum tensile stress (σ_3)

direction in the flat-lying layers, forming closely-spaced J1 fractures and widely-spaced J2 fractures.

The fracture pattern of the study region seems to indicate that quartz arenite layers are very possibly natural auxetic materials that demonstrate similar mechanical behavior to artificial auxetic materials fabricated in the laboratory (Lakes, 1987; Alderson & Alderson, 2007; Greaves et al., 2011; Ren et al., 2018). These rocks exhibit a natural ability to form geologically coeval, orthogonal joints upon vertical burial compression and horizontal extension. For this reason, the model proposed here for the Potsdam sandstone is believed to be applicable to the interpretation for the origin of similar fractures in other terrains of quartz arenite such as Eaglehawk Neck (Tasmania, Australia), St. Mary's Chapel (Caithness, Scotland) and Southwestern USA (e.g. Utah, Nevada and Arizona).

4.6.4 Implications

Orthogonal joints play an extremely important role in enhancing fracture interconnectivity and fluid flow in rocks. Weathering and erosion through ages have preferentially attacked the walls of the orthogonal joints in sandstones, giving rise to some of the most spectacular landforms on the Earth (e.g. Ji, 2018): tower karst in northern Australia, Danxia-style landscapes in China, buttes and rocky pillars, pinnacles and needles in southwest USA (e.g. the Canyonlands National Park, Arches National Park). The visual impression of the tall, flat-topped, steep, often vertical sided tables and towers of sandstone catch people's imagination, so these joint-bounded sandstone blocky structures have been dubbed with names like ruiniform reliefs in the western and central Sahara, and Southern Brazil, and rock cities in the Bohemian Cretaceous Basin in the Czech Republic, Germany and Poland (Melo & Coimbra, 1996; Adamovič & Coubal, 2015; Migoń et al., 2017). Furthermore, the effects of orthogonal joints should be taken into consideration when modeling underground migration of water, gas, oil, and pollutants in the sandstone terrains. In addition, the presence of mutual intersecting orthogonal joints in sandstones can substantially reduce the rock mass strength and slope stability, and hence increase the regional erosion rate.

4.7 Conclusions

Although a significant progress has been made, during the last hundred years, in the understanding of brittle fractures or joints in terms of stress and strain, many important and

interesting problems still require further investigations. Orthogonal joints can be geometrically classified as two types: ladder-pattern network and fracture grid-lock system. Detailed study on the characteristics and formation of these two types of orthogonal joints in the competent sandstone beds highlights the significant impact of rock mechanical properties (e.g., tensile strength, Poisson's ratio and Weibull modulus) on the formation and development of brittle fractures in layered sedimentary rocks.

Based on observation and measurements on the ladder-pattern systematic and cross joints in the sandstone beds of the Tourelle Formation in the region of Sainte-Anne-des-Monts, Quebec, Canada, joint spacing-bed thickness (*s*-*t*) relationships of different joint sets are investigated. The *s*-*t* relationships of both sets of joints roughly follow a power law: $s=mt^{1-1/k}$, where k is the Weibull modulus and m is half of the ratio between C_0 (the tensile strength of sandstone with a unity volume) and τ (the interfacial shear stress on the sandstone and shale interface). The m value of the cross joints is strikingly greater than that of the systematic joints, which implies that the interfacial shear stress normal to the systematic joints was greater than that normal to the cross joints by a factor of ~3.1 when the joints were formed.

Based on an anatomic investigation on the grid-lock type orthogonal joints in the Potsdam sandstone of Cambrian age at Ausable Chasm (NY, USA) and Beauharnois (Quebec, Canada), we propose that the vertical orthogonal joints may result from the auxetic effects of quartz-rich sandstone in the absence of local or regional stress rotation. In the terrains of flat-lying sandstone with widely spaced and narrowly spaced vertical, orthogonal joints, both σ_2^* and σ_3^* are tensile and perpendicular to widely spaced and narrowly spaced sets, respectively, whereas the vertical stress (overburden pressure) is always compressive (σ_1), at the time of fracturing. The aspect-ratio of sandstone blocks bounded by orthogonal joints is correlated with the value of negative Poisson's ratio of the sandstone. Actually, no independent geological evidence from the field has been systematically documented to support the local or regional rotation of the maximum tensile stress (σ_3) due to changes in the ratio of joint spacing to bed thickness of the systematic joints. Furthermore, this study highlights that mechanical properties of rocks other than layer thickness, applied stress, bulk strain and pore fluid pressure, play an extremely important role in affecting the joint arrays in natural rocks.

CHAPTER 5 GENERAL DISSCUSION

5.1 Significance of the research

Mountains, rifts, oceans and geological hazards such as earthquakes and volcanic eruptions are the consequences of plate movements driven by tectonic stresses. The present state of stress (magnitude and orientation) can be measured directly only in the accessible uppermost part of the continental crust (depth <12 km, for example, Kola ultradeep drill-hole). The states of stress in the Earth's past, which corresponded to the old tectonic processes, are required to be determined by the paleopiezometer methods. Chapters 2 and 3 of this thesis developed new paleopiezometers of tourmaline and feldspar microboudins, which help the assessments of temporal and spatial distributions of paleostresses in the orogenic belts.

Furthermore, knowledge of rheological properties is critically important for understanding, in both qualitative and quantitative manners, the tectonic deformation, structures, and geodynamics of the Earth's crust and mantle. The deformation behavior and flow laws of monomineralic aggregates (quartz, plagioclase, pyroxene and olivine) under various conditions of confining pressures, temperatures and strain rates have received extensive investigations during the last 40 years, owning to both laboratory rock deformation experiments (e.g., Paterson & Luan, 1990; Laun & Paterson, 1992; Karato & Wu, 1993; Kohlstedt et al., 1995; Gleason & Tullis, 1995; Rybacki & Dresen, 2000, 2004; Hirth & Kohlstedt, 2003) and microstructural observations of naturally deformed rocks (e.g., Ji et al., 1988; Ji & Mainprice, 1990; Passchier & Trouw, 2005; and many others). The upper and lower crusts and the upper mantle are often modeled using the monomineralic aggregates of quartz, plagioclase and olivine with power-law rheology (dislocation creep) (e.g., Kohlstedt et al., 1995; Ranalli, 1995; Bürgmann & Dresen, 2008; and many others) for simplicity.

However, most crustal and upper mantle rocks are polyphase composites (particulate or granular composites such as granite, granodiorite, gabbro, peridotite and their metamorphic counterparts, and layered composites such as interlayered sandstone and shale). Different constitutive minerals or compositional layers display different mechanical properties and deformation behaviors under the same conditions of temperature and pressure. In granitic mylonites deformed under the greenschist-facies conditions, for example, quartz and mica deformed plastically whereas

feldspar and tourmaline deformed in the brittle manner. Either stress or strain are partitioned among the phases, depending on the manner of their mutual mechanical interactions. The dynamically recrystallized grain-size piezometers (e.g., Twiss, 1977; Stipp & Tullis, 2003; Cross et al., 2017) provided a simple approach to quantify the average flow stresses of the plastic matrix minerals (e.g., quartz) at the temperature when the grain size was "frozen". These piezometers cannot be used for estimating the flow stresses in the rocks which have subjected to post-tectonic annealing or fluid-assisted grain growth. To date, the estimations of the ductile matrix flow stresses based on the brittle deformation structures of competent minerals embedded in the flowing matrix are still rare (Masuda et al., 1989, 1990, 1995, 2003, 2007; Ji & Zhao, 1993; Ji et al., 1997). The present study, which provided new microboudinage piezometers for tourmaline and feldspar, has taken a step forward in this research field. The microboudinage piezometers were derived from the first principle of mechanics (the refined shear-lag model) and have shown prospective applications to the characterization and quantification of rock rheological properties under the natural deformation conditions (e.g., the orogenic belt in the southeastern Tibetan Plateau). In addition, the basic mechanical principles of the shear-lag model can be applied to the study of extensional fractures or joints in layered sedimentary rocks.

Chapter 4 documented out detailed studies on the formation of orthogonal joints (tensile fractures) in the competent sandstone beds interlayered with incompetent shale beds. The results highlights the critical impact of rock mechanical properties (e.g., tensile strength, Poisson's ratio and Weibull modulus) other than the applied far-field stress and bulk strain on the development of brittle fractures in layered composite rocks. It is also the refined shear-lag model applied in Chapter 2 and 3 that provided a viable explanation for the stresses transferred from the surrounding weak layers (shale) to the strong sandstone beds. The correlation between joint spacing and bed thickness provides important parameters for modeling the permeability of water, gas and oil and mechanical strength and stability of subsurface rock masses. Our data also highlight substantial controls of orthogonal joints on the formation of characteristic landforms (e.g., tower karst in northern Australia, Danxia-style landscapes in China, buttes and rocky pillars, pinnacles and needles in southwest USA).

5.2 Comparison between microboudinage and quartz recrystallized grain size piezometers

The piezometer used most widely for estimating the flow stress magnitudes of the crustal rocks is the dynamic recrystallized grain size (*d*) of quartz (Twiss, 1977; Post & Tullis, 1999; Stipp & Tullis, 2003; Cross et al., 2017). The recrystallized grain sizes of quartz can be obtained by measuring the length (*L*) and width (*W*) of each neograin surrounded by grains of the same phase in order to eliminate the effects of pining of grain boundaries by other phases such as mica and feldspar. The actual grain diameter (*d*) is equal to $(LW)^{0.5}$. In the Chongshan shear zone, the mean aspect-ratios of quartz recrystallized grain sizes (*L/W*) are 1.74±0.44, 1.80±0.50, and 1.39±0.38 in samples CS10, CS45 and CS151, respectively (Table 5.1). In contrast to the equant grains formed by static recrystallization, the elongated neograins resulted from the dynamic recrystallization. The mean grain sizes of recrystallized quartz are 31.4 ± 12.9, 25.7 ± 9.6, and 40.6 ± 10.9 μm in samples from localities CS10, CS45 and CS151, respectively (Table 5.1).

Table 5.1 Data of the aspect-ratio (*L/W*) and grain size (*d*) of recrystallized quartz and flow stress (σ) estimation for granitic mylonites from the Chongshan shear zone

Sample	Parameter	N	Mean	St. Dev.	Min	Max
CS10	*L/W*	159	1.74	0.44	0.87	3.17
	d (μm)	159	31.42	12.88	9.49	77.46
	σ (MPa)	159	35.51	11.59	11.59	81.89
CS45	*L/W*	201	1.80	0.50	0.63	3.25
	d (μm)	201	25.67	9.59	8.06	63.54
	σ (MPa)	201	41.11	12.94	18.10	93.18
CS151	*L/W*	154	1.39	0.38	0.47	2.75
	d (μm)	154	40.55	10.90	17.03	65.29
	σ (MPa)	154	27.29	6.24	17.72	51.47

* Calculated using Stipp and Tullis (2003) piezometer modified by Holyoke and Kronenberg (2010).

Applying the piezometer of Stipp and Tullis (2003) modified by Holyoke and Kronenberg (2010), the estimated flow stresses are 36 ± 12, 41 ± 13, and 27 ± 6 MPa for samples CS10, CS45 and CS151, respectively (Table 5.1). When compared with the flow law derived from the tourmaline

microboudin piezometer, they correspond to deformation temperatures of 410 ± 29, 398 ± 27, and 434 ± 21 °C, respectively, at the strain rate of 10^{-14} s^{-1}. These data suggest that the mean recrystallized grain size recorded a long period deformation event at relatively high temperatures (~400 °C) while the microboudinage piezometer permits to estimate the mechanical strengths of rocks deformed even in the elastic-brittle regime at relatively low temperatures (250-300 °C).

Figure 5.1 also shows the comparison between the paleostress estimates from feldspar microboudinage and quartz recrystallized grain sizes for samples CS10 and CS45. The mean recrystallized grain size recorded a long period deformation event at temperatures around 360-370 °C while the microboudinage piezometer permits to estimate the differential stresses for each instantaneous deformation event in both the bulk ductile and brittle regimes.

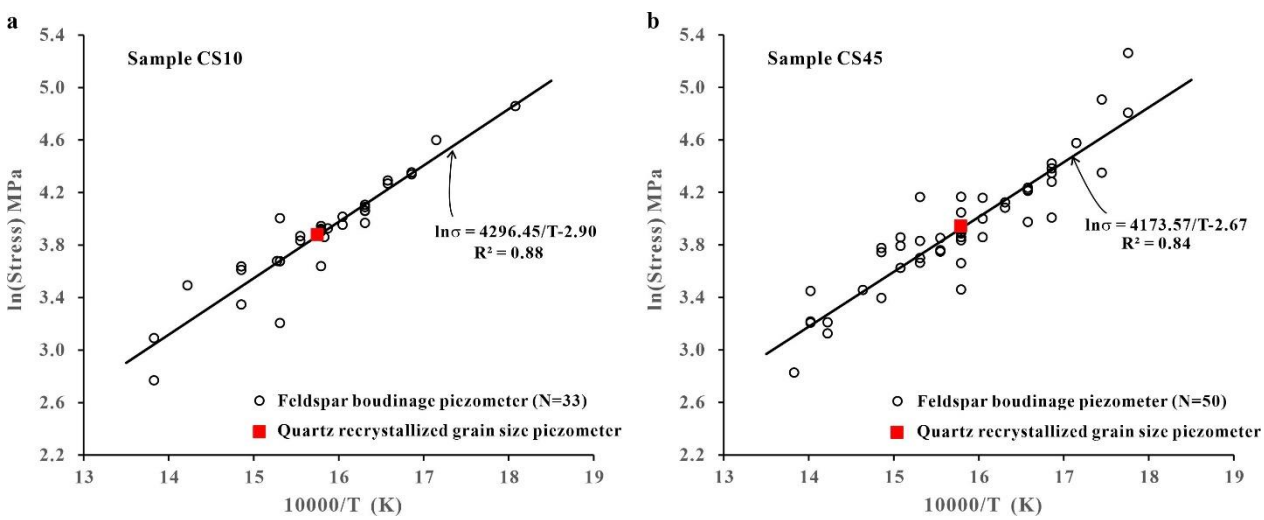

Figure 5.1 Comparison between the paleodifferential stresses estimated from feldspar microboudinage and quartz recrystallized grain size piezometers in granitic mylonite samples CS10 (a) and CS45 (b) from the Chongshan shear zone. Quartz recrystallized grain size piezometer of Stipp and Tullis (2003) was used.

It is important to keep in mind that the following limitations have been documented to be associated with the published experimental stress - recrystallized grain size relationships:

(1) Like the dislocation density and subgrain size piezometers, the recrystallized grain size piezometer becomes invalid for the rocks deformed by other mechanisms than steady-state dislocation creep.

(2) The experimental strains (17-46% shortening) used to calibrate the piezometers (e.g.,

Post & Tullis, 1999; Stipp & Tullis, 2003) could be insufficient to achieve a truly steady state.

(3) The experiments using a Griggs apparatus had poor stress resolution because the force on the σ_1 piston is measured with an external load cell and large errors in measured sample strengths arise from friction on the σ_1 piston, strength of the solid confining medium (NaCl, calcite, Cu and AlSiMag et al.), and uncertainty in the "hit point" where the piston comes in contact with the specimen and deformation begins (Stipp & Tullis, 2003).

(4) The prevailing deformation mechanism is not always correctly identified and different mechanisms yield different piezometers (e.g., Stipp et al., 2010).

(5) The effect of water content on piezometer remains unclear, and those in natural rocks are highly variable and different from those in the experimentally deformed samples.

(6) The recrystallized grain size measured from the rocks exhumed to the surface outcrops is often complicated by post-deformation annealing, fluid-assisted grain growth, and grain boundary pinning by other phases. If the grain boundaries were pinned by other phases, the recrystallized grain size should be smaller than the equilibrium size predicted by the piezometer (e.g., Ferguson & Lloyd, 1982). If the dynamic recrystallization was superposed by static annealing or fluid-assisted grain growth after tectonic deformation, the grain size should be larger than the equilibrium size predicted by the piezometer.

(7) The measurements of recrystallized grain size is a stereological issue, depending on the identification of grain boundary outlines, and thus on observation scales and related techniques (light-optical microscopy, transmission electron microscopy, and SEM-EBSD). The recrystallized neograin and relic grain size distributions often overlap, making their separation difficult (Cross et al., 2017).

(8) Extrapolation from laboratory higher temperature (900-1100 °C, to activate the deformation processes), higher pressure (1.5 GPa, to inhibit microcracking and cavitation) and faster strain-rate (10^{-4}-10^{-7} s^{-1}) experiments to the lower temperature (300-650 °C), lower pressure (0.2-1.0 GPa) and slower strain rate (10^{-13}-10^{-15} s^{-1}) naturally deformed rocks is highly questionable.

However, the microboudin piezometer proposed here has no such limitations encountered by the recrystallized grain size piezometer. Especially, when deformation may not reach to its steady state creep, the microboudin piezometer is preferred over the other piezometers.

5.3 Stereological correction for the estimation of the microboudin aspect-ratios (*L*/*W*)

In the above analyses, no stereological correction for the estimation of the microboudin widths (*W*) has been made. In the observations and measurements of mineral microstructures from petrological thin sections (e.g., size, shape and aspect ratio of grains), stereological effects indeed exist although the corrections have not always been conducted (e.g., Stipp et al., 2002; Stipp & Tullis, 2003; Kidder et al., 2016; Cross et al., 2017) because of the geometrical complexity (e.g., Underwood, 1972, 1973).

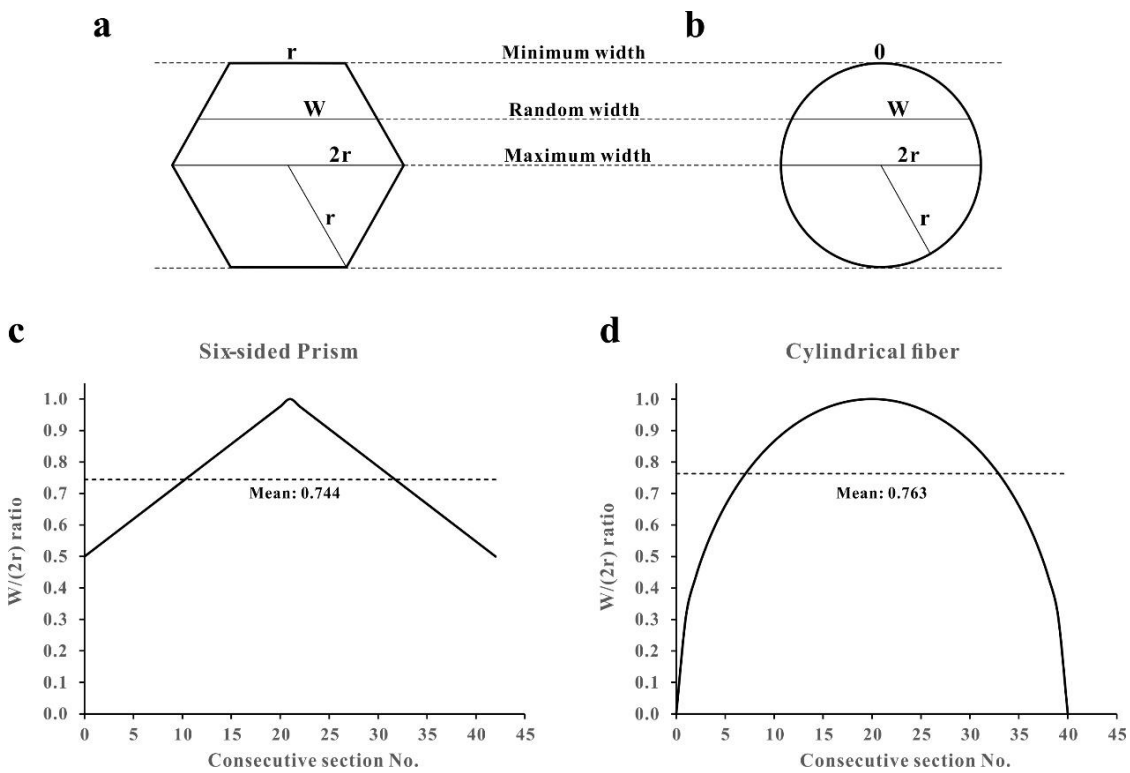

Figure 5.2 (a, b) Widths of possible longitudinal sections through a six-sided prism (a) and a cylindrical prism (b). Variations of *W*/(2*r*) ratios for a series of consecutive sections cut longitudinally through the six-sided prism (c) and the cylindrical prism (d). *r* is the radius of the circumscribed circle. The average sectional widths for the six-sided and cylindrical prisms are, respectively, 74.4% and 76.3% of the maximum values (2*r*), respectively. Each thin-section has a thickness of 30 μm. For (c) and (d), *r*=0.7275 mm and *r*= 0.6 mm.

In a simplest case where a six-sided prism with one of its rectangular sides parallel to the cutting plane, the apparent widths of the longitudinal sections cut should vary from *r* to 2*r*, where *r* is the

radius of the circumscribed circle (i.e., the circumradius). Then, the microboudin width (W) should vary between r and $2r$. The average W value for a series of consecutive parallel sections (with a constant thickness, for example, 30 μm for typical petrographic thin sections) through such as a six-sided prism should be equal to $1.488r$ ($=0.744\times 2r$) and is smaller than the maximum sectional width (i.e., circumdiameter, $2r$) by a factor of 1.344 (Fig. 5.2a and c). As the lengths of the longitudinal sections are a constant (L), the average L/W value for the consecutive parallel sections cut through the six-sided prism should be equal to 0.744 than $L/(2r)$. The smallest L/W ratio [$L/(2r)$] occurs in the section cut parallel to the circumdiameter.

When a cylindrical body with its axis being parallel to the cutting plane, the apparent widths of the longitudinal sections vary from 0 to $2r$, where r is the radius of the circular section (Fig. 5.2b and d). The microboudin aspect-ratios (L/W) thus vary between $L/(2r)$ and the infinite. The average W value for a series of consecutive parallel sections (with a constant thickness of 30 μm) through this cylindrical body is smaller than $2r$ by a factor of 1.311. Similarly, the L/W value for the consecutive parallel sections is equal to $0.763L/(2r)$ (Fig. 5.2b and d).

However, the above stereological correction is impossible to be done for each specific microboudin observed in a petrological thin section. The stereological correction, which will be taken into consideration in our future work, can be performed only for the mean aspect ratio (L/W) of all the microboudins measured from a given sample.

CHAPTER 6 CONCLUSIONS AND FUTURE WORK

6.1 Main conclusions

Based on the near-end fracturing stress transfer model, mineral (tourmaline and feldspar) microboudins occurring in ductile polycrystalline matrix of deformed rocks in the shear zones in Yunnan, Southwest China and joints (fractures) developing in the sandstones interlayered with mudstones and shales in Sainte-Anne-des-Monts area, Quebec, Canada have been studied in detail. The main conclusions of the studies are as follow:

(1) The measured results of tourmaline microboudins from the Gaoligong and Chongshan shear zones in Yunnan, Southwest China, reveals that the tensile fracturing successively fragmented the columnar tourmaline crystals embedded in the flowing matrix of felsic materials into two segments of unequal length and a linear correlation between fracture spacing and fiber mineral width. Therefore, the application of the microboudin piezometers established previously on the mid-point fracturing predicted by the conventional shear-lag model, which assumes perfectly welded interfaces, must be doubtful. The new, simple microboudin piezometer has been developed: $\tau=0.25C/(L/W)$, where τ is the shear flow stress of the ductile matrix, C is the tensile fracture strength of the columnar mineral, and L/W is the mean length/width ratio of the microboudins formed by near-end fracturing. It provides a straightforward method of estimating the magnitude of shear flow stresses responsible for ductile deformation of natural rocks no matter what the prevailing deformation mechanism is (dislocation creep, diffusion creep, hardening or weakening). The samples from the Gaoligong shear zone display that the earlier formed microboudins had consistently a larger mean length/width ratio than the later formed ones, indicating that the rocks recorded a geological history of continuous hardening prior to the cessation of quartz plasticity. The rheological hardening was most likely caused by tectonic exhumation and cooling up progressively to the brittle-ductile transition where temperature was about 300 ºC. For the felsic gneisses from the Gaoligong shear zone, the shear flow stresses are estimated to be in the range of 21 MPa to 61 MPa when taking the tensile strength of tourmaline as 145 MPa. Application of this piezometer on the felsic mylonites and mylonitic gneisses from the Chongshan shear zone, combined with microstructural observations and independent calibrations of deformation temperature, available $^{40}Ar/^{39}Ar$ ages of muscovite and biotite,

and regional geophysical data (e.g., heat flow, focal depths, seismic velocity structure, V_p/V_s (P- and S-wave velocities) ratios, and electrical conductivity structure), provides constraints on strain rates, flow stress and their correlations with temperature and depth for the polycrystalline quartz matrix. The application yields a flow law of $\dot{\varepsilon}=A\sigma^n\exp(-Q/RT)$ with n=4, Q=184 kJ/mol and A=7.180×10^{-7} $MPa^{-n}s^{-1}$ for the natural quartz deformed plastically below the brittle-ductile transition. The flow stresses described by this flow law do not coincide with those values given by either Luan and Paterson (1992) or Gleason and Tullis (1995), but lie between the extrapolations of these experimentally derived flow laws. The naturally derived flow stress-temperature profile is very close to the geometrical mean of the bounds defined by Luan and Paterson (1992) and Gleason and Tullis (1995). A strain rate of 10^{-14} s^{-1} is an optimal estimate for the study rocks, whereas the high strain rates (10^{-12}-10^{-11} s^{-1}) assumed by previous workers (e.g., Lu and Jiang, 2019) will result in a crustal rheology that is far too strong and thus is impossible at least for the study region. The results also offers a reliable interpretation for the distribution of focal depths and electrical resistivity structure in the Chongshan shear zone, which are actually controlled by the brittle-ductile transition and the peak stress at a depth of ~15 km below which the onset of quartz plasticity occurs.

(2) In felsic mylonites deformed under the greenschist facies (300-450 °C), feldspar porphyroclasts embedded in ductile flowing matrix of quartz commonly developed pull-apart microboudinage through repeated cycles of tensile fractures. Investigations of granitic mylonites from the Red River, Chongshan and Gaoligong shear zones, Yunnan, Southwest China provide the valuable information about magnitudes of finite strains and differential stresses and their evolutions during the cooling and exhumation of the mylonites upwards the brittle-ductile transition. Our developed feldspar microboudinage piezometer is applicable when the quartz matrix deforms in either ductile or brittle regime. In the ductile regime, for instance, the Red River, Chongshan and Gaoligong shear zones (Yunnan, China) display the paleodifferential stresses varying in the ranges of 16.3-185.9, 16.0-193.0 and 12.5-124.8 MPa, and increasing with progressively decreasing temperature from 450 °C to 300 °C. The results of paleostress estimates from the feldspar microboudinage piezometer and the quartz recrystallized grain-size piezometer are largely coincident within the range of uncertainties. The feldspar microboudinage piezometer that we developed is viable for felsic mylonites where feldspar porphyroclasts imbedded in a ductile matrix of quartz or quartz-mica

aggregate deform in the brittle pull-apart manner. However, the method may be directly used or adapted to a wide range of geological problems, for example, fractured pebbles in an unlithified matrix (Eidelman and Reches, 1992), chromite pods in the mantle rocks (Holtzman, 2000), and strong boudins in a soft material on any scale (e.g., Fagereng and Sibson, 2010).

(3) We have carefully studied orthogonal joints sandstone beds in the Early Ordovician Tourelle Formation from the region of Sainte-Anne-des-Monts (Quebec, Canada), and the Cambrian Potsdam formation at Ausable Chasm (New York State, USA) and Beaharnois (Quebec, Canada). These joints are normal to bedding. In the region of Sainte-Anne-des-Monts, the spacing (s) of cross joints is statistically larger than that of systematic joints by a factor of about 1.8. The joint spacing-bed thickness (s-t) relationship over the full range of bed thicknesses measured (0.9-760 cm) follows roughly a power law function: $s=mt^{1-1/k}$, where k is the Weibull modulus to describe the frequency of failure of sandstone, and $m=C_0/(2\tau)$ in which C_0 is the tensile strength of sandstone measured at a unity of volume, and τ is the interfacial shear stress between sandstone and shale, depending on overburden depth and fluid pressure. The m value for the cross joints is significantly larger than that for the systematic joints, indicating that the interfacial shear stress parallel the direction normal to the systematic joints was higher than the interfacial shear stress parallel the direction normal to the cross joints, by a factor of ~3.1, during their formation. In the Cambrian Potsdam sandstone at Ausable Chasm and Beauharnois, the orthogonal joints are vertical and arrayed in a grid pattern on the flat-lying bedding surface. It is proposed that these orthogonal joints may result from the auxetic effects of quartz-rich sandstone in the absence of local or regional stress rotation. Both effective stresses σ_2^* and σ_3^* were tensile and perpendicular to widely spaced and narrowly spaced sets of joints, respectively, whereas the vertical stress (overburden pressure) was always compressive (σ_1), at the time of fracturing. The aspect-ratio of sandstone blocks bounded by orthogonal joints was likely correlated with the value of negative Poisson's ratio of the sandstone. No independent geological evidence from the field has been documented to support the local or regional rotation of the maximum tensile stress (σ_3) due to changes in the ratio of joint spacing to bed thickness of the systematic joints. Furthermore, our study emphasizes that mechanical properties of rocks other than bulk strain,

applied stress, pore fluid pressure and layer thickness, play an important role in controlling the fracture patterns in natural rocks.

6.2 Future work

After reviewing the present outcome of my studies on the deformation of geological composite materials based on the stress transfer model with interfacial slip occurring between the competent and incompetent components, I propose that the following three key topics should be focused for future work:

(1) Experimental determination of mineral tensile strengths (e.g., tourmaline). In order to expand the application of the mineral microbouinage piezometer, the tensile strengths of minerals (e.g. tourmaline and feldspar) as a function of temperature and pressure should be experimentally determined, though they have been estimated empirically in Chapter 2 and 3. The tensile strength of a mineral is variable, depending on the composition, crystalline structure, crystal quality, and particularly flaws such as inclusions, microcracks and cleavage orientation. As far as we are aware, there is a dearth of tensile strength data for natural tourmaline or feldspar crystals from laboratory experiments. The ideal tensile strength of a perfect crystal is of the order of $E/10$, where E is Young's modulus (Idrissi et al., 2016). Take tourmaline for example, E=201.5 GPa (Özkan, 1979), and the ideal tensile strength of tourmaline is about 20 GPa, which is unrealistically too high. As discussed in Chapter 2, the tensile strengths of real solid materials ranges only from $E/1000$ to $E/250$ due to the presence of internal flaws. Kimura et al. (2006) performed some three-point bending tests on tourmaline at room temperature and pressure. They obtained

$$S^*=39W^{-0.5} \qquad (5.1)$$

for tourmaline. In Eq. (5.1), S^*, which is the bending fracture strength (MPa), decreases with increasing the sample width (W, in mm). The tourmaline grains from Wadi Tayin (Oman, Kimura et al., 2006) and Eskisehir (Turkey, Masuda et al., 2008) gave S^*=283 and 198 MPa, respectively. However, the flexure fracture strength S^* obtained from the three-point bending tests is not necessarily equal to the ultimate tensile fracture strength because failure by bending often initiates from the surface flaws and the flexure fracture strength result is in general highly sensitive to sample size. Therefore, experiments measuring the tensile

strength of tourmaline and feldspar under various temperature and pressure conditions are in urgent. The high-temperature and high-pressure experiments for measuring the tensile strength of gem-quality tourmaline embedded in the soft matrix (e.g., calcite aggregate) should be conducted using a Paterson gas-medium apparatus.

(2) Quantification of flow stress and strain rate and their spatial and temporal variations in a shear zone. This study is paramount to understand the tectonic evolution process of the shear zone. As shown in Fig. 5.1, the volume fraction of recrystallized quartz grains gradually increase from the edge to the center of the shear zone, while the grain size gradually decreases in the same ductile shear zone (Bell & Etheridge, 1973, 1976; White, 1979; An & He, 1987; Michibayashi, 1993; Dunlap et al., 1997; Ter Heege, 2002). The application of the quartz recrystallized grain size piezometer would lead to the conclusion that the differential stress gradually increases from the edges to the center of the shear zone, that is, the rock has undergone strain hardening, and the flow strength increases with the increasing strain. This phenomenon cannot be explained by shear heating, because shear heating causes the temperature to gradually increase from the edges to the center of the shear zone, which means that flow strength of rock will gradually decrease, so the quartz recrystallized grain size will increase from the edges to the center of the shear zone. More detailed work is needed in order to clarify this paradox. Previous research on the shear zones in Yunnan, Southwest China, provide us an excellent opportunity to figure out this problem with huge amount of geochemical, geochronological, geothermal and seismic data. However, our work (measuring the strain and estimate the flow stress and strain rate) presented in Chapter 2 and 3 is not delicate enough to reveal the temporal and spatial distributions of stress and strain in the large-scale shear zones, and therefore cannot provide enough clues to explain the paradox. In order to address the problem in a deep-going way, several cross-sections perpendicular to the shear zones, along which we would perform detailed mapping and sampling covering the edges to the center of the shear zones, should be selected. The strain and volume fraction of recrystallized quartz grains will be measured. Both the microboudinage piezometer and the quartz recrystallized grain size piezometer will be applied to estimate the paleo-stress and calibrate the strain rate. The resultant results, combined with geochronological and deformation temperature data, would give us a reasonable explanation for the paradox.

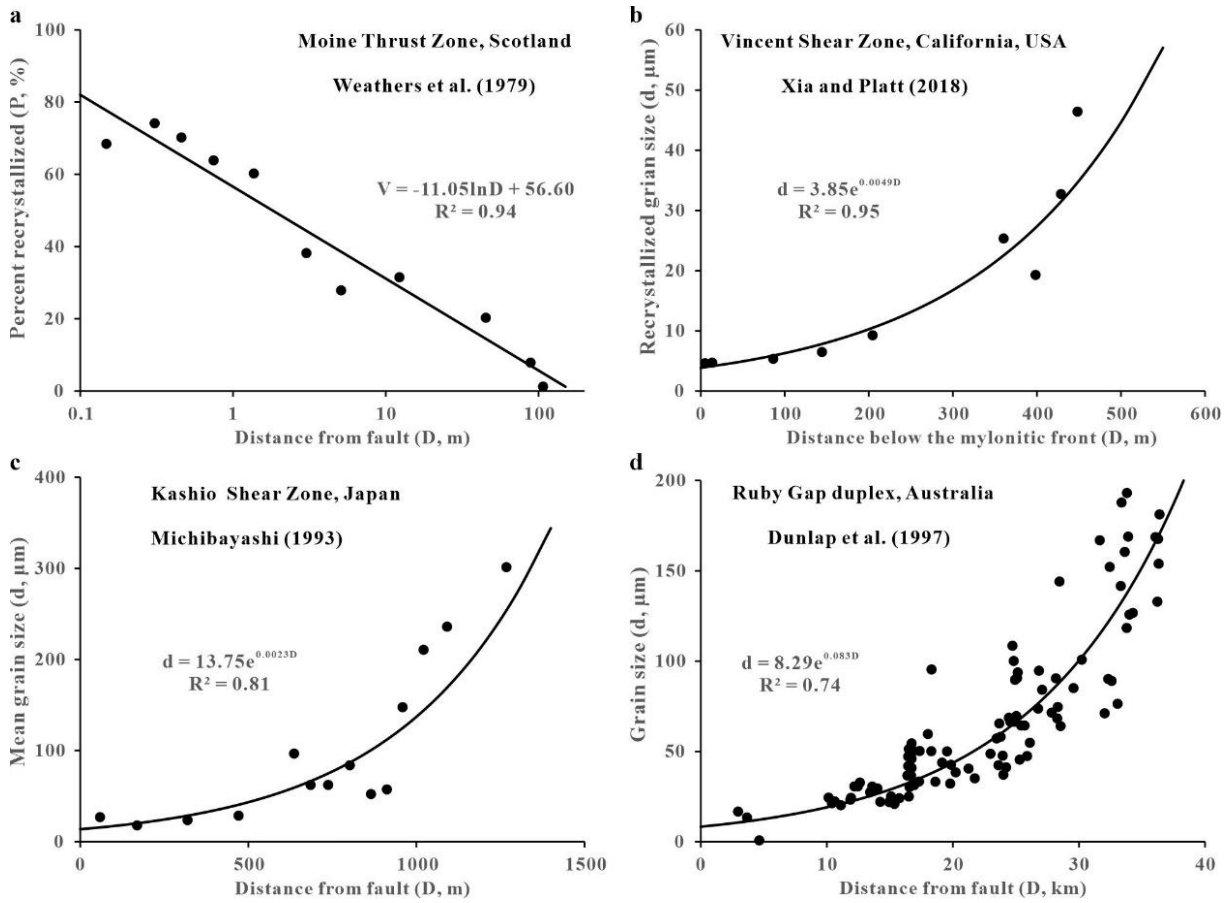

Figure 6.1 Volume fraction (*V*) of dynamic recrystallization (a) and quartz grain size (b-d) as a function of distance (*D*) from the center of each ductile shear zone. Modified from Ji et al. (2021b).

(3) Role of fluid in fracturing process of layered sedimentary rocks. Fluid-assisted dissolution-precipitation processes could result in the sealing of barren joints, and formation of veins. The difference between joints and veins has been under investigation for a long time. After reviewing the literature, Hooker and Katz (2015) reported that the ratios of fracture spacing to bed thickness of veins are strikingly smaller than that of joints. It is questionable whether the comparison between joints and veins is relevant and reliable, since the data of the veins and joints were collected from various researchers who investigated layered beds of various thicknesses from different regions with different lithologies, strains, structures and tectonic evolution histories. Furthermore, it is significant to quantify to what extent the cementation of barren fractures can cause rock strength to recover. This longstanding question still remains poorly understood because of lacking direct field observations. In order to shed light on this issue, we have measured data on the *s*-*t* relationships for joints and veins in

calcareous greywacke and limestone beds interlayered with mudstone and shale in the rocky beach of Saint-Jean-Port Joli, Gros Morne and Grande-Vallée, Quebec, Canada. Mechanical and statistical analyses will be carried out to improve our understanding of difference between joints and veins, and explore the implications of the results in terms of fracture mechanics.

6.3 Contribution of the author

The main content of the dissertation comes from the following 5 published articles:

Li, L., & Ji, S. (2021). A new interpretation for formation of orthogonal joints in quartz sandstone. *Journal of Rock Mechanics and Geotechnical Engineering*, *13*(2), 289-299.

Li, L., Ji, S., & Lin, W. (2020). Tourmaline microboudinage: An indicator of its host rheology. *Journal of Structural Geology*, *138*, 104096.

Li, L., & Ji, S. (2020). On microboudin paleopiezometers and their applications to constrain stress variations in tectonites. *Journal of Structural Geology*, *130*, 103928.

Ji, S., & Li, L. (2021). Feldspar microboudinage paleopiezometer and its applications to estimating differential stress magnitudes in the continental middle crust (examples from west Yunnan, China). *Tectonophysics*, *805*, 228778.

Ji, S., Li, L., & Marcotte, D. (2021). Power-law relationship between joint spacing and bed thickness in sedimentary rocks and implications for layered rock mechanics. *Journal of Structural Geology*, *150*, 104413.

The 3 first-author articles are mainly completed by myself. After discussing the ideas on the scientific problem on deformation of geological composite materials and the detailed research project with Prof. Ji, I started to collect samples (both from the field and samples collected by Prof. Ji during previous studies), make thin sections, measure the data (microboudin data in the laboratory and joint spacing data in the field), take photos, conduct data analysis, make figures and write the manuscript. The whole processes were supervised by Prof. Ji. Among them, Li and Ji (2020) and Li et al. (2020) make up Chapter 2 and Li et al. (2021) now makes up the main part of Chapter 4.

For the article Ji and Li (2021) making up Chapter 3, actually it was completed during July and August of 2020, when Polytechnique was closed for most of time. Therefore, Prof. Ji and I borrowed a microscope from the laboratory and took the samples to his house in order to conduct

the study. Then, I went to Prof. Ji's home for about three weeks everyday to complete the microstructural observation, taking microphotos and measuring the data of feldspar microboudin and discussed the mechanical model for feldspar microboudin piezometer together with Prof. Ji. Then I analysed the data, made the figures and write the draft. However, it was not well written and we were urged to submit the manuscript to be reviewed for an issue in honor of Prof. Adolphe Nicolas, so Prof. Ji rewrote the manuscript. Anyway, I have done some cuts on the original article, kept the parts related to my work, and incorporated some new contents into the revised Chapter 3, which were not presented in Ji and Li (2021).

For the article Ji et al. (2021) on joint, I took part in the measurements of joints in the field, data analysis, making figures, discussing the mechanical model and writing a part of the manuscript. My contribution for this article cannot be taken as major, so the I just leave the parts related to my work (measurements and data analysis) in Chapter 4.

BIBLIOGRAPHY

Abe, S., & Urai, J. L. (2012). Discrete element modeling of boudinage: Insights on rock rheology, matrix flow, and evolution of geometry. *Journal of Geophysical Research: Solid Earth*, *117*, B01407. https://doi.org/10.1029/2011JB008555

Adamovič, J., & Coubal, M. (2015). Orthogonal jointing in sandstone–possible causes. In *13th International symposium on Pseudokarst*.

Afferrante, L., Ciavarella, M., & Valenza, E. (2006). Is Weibull's modulus really a material constant? Example case with interacting collinear cracks. *International Journal of Solids and Structures*, *43*(17), 5147-5157. https://doi.org/10.1016/j.ijsolstr.2005.08.002

Akciz, S., Burchfiel, B. C., Crowley, J. L., Jiyun, Y., & Liangzhong, C. (2008). Geometry, kinematics, and regional significance of the Chong Shan shear zone, Eastern Himalayan Syntaxis, Yunnan, China. *Geosphere*, *4*(1), 292-314. https://doi.org/10.1130/GES00111.1

Alderson, A., & Alderson, K. L. (2007). Auxetic materials. *Proceedings of the Institution of Mechanical Engineers, Part G: Journal of Aerospace Engineering*, *221*(4), 565-575. https://doi.org/10.1243/09544100JAERO185

Allison, I., & Tour, T. E. L. (1977). Brittle deformation of hornblende in a mylonite: a direct geometrical analogue of ductile deformation by translation gliding. *Canadian Journal of Earth Sciences*, *14*(8), 1953-1958. https://doi.org/10.1139/e77-166

Altus, E., & Ishai, O. (1986). Transverse cracking and delamination interaction in the failure process of composite laminates. *Composites Science and Technology*, *26*(1), 59-77. https://doi.org/10.1016/0266-3538(86)90056-4

Amadei, B., & Stephansson, O. (1997). *Rock stress and its measurement*. Springer Science & Business Media.

An, L. J., & He, Y. N. (1987). Estimate of differential flow stress and strain rate for Honghe fault zone. *Seismology and Geology*, *9*, 45-54.

Andrews, J. R. (1984). Fracture controlled feldspar shape fabrics in deformed quartzo-feldspathic rocks. *Journal of Structural Geology*, *6*(1-2), 183-188. https://doi.org/10.1016/0191-8141(84)90095-6

Angelier, J., Souffaché, B., Barrier, E., Bergerat, F., Bouaziz, S., Bouroz, C., Creuzot, G., Ouali, J., & Tricart, P. (1989). Distribution de joints de tension dans un banc rocheux: loi théorique etespacements. *Comptes Rendus de l'Académie des Sciences, Série II*, *309*, 2119-2125.

Ashby, M. (2016). *Material property data for engineering materials* (4th ed.). Granta Design Ltd.. https://www.grantadesign.com

Askeland, D. R., Fulay, P. P., & Wright, W. J. (2010). *The science and engineering of materials* (6th ed.). Cengage Learning Inc..

Atkinson, B. K. (1982). Subcritical crack propagation in rocks: theory, experimental results and applications. *Journal of Structural Geology*, *4*(1), 41-56. https://doi.org/10.1016/0191-8141(82)90005-0

Aydan, Ö., & Kawamoto, T. (1990). Discontinuities and their effect on rock mass. In N. Barton & O. Stephansson (Eds.), *Rock joints* (pp. 149-156). Balkema.

Bahat, D. (1989). Fracture stresses at shallow depths during burial. *Tectonophysics*, *169*(1-3), 59-65. https://doi.org/10.1016/0040-1951(89)90183-2

Bai, D., Unsworth, M. J., Meju, M. A., Ma, X., Teng, J., Kong, X., Sun, Y., Sun, J., Wang, L., Jiang, C., Zhao, C., Xiao, P., & Liu, M. (2010). Crustal deformation of the eastern Tibetan plateau revealed by magnetotelluric imaging. *Nature geoscience*, *3*(5), 358-362. https://doi.org/10.1038/ngeo830

Bai, T., & Pollard, D. D. (2000). Fracture spacing in layered rocks: a new explanation based on the stress transition. *Journal of Structural Geology*, *22*(1), 43-57. https://doi.org/10.1016/S0191-8141(99)00137-6

Bai, T., Maerten, L., Gross, M. R., & Aydin, A. (2002). Orthogonal cross joints: do they imply a regional stress rotation?. *Journal of Structural Geology*, *24*(1), 77-88. https://doi.org/10.1016/S0191-8141(01)00050-5

Bai, T., Pollard, D. D., & Gao, H. (2000). Explanation for fracture spacing in layered materials. *Nature*, *403*(6771), 753-756. https://doi.org/10.1038/35001550

Bandyopadhyay, A., & Abdullah, H. (2013). A laboratory study of strong and weak sandstones. *Proceedings of the 7th international conference on case histories in geotechnical engineering*. http://scolarsmine.mst.edu/icchge/7icchge/session_06/3.

Bao, H., Zhai, Y., Lan, H., Zhang, K., Qi, Q., & Yan, C. (2019). Distribution characteristics and controlling factors of vertical joint spacing in sand-mud interbedded strata. *Journal of Structural Geology*, *128*, 103886. https://doi.org/10.1016/j.jsg.2019.103886

Bardsley, W. E., Major, T. J., & Selby, M. J. (1990). Note on a Weibull property for joint spacing analysis. *International Journal of Rock Mechanics and Mining Sciences*, *27*(2), 133-134. https://doi.org/10.1016/0148-9062(90)91049-D

Barredo, F. B., Pérez, A. P., Montero, P. G., Ruiz, J. T., & Crespo, P. P. G. (2009). Tourmaline $^{40}Ar/^{39}Ar$ chronology of tourmaline-rich rocks from Central Iberia dates the main Variscan deformation phases. *Geologica Acta*, *7*, 399-412. https://doi.org/10.1344/104.000001446

Barruol, G., & Mainprice, D. (1993). A quantitative evaluation of the contribution of crustal rocks to the shear-wave splitting of teleseismic SKS waves. *Physics of the Earth and Planetary Interiors*, *78*(3-4), 281-300. https://doi.org/10.1016/0031-9201(93)90161-2

Barton, C. A., & Zoback, M. D. (1990). Self-similar distribution of macroscopic fractures at depth in crystalline rock in the Cajon Pass scientific drillhole. In N. Barton & O. Stephansson (Eds.), *Rock joints* (pp. 163-170). Balkema.

Bažant, Z. P. (2000). Size effect. *International Journal of Solids and Structures*, *37*(1-2), 69-80. https://doi.org/10.1016/S0020-7683(99)00077-3

Bear, J., Tsang, C. F., & De Marsily, G. (1993). *Flow and contaminant transport in fractured rock*. Academic Press. Cambridge, USA.

Becker, A., & Gross, M. R. (1996). Mechanism for joint saturation in mechanically layered rocks: an example from southern Israel. *Tectonophysics*, *257*(2-4), 223-237. https://doi.org/10.1016/0040-1951(95)00142-5

Behr, W. M., & Platt, J. P. (2011). A naturally constrained stress profile through the middle crust in an extensional terrane. *Earth and Planetary Science Letters*, *303*(3-4), 181-192. https://doi.org/10.1016/j.epsl.2010.11.044

Behr, W. M., & Platt, J. P. (2014). Brittle faults are weak, yet the ductile middle crust is strong: Implications for lithospheric mechanics. *Geophysical Research Letters*, *41*(22), 8067-8075. https://doi.org/10.1002/2014GL061349

Béjina, F., Jaoul, O., & Liebermann, R. C. (1999). Activation volume of Si diffusion in San Carlos olivine: Implications for upper mantle rheology. *Journal of Geophysical Research: Solid Earth*, *104*(B11), 25529-25542. https://doi.org/10.1029/1999JB900270

Bell, T. H., & Etheridge, M. A. (1973). Microstructure of mylonites and their descriptive terminology. *Lithos*, *6*(4), 337-348. https://doi.org/10.1016/0024-4937(73)90052-2

Bell, T. H., & Etheridge, M. A. (1976). The deformation and recrystallization of quartz in a mylonite zone, central Australia. *Tectonophysics*, *32*(3-4), 235-267. https://doi.org/10.1016/0040-1951(76)90064-0

Bevis, M. (1988). Seismic slip and down-dip strain rates in Wadati-Benioff zones. *Science*, *240*(4857), 1317-1319. https://doi.org/10.1126/science.240.4857.1317

Billi, A., & Salvini, F. (2003). Development of systematic joints in response to flexure-related fibre stress in flexed foreland plates: the Apulian forebulge case history, Italy. *Journal of Geodynamics*, *36*(4), 523-536. https://doi.org/10.1016/S0264-3707(03)00086-3

Boersma, Q., Hardebol, N., Barnhoorn, A., & Bertotti, G. (2018). Mechanical factors controlling the development of orthogonal and nested fracture network geometries. *Rock Mechanics and Rock Engineering*, *51*(11), 3455-3469. https://doi.org/10.1007/s00603-018-1552-8

Bogdanov, A. A. (1947). The intensity of cleavage as related to the thickness of beds. *Soviet Geology*, *16*(000).

Bouchez, J. L., & Nicolas, A. (2021). *Principles of rock deformation and tectonics*. Oxford University Press, Oxford.

Boutonnet, E., Leloup, P. H., Sassier, C., Gardien, V., & Ricard, Y. (2013). Ductile strain rate measurements document long-term strain localization in the continental crust. *Geology*, *41*(8), 819-822. https://doi.org/10.1130/G33723.1

Branagan, D. F. (1983). Tesselated pavements. In R. W. Young & G. C. Nanson (Eds.), *Aspects of Australian sandstone landscapes* (pp. 11-20). University of Wollongong.

Briais, A., Patriat, P., & Tapponnier, P. (1993). Updated interpretation of magnetic anomalies and seafloor spreading stages in the South China Sea: Implications for the Tertiary tectonics of Southeast Asia. *Journal of Geophysical Research: Solid Earth*, *98*(B4), 6299-6328. https://doi.org/10.1029/92JB02280

Bridges, M. (1975). *Presentation of fracture data for rock mechanics.* 2nd Australian-New Zealand Conference on Geomechanics, Brisbane.

Burchfiel, B. C., Chen, L., Wang, E., & Swanson, E. (2008). Preliminary investigation into the complexities of the Ailao Shan and Day Nui Con Voi shear zones of SE Yunnan and Vietnam. In B. C. Burchfiel & E. Wang (Eds.), *Investigations into the Tectonics of the Tibetan Plateau* (pp. 45). Geological Society of America.

Bürgmann, R., & Dresen, G. (2008). Rheology of the lower crust and upper mantle: Evidence

from rock mechanics, geodesy, and field observations. *Annual Review of Earth and Planetary Sciences*, *36*, 531-567. https://doi.org/10.1146/annurev.earth.36.031207.124326

Burov, E. B. (2003). The upper crust is softer than dry quartzite. *Tectonophysics*, *361*(3-4), 321-326. https://doi.org/10.1016/S0040-1951(02)00608-X

Byerlee, J. (1978). Friction of rocks. *Pure and Applied Geophysics*, *116*, 615-626. https://doi.org/10.1007/BF00876528

Campbell-Stone, E., & John, B. E. (2002). Temporal changes in deformation mode: from failure to flow in the Colorado River extensional corridor. *International Geology Review*, *44*(6), 512-527. https://doi.org/10.2747/0020-6814.44.6.512

Cao, S., Neubauer, F., Liu, J., Bernroider, M., Cheng, X., Li, J., Yu, Z., & Genser, J. (2017). Rheological weakening of high-grade mylonites during low-temperature retrogression: The exhumed continental Ailao Shan-Red River fault zone, SE Asia. *Journal of Asian Earth Sciences*, *139*, 40-60. https://doi.org/10.1016/j.jseaes.2016.10.002

Cao, S., Neubauer, F., Liu, J., Genser, J., & Leiss, B. (2011). Exhumation of the Diancang Shan metamorphic complex along the Ailao Shan-Red River belt, southwestern Yunnan, China: Evidence from $^{40}Ar/^{39}Ar$ thermochronology. *Journal of Asian Earth Sciences*, *42*(3), 525-550. https://doi.org/10.1016/j.jseaes.2011.04.017

Caputo, R. (1995). Evolution of orthogonal sets of coeval extension joints. *Terra nova*, *7*(5), 479-490. https://doi.org/10.1111/j.1365-3121.1995.tb00549.x

Carslaw, H. S., & Jaeger, J. C. (1959). *Conduction of heat in solids* (2nd ed.). Oxford University Press, Oxford.

Carter, N. L., & Tsenn, M. C. (1987). Flow properties of continental lithosphere. *Tectonophysics*, *136*(1-2), 27-63. https://doi.org/10.1016/0040-1951(87)90333-7

Carter, N. L., Hansen, F. D., & Senseny, P. E. (1982). Stress magnitudes in natural rock salt. *Journal of Geophysical Research: Solid Earth*, *87*(B11), 9289-9300. https://doi.org/10.1029/JB087iB11p09289

Carter, N. L., Horseman, S. T., Russell, J. E., & Handin, J. (1993). Rheology of rocksalt. *Journal of Structural Geology*, *15*(9-10), 1257-1271. https://doi.org/10.1016/0191-8141(93)90168-A

Castaing, C., Halawani, M. A., Gervais, F., Chilès, J. P., Genter, A., Bourgine, B., Ouillon, G., Brosse, J.M., Martin, P., Genna, A., & Janjou, D. (1996). Scaling relationships in intraplate

fracture systems related to Red Sea rifting. *Tectonophysics*, *261*(4), 291-314. https://doi.org/10.1016/0040-1951(95)00177-8

Catlos, E. J., Reyes, E., Brookfield, M., & Stockli, D. F. (2017). Age and emplacement of the Permian–Jurassic Menghai batholith, Western Yunnan, China. *International Geology Review*, *59*(8), 919-945. https://doi.org/10.1080/00206814.2016.1237312

Ceccato, A., Menegon, L., Pennacchioni, G., & Morales, L. F. G. (2018). Myrmekite and strain weakening in granitoid mylonites. *Solid Earth*, *9*(6), 1399-1419. https://doi.org/10.3929/ethz-b-000313174

Chen, W. P., Hung, S. H., Tseng, T. L., Brudzinski, M., Yang, Z., & Nowack, R. L. (2012). Rheology of the continental lithosphere: Progress and new perspectives. *Gondwana Research*, *21*(1), 4-18. https://doi.org/10.1016/j.gr.2011.07.013

Chen, X., Liu, J., Tang, Y., Song, Z., & Cao, S. (2015). Contrasting exhumation histories along a crustal-scale strike-slip fault zone: The Eocene to Miocene Ailao Shan-Red River shear zone in southeastern Tibet. *Journal of Asian Earth Sciences*, *114*, 174-187. https://doi.org/10.1016/j.jseaes.2015.05.020

Cheng, C., & Johnston, D. H. (1981). Dynamic and static moduli. *Geophysical Research Letters*, *8*(1), 39-42. https://doi.org/10.1029/GL008i001p00039

Chester, F. M., Evans, J. P., & Biegel, R. L. (1993). Internal structure and weakening mechanisms of the San Andreas fault. *Journal of Geophysical Research: Solid Earth*, *98*(B1), 771-786. https://doi.org/10.1029/92JB01866

Chiarenzelli, J. R., & Selleck, B. W. (2016). Bedrock geology of the Adirondack Region. *Adirondack Journal of Environmental Studies*, *21*(1), 5.

Christensen, J. N., Rosenfeld, J. L., & DePaolo, D. J. (1989). Rates of tectonometamorphic processes from rubidium and strontium isotopes in garnet. *Science*, *244*, 1465-1469. https://doi.org/10.1126/science.244.4911.1465

Christensen, J. N., Selverstone, J., Rosenfeld, J. L., & DePaolo, D. J. (1994). Correlation by Rb-Sr geochronology of garnet growth histories from different structural levels within the Tauern Window, Eastern Alps. *Contributions to Mineralogy and Petrology*, *118*(1), 1-12. https://doi.org/10.1007/BF00310607

Christie, J. M., Ord, A., & Koch, P. S. (1980). Relationship between recrystallized grain size and flow stress in experimentally deformed quartzite. *Eos, Transactions American Geophysical*

Union, *61*, 377.

Ciccotti, M., & Mulargia, F. (2004). Differences between static and dynamic elastic moduli of a typical seismogenic rock. *Geophysical Journal International*, *157*(1), 474-477. https://doi.org/10.1111/j.1365-246X.2004.02213.x

Ciccotti, M., Almagro, R., & Mulargia, F. (2004). Static and dynamic moduli of the seismogenic layer in Italy. *Rock Mechanics and Rock Engineering*, *37*(3), 229-238. https://doi.org/10.1007/s00603-003-0019-7

Cilona, A., Aydin, A., Likerman, J., Parker, B., & Cherry, J. (2016). Structural and statistical characterization of joints and multi-scale faults in an alternating sandstone and shale turbidite sequence at the Santa Susana Field Laboratory: Implications for their effects on groundwater flow and contaminant transport. *Journal of Structural Geology*, *85*, 95-114. https://doi.org/10.1016/j.jsg.2016.02.003

Cobbold, P. R. (1979). Origin of periodicity: saturation or propagation? *Journal of Structural Geology*, *1*, 96-96.

Collettini, C., Niemeijer, A., Viti, C., & Marone, C. (2009). Fault zone fabric and fault weakness. *Nature*, *462*(7275), 907-910. https://doi.org/10.1038/nature08585

Cooke, M. L., Simo, J. A., Underwood, C. A., & Rijken, P. (2006). Mechanical stratigraphic controls on fracture patterns within carbonates and implications for groundwater flow. *Sedimentary Geology*, *184*(3-4), 225-239. https://doi.org/10.1016/j.sedgeo.2005.11.004

Cousineau, P. A. (1998). Large-scale liquefaction and fluidization in the Cap Chat Mélange, Quebec Appalachians. *Canadian Journal of Earth Sciences*, *35*(12), 1408-1422. https://doi.org/10.1139/e98-076

Cox, H. L. (1952). The elasticity and strength of paper and other fibrous materials. *British Journal of Applied Physics*, *3*(3), 72.

Cox, S. F., Etheridge, M. A., & Hobbs, B. E. (1981). The experimental ductile deformation of polycrystalline and single crystal pyrite. *Economic Geology*, *76*(8), 2105-2117. https://doi.org/10.2113/gsecongeo.76.8.2105

Cross, A. J., Kidder, S., & Prior, D. J. (2015). Using microstructures and TitaniQ thermobarometry of quartz sheared around garnet porphyroclasts to evaluate microstructural evolution and constrain an Alpine Fault Zone geotherm. *Journal of Structural Geology*, *75*, 17-31. https://doi.org/10.1016/j.jsg.2015.02.012

Cross, A. J., Prior, D. J., Stipp, M., & Kidder, S. (2017). The recrystallized grain size piezometer for quartz: An EBSD-based calibration. *Geophysical Research Letters*, *44*(13), 6667-6674. https://doi.org/10.1002/2017GL073836

D'Agostino, N., England, P., Hunstad, I., & Selvaggi, G. (2014). Gravitational potential energy and active deformation in the Apennines. *Earth and Planetary Science Letters*, *397*, 121-132. https://doi.org/10.1016/j.epsl.2014.04.013

Darot, M., Reuschlie, T., & Gueguen, Y. (1985). Fracture parameters of Fontainebleau sandstones: experimental study using a high temperature controlled atmosphere double torsion apparatus. In *The 26th US Symposium on Rock Mechanics (USRMS)*. OnePetro.

Davy, P., & Cobbold, P. R. (1988). Indentation tectonics in nature and experiment. 1. Experiments scaled for gravity. *Bulletin of the Geological Institutions of the University of Uppsala*, *14*, 129-141.

de Mello Franco, J. A., Armelin, J. L., Santiago, J. A. F., Telles, J. C. F., & Mansur, W. J. (2002). Determination of the natural stress state in a Brazilian rock mass by back analysing excavation measurements: a case study. *International Journal of Rock Mechanics and Mining Sciences*, *39*(8), 1005-1032. https://doi.org/10.1016/S1365-1609(02)00102-8

Delorey, A. A., Bokelmann, G. H., Johnson, C. W., & Johnson, P. A. (2021). Estimation of the orientation of stress in the Earth's crust without earthquake or borehole data. *Communications Earth & Environment*, *2*(1), 1-10. https://doi.org/10.1038/s43247-021-00244-1

Deng, J. M., Jin, M. P., Zhao, J. B., Gao, Q., & Chen, J. (2014). Tectonic implications from the distribution map of the crust thickness and Poisson's ratio in the Yunnan area. *Earthquake Research in China*, *30*(4), 583-596. https://doi.org/10.3969/j.issn.1001-4683.2014.04.011

Dewey, J. F., Cande, S., & Pitman, W. C. (1989). Tectonic evolution of the India/Eurasia collision zone. *Eclogae Geologicae Helvetiae*, *82*(3), 717-734.

Dietrich, R. V. (1985). *The Tourmaline Group*. Van Nostrand Reinhold Company, New York.

Ding, L. (1991). *The characteristics of deformation and tectonic implications in south Gaoligong, western Yunnan, China* [Master's thesis, Institute of Geology, Chinese Academy of Science].

Dix, G. R., Salad Hersi, O., & Nowlan, G. S. (2004). The Potsdam Beekmantown Group boundary, Nepean Formation type section (Ottawa, Ontario): a cryptic sequence boundary, not a conformable transition. *Canadian Journal of Earth Sciences*, *41*(8), 897-902. https://doi.org/10.1139/e04-040

Dodson, B. (2006). *The Weibull Analysis Handbook*. ASQ (American Society for Quality) Press.

Donnay, G. (1977). Structural mechanism of pyroelectricity in tourmaline. *Acta Crystallographica Section A: Crystal Physics, Diffraction, Theoretical and General Crystallography*, *33*(6), 927-932. https://doi.org/10.1107/S0567739477002241

Duebendorfer, E. M., & Christensen, C. H. (1998). Plastic-to-brittle deformation of microcline during deformation and cooling of a granitic pluton. In *Fault-related rocks a photographic atlas* (pp.176-179). Princeton University Press, Princeton.

Dunlap, W. J., Hirth, G., & Teyssier, C. (1997). Thermomechanical evolution of a ductile duplex. *Tectonics*, *16*(6), 983-1000. https://doi.org/10.1029/97TC00614

Dunne, W. M., & Hancock, P. L. (1994). Palaeostress analysis of small-scale brittle structures. In P. L. Hancock (Eds.), *Continental deformation* (pp. 101-120). Pergamon, Oxford, UK.

Dunne, W. M., & North, C. P. (1990). Orthogonal fracture systems at the limits of thrusting: an example from southwestern Wales. *Journal of Structural Geology*, *12*(2), 207-215. https://doi.org/10.1016/0191-8141(90)90005-J

Dutrow, B. L., & Henry, D. J. (2011). Tourmaline: a geologic DVD. *Elements*, *7*(5), 301-306. https://doi.org/10.2113/gselements.7.5.301

Eidelman, A., & Reches, Z. E. (1992). Fractured pebbles—A new stress indicator. *Geology*, *20*(4), 307-310. https://doi.org/10.1130/0091-7613(1992)020<0307:FPANSI>2.3.CO;2

Einstein, H. H., Veneziano, D., Baecher, G. B., & O'reilly, K. J. (1983). The effect of discontinuity persistence on rock slope stability. *International Journal of Rock Mechanics and Mining Sciences & Geomechanics Abstracts*, *20*(5), 227-236.

England, P., & Molnar, P. (1997). Active deformation of Asia: From kinematics to dynamics. *Science*, *278*(5338), 647-650. https://doi.org/10.1126/science.278.5338.647

England, P., & Molnar, P. (2015). Rheology of the lithosphere beneath the central and western Tien Shan. *Journal of Geophysical Research: Solid Earth*, *120*(5), 3803-3823. https://doi.org/10.1002/2014JB011733

England, P., Houseman, G., & Nocquet, J. M. (2016). Constraints from GPS measurements on the dynamics of deformation in Anatolia and the Aegean. *Journal of Geophysical Research: Solid Earth*, *121*(12), 8888-8916. https://doi.org/10.1002/2016JB013382

Ertl, A., Marschall, H. R., Giester, G., Henry, D. J., Schertl, H. P., Ntaflos, T., Luvizotto, G. L.,

Nasdala, L., & Tillmanns, E. (2010). Metamorphic ultrahigh-pressure tourmaline: Structure, chemistry, and correlations to PT conditions. *American Mineralogist*, *95*(1), 1-10. https://doi.org/10.2138/am.2010.3283

Etheridge, M. A. (1983). Differential stress magnitudes during regional deformation and metamorphism: upper bound imposed by tensile fracturing. *Geology*, *11*(4), 231-234. https://doi.org/10.1130/0091-7613(1983)11<231:DSMDRD>2.0.CO;2

Evans, K. E., & Alderson, K. L. (2000). Auxetic materials: the positive side of being negative. *Engineering Science and Education Journal*, *9*(4), 148-154. https://doi.org/10.1049/esej:20000402

Fagereng, Å., & Biggs, J. (2019). New perspectives on 'geological strain rates' calculated from both naturally deformed and actively deforming rocks. *Journal of Structural Geology*, *125*, 100-110. https://doi.org/10.1016/j.jsg.2018.10.004

Fagereng, Å., & Sibson, R. H. (2010). Melange rheology and seismic style. *Geology*, *38*(8), 751-754. https://doi.org/10.1130/G30868.1

Fazio, E., Fiannacca, P., Russo, D., & Cirrincione, R. (2020). Submagmatic to Solid-State Deformation Microstructures Recorded in Cooling Granitoids during Exhumation of Late-Variscan Crust in North-Eastern Sicily. *Geosciences*, *10*(8), 311. https://doi.org/10.3390/geosciences10080311

Fazio, E., Punturo, R., Cirrincione, R., Kern, H., Pezzino, A., Wenk, H. R., Goswami, S., & Mamtani, M. A. (2017). Quartz preferred orientation in naturally deformed mylonitic rocks (Montalto shear zone–Italy): a comparison of results by different techniques, their advantages and limitations. *International Journal of Earth Sciences*, *106*(7), 2259-2278. https://doi.org/10.1007/s00531-016-1424-y

Ferguson, C. C. (1981). A strain reversal method for estimating extension from fragmented rigid inclusions. *Tectonophysics*, *79*(3-4), T43-T52. https://doi.org/10.1016/0040-1951(81)90108-6

Ferguson, C. C. (1987). Fracture and separation histories of stretched belemnites and other rigid-brittle inclusions in tectonites. *Tectonophysics*, *139*(3-4), 255-273. https://doi.org/10.1016/0040-1951(87)90100-4

Ferguson, C. C., & Lloyd, G. E. (1982). Palaeostress and strain estimates from boudinage structure and their bearing on the evolution of a major Variscan fold-thrust complex in Southwest England. *Tectonophysics*, *88*(3-4), 269-289. https://doi.org/10.1016/0040-

1951(82)90240-2

Ferguson, C. C., & Lloyd, G. E. (1984). Extension analysis of stretched belemnites: a comparison of methods. *Tectonophysics*, *101*(1-2), 199-206. https://doi.org/10.1016/0040-1951(84)90052-0

Fischer, M. P., Gross, M. R., Engelder, T., & Greenfield, R. J. (1995). Finite-element analysis of the stress distribution around a pressurized crack in a layered elastic medium: implications for the spacing of fluid-driven joints in bedded sedimentary rock. *Tectonophysics*, *247*(1-4), 49-64. https://doi.org/10.1016/0040-1951(94)00200-S

Fisher, D. W. (1968). *Geology of the plattsburgh and rouses point, New York-Vermont Quadrangles*. University of the State of New York.

Flesch, L. M., Haines, A. J., & Holt, W. E. (2001). Dynamics of the India-Eurasia collision zone. *Journal of Geophysical Research: Solid Earth*, *106*(B8), 16435-16460. https://doi.org/10.1029/2001JB000208

Flowers, R. M., Ketcham, R. A., Shuster, D. L., & Farley, K. A. (2009). Apatite (U–Th)/He thermochronometry using a radiation damage accumulation and annealing model. *Geochimica et Cosmochimica Acta*, *73*(8), 2347-2365. https://doi.org/10.1016/j.gca.2009.01.015

Foster, D. A., & Gray, D. R. (2007). Strain rate in Paleozoic thrust sheets, the western Lachlan Orogen, Australia: Strain analysis and fabric geochronology. *Geological Society of America Special Papers*, *433*, 349-368. https://doi.org/10.1130/2007.2433(17)

Fowler, C. M. R. (1992). *The solid earth: an introduction to global geophysics* (2nd ed.). Cambridge University Press, Cambridge.

Freund, D. (1992). Ultrasonic compressional and shear velocities in dry clastic rocks as a function of porosity, clay content, and confining pressure. *Geophysical Journal International*, *108*(1), 125-135. https://doi.org/10.1111/j.1365-246X.1992.tb00843.x

Friedman, M., & Higgs, N. G. (1981). Calcite fabrics in experimental shear zones. *Washington DC American Geophysical Union Geophysical Monograph Series*, *24*, 11-27. https://doi.org/10.1029/GM024p0011

Fusseis, F., Regenauer-Lieb, K., Liu, J., Hough, R. M., & De Carlo, F. (2009). Creep cavitation can establish a dynamic granular fluid pump in ductile shear zones. *Nature*, *459*(7249), 974-977. https://doi.org/10.1038/nature08051

Gandais, M., & Willaime, C. (1984). Mechanical properties of feldspars. In W. L. Brown (Eds.),

Feldspars and feldspathoids (pp. 207-246). Springer, Dordrecht.

Gans, P. B., & Bohrson, W. A. (1998). Suppression of volcanism during rapid extension in the Basin and Range Province, United States. *Science*, *279*(5347), 66-68. https://doi.org/10.1126/science.279.5347.66

Gao. X., Guo, Z., Wang, W., & Yao, Z. (2008). Crust structure beneath Tengchong-Lincang region, Yunnan province, revealed by transform function. *Chinese Journal of Geophysics*, *51*, 451-459. https://doi.org/10.3321/j.issn:0001-5733.2008.02.017

Garrett, K. W., & Bailey, J. E. (1977). Multiple transverse fracture in 90 cross-ply laminates of a glass fibre-reinforced polyester. *Journal of Materials Science*, *12*(1), 157-168. https://doi.org/10.1007/BF00738481

Garthwaite, M. C., Wang, H., & Wright, T. J. (2013). Broadscale interseismic deformation and fault slip rates in the central Tibetan Plateau observed using InSAR. *Journal of Geophysical Research: Solid Earth*, *118*(9), 5071-5083. https://doi.org/10.1002/jgrb.50348

Gauthier, B., & Angelier, J. (1986). Distribution et signification géodynamique des systèmes de joints en contexte distensif: un exemple dans le rift de Suez. *Comptes rendus de l'Académie des sciences. Série 2, Mécanique, Physique, Chimie, Sciences de l'univers, Sciences de la Terre*, *303*(12), 1147-1152.

Ge, Y., Liu-Zeng, J., Zhang, J., Wang, W., Tian, Y., Fox, M., Zeng, L., Shen, X., Wang, H., Su, Z., & Xie, K. (2020). Spatio-temporal variation in rock exhumation linked to large-scale shear zones in the southeastern Tibetan Plateau. *Science China Earth Sciences*, *63*(4), 512-532. https://doi.org/10.1007/s11430-019-9567-y

Gilley, L. D., Harrison, T. M., Leloup, P. H., Ryerson, F. J., Lovera, O. M., & Wang, J. H. (2003). Direct dating of left-lateral deformation along the Red River shear zone, China and Vietnam. *Journal of Geophysical Research: Solid Earth*, *108*(B2), 2127. https://doi.org/10.1029/2001JB001726

Gleason, G. C., & Tullis, J. (1993). Improving flow laws and piezometers for quartz and feldspar aggregates. *Geophysical Research Letters*, *20*(19), 2111-2114. https://doi.org/10.1029/93GL02236

Gleason, G. C., & Tullis, J. (1995). A flow law for dislocation creep of quartz aggregates determined with the molten salt cell. *Tectonophysics*, *247*(1-4), 1-23. https://doi.org/10.1016/0040-1951(95)00011-B

Globensky, Y. (1987). *Géologie des Basses-Terres du Saint-Laurent* (Rapport MM 85-02). Direction générale de l'exploration géologique et minérale.

Goetze, C. (1975). Sheared Iherzolites: from the point of view of rock mechanics. *Geology*, *3*(4), 172-173. https://doi.org/10.1130/0091-7613(1975)3<172:SIFTPO>2.0.CO;2

Gottardi, R., & Teyssier, C. (2013). Thermomechanics of an extensional shear zone, Raft River metamorphic core complex, NW Utah. *Journal of Structural Geology*, *53*, 54-69. https://doi.org/10.1016/j.jsg.2013.05.012

Greaves, G. N., Greer, A. L., Lakes, R. S., & Rouxel, T. (2011). Poisson's ratio and modern materials. *Nature Materials*, *10*(11), 823-837. https://doi.org/10.1038/nmat3134

Gross, M. R. (1993). The origin and spacing of cross joints: examples from the Monterey Formation, Santa Barbara Coastline, California. *Journal of Structural Geology*, *15*(6), 737-751. https://doi.org/10.1016/0191-8141(93)90059-J

Gross, M. R., & Eyal, Y. (2007). Throughgoing fractures in layered carbonate rocks. *Geological Society of America Bulletin*, *119*(11-12), 1387-1404. https://doi.org/10.1130/0016-7606(2007)119[1387:TFILCR]2.0.CO;2

Gross, M. R., Bahat, D., & Becker, A. (1997). Relations between jointing and faulting based on fracture-spacing ratios and fault-slip profiles: A new method to estimate strain in layered rocks. *Geology*, *25*(10), 887-890. https://doi.org/10.1130/0091-7613(1997)025<0887:RBJAFB>2.3.CO;2

Gross, M. R., Fischer, M. P., Engelder, T., & Greenfield, R. J. (1995). Factors controlling joint spacing in interbedded sedimentary rocks: integrating numerical models with field observations from the Monterey Formation, USA. *Geological Society, London, Special Publications*, *92*(1), 215-233. https://doi.org/10.1144/GSL.SP.1995.092.01.12

Guduru, R. K., Darling, K. A., Kishore, R., Scattergood, R. O., Koch, C. C., & Murty, K. L. (2005). Evaluation of mechanical properties using shear–punch testing. *Materials Science and Engineering: A*, *395*(1-2), 307-314. https://doi.org/10.1016/j.msea.2004.12.048

Guenthner, W. R., Reiners, P. W., Ketcham, R. A., Nasdala, L., & Giester, G. (2013). Helium diffusion in natural zircon: Radiation damage, anisotropy, and the interpretation of zircon (U-Th)/He thermochronology. *American Journal of Science*, *313*(3), 145-198. https://doi.org/10.2475/03.2013.01

Guerriero, V., Dati, F., Giorgioni, M., Iannace, A., Mazzoli, S., & Vitale, S. (2015). The role of stratabound fractures for fluid migration pathways and storage in well-bedded carbonates. *Italian Journal of Geosciences*, *134*(3), 383-395. https://doi.org/10.3301/IJG.2014.27

Gueydan, F., Mehl, C., & Parra, T. (2005). Stress-strain rate history of a midcrustal shear zone and the onset of brittle deformation inferred from quartz recrystallized grain size. *Geological Society, London, Special Publications*, *243*(1), 127-142. https://doi.org/10.1144/GSL.SP.2005.243.01.10

Guillope, M., & Poirier, J. P. (1979). Dynamic recrystallization during creep of single-crystalline halite: An experimental study. *Journal of Geophysical Research: Solid Earth*, *84*(B10), 5557-5567. https://doi.org/10.1029/JB084iB10p05557

Hacker, B. R., Kelemen, P. B., & Behn, M. D. (2015). Continental lower crust. *Annual Review of Earth and Planetary Sciences*, *43*, 167-205. https://doi.org/10.1146/annurev-earth-050212-124117

Hames, W. E., & Bowring, S. A. (1994). An empirical evaluation of the argon diffusion geometry in muscovite. *Earth and Planetary Science Letters*, *124*(1-4), 161-169. https://doi.org/10.1016/0012-821X(94)00079-4

Hancock, P. L. (1985). Brittle microtectonics: principles and practice. *Journal of Structural Geology*, *7*(3-4), 437-457. https://doi.org/10.1016/0191-8141(85)90048-3

Hancock, P. L., Al-Kadhi, A., Barka, A. A., & Bevan, T. G. (1987). Aspects of analyzing brittle structures. *Annales Tectonicae*, *1*, 5-19.

Handin, J., Russell, J. E., & Carter, N. L. (1986). Experimental deformation of rocksalt. In *Mineral and rock deformation: laboratory studies* (pp. 117-160). American Geophysical Union.

Handy, M. R. (1994). Flow laws for rocks containing two non-linear viscous phases: a phenomenological approach. *Journal of Structural Geology*, *16*(3), 287-301. https://doi.org/10.1016/0191-8141(94)90035-3

Hanmer, S., & Passchier C. W. (1991). Shear-sense indicators: a review. *Geological Survey of Canada Paper*, *90*, 1-71.

Hansen, F. D. (1982). *Semibrittle creep of selected crustal rocks at 1000 MPa* [Doctoral dissertation, Texas A & M University].

Hansen, F. D. (1987). Physical and mechanical variability of natural rock salt. *Bulletin of the Association of Engineering Geologists*, *24*(2), 227-234. https://doi.org/10.2113/gseegeosci.xxiv.2.227

Hansen, F. D., & Carter N. L. (1982). Creep of selected crustal rocks at 1000 MPa. *Eos, Transactions American Geophysical Union*, *63*, 437.

Harrison, T. M., Duncan, I. A. N., & Mcdougall, I. A. N. (1985). Diffusion of ^{40}Ar in biotite: temperature, pressure and compositional effects. *Geochimica et Cosmochimica Acta*, *49*(11), 2461-2468. https://doi.org/10.1016/0016-7037(85)90246-7

Harrison, T. M., Leloup, P. H., Ryerson, F. J., Tapponnier, P., Lacassin, R., & Chen, W. (1996). Diachronous initiation of transtension along the Ailao Shan-Red River shear zone, Yunnan and Vietnam. In A. Yin & T. M. Harrison (Eds.), *The tectonic evolution of Asia* (pp. 208-226). Cambridge University Press, New York.

He, C. S., Zhu, L. P., & Wang, Q. C. (2009). The significance of crust structure and continental dynamics inferred from receiver functions in West Yunnan. *Acta Geologica Sinica*, *83*, 1163-1172. https://doi.org/10.1111/j.1755-6724.2009.00138.x

Henry, D. J., & Dutrow, B. L. (1992). Tourmaline in a low grade clastic metasedimentary rock: an example of the petrogenetic potential of tourmaline. *Contributions to Mineralogy and Petrology*, *112*(2-3), 203-218. https://doi.org/10.1007/BF00310455

Henry, D. J., & Dutrow, B. L. (1996). Metamorphic tourmaline and its petrologic applications. In E. S. Grew & L. M. Anovitz (Eds.), *Boron: mineralogy, petrology and geochemistry*. The Mineralogical Society of America, Washington DC, USA.

Henry, D. J., & Dutrow, B. L. (2018). Tourmaline studies through time: contributions to scientific advancements. *Journal of Geosciences*, *63*(2), 77-98. https://doi.org/10.3190/jgeosci.255

Hentschel, F., Trepmann, C. A., & Janots, E. (2019). Deformation of feldspar at greenschist facies conditions–the record of mylonitic pegmatites from the Pfunderer Mountains, Eastern Alps. *Solid Earth*, *10*(1), 95-116. https://doi.org/10.5194/se-10-95-2019, 2019.

Heyliger, P., Ledbetter, H., & Kim, S. (2003). Elastic constants of natural quartz. *The Journal of the Acoustical Society of America*, *114*(2), 644-650. https://doi.org/10.1121/1.1593063

Hippertt, J. F. M. (1993). ‘V’-pull-apart microstructures: a new shear-sense indicator. *Journal of Structural Geology*, *15*(12), 1393-1403. https://doi.org/10.1016/0191-8141(93)90001-Q

Hirauchi, K. I., Fukushima, K., Kido, M., Muto, J., & Okamoto, A. (2016). Reaction-induced

rheological weakening enables oceanic plate subduction. *Nature communications*, *7*(1), 12550. https://doi.org/10.1038/ncomms12550

Hirth, G., & Kohlstedt, D. (2003). Rheology of the upper mantle and the mantle wedge: A view from the experimentalists. *Geophysical Monograph-American Geophysical Union*, *138*, 83-106.

Hirth, G., & Tullis, J. A. N. (1992). Dislocation creep regimes in quartz aggregates. *Journal of Structural Geology*, *14*(2), 145-159. https://doi.org/10.1016/0191-8141(92)90053-Y

Hirth, G., Teyssier, C., & Dunlap, J. W. (2001). An evaluation of quartzite flow laws based on comparisons between experimentally and naturally deformed rocks. *International Journal of Earth Sciences*, *90*(1), 77-87. https://doi.org/10.1007/s005310000152

Hiscott, R. N. (1978). Provenance of Ordovician deep-water sandstones, Tourelle Formation, Quebec, and implications for initiation of the Taconic orogeny. *Canadian Journal of Earth Sciences*, *15*(10), 1579-1597. https://doi.org/10.1139/e78-163

Hiscott, R. N. (1980). Depositional framework of sandy mid-fan complexes of Tourelle Formation, Ordovician, Quebec. *AAPG Bulletin*, *64*(7), 1052-1077. https://doi.org/10.1306/2F91942C-16CE-11D7-8645000102C1865D

Hiscott, R. N., & DeVries, M. (1995). Internal characteristics of sandbodies of the Ordovician Tourelle Formation, Quebec, Canada. In *Atlas of deep water environments* (pp. 207-211). Springer, Dordrecht. https://doi.org/10.1007/978-94-011-1234-5_30

Hiscott, R. N., & Middleton, G. V. (1980). Fabric of coarse deep-water sandstones, Tourelle Formation, Quebec, Canada. *Journal of Sedimentary Research*, *50*(3), 703-721. https://doi.org/10.1306/212F7AC7-2B24-11D7-8648000102C1865D

Hobbs, D. W. (1967). The formation of tension joints in sedimentary rocks: an explanation. *Geological Magazine*, *104*(6), 550-556.

Holt, W. E., Li, M., & Haines, A. J. (1995). Earthquake strain rates and instantaneous relative motions within central and eastern Asia. *Geophysical Journal International*, *122*(2), 569-593. https://doi.org/10.1111/j.1365-246X.1995.tb07014.x

Holtzman, B. (2000). Gauging stress from mantle chromitite pods in the Oman ophiolite. *Geological Society of America Special Paper*, *349*, 149-158.

Holyoke III, C. W., & Kronenberg, A. K. (2010). Accurate differential stress measurement using the molten salt cell and solid salt assemblies in the Griggs apparatus with applications to

strength, piezometers and rheology. *Tectonophysics*, *494*(1-2), 17-31. https://doi.org/10.1016/j.tecto.2010.08.001

Howatson, A. M. (2012). *Engineering tables and data*. Springer Science & Business Media, Berlin, Germany.

Hu, J., Yang, H., Li, G., & Wen, L. (2013). Seismic signature of the mantle transition zone beneath eastern Tibet and Sichuan Basin. *Journal of Asian Earth Sciences*, *62*, 606-615. https://doi.org/10.1016/j.jseaes.2012.11.009

Huang, Q., & Angelier, J. (1989). Fracture spacing and its relation to bed thickness. *Geological Magazine*, *126*(4), 355-362. https://doi.org/10.1017/S0016756800006555

Hubbert, M. K., & Willis, D. G. (1957). Mechanics of hydraulic fracturing. *Transactions of the AIME*, *210*(01), 153-168. https://doi.org/10.2118/686-G

Idrissi, H., Bollinger, C., Boioli, F., Schryvers, D., & Cordier, P. (2016). Low-temperature plasticity of olivine revisited with in situ TEM nanomechanical testing. *Science Advances*, *2*(3), e1501671. https://doi.org/10.1126/sciadv.1501671

Isachsen, Y. W. (1975). Possible evidence for contemporary doming of the Adirondack Mountains, New York, and suggested implications for regional tectonics and seismicity. *Tectonophysics*, *29*(1-4), 169-181. https://doi.org/10.1016/0040-1951(75)90142-0

Iyer, K., & Podladchikov, Y. Y. (2009). Transformation-induced jointing as a gauge for interfacial slip and rock strength. *Earth and Planetary Science Letters*, *280*(1-4), 159-166. https://doi.org/10.1016/j.epsl.2009.01.028

Jaeger, J. C., Cook, N. G., & Zimmerman, R. (2009). *Fundamentals of rock mechanics*. John Wiley & Sons.

Jain, A., Guzina, B. B., & Voller, V. R. (2007). Effects of overburden on joint spacing in layered rocks. *Journal of Structural Geology*, *29*(2), 288-297. https://doi.org/10.1016/j.jsg.2006.08.010

Jaoul, O., Tullis, J., & Kronenberg, A. (1984). The effect of varying water contents on the creep behavior of Heavitree quartzite. *Journal of Geophysical Research: Solid Earth*, *89*(B6), 4298-4312. https://doi.org/10.1029/JB089iB06p04298

Jeřábek, P., Stünitz, H., Heilbronner, R., Lexa, O., & Schulmann, K. (2007). Microstructural-deformation record of an orogen-parallel extension in the Vepor Unit, West Carpathians. *Journal of Structural Geology*, *29*(11), 1722-1743.

https://doi.org/10.1016/j.jsg.2007.09.002

Ji, J. Q., Zhong, D. L., Sang, H. Q., Qiu, J., & Hu, S. L. (2000). Dating of two metamorphic events on the basalt granulite from the Nabang area on the border of China and Burma. *Acta Petrologica Sinica*, *16*(2), 227-232.

Ji, S. (2004). A generalized mixture rule for estimating the viscosity of solid-liquid suspensions and mechanical properties of polyphase rocks and composite materials. *Journal of Geophysical Research: Solid Earth*, *109*, B10207. https://doi.org/10.1029/2004JB003124

Ji, S. (2018). Canyons of sculpted rocks. *Chinese National Geography*, 7, 104-121 (in Chinese).

Ji, S., & Li, L. (2020). An alternative interpretation for the formation of doubly plunging folds in sandstone terrains. *Terra Nova*, *32*(5), 325-333. https://doi.org/10.1111/ter.12469

Ji, S., & Li, L. (2021). Feldspar microboudinage paleopiezometer and its applications to estimating differential stress magnitudes in the continental middle crust (examples from west Yunnan, China). *Tectonophysics*, *805*, 228778. https://doi.org/10.1016/j.tecto.2021.228778

Ji, S., & Mainprice, D. (1987). Experimental deformation of sintered albite above and below the order-disorder transition. *Geodinamica Acta*, *1*(2), 113-124. https://doi.org/10.1080/09853111.1987.11105130

Ji, S., & Mainprice, D. (1990). Recrystallization and fabric development in plagioclase. *The Journal of Geology*, *98*(1), 65-79.

Ji, S., & Martignole, J. (1994). Ductility of garnet as an indicator of extremely high temperature deformation. *Journal of Structural Geology*, *16*(7), 985-996. https://doi.org/10.1016/0191-8141(94)90080-9

Ji, S., & Saruwatari, K. (1998). A revised model for the relationship between joint spacing and layer thickness. *Journal of Structural Geology*, *20*(11), 1495-1508. https://doi.org/10.1016/S0191-8141(98)00042-X

Ji, S., & Xia, B. (2002). *Rheology of polyphase earth materials*. Polytechnique International Press, Montreal, Canada.

Ji, S., & Zhao, P. (1993). Location of tensile fracture within rigid-brittle inclusions in a ductile flowing matrix. *Tectonophysics*, *220*(1-4), 23-31. https://doi.org/10.1016/0040-1951(93)90221-5

Ji, S., & Zhao, P. (1994). Strength of two-phase rocks: a model based on fiber-loading theory. *Journal of Structural Geology*, *16*(2), 253-262. https://doi.org/10.1016/0191-

8141(94)90108-2

Ji, S., Li, L., & Marcotte, D. (2021a). Power-law relationship between joint spacing and bed thickness in sedimentary rocks and implications for layered rock mechanics. *Journal of Structural Geology*, *150*, 104413. https://doi.org/10.1016/j.jsg.2021.104413

Ji, S., Li, L., & Xu, Z. (2021b). Dislocation creep and flow strength of the earth's crust. *Acta Geologica Sinica*, *95*(1), 159-181.

Ji, S., Li, L., Motra, H. B., Wuttke, F., Sun, S., Michibayashi, K., & Salisbury, M. H. (2018). Poisson's ratio and auxetic properties of natural rocks. *Journal of Geophysical Research: Solid Earth*, *123*(2), 1161-1185. https://doi.org/10.1002/2017JB014606

Ji, S., Mainprice, D., & Boudier, F. (1988). Sense of shear in high-temperature movement zones from the fabric asymmetry of plagioclase feldspars. *Journal of Structural Geology*, *10*(1), 73-81. https://doi.org/10.1016/0191-8141(88)90129-0

Ji, S., Shao, T., Michibayashi, K., Oya, S., Satsukawa, T., Wang, Q., Wang, Q., Zhao, W., & Salisbury, M. H. (2015). Magnitude and symmetry of seismic anisotropy in mica-and amphibole-bearing metamorphic rocks and implications for tectonic interpretation of seismic data from the southeast Tibetan Plateau. *Journal of Geophysical Research: Solid Earth*, *120*(9), 6404-6430. https://doi.org/10.1002/2015JB012209

Ji, S., Wang, Q., & Li, L. (2019). Seismic velocities, Poisson's ratios and potential auxetic behavior of volcanic rocks. *Tectonophysics*, *766*, 270-282. https://doi.org/10.1016/j.tecto.2019.06.013

Ji, S., Wang, Q., & Salisbury, M. H. (2009). Composition and tectonic evolution of the Chinese continental crust constrained by Poisson's ratio. *Tectonophysics*, *463*(1-4), 15-30. https://doi.org/10.1016/j.tecto.2008.09.007

Ji, S., Wang, Q., & Xia, B. (2002). *Handbook of seismic properties of minerals, rocks and ores*. Polytechnique International Press, Montreal, Canada.

Ji, S., Wang, Q., Marcotte, D., Salisbury, M. H., & Xu, Z. (2007). P wave velocities, anisotropy and hysteresis in ultrahigh-pressure metamorphic rocks as a function of confining pressure. *Journal of Geophysical Research: Solid Earth*, *112*, B09204. https://doi.org/10.1029/2006JB004867

Ji, S., Wang, Q., Salisbury, M. H., Wang, Y., & Jia, D. (2016). P-wave velocities and anisotropy of typical rocks from the Yunkai Mts.(Guangdong and Guangxi, China) and constraints on the

composition of the crust beneath the South China Sea. *Journal of Asian Earth Sciences*, *131*, 40-61. https://doi.org/10.1016/j.jseaes.2016.09.006

Ji, S., Zhao, P., & Saruwatari, K. (1997). Fracturing of garnet crystals in anisotropic metamorphic rocks during uplift. *Journal of Structural Geology*, *19*(5), 603-620. https://doi.org/10.1016/S0191-8141(97)00006-0

Ji, S., Zhu, Z., & Wang, Z. (1998). Relationship between joint spacing and bed thickness in sedimentary rocks: effects of interbed slip. *Geological Magazine*, *135*(5), 637-655. https://doi.org/10.1017/S0016756898001459

Karato, S. I. (2008). *Deformation of earth materials: an introduction to the rheology of solid Earth*. Cambridge University Press.

Karato, S. I. (2010). Rheology of the deep upper mantle and its implications for the preservation of the continental roots: A review. *Tectonophysics*, *481*(1-4), 82-98. https://doi.org/10.1016/j.tecto.2009.04.011

Karato, S. I., & Wu, P. (1993). Rheology of the upper mantle: A synthesis. *Science*, *260*(5109), 771-778. https://doi.org/10.1126/science.260.5109.771

Karato, S. I., Toriumi, M., & Fujii, T. (1980). Dynamic recrystallization of olivine single crystals during high-temperature creep. *Geophysical Research Letters*, *7*(9), 649-652. https://doi.org/10.1029/GL007i009p00649

Kawakami, T. (2004). Tourmaline and boron as indicators of the presence, segregation and extraction of melt in pelitic migmatites: examples from the Ryoke metamorphic belt, SW Japan. *Earth and Environmental Science Transactions of The Royal Society of Edinburgh*, *95*(1-2), 111-123. https://doi.org/10.1017/S0263593300000961

Kehle, R. O. (1964). The determination of tectonic stresses through analysis of hydraulic well fracturing. *Journal of Geophysical Research*, *69*(2), 259-273. https://doi.org/10.1029/JZ069i002p00259

Kelly, A., & Tyson, A. W. (1965). Tensile properties of fibre-reinforced metals: copper/tungsten and copper/molybdenum. *Journal of the Mechanics and Physics of Solids*, *13*(6), 329-350. https://doi.org/10.1016/0022-5096(65)90035-9

Kidder, S., Avouac, J. P., & Chan, Y. C. (2012). Constraints from rocks in the Taiwan orogen on crustal stress levels and rheology. *Journal of Geophysical Research: Solid Earth*, *117*, B09408. https://doi.org/10.1029/2012JB009303

Kidder, S., Hirth, G., Avouac, J. P., & Behr, W. (2016). The influence of stress history on the grain size and microstructure of experimentally deformed quartzite. *Journal of Structural Geology*, *83*, 194-206. https://doi.org/10.1016/j.jsg.2015.12.004

Kimura, N., Awaji, H., Okamoto, M., Matsumura, Y., & Masuda, T. (2006). Fracture strength of tourmaline and epidote by three-point bending test: application to microboudin method for estimating absolute magnitude of palaeodifferential stress. *Journal of Structural Geology*, *28*(6), 1093-1102. https://doi.org/10.1016/j.jsg.2006.03.020

Kimura, N., Nakayama, S., Tsukimura, K., Miwa, S., Okamoto, A., & Masuda, T. (2010). Determination of amphibole fracture strength for quantitative palaeostress analysis using microboudinage structures. *Journal of Structural Geology*, *32*(2), 136-150. https://doi.org/10.1016/j.jsg.2009.10.008

Knipe, R. J. (1989). Deformation mechanisms—recognition from natural tectonites. *Journal of Structural Geology*, *11*(1-2), 127-146. https://doi.org/10.1016/0191-8141(89)90039-4

Koch, P. S. (1983). *Rheology and microstructures of experimentally deformed quartz aggregates* [Doctoral dissertation, University California at Los Angeles].

Koch, P. S., Christie, J. M., & George Jr, R. P. (1980). Flow law of “wet” quartzite in the alpha quartz field. *Eos, Transactions American Geophysical Union*, *61*, 376.

Koch, P. S., Christie, J. M., Ord, A., & George Jr, R. P. (1989). Effect of water on the rheology of experimentally deformed quartzite. *Journal of Geophysical Research: Solid Earth*, *94*(B10), 13975-13996. https://doi.org/10.1029/JB094iB10p13975

Kohli, A. H., & Zoback, M. D. (2013). Frictional properties of shale reservoir rocks. *Journal of Geophysical Research: Solid Earth*, *118*(9), 5109-5125. https://doi.org/10.1002/jgrb.50346

Kohlstedt, D. L., & Weathers, M. S. (1980). Deformation-induced microstructures, paleopiezometers, and differential stresses in deeply eroded fault zones. *Journal of Geophysical Research: Solid Earth*, *85*(B11), 6269-6285. https://doi.org/10.1029/JB085iB11p06269

Kohlstedt, D. L., Evans, B., & Mackwell, S. J. (1995). Strength of the lithosphere: Constraints imposed by laboratory experiments. *Journal of Geophysical Research: Solid Earth*, *100*(B9), 17587-17602. https://doi.org/10.1029/95JB01460

Konstantinovskaya, E., Malo, M., & Castillo, D. A. (2012). Present-day stress analysis of the St. Lawrence Lowlands sedimentary basin (Canada) and implications for caprock integrity during CO_2 injection operations. *Tectonophysics*, 518, 119-137.

Kronenberg, A. K., & Tullis, J. (1984). Flow strengths of quartz aggregates: grain size and pressure effects due to hydrolytic weakening. *Journal of Geophysical Research: Solid Earth*, *89*(B6), 4281-4297. https://doi.org/10.1029/JB089iB06p04281

Krumbein, W. C., & Graybill, F. A. (1965). *An introduction to statistical models in geology*. McGraw-Hill, New York.

La Pointe, P. R., & Hudson, J. A. (1985). *Characterization and interpretation of rock mass joint patterns*. The Geological Society of America Inc., Boulder, Colorado.

Lachenbruch, A. H. (1961). Depth and spacing of tension cracks. *Journal of Geophysical Research*, *66*(12), 4273-4292. https://doi.org/10.1029/JZ066i012p04273

Lacombe, O. (2001). Paleostress magnitudes associated with development of mountain belts: Insights from tectonic analyses of calcite twins in the Taiwan Foothills. *Tectonics*, *20*(6), 834-849. https://doi.org/10.1029/2001TC900019

Ladeira, F. L., & Price, N. J. (1981). Relationship between fracture spacing and bed thickness. *Journal of Structural Geology*, *3*(2), 179-183. https://doi.org/10.1016/0191-8141(81)90013-4

Lakes, R. (1987). Foam structures with a negative Poisson's ratio. *Science*, *235*, 1038-1041.

Lakshtanov, D. L., Sinogeikin, S. V., & Bass, J. D. (2007). High-temperature phase transitions and elasticity of silica polymorphs. *Physics and Chemistry of Minerals*, *34*(1), 11-22. https://doi.org/10.1007/s00269-006-0113-y

Landing, E. D., Amati, L., & Franzi, D. A. (2009). Epeirogenic transgression near a triple junction: the oldest (latest early-middle Cambrian) marine onlap of cratonic New York and Quebec. *Geological Magazine*, *146*(4), 552-566. https://doi.org/10.1017/S0016756809006013

Lavoie, D. (2008). Appalachian foreland basin of Canada. *Sedimentary Basins of the World*, *5*, 65-103. https://doi.org/10.1016/S1874-5997(08)00003-8

Lavoie, D., Burden, E., & Lebel, D. (2003). Stratigraphic framework for the Cambrian Ordovician rift and passive margin successions from southern Quebec to western Newfoundland. *Canadian Journal of Earth Sciences*, *40*(2), 177-205. https://doi.org/10.1139/e02-078

Lawn, B. (1995). *Fracture of brittle solids* (2nd ed.). Cambridge University Press, Cambridge.

Lee, H. Y., Chung, S. L., Wang, J. R., Wen, D. J., Lo, C. H., Yang, T. F., Zhang, Y., Xie, Y., Lee, T. Y., Wu, G., & Ji, J. (2003). Miocene Jiali faulting and its implications for Tibetan tectonic evolution. *Earth and Planetary Science Letters*, *205*(3-4), 185-194. https://doi.org/10.1016/S0012-821X(02)01040-3

Lei, Q., & Gao, K. (2018). Correlation between fracture network properties and stress variability in geological media. *Geophysical Research Letters*, *45*(9), 3994-4006. https://doi.org/10.1002/2018GL077548

Leloup, P. H., Arnaud, N., Lacassin, R., Kienast, J. R., Harrison, T. M., Trong, T. P., Replumaz, A., & Tapponnier, P. (2001). New constraints on the structure, thermochronology, and timing of the Ailao Shan-Red River shear zone, SE Asia. *Journal of Geophysical Research: Solid Earth*, *106*(B4), 6683-6732. https://doi.org/10.1029/2000JB900322

Leloup, P. H., Lacassin, R., Tapponnier, P., Schärer, U., Zhong, D., Liu, X., Zhang, L., Ji, S., & Trinh, P. T. (1995). The Ailao Shan-Red river shear zone (Yunnan, China), tertiary transform boundary of Indochina. *Tectonophysics*, *251*(1-4), 3-84. https://doi.org/10.1016/0040-1951(95)00070-4

Li, L., & Fjær, E. (2012). Modeling of stress-dependent static and dynamic moduli of weak sandstones. *Journal of Geophysical Research: Solid Earth*, *117*, B05206,. https://doi.org/10.1029/2011JB009019

Li, L., & Ji, S. (2020). On microboudin paleopiezometers and their applications to constrain stress variations in tectonites. *Journal of Structural Geology*, *130*, 103928. https://doi.org/10.1016/j.jsg.2019.103928

Li, L., & Ji, S. (2021). A new interpretation for formation of orthogonal joints in quartz sandstone. *Journal of Rock Mechanics and Geotechnical Engineering*, *13*(2), 289-299. https://doi.org/10.1016/j.jrmge.2020.08.003

Li, L., Ji, S., & Lin, W. (2020). Tourmaline microboudinage: An indicator of its host rheology. *Journal of Structural Geology*, *138*, 104096. https://doi.org/10.1016/j.jsg.2020.104096

Li, R., Tang, J., & Dong, Z. Y. (2014). Deep electrical conductivity structure of the southern area in Yunnan Province. *Chinese Journal of Geophysics*, *57*(4), 1111-1122. https://doi.org/10.6038/cjg20140409

Li, Y., & Yang, C. (2007). On fracture saturation in layered rocks. *International Journal of Rock Mechanics and Mining Sciences*, *44*(6), 936-941. https://doi.org/10.1016/j.ijrmms.2006.11.009

Lin, T. H., Lo, C. H., Chung, S. L., Hsu, F. J., Yeh, M. W., Lee, T. Y., Ji, J. Q., Wang, Y. Z., & Liu, D. (2009). $^{40}Ar/^{39}Ar$ dating of the Jiali and Gaoligong shear zones: Implications for crustal deformation around the Eastern Himalayan Syntaxis. *Journal of Asian Earth Sciences*, *34*(5), 674-685. https://doi.org/10.1016/j.jseaes.2008.10.009

Linckens, J., Bruijn, R. H., & Skemer, P. (2014). Dynamic recrystallization and phase mixing in experimentally deformed peridotite. *Earth and Planetary Science Letters*, *388*, 134-142. https://doi.org/10.1016/j.epsl.2013.11.037

Lithgow-Bertelloni, C., & Guynn, J. H. (2004). Origin of the lithospheric stress field. *Journal of Geophysical Research: Solid Earth*, *109*, B01408. https://doi.org/10.1029/2003JB002467

Ljunggren, C., Chang, Y., Janson, T., & Christiansson, R. (2003). An overview of rock stress measurement methods. *International Journal of Rock Mechanics and Mining Sciences*, *40*(7-8), 975-989. https://doi.org/10.1016/j.ijrmms.2003.07.003

Lloyd, C. H. (1982). The fracture toughness of dental composites: II. The environmental and temperature dependence of the stress intensification factor (K_{Ic}). *Journal of Oral Rehabilitation*, *9*(2), 133-138. https://doi.org/10.1111/j.1365-2842.1982.tb00543.x

Lloyd, G. E., & Condliffe, E. (2003). 'Strain Reversal': a Windows™ program to determine extensional strain from rigid–brittle layers or inclusions. *Journal of Structural Geology*, *25*(7), 1141-1145. https://doi.org/10.1016/S0191-8141(02)00056-1

Lloyd, G. E., & Ferguson, C. C. (1981). Boudinage structure: some new interpretations based on elastic-plastic finite element simulations. *Journal of Structural Geology*, *3*(2), 117-128. https://doi.org/10.1016/0191-8141(81)90009-2

Lloyd, G. E., & Ferguson, C. C. (1989). Belemnites, strain analysis and regional tectonics: a critical appraisal. *Tectonophysics*, *168*(4), 239-253. https://doi.org/10.1016/0040-1951(89)90220-5

Lloyd, G. E., Ferguson, C. C., & Reading, K. (1982). A stress-transfer model for the development of extension fracture boudinage. *Journal of Structural Geology*, *4*(3), 355-372. https://doi.org/10.1016/0191-8141(82)90019-0

Lobo-Guerrero, S., & Vallejo, L. E. (2006). Application of Weibull statistics to the tensile strength of rock aggregates. *Journal of Geotechnical and Geoenvironmental Engineering*, *132*(6), 786-790. https://doi.org/10.1061/(ASCE)1090-0241(2006)132:6(786)

Lockner, D. A. (1995). Rock failure. In *Rock physics and phase relations: A handbook of physical constants* (pp. 127-147). American Geophysical Union.

London, D. (2008). Pegmatites. *The Canadian Mineralogist*, *10*, 347.

London, D. (2011). Experimental synthesis and stability of tourmaline: a historical overview. *The Canadian Mineralogist*, *49*(1), 117-136. https://doi.org/10.3749/canmin.49.1.117

London, D. (2016). Reading pegmatites—Part 2: what tourmaline says. *Rocks & Minerals*, *91*(2), 132-149. https://doi.org/10.1080/00357529.2016.1113464

London, D., Morgan, G. B., Paul, K. A., & Guttery, B. M. (2012). Internal evolution of miarolitic granitic pegmatites at the Little Three mine, Ramona, California, USA. *The Canadian Mineralogist*, *50*(4), 1025-1054. https://doi.org/10.3749/canmin.50.4.1025

Lowe, D. G., Brink, R., Mehrtens, C., & Franzi, D. A. (2015). Stratigraphy and terrestrial to shallow marine environments of the Potsdam Group in the southwestern Ottawa Embayment. In *Geology of the Northeastern Adirondack Mountains and Champlain–St. Lawrence Lowlands of New York, Vermont and Québec: New York State Geological Association 87th Annual Meeting Guidebook* (pp. 143-189).

Lu, L. X., & Jiang, D. (2019). Quartz flow law revisited: the significance of pressure dependence of the activation enthalpy. *Journal of Geophysical Research: Solid Earth*, *124*(1), 241-256. https://doi.org/10.1029/2018JB016226

Luan, F. C., & Paterson, M. S. (1992). Preparation and deformation of synthetic aggregates of quartz. *Journal of Geophysical Research: Solid Earth*, *97*(B1), 301-320. https://doi.org/10.1029/91JB01748

Lynch, H. D., & Morgan, P. (1987). The tensile strength of the lithosphere and the localization of extension. *Geological Society, London, Special Publications*, *28*(1), 53-65. https://doi.org/10.1144/GSL.SP.1987.028.01.05

Mahmoud, A. A., Elkatatny, S., Ali, A., & Moussa, T. (2019). Estimation of static young's modulus for sandstone formation using artificial neural networks. *Energies*, *12*(11), 2125. https://doi.org/10.3390/en12112125

Malhame, P., & Hesse, R. (2015). Quartz arenites of the Cambro–Ordovician Kamouraska Formation, Quebec Appalachians, Canada: II. Eolian sands in deep-sea sedimentary gravity-flow deposits. *Canadian Journal of Earth Sciences*, *52*(4), 261-277. https://doi.org/10.1139/cjes-2014-0030

Malo, M. (2004). Paleogeography of the Matapédia basin in the Gaspé Appalachians: initiation of the Gaspé Belt successor basin. *Canadian Journal of Earth Sciences*, *41*(5), 553-570. https://doi.org/10.1139/e03-100

Malo, M., Cousineau, P. A., Sacks, P. E., Riva, J. F., Asselin, E., & Gosselin, P. (2001). Age and composition of the Ruisseau Isabelle Mélange along the Shickshock Sud fault zone: constraints on the timing of mélanges formation in the Gaspé Appalachians. *Canadian Journal of Earth Sciences*, *38*(1), 21-42. https://doi.org/10.1139/e00-072

Mandal, N., Chakraborty, C., & Samanta, S. K. (2001). Controls on the failure mode of brittle inclusions hosted in a ductile matrix. *Journal of Structural Geology*, *23*(1), 51-66. https://doi.org/10.1016/S0191-8141(00)00127-9

Mandal, N., Deb, S. K., & Khan, D. (1994). Evidence for a non-linear relationship between fracture spacing and layer thickness. *Journal of Structural Geology*, *16*(9), 1275-1281. https://doi.org/10.1016/0191-8141(94)90069-8

Mandl, G. (2005). *Rock joints the mechanical genesis*. Springer, Berlin.

Mareschal, J. C., & Jaupart, C. (2013). Radiogenic heat production, thermal regime and evolution of continental crust. *Tectonophysics*, *609*, 524-534. https://doi.org/10.1016/j.tecto.2012.12.001

Mareschal, M., Kellett, R. L., Kurtz, R. D., Ludden, J. N., Ji, S., & Bailey, R. C. (1995). Archaean cratonic roots, mantle shear zones and deep electrical anisotropy. *Nature*, *375*(6527), 134-137. https://doi.org/10.1038/375134a0

Martínez-Martínez, J. M., Torres-Ruiz, J., Pesquera, A., & Gil-Crespo, P. P. (2010). Geological relationships and U-Pb zircon and $^{40}Ar/^{39}Ar$ tourmaline geochronology of gneisses and tourmalinites from the Nevado–Filabride complex (western Sierra Nevada, Spain): tectonic implications. *Lithos*, *119*(3-4), 238-250. https://doi.org/10.1016/j.lithos.2010.07.002

Mastella, L. (1972). Interdependence of joint density and thickness of layers in the Podhale Flysch. *Bulletin L'Académie Polonaise des Science*, 20, 187-196.

Masuda, T., & Kimura, N. (2004). Can a Newtonian viscous-matrix model be applied to microboudinage of columnar grains in quartzose tectonites?. *Journal of Structural*

Geology, *26*(10), 1749-1754. https://doi.org/10.1016/j.jsg.2004.02.008

Masuda, T., & Kuriyama, M. (1988). Successive “mid-point” fracturing during microboudinage: an estimate of the stress-strain relation during a natural deformation. *Tectonophysics*, *147*(3-4), 171-177. https://doi.org/10.1016/0040-1951(88)90185-0

Masuda, T., Kimura, N., & Hara, Y. (2003). Progress in microboudin method for palaeo-stress analysis of metamorphic tectonites: application of mathematically refined expression. *Tectonophysics*, *364*(1-2), 1-8. https://doi.org/10.1016/S0040-1951(03)00045-3

Masuda, T., Kimura, N., Fu, B., & Li, X. (2004). Validity of the microboudin method for palaeo-stress analysis: application to extraordinarily long sodic amphibole grains in a metachert from Aksu, China. *Journal of Structural Geology*, *26*(2), 203-206. https://doi.org/10.1016/j.jsg.2003.07.001

Masuda, T., Kimura, N., Okamoto, A., Miyake, T., & Omori, Y. (2007). Cessation of plastic deformation during exhumation of metamorphic tectonites revealed by microboudinage structures. *Journal of Structural Geology*, *29*(1), 159-165. https://doi.org/10.1016/j.jsg.2006.06.019

Masuda, T., Miyake, T., Kimura, N., & Okamoto, A. (2011). Application of the microboudin method to palaeodifferential stress analysis of deformed impure marbles from Syros, Greece: Implications for grain-size and calcite-twin palaeopiezometers. *Journal of Structural Geology*, *33*(1), 20-31. https://doi.org/10.1016/j.jsg.2010.11.002

Masuda, T., Nakayama, S., Kimura, N., & Okamoto, A. (2008). Magnitude of σ_1, σ_2, and σ_3 at mid-crustal levels in an orogenic belt: Microboudin method applied to an impure metachert from Turkey. *Tectonophysics*, *460*(1-4), 230-236. https://doi.org/10.1016/j.tecto.2008.08.025

Masuda, T., Shibutani, T., & Yamaguchi, H. (1995). Practical stress analysis using piedmontite microboudinage structures. *Journal of Structural Geology*, *17*(12), 1793-1795. https://doi.org/10.1016/0191-8141(95)00079-S

Masuda, T., Shibutani, T., Igarashi, T., & Kuriyama, M. (1989). Microboudin structure of piedmontite in quartz schists: a proposal for a new indicator of relative palaeodifferential stress. *Tectonophysics*, *163*(1-2), 169-180. https://doi.org/10.1016/0040-1951(89)90124-8

Masuda, T., Shibutani, T., Kuriyama, M., & Igarashi, T. (1990). Development of microboudinage: an estimate of changing differential stress with increasing strain. *Tectonophysics*, *178*(2-4), 379-387. https://doi.org/10.1016/0040-1951(90)90160-A

Matsumura, T., Kuwatani, T., & Masuda, T. (2017). The relationship between the proportion of microboudinaged columnar grains and far–field differential stress: A numerical model for analyzing paleodifferential stress. *Journal of Mineralogical and Petrological Sciences*, *112*(1), 25-30. https://doi.org/10.2465/jmps.160711

McConaughy, D. T., & Engelder, T. (2001). Joint initiation in bedded clastic rocks. *Journal of Structural Geology*, *23*(2-3), 203-221. https://doi.org/10.1016/S0191-8141(00)00091-2

McCormick, J. W. (1977). *Transmission electron microscopy of experimentally deformed synthetic quartz* [Doctoral dissertation, University of California].

McGarr, A., & Gay, N. C. (1978). State of stress in the Earth's crust. *Annual Review of Earth and Planetary Sciences*, *6*(1), 405-436.

McLintock, F. A., & Walsh, J. B. (1962). Friction on Griffith cracks in rocks under pressure. *Proceedings, National Congress of Applied Mechanics*, *2*, 1015-1022.

McQuillan, H. (1973). Small-scale fracture density in Asmari Formation of southwest Iran and its relation to bed thickness and structural setting. *AAPG Bulletin*, *57*(12), 2367-2385. https://doi.org/10.1306/83D9131C-16C7-11D7-8645000102C1865D

McSkimin, H. J., Andreatch Jr, P., & Thurston, R. N. L. (1965). Elastic moduli of quartz versus hydrostatic pressure at 25 °C and −195.8 °C. *Journal of Applied Physics*, *36*(5), 1624-1632. https://doi.org/10.1063/1.1703099

Melo, M. S., & Coimbra, A. M. (1996). Ruiniform relief in sandstones: the examples of Vila Velha, Carboniferous of the Paraná Basin, Southern Brazil. *Acta Geológica Hispánica*, 25-40.

Mercier, J. C. C. (1985). Olivine and pyroxene. In H. R. Wenk (Eds.), *Preferred orientation in deformed metals and rocks: an introduction to modern texture analysis*. Academic Press.

Mercier, J. C. C., Anderson, D. A., & Carter, N. L. (1977). Stress in the lithosphere: inferences from steady state flow of rocks. In *Stress in the Earth* (pp. 199-226). Birkhäuser, Basel. https://doi.org/10.1007/978-3-0348-5745-1_12

Mercier, J. L., Sorel, O., & Simeakis, K. (1987). Changes in the state of stress in the overriding plate of a subduction zone: the Aegean Arc from the Pliocene to the Present. *Annales Tectonicae*, *1*, 20-39.

Michibayashi, K. (1993). Syntectonic development of a strain-independent steady-state grain size during mylonitization. *Tectonophysics*, *222*(2), 151-164. https://doi.org/10.1016/0040-1951(93)90046-M

Michibayashi, K. (1996). The role of intragranular fracturing on grain size reduction in feldspar during mylonitization. *Journal of Structural Geology*, *18*(1), 17-25. https://doi.org/10.1016/0191-8141(95)00074-N

Migoń, P., Duszyński, F., & Goudie, A. (2017). Rock cities and ruiniform relief: Forms–processes–terminology. *Earth-Science Reviews*, *171*, 78-104. https://doi.org/10.1016/j.earscirev.2017.05.012

Morrison, J. K., Shah, S. P., & Jenq, Y. S. (1988). Analysis of fiber debonding and pullout in composites. *Journal of Engineering Mechanics*, *114*(2), 277-294. https://doi.org/10.1061/(ASCE)0733-9399(1988)114:2(277)

Müller, W., Aerden, D., & Halliday, A. N. (2000). Isotopic dating of strain fringe increments: duration and rates of deformation in shear zones. *Science*, *288*(5474), 2195-2198. https://doi.org/10.1126/science.288.5474.2195

Nardone, V. C., & Prewo, K. M. (1986). On the strength of discontinuous silicon carbide reinforced aluminum composites. *Scripta Metallurgica*, *20*(1), 43-48. https://doi.org/10.1016/0036-9748(86)90210-3

Narr, W., & Suppe, J. (1991). Joint spacing in sedimentary rocks. *Journal of Structural Geology*, *13*(9), 1037-1048. https://doi.org/10.1016/0191-8141(91)90055-N

Nicolas, A. (1987). *Principles of Rock Deformation*. Reidel Publishing Company, Dordrecht.

Nicolas, A., & Poirier, J. P. (1976). *Crystalline plasticity and solid state flow in metamorphic rocks*. Wiley, London.

Niemeijer, A., Marone, C., & Elsworth, D. (2010). Fabric induced weakness of tectonic faults. *Geophysical Research Letters*, *37*, L03304. https://doi.org/10.1029/2009GL041689

Norris, D. K. (1966). The about mesoscopic fabric of rock masses some Canadian coal mines. In *1st ISRM Congress*. OnePetro.

Norris, R. J., & Cooper, A. F. (2003). Very high strains recorded in mylonites along the Alpine Fault, New Zealand: implications for the deep structure of plate boundary faults. *Journal of Structural Geology*, *25*(12), 2141-2157. https://doi.org/10.1016/S0191-8141(03)00045-2

Novikova, A. C. (1947). The intensity of cleavage as related to the thickness of the bed. *Soviet Geology*, *16*.

Ohsawa, T., Nakayama, A., Miwa, M., & Hasegawa, A. (1978). Temperature dependence of critical fiber length for glass fiber-reinforced thermosetting resins. *Journal of Applied Polymer*

Science, *22*(11), 3203-3212. https://doi.org/10.1002/app.1978.070221115

Olson, J. E. (2004). Predicting fracture swarms—The influence of subcritical crack growth and the crack-tip process zone on joint spacing in rock. *Geological Society, London, Special Publications*, *231*(1), 73-88. https://doi.org/10.1144/GSL.SP.2004.231.01.05

Olson, J. E., Holder, J., & Rijken, P. (2002). Quantifying the fracture mechanics properties of rock for fractured reservoir characterization. In *SPE/ISRM Rock Mechanics Conference*. OnePetro.

Olson, J. E., Laubach, S. E., & Lander, R. H. (2009). Natural fracture characterization in tight gas sandstones: Integrating mechanics and diagenesis. *AAPG Bulletin*, *93*(11), 1535-1549. https://doi.org/10.1306/08110909100

Omori, Y., Barresi, A., Kimura, N., Okamoto, A., & Masuda, T. (2016). Contrast in stress–strain history during exhumation between high-and ultrahigh-pressure metamorphic units in the Western Alps: Microboudinage analysis of piemontite in metacherts. *Journal of Structural Geology*, *89*, 168-180. https://doi.org/10.1016/j.jsg.2016.06.004

Owens, T. J., & Zandt, G. (1997). Implications of crustal property variations for models of Tibetan plateau evolution. *Nature*, *387*(6628), 37-43. https://doi.org/10.1038/387037a0

Özkan, H. (1979). Elastic constants of tourmaline. *Journal of Applied Physics*, *50*(9), 6006-6008. https://doi.org/10.1063/1.326707

Parrish, R. R. (2001). The response of mineral chronometers to metamorphism and deformation in orogenic belts. *Geological Society, London, Special Publications*, *184*(1), 289-301. https://doi.org/10.1144/GSL.SP.2001.184.01.14

Pascal, C., Angelier, J., Cacas, M. C., & Hancock, P. L. (1997). Distribution of joints: probabilistic modelling and case study near Cardiff (Wales, UK). *Journal of Structural Geology*, *19*(10), 1273-1284. https://doi.org/10.1016/S0191-8141(97)00047-3

Passchier, C. W., & Trouw, R. A. (2005). *Microtectonics*. Springer Science & Business Media, Berlin.

Paterson, M. S., & Luan, F. C. (1990). Quartzite rheology under geological conditions. *Geological Society, London, Special Publications*, *54*(1), 299-307. https://doi.org/10.1144/GSL.SP.1990.054.01.26

Paterson, M. S., & Olgaard, D. L. (2000). Rock deformation tests to large shear strains in torsion. *Journal of Structural Geology*, *22*(9), 1341-1358. https://doi.org/10.1016/S0191-

8141(00)00042-0

Paterson, M. S., & Wong, T. F. (2005). *Experimental rock deformation-the brittle field*. Springer Science & Business Media, Berlin.

Peng, T., Wang, Y., Fan, W., Liu, D., Shi, Y., & Miao, L. (2006). SHRIMP ziron U-Pb geochronology of early Mesozoic felsic igneous rocks from the southern Lancangjiang and its tectonic implications. *Science in China Series D: Earth Sciences*, *49*(10), 1032-1042. https://doi.org/10.1007/s11430-006-1032-y

Pesquera, A., Torres-Ruiz, J., Gil-Crespo, P. P., & Roda-Robles, E. (2009). Multistage boron metasomatism in the Alamo Complex (Central Iberian Zone, Spain): Evidence from field relations, petrography, and $^{40}Ar/^{39}Ar$ tourmaline dating. *American Mineralogist*, *94*(10), 1468-1478. https://doi.org/10.2138/am.2009.3100

Pfiffner, O. A., & Ramsay, J. G. (1982). Constraints on geological strain rates: arguments from finite strain states of naturally deformed rocks. *Journal of Geophysical Research: Solid Earth*, *87*(B1), 311-321. https://doi.org/10.1029/JB087iB01p00311

Pincivy, A. (2003). *Géochronologie $^{40}Ar/^{39}Ar$ et analyse structurale de la zone de Humber des Appalaches de Gaspésie (Québec, Canada): implication sur la tectonique des Appalaches du nord* [Doctoral dissertation, Université du Québec].

Pitzer, K. S., & Sterner, S. M. (1994). Equations of state valid continuously from zero to extreme pressures for H_2O and CO_2. *The Journal of Chemical Physics*, *101*(4), 3111-3116. https://doi.org/10.1063/1.467624

Platt, J. P. (2015a). Influence of shear heating on microstructurally defined plate boundary shear zones. *Journal of Structural Geology*, *79*, 80-89. https://doi.org/10.1016/j.jsg.2015.07.009

Platt, J. P. (2015b). Rheology of two-phase systems: A microphysical and observational approach. *Journal of Structural Geology*, *77*, 213-227. https://doi.org/10.1016/j.jsg.2015.05.003

Pollard, D. D., & Segall, P. (1987). Theoretical displacements and stresses near fractures in rock: with applications to faults, joints, veins, dikes, and solution surfaces. In A. K. Atkinson (Eds.), *Fracture mechanics of rock* (pp. 277-347). Elsevier, Amsterdam.

Post Jr, R. L. (1977). High-temperature creep of Mt. Burnet dunite. *Tectonophysics*, *42*(2-4), 75-110. https://doi.org/10.1016/0040-1951(77)90162-7

Post, A., & Tullis, J. (1999). A recrystallized grain size piezometer for experimentally deformed

feldspar aggregates. *Tectonophysics*, *303*(1-4), 159-173. https://doi.org/10.1016/S0040-1951(98)00260-1

Price, N. J. (2016). *Fault and joint development: in brittle and semi-brittle rock*. Elsevier, Amsterdam.

Price, N. J., & Cosgrove, J. W. (1990). *Analysis of geological structures*. Cambridge University Press, Cambridge.

Priest, S. D., & Hudson, J. A. (1976). Discontinuity spacings in rock. *International Journal of Rock Mechanics and Mining Sciences & Geomechanics Abstracts*, *13*, 135-148. https://doi.org/10.1016/0148-9062(76)90818-4

Ramberg, H. (1955). Natural and experimental boudinage and pinch-and-swell structures. *The Journal of Geology*, *63*(6), 512-526.

Ranalli, G. (2003). How soft is the crust?. *Tectonophysics*, *3*(361), 319-320. https://doi.org/10.1016/S0040-1951(02)00607-8

Ranalli, G., & Murphy, D. C. (1987). Rheological stratification of the lithosphere. *Tectonophysics*, *132*(4), 281-295. https://doi.org/10.1016/0040-1951(87)90348-9

Rawnsley, K. D., Peacock, D. C. P., Rives, T., & Petit, J. P. (1998). Joints in the Mesozoic sediments around the Bristol Channel Basin. *Journal of Structural Geology*, *20*(12), 1641-1661. https://doi.org/10.1016/S0191-8141(98)00070-4

Rawnsley, K. D., Rives, T., Petti, J. P., Hencher, S. R., & Lumsden, A. C. (1992). Joint development in perturbed stress fields near faults. *Journal of Structural Geology*, *14*(8-9), 939-951. https://doi.org/10.1016/0191-8141(92)90025-R

Reiners, P. W. (2005). Zircon (U-Th)/He thermochronometry. *Reviews in Mineralogy and Geochemistry*, *58*(1), 151-179. https://doi.org/10.2138/rmg.2005.58.6

Ren, X., Das, R., Tran, P., Ngo, T. D., & Xie, Y. M. (2018). Auxetic metamaterials and structures: a review. *Smart Materials and Structures*, *27*(2), 023001. https://doi.org/10.1088/1361-665X/aaa61c

Resser, C. E. (1942). Evolution of Ausable Chasm. *The Scientific Monthly*, *54*(1), 29-42.

Rives, T., Rawnsley, K. D., & Petit, J. P. (1994). Analogue simulation of natural orthogonal joint set formation in brittle varnish. *Journal of Structural Geology*, *16*(3), 419-429. https://doi.org/10.1016/0191-8141(94)90045-0

Rives, T., Razack, M., Petit, J. P., & Rawnsley, K. D. (1992). Joint spacing: analogue and numerical simulations. *Journal of Structural Geology*, *14*(8-9), 925-937. https://doi.org/10.1016/0191-8141(92)90024-Q

Ross, J. V., AvéLallemant, H. G., & Carter, N. L. (1980). Stress dependence of recrystallized-grain and subgrain size in olivine. *Tectonophysics*, *70*(1-2), 39-61. https://doi.org/10.1016/0040-1951(80)90020-7

Rouleau, A., & Gale, J. E. (1985). Statistical characterization of the fracture system in the Stripa granite, Sweden. *International Journal of Rock Mechanics and Mining Sciences & Geomechanics Abstracts*, *22*, 353-367. https://doi.org/10.1016/0148-9062(85)90001-4

Rubie, D. C. (1990). Mechanisms of reaction-enhanced deformability in minerals and rocks. In: *Deformation processes in minerals, ceramics and rocks*. Springer, Dordrecht.

Ruf, J. C., Rust, K. A., & Engelder, T. (1998). Investigating the effect of mechanical discontinuities on joint spacing. *Tectonophysics*, *295*(1-2), 245-257. https://doi.org/10.1016/S0040-1951(98)00123-1

Rummel, F., Klee, G., & Weber, U. (2002). *Hydraulic fracturing and core testing in borehole KOV01* (Report No. IPR-02-01).

Rustichelli, A., Agosta, F., Tondi, E., & Spina, V. (2013). Spacing and distribution of bed-perpendicular joints throughout layered, shallow-marine carbonates (Granada Basin, southern Spain). *Tectonophysics*, *582*, 188-204. https://doi.org/10.1016/j.tecto.2012.10.007

Rutter, E. H. (1995). Experimental study of the influence of stress, temperature, and strain on the dynamic recrystallization of Carrara marble. *Journal of Geophysical Research: Solid Earth*, *100*(B12), 24651-24663. https://doi.org/10.1029/95JB02500

Rutter, E. H., & Brodie, K. H. (1992). Rheology of the lower crust. In *Continental Lower Crust* (pp. 201-267). Elsevier.

Rutter, E. H., & Brodie, K. H. (2004). Experimental intracrystalline plastic flow in hot-pressed synthetic quartzite prepared from Brazilian quartz crystals. *Journal of Structural Geology*, *26*(2), 259-270. https://doi.org/10.1016/S0191-8141(03)00096-8

Rybacki, E., & Dresen, G. (2000). Dislocation and diffusion creep of synthetic anorthite aggregates. *Journal of Geophysical Research: Solid Earth*, *105*(B11), 26017-26036. https://doi.org/10.1029/2000JB900223

Rybacki, E., & Dresen, G. (2004). Deformation mechanism maps for feldspar rocks. *Tectonophysics*, *382*(3-4), 173-187. https://doi.org/10.1016/j.tecto.2004.01.006

Rybacki, E., Gottschalk, M., Wirth, R., & Dresen, G. (2006). Influence of water fugacity and activation volume on the flow properties of fine-grained anorthite aggregates. *Journal of Geophysical Research: Solid Earth*, *111*, B03203. https://doi.org/10.1029/2005JB003663

Saein, A. F., & Riahi, Z. T. (2019). Controls on fracture distribution in Cretaceous sedimentary rocks from the Isfahan region, Iran. *Geological Magazine*, *156*(6), 1092-1104. https://doi.org/10.1017/S0016756817000346

Salad Hersi, O., Lavoie, D., & Nowlan, G. S. (2003). Reappraisal of the Beekmantown Group sedimentology and stratigraphy, Montreal area, southwestern Quebec: implications for understanding the depositional evolution of the Lower-Middle Ordovician Laurentian passive margin of eastern Canada. *Canadian Journal of Earth Sciences*, *40*(2), 149-176. https://doi.org/10.1139/e02-077

Salad Hersi, O., Mohamed, A. H., Lavoie, D., & Nowlan, G. S. (2002). Subaerial unconformity at the Potsdam–Beekmantown contact in the Quebec Reentrant: regional significance for the Laurentian continental margin history. *Bulletin of Canadian Petroleum Geology*, *50*(3), 419-440. https://doi.org/10.2113/50.3.419

Samanta, S. K., Mandal, N., & Chakraborty, C. (2002). Development of different types of pull-apart microstructures in mylonites: an experimental investigation. *Journal of structural Geology*, *24*(8), 1345-1355. https://doi.org/10.1016/S0191-8141(01)00139-0

Sanford, B. V., & Arnott, R. W. C. (2009). *Stratigraphic and structural framework of the Potsdam Group in eastern Ontario, western Quebec, and northern New York state*. Geological Survey of Canada. https://doi.org/10.4095/247673.

Sassier, C., Leloup, P. H., Rubatto, D., Galland, O., Yue, Y., & Lin, D. (2009). Direct measurement of strain rates in ductile shear zones: A new method based on syntectonic dikes. *Journal of Geophysical Research: Solid Earth*, *114*, B01406. https://doi.org/10.1029/2008JB005597

Schärer, U., Tapponnier, P., Lacassin, R., Leloup, P. H., Zhong, D. L., & Ji, S. (1990). Intraplate tectonics in Asia: a precise age for large-scale Miocene movement along the Ailao Shan-Red River shear zone, China. *Earth and Planetary Science Letters*, *97*(1-2), 65-77. https://doi.org/10.1016/0012-821X(90)90099-J

Scholz, C. H. (2019). *The mechanics of earthquakes and faulting*. Cambridge University Press, Cambridge.

Schöpfer, M. P., Arslan, A., Walsh, J. J., & Childs, C. (2011). Reconciliation of contrasting theories for fracture spacing in layered rocks. *Journal of Structural Geology*, *33*(4), 551-565. https://doi.org/10.1016/j.jsg.2011.01.008

Searle, M. P. (2006). Role of the Red River Shear zone, Yunnan and Vietnam, in the continental extrusion of SE Asia. *Journal of the Geological Society*, *163*(6), 1025-1036. https://doi.org/10.1144/0016-76492005-144

Searle, M. P., Yeh, M. W., Lin, T. H., & Chung, S. L. (2010). Structural constraints on the timing of left-lateral shear along the Red River shear zone in the Ailao Shan and Diancang Shan Ranges, Yunnan, SW China. *Geosphere*, *6*(4), 316-338. https://doi.org/10.1130/GES00580.1

Secor, D. T. (1965). Role of fluid pressure in jointing. *American Journal of Science*, *263*(8), 633-646.

Selleck, B. (1993). Sedimentology and diagenesis of the Potsdam sandstone and Theresa formation, southwestern St. Lawrence valley. In *Field trip guidebook for the northeastern United States: geological society of America 85th annual meeting and New England intercollegiate geological conference* (pp. 219-228).

Shang, J., Hencher, S. R., & West, L. J. (2016). Tensile strength of geological discontinuities including incipient bedding, rock joints and mineral veins. *Rock Mechanics and Rock Engineering*, *49*(11), 4213-4225. https://doi.org/10.1007/s00603-016-1041-x

Shang, J., West, L. J., Hencher, S. R., & Zhao, Z. (2018). Geological discontinuity persistence: Implications and quantification. *Engineering Geology*, *241*, 41-54. https://doi.org/10.1016/j.enggeo.2018.05.010Get rights and content

Shao, T., Song, M., Ji, S., Li, J., & Wang, Q. (2013). Influence of water on deformation of NAMs: a review. *Geotectonica et Metallogenia*, *1*, 138-163 (in Chinese with English abstract).

Shekhar Pandey, C., & Schreuer, J. (2012). Elastic and piezoelectric constants of tourmaline single crystals at non-ambient temperatures determined by resonant ultrasound spectroscopy. *Journal of Applied Physics*, *111*(1), 013516. https://doi.org/10.1063/1.3673820

Shelton, G. L., & Tullis, J. (1981). Experimental flow laws for crustal rocks. *Eos, Transactions American Geophysical Union*, *62*, 396.

Shimizu, I. (2008). Theories and applicability of grain size piezometers: The role of dynamic

recrystallization mechanisms. *Journal of Structural Geology*, *30*(7), 899-917. https://doi.org/10.1016/j.jsg.2008.03.004

Sibson, R. H. (1974). Frictional constraints on thrust, wrench and normal faults. *Nature*, *249*(5457), 542-544. https://doi.org/10.1038/249542a0

Sibson, R. H. (2017). Tensile overpressure compartments on low-angle thrust faults. *Earth, Planets and Space*, *69*(1), 1-15. https://doi.org/10.1186/s40623-017-0699-y

Sibson, R. H., Robert, F., & Poulsen, K. H. (1988). High-angle reverse faults, fluid-pressure cycling, and mesothermal gold-quartz deposits. *Geology*, *16*(6), 551-555. https://doi.org/10.1130/0091-7613(1988)016<0551:HARFFP>2.3.CO;2

Simmons, G., & Brace, W. F. (1965). Comparison of static and dynamic measurements of compressibility of rocks. *Journal of Geophysical Research*, *70*(22), 5649-5656. https://doi.org/10.1029/JZ070i022p05649

Simón, J. L., Arlegui, L. E., & Pocovi, A. (2006). Fringe cracks and plumose structures in layered rocks: stepping senses and their implications for palaeostress interpretation. *Journal of Structural Geology*, *28*(6), 1103-1113. https://doi.org/10.1016/j.jsg.2006.03.015

Simón, J. L., Seron, F. J., & Casas, A. M. (1988). Stress deflection and fracture development in a multidirectional extension regime. Mathematical and experimental approach with field examples. *Annales Tectonicae*, *2*, 21-32.

Simpson, C., & Schmid, S. M. (1983). An evaluation of criteria to deduce the sense of movement in sheared rocks. *Geological Society of America Bulletin*, *94*(11), 1281-1288. https://doi.org/10.1130/0016-7606(1983)94<1281:AEOCTD>2.0.CO;2

Simpson, C., & Wintsch, R. P. (1989). Evidence for deformation-induced K-feldspar replacement by myrmekite. *Journal of Metamorphic Geology*, *7*(2), 261-275. https://doi.org/10.1111/j.1525-1314.1989.tb00588.x

Snoke, A. W., & Tullis, J. (1998). An overview of fault rocks. In *Fault-related rocks: a photographic atlas*. Princeton University Press, Princeton.

Snow, D. T. (1968). Anisotropic permeability of fractured rocks. *Journal of the Soil Mechanics and Foundations Division*, *84*, 73-91.

Socquet, A., & Pubellier, M. (2005). Cenozoic deformation in western Yunnan (China–Myanmar border). *Journal of Asian Earth Sciences*, *24*(4), 495-515. https://doi.org/10.1016/j.jseaes.2004.03.006

Song, S., Niu, Y., Wei, C., Ji, J., & Su, L. (2010). Metamorphism, anatexis, zircon ages and tectonic evolution of the Gongshan block in the northern Indochina continent—an eastern extension of the Lhasa Block. *Lithos*, *120*(3-4), 327-346. https://doi.org/10.1016/j.lithos.2010.08.021

Souffaché, B., & Angelier, J. (1989). Distribution de joints de tension dans un banc rocheux: principe d'une modélisation énergétique. *Comptes Rendus de l'Académie des Sciences, Série II*, *308*(15), 1385-1390.

Sowers, G. M. (1973). Theory of spacing of extension fracture. *Engineering Geology Case Histories*, *9*, 27-53.

Stavropoulou, M. (2014). Discontinuity frequency and block volume distribution in rock masses. *International Journal of Rock Mechanics and Mining Sciences*, *65*, 62-74. https://doi.org/10.1016/j.ijrmms.2013.11.003

Stewart, I. S., & Hancock, P. L. (1990). Brecciation and fracturing within neotectonic normal fault zones in the Aegean region. *Geological Society, London, Special Publications*, *54*(1), 105-110. https://doi.org/10.1144/GSL.SP.1990.054.01.11

Stipp, M., & Tullis, J. (2003). The recrystallized grain size piezometer for quartz. *Geophysical Research Letters*, *30*(21), 2088. https://doi.org/10.1029/2003GL018444

Stipp, M., Stünitz, H., Heilbronner, R., & Schmid, S. M. (2002). Dynamic recrystallization of quartz: correlation between natural and experimental conditions. *Geological Society, London, Special Publications*, *200*(1), 171-190. https://doi.org/10.1144/GSL.SP.2001.200.01.11

Stipp, M., Tullis, J., & Behrens, H. (2006). Effect of water on the dislocation creep microstructure and flow stress of quartz and implications for the recrystallized grain size piezometer. *Journal of Geophysical Research: Solid Earth*, *111*, B04201. https://doi.org/10.1029/2005JB003852

Stipp, M., Tullis, J., Scherwath, M., & Behrmann, J. H. (2010). A new perspective on paleopiezometry: Dynamically recrystallized grain size distributions indicate mechanism changes. *Geology*, *38*(8), 759-762. https://doi.org/10.1130/G31162.1

St-Julien, P. (1967). Tectonics of part of the Appalachian region of southeastern Quebec (southwest of the Chaudière River). In *Appalachian Tectonics* (pp. 41-47). University of Toronto Press, Toronto.

St-Julien, P., & Hubert, C. (1975). Evolution of the Taconian orogen in the Quebec Appalachians. *American Journal of Science*, *275*, 337-362.

Stöckhert, B., Brix, M. R., Kleinschrodt, R., Hurford, A. J., & Wirth, R. (1999). Thermochronometry and microstructures of quartz—a comparison with experimental flow laws and predictions on the temperature of the brittle–plastic transition. *Journal of Structural Geology*, *21*(3), 351-369. https://doi.org/10.1016/S0191-8141(98)00114-X

Sun, X., Bao, X., Xu, M., Eaton, D. W., Song, X., Wang, L., Ding, Z., Mi, N., Yu, D., & Li, H. (2014). Crustal structure beneath SE Tibet from joint analysis of receiver functions and Rayleigh wave dispersion. *Geophysical Research Letters*, *41*(5), 1479-1484. https://doi.org/10.1002/2014GL059269

Sun, Y., Niu, F., Liu, H., Chen, Y., & Liu, J. (2012). Crustal structure and deformation of the SE Tibetan plateau revealed by receiver function data. *Earth and Planetary Science Letters*, *349*, 186-197. https://doi.org/10.1016/j.epsl.2012.07.007

Sutherland, R., Nathan, S., Turnbull, I. M., & Beu, A. G. (1995). Pliocene-Quaternary sedimentation and Alpine fault related tectonics in the lower Cascade Valley, South Westland, New Zealand. *New Zealand Journal of Geology and Geophysics*, *38*(4), 431-450. https://doi.org/10.1080/00288306.1995.9514670

Tan, Y., Johnston, T., & Engelder, T. (2014). The concept of joint saturation and its application. *AAPG Bulletin*, *98*(11), 2347-2364. https://doi.org/10.1306/06231413113

Tang, C. A., Liang, Z. Z., Zhang, Y. B., Chang, X., Tao, X., Wang, D. G., Zhang, J. X., Liu, J. S., Zhu, W. C., & Elsworth, D. (2008). Fracture spacing in layered materials: a new explanation based on two-dimensional failure process modeling. *American Journal of Science*, *308*(1), 49-72. https://doi.org/10.2475/01.2008.02

Tang, C. A., Zhang, Y. B., Liang, Z. Z., Xu, T., Tham, L. G., Lindqvist, P. A., Kou, S. Q., & Liu, H. Y. (2006). Fracture spacing in layered materials and pattern transition from parallel to polygonal fractures. *Physical Review E*, *73*(5), 056120. https://doi.org/10.1103/PhysRevE.73.056120

Tang, J., Xiao, Q., Zhan, Y., Li, R., & Dong, Z. (2012). Research on the electrical and regional structure characteristics of the seismic region in South Yunnan. *Recent Developments in World Seismology*, *6*, 71. https://doi.org/10.3969/j.issn.0253-4975.2012.06.071

Tang, Y., Liu, J., Tran, M. D., Song, Z., Wu, W., Zhang, Z., Zhao, Z., & Chen, W. (2013).

Timing of left-lateral shearing along the Ailao Shan-Red River shear zone: constraints from zircon U–Pb ages from granitic rocks in the shear zone along the Ailao Shan Range, Western Yunnan, China. *International Journal of Earth Sciences*, *102*(3), 605-626. https://doi.org/10.1007/s00531-012-0831-y

Tang, Y., Wang, D., Liao, S., Wang, B., & Yin, F. (2020). Fabrics and $^{40}Ar/^{39}Ar$ ages of metamorphic rocks in the Gaoligong tectonic belt: Implications for Cenozoic metamorphism and deformation in the SE Tibetan Plateau. *Journal of Asian Earth Sciences*, *192*, 104270. https://doi.org/10.1016/j.jseaes.2020.104270

Tapponnier, P., Lacassin, R., Leloup, P. H., Schärer, U., Zhong, D. L., Wu, H. W., Liu, X. H., Ji, S. C., Zhang, L. S., & Zhong, J. Y. (1990). The Ailao Shan/Red River metamorphic belt: tertiary left-lateral shear between Indochina and South China. *Nature*, *343*(6257), 431-437. https://doi.org/10.1038/343431a0

Tapponnier, P., Peltzer, G., & Armijo, R. (1986). On the mechanics of the collision between India and Asia. *Geological Society, London, Special Publications*, *19*(1), 113-157. https://doi.org/10.1144/GSL.SP.1986.019.01.07

Tapponnier, P., Xu, Z. Q., Roger, F., Meyer, B., Arnaud, N., Wittlinger, G., & Yang, J. S. (2001). Oblique stepwise rise and growth of the Tibet Plateau. *Science*, *294*(5547), 1671-1677. https://doi.org/10.1126/science.105978

Tee, G. J. (2005). *Surface area of ellipsoid segment*. The University of Auckland, New Zealand.

Ter Heege, J. H. (2002). *Relationship between dynamic recrystallization, grain size distribution and rheology* [Doctoral dissertation, Utrecht University].

Thunvik, R., & Braester, C. (1990). Gas migration in discrete fracture networks. *Water Resources Research*, *26*(10), 2425-2434. https://doi.org/10.1029/WR026i010p02425

Tinni, A., Sondergeld, C., & Chandra, R. (2019). Hydraulic fracture propagation velocity and implications for hydraulic fracture diagnostics. In *53rd US Rock Mechanics/Geomechanics Symposium*. OnePetro.

Tödheide, K. (1972). Water at high temperatures and pressures. In *The physics and physical chemistry of water*. Springer.

Tokle, L., Hirth, G., & Behr, W. M. (2019). Flow laws and fabric transitions in wet quartzite. *Earth and Planetary Science Letters*, *505*, 152-161. https://doi.org/10.1016/j.epsl.2018.10.017

Tripathi, D., & Jones, F. R. (1998). Single fibre fragmentation test for assessing adhesion in fibre reinforced composites. *Journal of Materials Science*, *33*(1), 1-16. https://doi.org/10.1023/A:1004351606897

Tullis, J. (2002). Deformation of granitic rocks: Experimental studies and natural examples. *Reviews in Mineralogy and Geochemistry*, *51*(1), 51-95. https://doi.org/10.2138/gsrmg.51.1.51

Tullis, J., & Yund, R. A. (1985). Dynamic recrystallization of feldspar: A mechanism for ductile shear zone formation. *Geology*, *13*(4), 238-241. https://doi.org/10.1130/0091-7613(1985)13<238:DROFAM>2.0.CO;2

Tullis, J., & Yund, R. A. (1987). Transition from cataclastic flow to dislocation creep of feldspar: Mechanisms and microstructures. *Geology*, *15*(7), 606-609. https://doi.org/10.1130/0091-7613(1987)15<606:TFCFTD>2.0.CO;2

Tullis, T. E., Horowitz, F. G., & Tullis, J. (1991). Flow laws of polyphase aggregates from end-member flow laws. *Journal of Geophysical Research: Solid Earth*, *96*(B5), 8081-8096.

Twiss, R. J. (1977). Theory and applicability of a recrystallized grain size paleopiezometer. *Pure and Applied Geophysics*, *115*, 227-244. https://doi.org/10.1007/BF01637105

Twiss, R. J. (1986). Variable sensitivity piezometric equations for dislocation density and subgrain diameter and their relevance to olivine and quartz. *Mineral and Rock Deformation: Laboratory Studies, AGU Geophysical Monographs*, *36*, 247-261. https://doi.org/10.1029/GM036p0247

Twiss, R. J., & Moores, E. M. (2001). *Structural geology*. WH Freeman and Company.

Underwood, E. E. (1972). The mathematical foundations of quantitative stereology. In *Stereology and quantitative metallography*. ASTM International.

Underwood, E. E. (1973). Quantitative stereology for microstructural analysis. In *Microstructural analysis* (pp. 35-66). Springer, Dordrecht.

Van der Pluijm, B. A., & Marshak, S. (2003). *Earth structure: an introduction to structural geology and tectonics*. W. W. Norton & Company, New York.

Van der Wal, D., Chopra, P., Drury, M., & Gerald, J. F. (1993). Relationships between dynamically recrystallized grain size and deformation conditions in experimentally deformed olivine rocks. *Geophysical Research Letters*, *20*(14), 1479-1482. https://doi.org/10.1029/93GL01382

Van Hinsberg, V. J., Henry, D. J., & Marschall, H. R. (2011). Tourmaline: an ideal indicator of its host environment. *The Canadian Mineralogist*, *49*(1), 1-16. https://doi.org/10.3749/canmin.49.1.1

Van Noten, K., & Sintubin, M. (2010). Linear to non-linear relationship between vein spacing and layer thickness in centimetre-to decimetre-scale siliciclastic multilayers from the High-Ardenne slate belt (Belgium, Germany). *Journal of Structural Geology*, *32*(3), 377-391. https://doi.org/10.1016/j.jsg.2010.01.011

Villaescusa, E., & Brown, E. T. (1990). Characterizing joint spatial correlation using geostatistical methods. In N. Barton & O. Stephansson (Eds.), *Rock joints* (pp. 115-122). Balkema, Rotterdam.

Viola, G., & Anczkiewicz, R. (2008). Exhumation history of the Red River shear zone in northern Vietnam: New insights from zircon and apatite fission-track analysis. *Journal of Asian Earth Sciences*, *33*(1-2), 78-90. https://doi.org/10.1016/j.jseaes.2007.08.006

Walters, R. J., England, P. C., & Houseman, G. A. (2017). Constraints from GPS measurements on the dynamics of the zone of convergence between Arabia and Eurasia. *Journal of Geophysical Research: Solid Earth*, *122*(2), 1470-1495. https://doi.org/10.1002/2016JB013370

Wang, D., Li, B., Ji, J., Song, S., Wei, C., & Gong, J. (2013). The thermal evolution and deformation time limit of the Gaoligong metamorphic belt in Western Yunnan. *Acta Geologica Sinica*, *87*, 1887-1900.

Wang, E., & Burchfiel, B. C. (1997). Interpretation of Cenozoic tectonics in the right-lateral accommodation zone between the Ailao Shan shear zone and the eastern Himalayan syntaxis. *International Geology Review*, *39*(3), 191-219. https://doi.org/10.1080/00206819709465267

Wang, F., Zhang, S., & Li, M. (2018). Crustal structure of yunnan province of China from teleseismic receiver functions: implications for regional crust evolution. *Journal of Earth Science*, *29*(6), 1419-1430. https://doi.org/10.1007/s12583-017-0822-9

Wang, H., & Wright, T. J. (2012). Satellite geodetic imaging reveals internal deformation of western Tibet. *Geophysical Research Letters*, *39*, L07303. https://doi.org/10.1029/2012GL051222

Wang, J. N., Hobbs, B. E., Ord, A., Shimamoto, T., & Toriumi, M. (1994). Newtonian dislocation creep in quartzites: Implications for the rheology of the lower crust. *Science*, *265*(5176), 1204-1206. https://doi.org/10.1126/science.265.5176.1204

Wang, J. Y., & Huang, S. P. (1990). Compilation of heat flow data in the China continental area. *Seismology and Geology*, *12*, 351-366.

Wang, Y., Fan, W., Zhang, Y., Peng, T., Chen, X., & Xu, Y. (2006). Kinematics and 40Ar/39Ar geochronology of the Gaoligong and Chongshan shear systems, western Yunnan, China: Implications for early Oligocene tectonic extrusion of SE Asia. *Tectonophysics*, *418*(3-4), 235-254. https://doi.org/10.1016/j.tecto.2006.02.005

Wang, Y., Wang, Y., Schoenbohm, L. M., Zhang, P., Zhang, B., Sobel, E. R., Zhou, R., Shi, X., Zhang, J., Stockli, D. F., & Guo, X. (2020). Cenozoic exhumation of the Ailaoshan-Red River shear zone: New insights from low-temperature thermochronology. *Tectonics*, *39*(9), e2020TC006151.

Wang, Y., Zhang, B., Schoenbohm, L. M., Zhang, J., Zhou, R., Hou, J., & Ai, S. (2016). Late Cenozoic tectonic evolution of the Ailao Shan-Red River fault (SE Tibet): Implications for kinematic change during plateau growth. *Tectonics*, *35*(8), 1969-1988. https://doi.org/10.1002/2016TC004229

Wang, Y., Zhang, P., Schoenbohm, L. M., Zheng, W., Zhang, B., Zhang, J., Zheng, D., Zhou, R., & Tian, Y. (2018). Two-phase exhumation along major shear zones in the SE Tibetan plateau in the late Cenozoic. *Tectonics*, *37*(8), 2675-2694. https://doi.org/10.1029/2018TC004979

Wang, Z., & Ji, S. (2000). Diffusion creep of fine-grained garnetite: Implications for the flow strength of subducting slabs. *Geophysical Research Letters*, *27*(15), 2333-2336. https://doi.org/10.1029/1999GL008474

Weathers, M. S., Bird, J. M., Cooper, R. F., & Kohlstedt, D. L. (1979). Differential stress determined from deformation-induced microstructures of the Moine Thrust Zone. *Journal of Geophysical Research: Solid Earth*, *84*(B13), 7495-7509. https://doi.org/10.1029/JB084iB13p07495

Weibull, W. (1939). *A statistical theory of strength of materials*. Generalstabens litografiska anstalts förlag, Stockholm.

Weibull, W. (1951). A statistical distribution function of wide applicability. *Journal of Applied Mechanics*, *18*(3), 293-297.

Weibull, W. (1952). A survey of statistical effects in the field of material failure. *Applied Mechanics Reviews*, *5*(11), 449-451.

Weisbrod, A., Polak, C., & Roy, D. (1986). Experimental study of tourmaline solubility in the system Na-Mg-Al-Si-BOH: applications to the boron content of natural hydrothermal fluids and tourmalinization processes. In *International Symposium on Experimental Mineralogy and Geochemistry*. Nancy, France.

Wheeler, J. (1992). Importance of pressure solution and Coble creep in the deformation of polymineralic rocks. *Journal of Geophysical Research: Solid Earth*, *97*(B4), 4579-4586. https://doi.org/10.1029/91JB02476

White, S. (1979). Grain and sub-grain size variations across a mylonite zone. *Contributions to Mineralogy and Petrology*, *70*(2), 193-202. https://doi.org/10.1007/BF00374448

Williams, H. (1995). *Geology of the Appalachian—Caledonian Orogen in Canada and Greenland*. The Geological Society of America Inc., Boulder, Colorado.

Wolf, M. B., & London, D. (1997). Boron in granitic magmas: stability of tourmaline in equilibrium with biotite and cordierite. *Contributions to Mineralogy and Petrology*, *130*(1), 12-30. https://doi.org/10.1007/s004100050346

Wong, L. N. Y., Lai, V. S. K., & Tam, T. P. Y. (2018). Joint spacing distribution of granites in Hong Kong. *Engineering Geology*, *245*, 120-129. https://doi.org/10.1016/j.enggeo.2018.08.009

Wong, T. F., Wong, R. H., Chau, K. T., & Tang, C. A. (2006). Microcrack statistics, Weibull distribution and micromechanical modeling of compressive failure in rock. *Mechanics of Materials*, *38*(7), 664-681. https://doi.org/10.1016/j.mechmat.2005.12.002

Wu, H., & Pollard, D. D. (1995). An experimental study of the relationship between joint spacing and layer thickness. *Journal of Structural Geology*, *17*(6), 887-905. https://doi.org/10.1016/0191-8141(94)00099-L

Wu, H., & Pollard, D. D. (2002). Imaging 3-D fracture networks around boreholes. *AAPG Bulletin*, *86*(4), 593-604. https://doi.org/10.1306/61EEDB52-173E-11D7-8645000102C1865D

Wu, H., Zhang, L., & Ji, S. (1989). Himalayan ductile shear in the large sinistral strike-slip of Honghe-Ailaoshan. *Scientia Geologica Sinica*, *1*, 1-7.

Xu, H., Zhou, W., Xie, R., Da, L., Xiao, C., Shan, Y., & Zhang, H. (2016). Characterization of

rock mechanical properties using lab tests and numerical interpretation model of well logs. *Mathematical Problems in Engineering*, *2016*. https://doi.org/10.1155/2016/5967159

Xu, Q., Wang, J., Wang, J., & Zhang, W. (1992). Terrestrial heat flow and its tectonic significance in Yunnan, China. *Geotectonica et Metallogenia*, *16*, 285-299.

Xu, Y., Yang, X. T., & Liu, J. H. (2013). Tomographic study of crustal velocity structures in the Yunnan region southwest China. *Chinese Journal of Geophysics*, *56*(6), 1904-1914. https://doi.org/10.6038/cjg20130613

Xu, Z., Wang, Q., Cai, Z., Dong, H., Li, H., Chen, X., Duan, X., Cao, H., Li, J., & Burg, J. P. (2015). Kinematics of the Tengchong Terrane in SE Tibet from the late Eocene to early Miocene: Insights from coeval mid-crustal detachments and strike-slip shear zones. *Tectonophysics*, *665*, 127-148. https://doi.org/10.1016/j.tecto.2015.09.033

Yang, J., Yang, Z., & Zhang, H. (2018). Study on crustal velocity model and its application in the Yunnan region. *Earthquake Research in China*, *34*, 112-121.

Yu, C. Q., Zhang, G., Wang, X. B., Luo, W., Li, D. W., Cai, X. L., & Guo, Z. M. (2017). Deep electrical resistivity structure of Sanjiang Area of west Yunnan and its significance. *Chinese Journal of Geophysics*, *60*, 2385-2396. https://doi.org/10.6038/cjg20170628

Yu, C., Ji, S., & Li, Q. (2016). Effects of porosity on seismic velocities, elastic moduli and Poisson's ratios of solid materials and rocks. *Journal of Rock Mechanics and Geotechnical Engineering*, *8*(1), 35-49. https://doi.org/10.1016/j.jrmge.2015.07.004

Zandt, G., & Ammon, C. J. (1995). Continental crust composition constrained by measurements of crustal Poisson's ratio. *Nature*, *374*(6518), 152-154. https://doi.org/10.1038/374152a0

Zang, A., & Stephansson, O. (2010). *Stress field of the Earth's crust*. Springer Science & Business Media.

Zha, X., & Lei, J. (2013). Crustal thickness and Poisson's ratio beneath the Yunnan region. *Science China Earth Sciences*, *56*(4), 693-702. https://doi.org/10.1007/s11430-013-4583-8

Zhang, B. L., Liu, R. X., Xiang, H. F., Chu, Q. Z., Huang, X. N., & Zheng, Y. G. (2008). Features of mylonite at central southern section of the Red river fault zone and estimation of its primary theological parameters. *Seismology and Geology*, *30*(2), 473-483.

Zhang, B., Cai, F., Chen, S., Li, X., & Zhang, L. (2020). Sinistral strike-slip shearing along the Jiali shear zone around the Eastern Himalaya syntaxis region: Evidences for Oligocene

eastward limited translation of Tibet. *Journal of Structural Geology*, *139*, 104136. https://doi.org/10.1016/j.jsg.2020.104136

Zhang, B., Chai, Z., Yin, C. Y., Huang, W. T., Wang, Y., Zhang, J. J., Wang, X. X., & Cao, K. (2017). Intra-continental transpression and gneiss doming in an obliquely convergent regime in SE Asia. *Journal of Structural Geology*, *97*, 48-70. https://doi.org/10.1016/j.jsg.2017.02.010

Zhang, B., Zhang, J., & Zhong, D. (2010). Structure, kinematics and ages of transpression during strain-partitioning in the Chongshan shear zone, western Yunnan, China. *Journal of Structural Geology*, *32*(4), 445-463. https://doi.org/10.1016/j.jsg.2010.02.001

Zhang, B., Zhang, J., Chang, Z., Wang, X., Cai, F., & Lai, Q. (2012a). The Biluoxueshan transpressive deformation zone monitored by synkinematic plutons, around the Eastern Himalayan Syntaxis. *Tectonophysics*, *574*, 158-180. https://doi.org/10.1016/j.tecto.2012.08.017

Zhang, B., Zhang, J., Liu, J., Wang, Y., Yin, C., Guo, L., Zhong, D., Lai, Q., & Yue, Y. (2014). The Xuelongshan high strain zone: Cenozoic structural evolution and implications for fault linkages and deformation along the Ailao Shan–Red River shear zone. *Journal of Structural Geology*, *69*, 209-233. https://doi.org/10.1016/j.jsg.2014.10.008

Zhang, B., Zhang, J., Zhong, D., Wang, X., Qu, J., & Guo, L. (2011). Structural feature and its significance of the northernmost segment of the Tertiary Biluoxueshan-Chongshan shear zone, east of the Eastern Himalayan Syntaxis. *Science China Earth Sciences*, *54*(7), 959-974. https://doi.org/10.1007/s11430-011-4197-y

Zhang, B., Zhang, J., Zhong, D., Yang, L., Yue, Y., & Yan, S. (2012b). Polystage deformation of the Gaoligong metamorphic zone: Structures, $^{40}Ar/^{39}Ar$ mica ages, and tectonic implications. *Journal of Structural Geology*, *37*, 1-18. https://doi.org/10.1016/j.jsg.2012.02.007

Zhang, J., & Green, H. W. (2007). Experimental investigation of eclogite rheology and its fabrics at high temperature and pressure. *Journal of Metamorphic Geology*, *25*(2), 97-115. https://doi.org/10.1111/j.1525-1314.2006.00684.x

Zhang, L. S., & Schärer, U. (1999). Age and origin of magmatism along the Cenozoic Red River shear belt, China. *Contributions to Mineralogy and Petrology*, *134*(1), 67-85. https://doi.org/10.1007/s004100050469

Zhao, P. L., & Ji, S. (1992). Comment on “strengthening behavior of particulate reinforced MMCs” by Y. Wu and EJ Lavernia, and “on the strength of discontinuous silicon carbide reinforced aluminum composites” by VC Nardone and KM Prewo. *Scripta Metallurgica et Materialia*, *27*(10), 1443-1444.

Zhao, P., & Ji, S. (1997). Refinements of shear-lag model and its applications. *Tectonophysics*, *279*(1-4), 37-53. https://doi.org/10.1016/S0040-1951(97)00129-7

Zhao, X., Ji, S., & Martignole, J. (1997). Quartz c-axis fabrics and their tectonic implications for high temperature deformation of the Morin granulite complex. *Grenville Province: Canadian Journal of Earth Sciences*, *34*, 819-832.

Zheng, Y., Xia, L., & Yu, Q. (2015). Analysis of removability and stability of rock blocks by considering the rock bridge effect. *Canadian Geotechnical Journal*, *53*(3), 384-395. https://doi.org/10.1139/cgj-2014-0503

Zhong, D. L. (2000). *Paleotethysides in West Yunnan and Sichuan, China* (pp. 37-248). Science Press, Beijing.

Zhou, G., Liu, H., Chen, K., Gai, X., Zhao, C., Liao, L., Shen, K., Fan, Z., & Shan, Y. (2018). The origin of pyroelectricity in tourmaline at varying temperature. *Journal of Alloys and Compounds*, *744*, 328-336. https://doi.org/10.1016/j.jallcom.2018.02.064

Zoback, M. D. (2007). *Reservoir geomechanics*. Cambridge University Press.

APPENDIX A DATA MEASURED OF SAMPLE FROM THE CHONGSHAN SHEAR ZONE

		Original grain					Microboudin		
Sample	**Tourmaline**	***L* (mm)**	***W* (mm)**	***L/W* ratio**	**Sample**	**No**	***L* (mm)**	***W* (mm)**	***L/W* ratio**
CS45-1	Grain 1	1.525	0.450	3.389	CS45-1	Grain 1			
	Grain 2	3.150	1.075	2.930		1	0.300	0.260	1.154
	Grain 3	1.685	0.650	2.592		2	0.175	0.345	0.507
	Grain 4	0.875	0.550	1.591		3	0.150	0.345	0.435
	Grain 5	2.590	0.810	3.198		4	0.200	0.375	0.533
	Grain 6	1.750	0.665	2.632		5	0.135	0.310	0.435
	Grain 7	1.760	0.485	3.629		6	0.090	0.290	0.310
	Grain 8	1.325	0.725	1.828		7	0.135	0.360	0.375
	Grain 9	1.650	0.650	2.538		8	0.155	0.225	0.689
	Grain 10	1.665	1.075	1.549		9	0.135	0.175	0.771
	Grain 11	0.560	0.300	1.867		10	0.050	0.100	0.500
	Grain 12	0.865	0.295	2.932		Grain 2			
	Grain 13	0.900	0.425	2.118		1	1.275	0.725	1.759
	Grain 14	3.330	1.175	2.834		2	0.800	0.925	0.865
	Grain 15	1.060	0.235	4.511		3	0.425	1.075	0.395
	Grain 16	1.375	0.525	2.619		4	0.650	0.900	0.722
	Grain 17	2.745	0.775	3.542		Grain 3			
	Grain 18	1.220	0.500	2.440		1	0.150	0.250	0.600
	Grain 19	0.665	0.300	2.217		2	0.160	0.300	0.533
	Grain 20	4.205	0.975	4.313		3	0.300	0.475	0.632
	Grain 21	1.475	0.525	2.810		4	1.075	0.650	1.654
	Grain 22	1.200	0.910	1.319		Grain 4			
	Grain 23	2.940	0.825	3.564		1	0.300	0.450	0.667
	Grain 24	2.195	1.000	2.195		2	0.225	0.475	0.474
	Grain 25	1.330	0.290	4.586		3	0.350	0.550	0.636
	Grain 26	1.655	0.585	2.829		Grain 5			
	Grain 27	1.170	0.550	2.127		1	0.475	0.810	0.586
	Grain 28	0.520	0.195	2.667		2	0.210	0.455	0.462
CS45-2	Grain 1	1.215	0.610	1.992		3	0.090	0.480	0.188
	Grain 2	2.090	0.530	3.943		4	0.200	0.530	0.377
	Grain 3	1.890	0.550	3.436		5	0.240	0.610	0.393
	Grain 4	0.555	0.185	3.000		6	1.375	0.770	1.786
	Grain 5	1.285	0.685	1.876		Grain 6			
	Grain 6	0.710	0.350	2.029		1	0.450	0.375	1.200
	Grain 7	0.755	0.340	2.221		2	0.145	0.460	0.315
	Grain 8	2.285	0.350	6.529		3	0.230	0.665	0.346
	Grain 9	0.855	0.485	1.763		4	0.425	0.625	0.680

Grain 10	0.530	0.255	2.078
Grain 11	1.395	0.490	2.847
Grain 12	1.445	0.975	1.482
Grain 13	1.365	0.515	2.650
Grain 14	1.320	0.425	3.106
Grain 15	3.160	1.025	3.083
Grain 16	1.220	0.265	4.604
Grain 17	4.870	1.125	4.329
Grain 18	2.250	1.050	2.143
Grain 19	0.845	0.425	1.988

5	0.500	0.525	0.952
Grain 7			
1	0.600	0.485	1.237
2	0.250	0.480	0.521
3	0.075	0.450	0.167
4	0.160	0.450	0.356
5	0.125	0.440	0.284
6	0.550	0.425	1.294
Grain 8			
1	0.250	0.600	0.417
2	0.200	0.725	0.276
3	0.130	0.675	0.193
4	0.270	0.575	0.470
5	0.075	0.470	0.160
6	0.400	0.375	1.067
Grain 9			
1	0.225	0.475	0.474
2	0.065	0.575	0.113
3	0.200	0.625	0.320
4	0.350	0.650	0.538
5	0.325	0.645	0.504
6	0.260	0.545	0.477
7	0.225	0.485	0.464
Grain 10			
1	0.500	1.075	0.465
2	0.080	1.050	0.076
3	0.395	1.000	0.395
4	0.325	0.975	0.333
5	0.365	0.750	0.487
Grain 11			
1	0.135	0.280	0.482
2	0.075	0.275	0.273
3	0.025	0.275	0.091
4	0.325	0.300	1.083
Grain 12			
1	0.100	0.275	0.364
2	0.155	0.295	0.525
3	0.110	0.290	0.379
4	0.175	0.260	0.673
5	0.250	0.200	1.250
6	0.075	0.105	0.714
Grain 13			
1	0.250	0.325	0.769

2	0.100	0.425	0.235
3	0.250	0.425	0.588
4	0.300	0.425	0.706
Grain 14			
1	0.925	1.175	0.787
2	0.725	1.050	0.690
3	0.350	0.950	0.368
4	0.360	1.000	0.360
5	0.370	1.025	0.361
6	0.600	0.975	0.615
Grain 15			
1	0.325	0.230	1.413
2	0.105	0.210	0.500
3	0.150	0.235	0.638
4	0.275	0.205	1.341
5	0.075	0.175	0.429
6	0.130	0.150	0.867
Grain 16			
1	0.145	0.350	0.414
2	0.375	0.525	0.714
3	0.355	0.500	0.710
4	0.500	0.485	1.031
Grain 17			
1	0.300	0.425	0.706
2	0.325	0.550	0.591
3	0.200	0.700	0.286
4	0.400	0.600	0.667
5	1.100	0.700	1.571
6	0.300	0.775	0.387
7	0.120	0.750	0.160
Grain 18			
1	0.250	0.275	0.909
2	0.545	0.500	1.090
3	0.425	0.360	1.181
Grain 19			
1	0.075	0.275	0.273
2	0.135	0.285	0.474
3	0.130	0.300	0.433
4	0.125	0.250	0.500
5	0.200	0.200	1.000
Grain 20			
1	1.350	0.975	1.385
2	0.205	0.935	0.219

3	0.150	0.925	0.162
4	0.750	0.850	0.882
5	1.750	0.825	2.121
Grain 21			
1	0.360	0.450	0.800
2	0.160	0.525	0.305
3	0.180	0.450	0.400
4	0.150	0.475	0.316
5	0.300	0.350	0.857
6	0.325	0.340	0.956
Grain 22			
1	0.375	0.850	0.441
2	0.215	0.910	0.236
3	0.300	0.875	0.343
4	0.310	0.625	0.496
Grain 23			
1	0.375	0.695	0.540
2	0.340	0.675	0.504
3	0.200	0.695	0.288
4	0.150	0.800	0.188
5	0.325	0.825	0.394
6	0.090	0.725	0.124
7	0.325	0.650	0.500
8	0.735	0.600	1.225
9	0.400	0.565	0.708
Grain 24			
1	0.725	1.000	0.725
2	0.775	0.825	0.939
3	0.250	0.575	0.435
4	0.145	0.500	0.290
5	0.300	0.440	0.682
Grain 25			
1	0.495	0.290	1.707
2	0.060	0.150	0.400
3	0.190	0.200	0.950
4	0.060	0.210	0.286
5	0.185	0.270	0.685
6	0.055	0.160	0.344
7	0.115	0.130	0.885
8	0.055	0.125	0.440
9	0.115	0.125	0.920
Grain 26			
1	0.050	0.325	0.154

	2	0.240	0.390	0.615
	3	0.370	0.525	0.705
	4	0.170	0.535	0.318
	5	0.300	0.575	0.522
	6	0.525	0.585	0.897
	Grain 27			
	1	0.500	0.550	0.909
	2	0.070	0.550	0.127
	3	0.600	0.475	1.263
	Grain 28			
	1	0.260	0.195	1.333
	2	0.100	0.175	0.571
	3	0.160	0.145	1.103
CS45-2	Grain 1			
	1	0.195	0.475	0.411
	2	0.630	0.610	1.033
	3	0.145	0.575	0.252
	4	0.245	0.450	0.544
	Grain 2			
	1	0.450	0.515	0.874
	2	0.040	0.515	0.078
	3	0.100	0.530	0.189
	4	0.215	0.520	0.413
	5	0.385	0.510	0.755
	6	0.305	0.460	0.663
	7	0.215	0.400	0.538
	8	0.380	0.360	1.056
	Grain 3			
	1	0.265	0.390	0.679
	2	0.250	0.550	0.455
	3	0.150	0.540	0.278
	4	0.275	0.535	0.514
	5	0.295	0.500	0.590
	6	0.170	0.415	0.410
	7	0.210	0.355	0.592
	8	0.275	0.240	1.146
	Grain 4			
	1	0.210	0.115	1.826
	2	0.040	0.125	0.320
	3	0.240	0.185	1.297
	4	0.065	0.145	0.448
	Grain 5			
	1	0.410	0.580	0.707

2	0.175	0.660	0.265
3	0.700	0.685	1.022
Grain 6			
1	0.165	0.205	0.805
2	0.160	0.195	0.821
3	0.085	0.340	0.250
4	0.055	0.350	0.157
5	0.245	0.325	0.754
Grain 7			
1	0.105	0.210	0.500
2	0.165	0.245	0.673
3	0.110	0.260	0.423
4	0.375	0.340	1.103
Grain 8			
1	0.170	0.285	0.596
2	0.560	0.310	1.806
3	0.290	0.345	0.841
4	0.275	0.350	0.786
5	0.190	0.350	0.543
6	0.290	0.280	1.036
7	0.510	0.290	1.759
Grain 9			
1	0.225	0.325	0.692
2	0.205	0.375	0.547
3	0.425	0.485	0.876
Grain 10			
1	0.175	0.255	0.686
2	0.100	0.225	0.444
3	0.080	0.250	0.320
4	0.175	0.245	0.714
Grain 11			
1	0.475	0.490	0.969
2	0.260	0.465	0.559
3	0.160	0.445	0.360
4	0.500	0.415	1.205
Grain 12			
1	0.325	0.760	0.428
2	0.625	0.975	0.641
3	0.170	0.925	0.184
4	0.325	0.975	0.333
Grain 13			
1	0.250	0.495	0.505
2	0.190	0.515	0.369

3	0.195	0.485	0.402
4	0.420	0.450	0.933
5	0.310	0.450	0.689
Grain 14			
1	0.695	0.425	1.635
2	0.110	0.410	0.268
3	0.240	0.350	0.686
4	0.275	0.340	0.809
Grain 15			
1	0.815	1.025	0.795
2	0.230	0.765	0.301
3	0.170	0.825	0.206
4	0.375	0.905	0.414
5	0.250	0.950	0.263
6	0.390	0.900	0.433
7	0.330	0.890	0.371
8	0.600	0.840	0.714
Grain 16			
1	0.245	0.225	1.089
2	0.100	0.250	0.400
3	0.615	0.265	2.321
4	0.260	0.240	1.083
Grain 17			
1	0.675	1.125	0.600
2	0.700	0.910	0.769
3	0.190	0.750	0.253
4	0.340	0.650	0.523
5	0.225	0.750	0.300
6	0.800	0.925	0.865
7	0.215	0.925	0.232
8	0.450	0.920	0.489
9	1.275	1.000	1.275
Grain 18			
1	0.525	1.050	0.500
2	0.250	0.975	0.256
3	0.300	0.710	0.423
4	0.200	0.800	0.250
5	0.210	0.690	0.304
6	0.115	0.690	0.167
7	0.650	0.680	0.956
Grain 19			
1	0.250	0.295	0.847
2	0.180	0.365	0.493

3	0.280	0.405	0.691
4	0.135	0.425	0.318

APPENDIX B STRAIN, SHEAR STRESS AND DEFORMATION DEFORMATION ESTIMATED FOR EACH MICROBOUDIN FROM THE STUDIED SAMPLES

Sample-Grain	Gap No.	Natural Strain	Microboudin L/W	Fracture C-value	Shear stress	Estimated T (°C)	Depth (km)	Deformation regime
CM10-Grain 22	Gap 1	0.2320	0.1714	90	131.3	270	13.66	Brittle
CM10-Grain 22	Gap 2	0.2202	0.7571	145	47.9	350	18.98	Ductile
CM10-Grain 22	Gap 3	0.2122	1.5918	145	22.8	400	22.56	Ductile
CM10-Grain1	Gap 1	0.2279	0.2105	115	137.1	280	14.30	Ductile
CM10-Grain1	Gap 2	0.2164	0.3474	145	104.4	300	15.60	Ductile
CM10-Grain1	Gap 3	0.1671	0.8824	145	41.1	350	18.98	Ductile
CM10-Grain1	Gap 4	0.1257	0.8780	145	41.3	360	19.68	Ductile
CM10-Grain1	Gap 5	0.1194	1.1333	145	32.0	370	20.39	Ductile
CM10-Grain1	Gap 6	0.1194	1.2917	145	28.1	390	21.83	Ductile
CM10-Grain10	Gap 1	0.1823	0.1296	70	135.0	250	12.41	Brittle
CM10-Grain10	Gap 2	0.1665	0.0930	45	120.9	280	14.30	Ductile
CM10-Grain10	Gap 3	0.1373	0.3086	115	93.5	295	15.27	Ductile
CM10-Grain10	Gap 4	0.0970	0.2096	75	89.5	305	15.93	Ductile
CM10-Grain10	Gap 5	0.0728	0.2353	75	79.7	320	16.93	Ductile
CM10-Grain10	Gap 6	0.0515	0.2625	75	71.5	320	16.93	Ductile
CM10-Grain10	Gap 7	0.0515	0.6163	145	58.8	330	17.61	Ductile
CM10-Grain10	Gap 8	0.0370	0.4671	90	48.2	350	18.98	Ductile
CM10-Grain10	Gap 9	0.0370	0.3519	60	42.6	360	19.68	Ductile
CM10-Grain11	Gap 1	0.1325	0.1586	87	136.5	270	13.66	Brittle
CM10-Grain11	Gap 2	0.1230	0.4000	145	90.6	300	15.60	Ductile
CM10-Grain11	Gap 3	0.0922	0.4345	115	66.4	320	16.93	Ductile
CM10-Grain11	Gap 4	0.0922	0.9451	145	38.4	360	19.68	Ductile
CM10-Grain11	Gap 5	0.0107	0.7500	90	30.0	390	21.83	Ductile
CM10-Grain12	Gap 1	0.2310	0.4462	145	81.3	310	16.26	Ductile
CM10-Grain12	Gap 2	0.2184	0.7925	145	45.7	350	18.98	Ductile
CM10-Grain13	Gap 1	0.0817	0.3333	145	108.8	300	15.60	Ductile
CM10-Grain13	Gap 2	0.0211	1.1667	145	31.1	380	21.11	Ductile
CM10-Grain14	Gap 1	0.1759	0.2941	145	123.3	280	14.30	Ductile
CM10-Grain14	Gap 2	0.1704	0.2097	90	107.3	300	15.60	Ductile
CM10-Grain14	Gap 3	0.1654	0.1951	70	89.7	310	16.26	Ductile
CM10-Grain14	Gap 4	0.1566	0.4390	145	82.6	320	16.93	Ductile
CM10-Grain14	Gap 5	0.1487	0.6667	145	54.4	340	18.29	Ductile
CM10-Grain14	Gap 6	0.1283	1.1798	200	42.4	350	18.98	Ductile
CM10-Grain14	Gap 7	0.1168	0.8222	130	39.5	360	19.68	Ductile
CM10-Grain14	Gap 8	0.0885	1.0494	145	34.5	370	20.39	Ductile
CM10-Grain14	Gap 9	0.0668	1.6944	145	21.4	400	22.56	Ductile

CM10-Grain15	Gap 1	0.0445	0.2326	115	124.1	280	14.30	Ductile
CM10-Grain15	Gap 2	0.0310	0.6522	145	55.6	340	18.29	Ductile
CM10-Grain15	Gap 3	0.0208	0.9250	145	39.2	360	19.68	Ductile
CM10-Grain15	Gap 4	0.0070	0.8400	115	34.4	370	20.39	Ductile
CM10-Grain16	Gap 1	0.3081	0.4688	145	77.3	310	16.26	Ductile
CM10-Grain16	Gap 2	0.2773	0.6383	145	56.8	330	17.61	Ductile
CM10-Grain16	Gap 3	0.2536	1.6563	145	21.9	400	22.56	Ductile
CM10-Grain16	Gap 4	0.0792	2.8333	145	12.8	450	26.33	Ductile
CM10-Grain17	Gap 1	0.4537	0.2111	115	136.7	280	14.30	Ductile
CM10-Grain17	Gap 2	0.4162	0.3556	145	102.0	300	15.60	Ductile
CM10-Grain17	Gap 3	0.3903	0.8587	145	42.2	350	18.98	Ductile
CM10-Grain18	Gap 1	0.1133	0.8750	145	41.4	340	18.29	Ductile
CM10-Grain18	Gap 2	0.0770	1.0000	145	36.3	360	19.68	Ductile
CM10-Grain19	Gap 1	0.2115	0.4000	200	125.0	280	14.30	Ductile
CM10-Grain19	Gap 2	0.2024	0.1412	60	106.3	290	14.94	Ductile
CM10-Grain19	Gap 3	0.1945	0.2857	105	91.9	300	15.60	Ductile
CM10-Grain19	Gap 4	0.1403	0.4700	145	77.1	310	16.26	Ductile
CM10-Grain19	Gap 5	0.0947	0.6000	145	60.4	320	16.93	Ductile
CM10-Grain19	Gap 6	0.0408	0.3882	90	58.0	340	18.29	Ductile
CM10-Grain19	Gap 7	0.0032	1.4300	145	25.3	400	22.56	Ductile
CM10-Grain2	Gap 1	0.3645	0.0882	50	141.7	270	13.66	Brittle
CM10-Grain2	Gap 2	0.3573	0.1667	90	135.0	290	14.94	Ductile
CM10-Grain2	Gap 3	0.3510	0.1176	45	95.6	300	15.60	Ductile
CM10-Grain2	Gap 4	0.3401	0.5364	175	81.6	310	16.26	Ductile
CM10-Grain2	Gap 5	0.3124	0.2054	60	73.0	320	16.93	Ductile
CM10-Grain2	Gap 6	0.2663	0.3810	90	59.1	340	18.29	Ductile
CM10-Grain2	Gap 7	0.2180	0.3404	60	44.1	360	19.68	Ductile
CM10-Grain2	Gap 8	0.1802	1.4275	145	25.4	400	22.56	Ductile
CM10-Grain20	Gap 1	0.5639	0.0952	50	131.3	250	12.41	Brittle
CM10-Grain20	Gap 10	0.3886	1.1667	145	31.1	380	21.11	Ductile
CM10-Grain20	Gap 11	0.3598	0.9959	105	26.4	390	21.83	Ductile
CM10-Grain20	Gap 12	0.3455	2.1098	145	17.2	430	24.80	Ductile
CM10-Grain20	Gap 2	0.5575	0.1244	70	140.6	270	13.66	Brittle
CM10-Grain20	Gap 3	0.5457	0.2033	105	129.2	280	14.30	Ductile
CM10-Grain20	Gap 4	0.5294	0.2381	105	110.3	285	14.62	Ductile
CM10-Grain20	Gap 5	0.5145	0.2311	90	97.4	290	14.94	Ductile
CM10-Grain20	Gap 6	0.5101	0.3953	145	91.7	300	15.60	Ductile
CM10-Grain20	Gap 7	0.5062	0.2727	90	82.5	310	16.26	Ductile
CM10-Grain20	Gap 8	0.4926	0.7708	145	47.0	350	18.98	Ductile
CM10-Grain20	Gap 9	0.4521	0.6178	90	36.4	370	20.39	Ductile
CM10-Grain21	Gap 1	0.0400	0.3750	145	96.7	300	15.60	Ductile
CM10-Grain21	Gap 2	0.0321	0.4691	145	77.3	320	16.93	Ductile
CM10-Grain21	Gap 3	0.0054	0.9136	145	39.7	360	19.68	Ductile

CM10-Grain23	Gap 1	0.1488	0.1449	80	138.0	260	13.03	Brittle
CM10-Grain23	Gap 2	0.1416	0.2375	100	105.3	300	15.60	Ductile
CM10-Grain23	Gap 3	0.1361	0.5000	145	72.5	320	16.93	Ductile
CM10-Grain23	Gap 4	0.1288	1.2778	145	28.4	380	21.11	Ductile
CM10-Grain24	Gap 1	0.1639	0.4423	200	113.0	290	14.94	Ductile
CM10-Grain24	Gap 2	0.1233	0.1818	70	96.3	300	15.60	Ductile
CM10-Grain24	Gap 3	0.1010	0.1875	60	80.0	310	16.26	Ductile
CM10-Grain24	Gap 4	0.0488	1.2308	145	29.5	380	21.11	Ductile
CM10-Grain24	Gap 5	0.0062	1.7969	145	20.2	410	23.30	Ductile
CM10-Grain25	Gap 1	0.0308	0.4118	145	88.0	300	15.60	Ductile
CM10-Grain25	Gap 2	0.0186	0.5263	145	68.9	320	16.93	Ductile
CM10-Grain3	Gap 1	0.1054	0.5273	175	83.0	300	15.60	Ductile
CM10-Grain3	Gap 2	0.0541	0.5610	145	64.6	330	17.61	Ductile
CM10-Grain3	Gap 3	0.0183	0.8537	145	42.5	360	19.68	Ductile
CM10-Grain4	Gap 1	0.3398	0.4516	145	80.3	310	16.26	Ductile
CM10-Grain4	Gap 2	0.3243	0.6667	145	54.4	340	18.29	Ductile
CM10-Grain4	Gap 3	0.3204	0.8772	145	41.3	360	19.68	Ductile
CM10-Grain4	Gap 4	0.2832	2.3125	145	15.7	430	24.80	Ductile
CM10-Grain5	Gap 1	0.0594	0.2903	145	124.9	290	14.94	Ductile
CM10-Grain5	Gap 2	0.0020	0.9211	145	39.4	360	19.68	Ductile
CM10-Grain5	Gap 3	0.0007	1.4118	145	25.7	400	22.56	Ductile
CM10-Grain6	Gap 1	0.1823	0.2273	115	127.0	280	14.30	Ductile
CM10-Grain6	Gap 2	0.1525	0.7293	200	68.6	320	16.93	Ductile
CM10-Grain6	Gap 3	0.1525	0.6061	130	53.6	340	18.29	Ductile
CM10-Grain6	Gap 4	0.1091	0.3279	60	45.8	350	18.98	Ductile
CM10-Grain6	Gap 5	0.1049	1.4436	145	25.1	400	22.56	Ductile
CM10-Grain7	Gap 1	0.2864	0.2000	105	131.3	260	13.03	Brittle
CM10-Grain7	Gap 2	0.2581	0.2237	115	129.1	300	15.60	Ductile
CM10-Grain7	Gap 3	0.2205	0.3048	100	82.0	315	16.59	Ductile
CM10-Grain7	Gap 4	0.1315	0.6320	145	57.4	330	17.61	Ductile
CM10-Grain7	Gap 5	0.1128	0.4545	90	49.5	340	18.29	Ductile
CM10-Grain7	Gap 6	0.0390	0.8158	145	44.4	350	18.98	Ductile
CM10-Grain7	Gap 7	0.0288	0.8859	130	36.7	370	20.39	Ductile
CM10-Grain8	Gap 1	0.0191	0.5495	145	66.0	320	16.93	Ductile
CM10-Grain8	Gap 2	0.0157	1.1111	145	32.6	380	21.11	Ductile
CM10-Grain9	Gap 1	0.2226	0.7755	345	111.2	300	15.60	Ductile
CM10-Grain9	Gap 2	0.2136	0.2941	90	76.5	320	16.93	Ductile
CM10-Grain9	Gap 3	0.1897	0.8070	200	62.0	330	17.61	Ductile
CM10-Grain9	Gap 4	0.1758	0.6744	145	53.8	340	18.29	Ductile
CM10-Grain9	Gap 5	0.1401	0.9000	145	40.3	360	19.68	Ductile
CM10-Grain9	Gap 6	0.0489	1.0294	145	35.2	370	20.39	Ductile
CM10-Grain9	Gap 7	0.0409	0.5574	70	31.4	380	21.11	Ductile
CM10-Grain9	Gap 8	0.0083	2.3265	145	15.6	440	25.57	Ductile

CM151-A-Grain1	Gap 1	0.1888	0.4722	200	105.9	295	15.60	Ductile
CM151-A-Grain1	Gap 2	0.1448	0.3551	115	81.3	310	16.26	Ductile
CM151-A-Grain1	Gap 3	0.1259	0.5660	145	64.0	330	17.61	Ductile
CM151-A-Grain1	Gap 4	0.1105	1.2130	145	29.9	380	21.11	Ductile
CM151-A-Grain1	Gap 5	0.0870	1.0000	105	26.3	390	21.83	Ductile
CM151-A-Grain1	Gap 6	0.0548	1.9615	145	18.5	420	24.05	Ductile
CM151-A-Grain2	Gap 1	0.0670	0.6222	145	58.3	330	17.61	Ductile
CM151-A-Grain2	Gap 2	0.0424	1.1333	145	32.0	380	21.11	Ductile
CM151-A-Grain3	Gap 1	0.0854	0.4531	145	80.0	300	15.60	Ductile
CM151-A-Grain3	Gap 2	0.0388	1.5571	145	23.3	400	22.56	Ductile
CM151-A-Grain4	Gap 1	0.0392	0.9091	145	39.9	350	18.98	Ductile
CM151-A-Grain4	Gap 2	0.0080	1.0526	145	34.4	380	21.11	Ductile
CM151-A-Grain5	Gap 1	0.2045	2.4000	200	20.8	400	22.56	Ductile
CM151-A-Grain5	Gap 2	0.1572	2.1000	145	17.3	420	24.05	Ductile
CM151-B-Grain1	Gap 1	0.0899	0.5122	145	70.8	320	16.93	Ductile
CM151-B-Grain1	Gap 2	0.0739	0.9647	230	59.6	330	17.61	Ductile
CM151-B-Grain1	Gap 3	0.0608	0.3600	70	48.6	340	18.29	Ductile
CM151-B-Grain1	Gap 4	0.0509	0.7895	145	45.9	350	18.98	Ductile
CM151-B-Grain1	Gap 5	0.0309	1.4800	145	24.5	400	22.56	Ductile
CM151-B-Grain2	Gap 1	0.0185	0.6207	145	58.4	330	17.61	Ductile
CM151-B-Grain2	Gap 2	0.0037	1.0909	145	33.2	380	21.11	Ductile
CM151-B-Grain3	Gap 1	0.2607	0.4508	145	80.4	300	15.60	Ductile
CM151-B-Grain3	Gap 2	0.1929	0.3409	90	66.0	320	16.93	Ductile
CM151-B-Grain3	Gap 3	0.1730	0.7857	145	46.1	350	18.98	Ductile
CM151-B-Grain3	Gap 4	0.1272	0.9098	145	39.8	360	19.68	Ductile
CM151-B-Grain4	Gap 1	0.0888	0.2500	135	135.0	250	12.41	Brittle
CM151-B-Grain4	Gap 2	0.0830	0.2667	90	84.4	310	16.26	Ductile
CM151-B-Grain4	Gap 3	0.0783	0.7333	145	49.4	340	18.29	Ductile
CM151-B-Grain4	Gap 4	0.0569	1.8438	200	27.1	380	21.11	Ductile
CM151-B-Grain4	Gap 5	0.0226	1.7361	145	20.9	400	22.56	Ductile
CM151-C-Grain1	Gap 1	0.2106	0.2538	135	133.0	260	13.03	Brittle
CM151-C-Grain1	Gap 2	0.0458	0.2813	90	80.0	310	16.26	Ductile
CM151-C-Grain1	Gap 3	0.0232	1.4800	175	29.6	380	21.11	Ductile
CM151-C-Grain1	Gap 4	0.0078	1.5478	145	23.4	400	22.56	Ductile
CM151-C-Grain2	Gap 1	0.0473	0.7778	145	46.6	350	18.98	Ductile
CM151-C-Grain2	Gap 2	0.0160	2.5000	145	14.5	440	25.57	Ductile
CM151-C-Grain3	Gap 1	0.1009	1.2500	145	29.0	370	20.39	Ductile
CM151-C-Grain3	Gap 2	0.0630	1.4565	145	24.9	390	21.83	Ductile
CM151-C-Grain3	Gap 3	0.0566	2.2000	145	16.5	430	24.80	Ductile
CM151-C-Grain4	Gap 1	0.1341	1.4200	145	25.5	400	22.56	Ductile
CM45-E1-grain1	Gap 1	0.3619	0.4348	175	100.6	290	14.94	Ductile
CM45-E1-grain1	Gap 2	0.3411	0.3889	130	83.6	307	16.05	Ductile
CM45-E1-grain1	Gap 3	0.3411	0.5000	145	72.5	312	16.42	Ductile

CM45-E1-grain1	Gap 4	0.3247	0.6889	175	63.5	320	16.93	Ductile
CM45-E1-grain1	Gap 5	0.3247	0.3750	90	60.0	330	17.61	Ductile
CM45-E1-grain1	Gap 6	0.3128	0.4355	85	48.8	340	18.29	Ductile
CM45-E1-grain1	Gap 7	0.2433	0.3103	60	48.3	350	18.98	Ductile
CM45-E1-grain1	Gap 8	0.2039	1.3194	145	27.5	380	21.11	Ductile
CM45-E1-grain1	Gap 9	0.1768	1.1538	115	25.0	400	22.56	Ductile
CM45-E1-grain10	Gap 1	0.1758	0.0762	45	147.7	250	12.41	Brittle
CM45-E1-grain10	Gap 2	0.1451	0.3333	145	108.8	300	15.60	Ductile
CM45-E1-grain10	Gap 3	0.1373	0.4750	145	76.3	310	16.26	Ductile
CM45-E1-grain10	Gap 4	0.1320	0.4651	115	62.1	330	17.61	Ductile
CM45-E1-grain11	Gap 1	0.0904	0.0909	50	137.5	250	12.41	Brittle
CM45-E1-grain11	Gap 2	0.0880	0.2727	90	82.5	320	16.93	Ductile
CM45-E1-grain11	Gap 3	0.0814	0.7500	145	48.3	350	18.98	Ductile
CM45-E1-grain12	Gap 1	0.1962	0.3793	145	95.6	300	15.60	Ductile
CM45-E1-grain12	Gap 2	0.1842	0.3636	115	79.4	320	16.93	Ductile
CM45-E1-grain12	Gap 3	0.1550	0.6731	145	53.9	340	18.29	Ductile
CM45-E1-grain12	Gap 4	0.1094	0.7143	145	50.8	350	18.98	Ductile
CM45-E1-grain12	Gap 5	0.0778	1.6250	145	22.3	400	22.56	Ductile
CM45-E1-grain13	Gap 1	0.3646	0.2353	115	122.7	290	14.94	Ductile
CM45-E1-grain13	Gap 2	0.3623	0.7059	145	51.4	340	18.29	Ductile
CM45-E1-grain13	Gap 3	0.2495	0.7692	145	47.1	350	18.98	Ductile
CM45-E1-grain14	Gap 1	0.2637	0.3600	145	100.7	300	15.60	Ductile
CM45-E1-grain14	Gap 2	0.2345	0.3610	115	80.0	320	16.93	Ductile
CM45-E1-grain14	Gap 3	0.2297	0.7100	145	51.1	340	18.29	Ductile
CM45-E1-grain14	Gap 4	0.0668	0.6905	115	41.8	360	19.68	Ductile
CM45-E1-grain14	Gap 5	0.0267	1.4043	145	25.8	400	22.56	Ductile
CM45-E1-grain15	Gap 1	0.2674	0.4286	145	84.6	300	15.60	Ductile
CM45-E1-grain15	Gap 2	0.2307	0.5000	145	72.5	320	16.93	Ductile
CM45-E1-grain15	Gap 3	0.2002	0.8667	145	41.8	360	19.68	Ductile
CM45-E1-grain15	Gap 4	0.1528	0.6383	90	35.3	380	21.11	Ductile
CM45-E1-grain15	Gap 5	0.1447	2.3415	145	15.5	430	24.80	Ductile
CM45-E1-grain16	Gap 1	0.1421	0.4143	145	87.5	300	15.60	Ductile
CM45-E1-grain16	Gap 2	0.1326	0.7100	145	51.1	340	18.29	Ductile
CM45-E1-grain16	Gap 3	0.1068	1.0309	145	35.2	370	20.39	Ductile
CM45-E1-grain17	Gap 1	0.3019	0.2857	145	126.9	290	14.94	Ductile
CM45-E1-grain17	Gap 2	0.2979	0.5909	170	71.9	310	16.26	Ductile
CM45-E1-grain17	Gap 3	0.2600	0.1600	45	70.3	320	16.93	Ductile
CM45-E1-grain17	Gap 4	0.2257	0.8571	145	42.3	360	19.68	Ductile
CM45-E1-grain17	Gap 5	0.1902	1.5714	145	23.1	400	22.56	Ductile
CM45-E1-grain17	Gap 6	0.0091	0.5419	45	20.8	410	23.30	Ductile
CM45-E1-grain18	Gap 1	0.0323	0.9091	145	39.9	360	19.68	Ductile
CM45-E1-grain18	Gap 2	0.0243	1.1806	145	30.7	380	21.11	Ductile
CM45-E1-grain19	Gap 1	0.0760	0.2727	145	132.9	290	14.94	Ductile

CM45-E1-grain19	Gap 2	0.0620	0.4333	145	83.7	310	16.26	Ductile
CM45-E1-grain19	Gap 3	0.0513	0.7368	145	49.2	340	18.29	Ductile
CM45-E1-grain19	Gap 4	0.0075	1.0000	145	36.3	370	20.39	Ductile
CM45-E1-grain2	Gap 1	0.3677	0.3953	145	91.7	300	15.60	Ductile
CM45-E1-grain2	Gap 2	0.0616	0.7222	145	50.2	350	18.98	Ductile
CM45-E1-grain2	Gap 3	0.0157	1.7442	145	20.8	400	22.56	Ductile
CM45-E1-grain20	Gap 1	0.0600	0.1622	90	138.8	290	14.94	Ductile
CM45-E1-grain20	Gap 2	0.0510	0.3797	145	95.5	310	16.26	Ductile
CM45-E1-grain20	Gap 3	0.0235	0.8824	145	41.1	360	19.68	Ductile
CM45-E1-grain20	Gap 4	0.0047	2.1212	145	17.1	430	24.80	Ductile
CM45-E1-grain21	Gap 1	0.2074	0.3158	145	114.8	290	14.94	Ductile
CM45-E1-grain21	Gap 2	0.1795	0.3048	115	94.7	300	15.60	Ductile
CM45-E1-grain21	Gap 3	0.1681	0.8571	145	42.3	350	18.98	Ductile
CM45-E1-grain21	Gap 4	0.0301	0.8000	115	36.1	360	19.68	Ductile
CM45-E1-grain21	Gap 5	0.0168	1.6190	145	22.4	400	22.56	Ductile
CM45-E1-grain22	Gap 1	0.1141	0.2363	130	137.6	250	12.41	Brittle
CM45-E1-grain22	Gap 2	0.0800	0.4412	145	82.2	300	15.60	Ductile
CM45-E1-grain22	Gap 3	0.0488	0.4960	145	73.1	320	16.93	Ductile
CM45-E1-grain23	Gap 1	0.2605	0.1875	90	120.0	240	11.79	Brittle
CM45-E1-grain23	Gap 2	0.2500	0.3939	145	92.0	300	15.60	Ductile
CM45-E1-grain23	Gap 3	0.2407	0.5000	145	72.5	320	16.93	Ductile
CM45-E1-grain23	Gap 4	0.2245	0.7080	170	60.0	330	17.61	Ductile
CM45-E1-grain23	Gap 5	0.1970	0.1241	30	60.4	340	18.29	Ductile
CM45-E1-grain23	Gap 6	0.1914	0.5037	90	44.7	350	18.98	Ductile
CM45-E1-grain23	Gap 7	0.1744	1.2303	145	29.5	380	21.11	Ductile
CM45-E1-grain23	Gap 8	0.1600	0.5396	60	27.8	390	21.83	Ductile
CM45-E1-grain24	Gap 1	0.1420	0.2900	145	125.0	290	14.94	Ductile
CM45-E1-grain24	Gap 2	0.1341	0.6818	145	53.2	340	18.29	Ductile
CM45-E1-grain24	Gap 3	0.0532	0.9394	145	38.6	360	19.68	Ductile
CM45-E1-grain24	Gap 4	0.0402	0.7250	90	31.0	380	21.11	Ductile
CM45-E1-grain25	Gap 1	0.3137	0.2857	145	126.9	280	14.30	Ductile
CM45-E1-grain25	Gap 2	0.2687	0.3438	145	105.5	300	15.60	Ductile
CM45-E1-grain25	Gap 3	0.2484	0.4000	145	90.6	310	16.26	Ductile
CM45-E1-grain25	Gap 4	0.2126	0.4400	115	65.6	330	17.61	Ductile
CM45-E1-grain25	Gap 5	0.1972	1.0625	145	34.1	360	19.68	Ductile
CM45-E1-grain25	Gap 6	0.1972	0.6852	85	31.0	380	21.11	Ductile
CM45-E1-grain25	Gap 7	0.1401	1.7069	145	21.2	400	22.56	Ductile
CM45-E1-grain25	Gap 8	0.0584	2.1250	145	17.1	430	24.80	Ductile
CM45-E1-grain26	Gap 1	0.3612	0.1538	90	146.3	270	13.66	Brittle
CM45-E1-grain26	Gap 2	0.3182	0.3178	145	114.1	300	15.60	Ductile
CM45-E1-grain26	Gap 3	0.2915	0.7048	145	51.4	340	18.29	Ductile
CM45-E1-grain26	Gap 4	0.1768	0.8974	145	40.4	360	19.68	Ductile
CM45-E1-grain26	Gap 5	0.0868	0.7436	90	30.3	380	21.11	Ductile

CM45-E1-grain27	Gap 1	0.1357	0.1273	65	127.7	240	11.79	Brittle
CM45-E1-grain27	Gap 2	0.1054	0.9091	145	39.9	360	19.68	Ductile
CM45-E1-grain28	Gap 1	0.1431	0.5714	145	63.4	330	17.61	Ductile
CM45-E1-grain28	Gap 2	0.1263	1.1034	145	32.9	380	21.11	Ductile
CM45-E1-grain3	Gap 1	0.0961	0.6316	145	57.4	320	16.93	Ductile
CM45-E1-grain3	Gap 2	0.0292	0.5333	105	49.2	340	18.29	Ductile
CM45-E1-grain3	Gap 3	0.0176	1.0333	145	35.1	360	19.68	Ductile
CM45-E1-grain4	Gap 1	0.0226	0.4737	145	76.5	320	16.93	Ductile
CM45-E1-grain4	Gap 2	0.0000	0.6667	145	54.4	340	18.29	Ductile
CM45-E1-grain5	Gap 1	0.1536	0.1875	95	127.0	240	11.79	Brittle
CM45-E1-grain5	Gap 2	0.1369	0.4615	145	78.5	310	16.26	Ductile
CM45-E1-grain5	Gap 3	0.1301	0.5472	145	66.3	320	16.93	Ductile
CM45-E1-grain5	Gap 4	0.0726	0.3934	85	54.0	340	18.29	Ductile
CM45-E1-grain5	Gap 5	0.0134	1.5000	145	24.2	400	22.56	Ductile
CM45-E1-grain6	Gap 1	0.0796	0.3152	145	115.0	290	14.94	Ductile
CM45-E1-grain6	Gap 2	0.0690	0.5639	145	64.3	330	17.61	Ductile
CM45-E1-grain6	Gap 3	0.0529	0.9524	145	38.1	360	19.68	Ductile
CM45-E1-grain6	Gap 4	0.0309	1.2000	145	30.2	380	21.11	Ductile
CM45-E1-grain7	Gap 1	0.1452	0.5208	170	81.6	300	15.60	Ductile
CM45-E1-grain7	Gap 2	0.1328	0.2841	90	79.2	320	16.93	Ductile
CM45-E1-grain7	Gap 3	0.1127	0.6333	145	57.2	330	17.61	Ductile
CM45-E1-grain7	Gap 4	0.0579	0.1667	30	45.0	350	18.98	Ductile
CM45-E1-grain7	Gap 5	0.0526	1.7526	145	20.7	400	22.56	Ductile
CM45-E1-grain8	Gap 1	0.4629	0.1926	105	136.3	240	11.79	Brittle
CM45-E1-grain8	Gap 2	0.4510	0.4552	145	79.6	310	16.26	Ductile
CM45-E1-grain8	Gap 3	0.3813	0.1596	45	70.5	320	16.93	Ductile
CM45-E1-grain8	Gap 4	0.3657	0.8276	145	43.8	350	18.98	Ductile
CM45-E1-grain8	Gap 5	0.3445	0.4167	60	36.0	370	20.39	Ductile
CM45-E1-grain9	Gap 1	0.1489	0.3200	145	113.3	290	14.94	Ductile
CM45-E1-grain9	Gap 2	0.1411	0.1130	45	99.5	300	15.60	Ductile
CM45-E1-grain9	Gap 3	0.1345	0.4639	145	78.1	310	16.26	Ductile
CM45-E1-grain9	Gap 4	0.0967	0.5039	145	71.9	320	16.93	Ductile
CM45-E1-grain9	Gap 5	0.0926	0.8899	145	40.7	360	19.68	Ductile
CM45-E1-grain9	Gap 6	0.0240	0.4737	60	31.7	380	21.11	Ductile
CM45-E2-Grain1	Gap 1	0.1054	0.2522	140	138.8	260	13.03	Brittle
CM45-E2-Grain1	Gap 2	0.0942	0.4105	145	88.3	300	15.60	Ductile
CM45-E2-Grain1	Gap 3	0.0560	0.6783	145	53.4	340	18.29	Ductile
CM45-E2-Grain10	Gap 1	0.1447	0.3200	145	113.3	300	15.60	Ductile
CM45-E2-Grain10	Gap 2	0.1324	0.7143	145	50.8	350	18.98	Ductile
CM45-E2-Grain10	Gap 3	0.0902	0.6863	90	32.8	380	21.11	Ductile
CM45-E2-Grain11	Gap 1	0.0107	0.3596	145	100.8	300	15.60	Ductile
CM45-E2-Grain11	Gap 2	0.0054	0.5591	145	64.8	330	17.61	Ductile
CM45-E2-Grain11	Gap 3	0.0018	0.9694	145	37.4	360	19.68	Ductile

CM45-E2-Grain12	Gap 1	0.1050	0.1838	105	142.8	260	13.03	Brittle
CM45-E2-Grain12	Gap 2	0.0956	0.4276	145	84.8	305	15.93	Ductile
CM45-E2-Grain12	Gap 3	0.0572	0.5077	145	71.4	320	16.93	Ductile
CM45-E2-Grain13	Gap 1	0.1942	0.3689	145	98.3	300	15.60	Ductile
CM45-E2-Grain13	Gap 2	0.1893	0.6889	145	52.6	340	18.29	Ductile
CM45-E2-Grain13	Gap 3	0.1884	0.7476	145	48.5	350	18.98	Ductile
CM45-E2-Grain13	Gap 4	0.1878	0.5051	60	29.7	390	21.83	Ductile
CM45-E2-Grain14	Gap 1	0.0517	0.2683	145	135.1	280	14.30	Ductile
CM45-E2-Grain14	Gap 2	0.0408	0.6857	145	52.9	340	18.29	Ductile
CM45-E2-Grain14	Gap 3	0.0335	1.4714	145	24.6	400	22.56	Ductile
CM45-E2-Grain15	Gap 1	0.2338	0.2632	145	137.8	270	13.66	Brittle
CM45-E2-Grain15	Gap 2	0.2250	0.3708	145	97.8	300	15.60	Ductile
CM45-E2-Grain15	Gap 3	0.2212	0.2061	70	84.9	310	16.26	Ductile
CM45-E2-Grain15	Gap 4	0.2181	0.3007	90	74.8	320	16.93	Ductile
CM45-E2-Grain15	Gap 5	0.1818	0.7143	145	50.8	335	17.95	Ductile
CM45-E2-Grain15	Gap 6	0.1537	0.8368	145	43.3	350	18.98	Ductile
CM45-E2-Grain15	Gap 7	0.0204	1.0195	145	35.6	370	20.39	Ductile
CM45-E2-Grain16	Gap 1	0.2231	0.4000	145	90.6	300	15.60	Ductile
CM45-E2-Grain16	Gap 2	0.2133	1.3800	175	31.7	370	20.39	Ductile
CM45-E2-Grain16	Gap 3	0.0163	1.0833	115	26.6	390	21.83	Ductile
CM45-E2-Grain17	Gap 1	0.3062	0.2324	130	139.8	260	13.03	Brittle
CM45-E2-Grain17	Gap 2	0.3032	0.4891	170	86.9	290	14.94	Ductile
CM45-E2-Grain17	Gap 3	0.3006	0.2533	90	88.8	300	15.60	Ductile
CM45-E2-Grain17	Gap 4	0.2983	0.7067	200	70.8	310	16.26	Ductile
CM45-E2-Grain17	Gap 5	0.2614	0.3000	70	58.3	320	16.93	Ductile
CM45-E2-Grain17	Gap 6	0.2582	0.6000	115	48.1	350	18.98	Ductile
CM45-E2-Grain17	Gap 7	0.2463	1.2750	145	28.4	380	21.11	Ductile
CM45-E2-Grain17	Gap 8	0.0656	1.8933	145	19.1	420	24.05	Ductile
CM45-E2-Grain18	Gap 1	0.3253	0.1667	95	142.9	250	12.41	Brittle
CM45-E2-Grain18	Gap 2	0.3205	0.2500	145	145.0	280	14.30	Ductile
CM45-E2-Grain18	Gap 3	0.3124	0.2564	145	141.4	290	14.94	Ductile
CM45-E2-Grain18	Gap 4	0.3091	0.4225	145	85.8	310	16.26	Ductile
CM45-E2-Grain18	Gap 5	0.2329	0.6563	145	55.2	340	18.29	Ductile
CM45-E2-Grain18	Gap 6	0.1786	0.9559	145	37.9	360	19.68	Ductile
CM45-E2-Grain19	Gap 1	0.1213	0.3176	145	114.1	290	14.94	Ductile
CM45-E2-Grain19	Gap 2	0.1166	0.4932	145	73.5	320	16.93	Ductile
CM45-E2-Grain19	Gap 3	0.1145	0.8475	145	42.8	350	18.98	Ductile
CM45-E2-Grain2	Gap 1	0.1499	0.0777	45	144.8	260	13.03	Brittle
CM45-E2-Grain2	Gap 2	0.1485	0.1887	90	119.3	290	14.94	Ductile
CM45-E2-Grain2	Gap 3	0.1435	0.4135	145	87.7	300	15.60	Ductile
CM45-E2-Grain2	Gap 4	0.1383	0.5375	145	67.4	320	16.93	Ductile
CM45-E2-Grain2	Gap 5	0.1215	0.7549	145	48.0	350	18.98	Ductile
CM45-E2-Grain2	Gap 6	0.0353	1.0556	145	34.3	370	20.39	Ductile

CM45-E2-Grain2	Gap 7	0.0306	1.9565	145	18.5	420	24.05	Ductile
CM45-E2-Grain3	Gap 1	0.5694	0.2778	145	130.5	280	14.30	Ductile
CM45-E2-Grain3	Gap 2	0.5375	0.6795	170	62.5	320	16.93	Ductile
CM45-E2-Grain3	Gap 3	0.5281	0.4096	100	61.0	330	17.61	Ductile
CM45-E2-Grain3	Gap 4	0.5203	0.9157	175	47.8	340	18.29	Ductile
CM45-E2-Grain3	Gap 5	0.4553	0.5140	90	43.8	350	18.98	Ductile
CM45-E2-Grain3	Gap 6	0.3768	1.0654	145	34.0	370	20.39	Ductile
CM45-E2-Grain3	Gap 7	0.3361	1.5783	145	23.0	400	22.56	Ductile
CM45-E2-Grain4	Gap 1	0.0310	0.3200	145	113.3	290	14.94	Ductile
CM45-E2-Grain4	Gap 2	0.0179	0.4483	145	80.9	310	16.26	Ductile
CM45-E2-Grain4	Gap 3	0.0090	1.8261	145	19.9	420	24.05	Ductile
CM45-E2-Grain5	Gap 1	0.3060	0.2652	145	136.7	280	14.30	Ductile
CM45-E2-Grain5	Gap 2	0.2887	0.8864	145	40.9	360	19.68	Ductile
CM45-E2-Grain6	Gap 1	0.1036	0.1571	90	143.2	270	13.66	Brittle
CM45-E2-Grain6	Gap 2	0.0908	0.8049	175	54.4	340	18.29	Ductile
CM45-E2-Grain6	Gap 3	0.0811	0.2500	45	45.0	360	19.68	Ductile
CM45-E2-Grain6	Gap 4	0.0681	1.1000	145	33.0	380	21.11	Ductile
CM45-E2-Grain7	Gap 1	0.0579	0.5000	200	100.0	300	15.60	Ductile
CM45-E2-Grain7	Gap 2	0.0197	0.4231	115	68.2	320	16.93	Ductile
CM45-E2-Grain7	Gap 3	0.0066	1.1020	145	32.9	380	21.11	Ductile
CM45-E2-Grain8	Gap 1	0.1576	0.5429	175	80.6	310	16.26	Ductile
CM45-E2-Grain8	Gap 2	0.1463	1.0357	145	35.0	360	19.68	Ductile
CM45-E2-Grain8	Gap 3	0.0879	1.3286	175	32.9	380	21.11	Ductile
CM45-E2-Grain8	Gap 4	0.0553	0.8406	90	26.8	400	22.56	Ductile
CM45-E2-Grain8	Gap 5	0.0365	0.5965	60	25.1	410	23.30	Ductile
CM45-E2-Grain8	Gap 6	0.0323	2.9565	145	12.3	450	26.33	Ductile
CM45-E2-Grain9	Gap 1	0.0841	0.5467	145	66.3	320	16.93	Ductile
CM45-E2-Grain9	Gap 2	0.0733	0.8763	145	41.4	360	19.68	Ductile